Small scale tectonism on Venus: an experimental and image based study.

Matthew Russell Balme

Dept. of Geological Sciences
University College London
Gower Street
London WC1E 6BT

This thesis is submitted for the degree of Doctor of Philosophy at the University College London.

January 2001

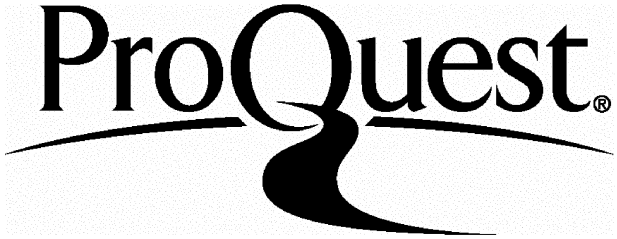

Abstract.

Closely spaced parallel lineations in the plains of Venus are interpreted as extensional rubble-filled fractures because they show no structure and are radar-bright irrespective of look angle. Their formation was investigated using a new methodology which combines material science and fracture mechanics principles together with experimental measurement and the analysis of Magellan data.

Mapping in the Guinevere and Sedna Planitia regions shows that the closely spaced parallel fractures (CSPF) follow a concentric pattern around the edge of the large topographic rise of Western Eistla Regio. 13 spacing profiles show that most of the CSPF have spacings of between 0.8 and 1.2km.

Using a new fracture mechanics apparatus designed to simulate Venusian surface conditions (90bar of CO_2, 450°C), the fracture toughness of basalt was measured from atmospheric to 200 bar confining pressure and from room temperature to 600°C. Fracture toughness was found to increase from ~2.4 $MPam^{1/2}$ at ambient pressure to about ~3.0 $MPam^{1/2}$ at 50 bar confining pressure. Higher confining pressures have no further effect. Fracture toughness shows no clear trend with temperature, rising from an ambient level of ~2.4$MPam^{1/2}$ to ~3.0$MPa^{1/2}$ at 150°C and returning to ~2.4$MPam^{1/2}$ at higher temperatures.

A new, two-dimensional model based upon fracture mechanics is described. The depth of the CSPF is controlled by the stress intensity factor but their spacing is controlled by the initiation of new cracks. Application of a faulting criterion to limit the conditions under which the CSPF can form shows that the spacing is consistent with a regional tensile stress of 5.5-8.5MPa. This stress could have resulted from uplift of Western Eistla Regio by ~2km.

Contents.

List of figures.

Figures contained in chapter 3.

Figures contained in chapter 4.

Figures contained in chapter 5.

Figures contained in chapter 6.

Figures contained in chapter 7.

Figures contained in chapter 8.

Figures contained in chapter 9.

Figures contained in chapter 10.

Figures contained in chapter 11.

Figures contained in appendix I.

List of tables.

Table contained in chapter 10.

Tables contained in appendix I.

List of symbols.

a	crack length (in specimens or in half plane)
A	area
b	crack half width; 2b = crack spacing in chapter 10
c	crack half length
c_0	critical crack length
C_k	specimen size correction factor
C_m	penetration coefficient
d	depth; spacing of fractures in shear lag model
D	diameter (of specimens)
E	Young's modulus
E'	Young's modulus in plane stress
f	friction factor
F	force
F_c	corrected force (in level II tests)
F_i	force at i^{th} cycle in level II test
F_{max}	force required for specimen failure
g	gravitational strength; sample geometry based compliance
G	fracture energy
H	enthalpy
i	subscript meaning 'initial'
I	impulse
k	thermal diffusivity
K	stress intensity factor; level I fracture toughness; bulk modulus; pressure vessel wall thickness parameter
K_c	fracture toughness (in measurements, corrected for anelasticity)
L	latent heat of fusion
m	mass
P	anelasticity correction factor
P	pressure
P_y	yield pressure

P_b burst pressure

Q Heat loss from a surface.

R Rheological function; crack resistance energy

r statistical correlation factor; distance

Re Reynolds number

s slot thickness (in specimens)

s_0 inherent shear stress

S rock mass fracture resistance; stiffness

t slit width (in specimens); penetration depth of fragments

T temperature

T_m temperature of molten material

T_o ambient temperature; tensile strength

U energy of a system

u velocity of lava flow

U_A loading system energy

U_E elastic strain energy

U_m mechanical energy

U_s surface energy

V voltage; velocity

V_p P wave velocity

V_s S wave velocity

w length (of specimens)

x distance

X_c critical spacing of fractures in shear lag model

Y non-dimensional stress intensity factor

z depth of crack penetration; depth into the crust

α slope; a/D (for Matsuki method calculations)

χ P-wave modulus

ε strain

γ free energy per unit area of a crack surface

λ fluid pressure factor

μ	coefficient of friction
θ	chevron notch angle (in specimens)
ρ	density
σ	standard deviation; stress
σ_{ij}	stress tensor
τ	shear stress
ν	kinematic viscosity; Poisson's ratio
ν_0	Poisson's ratio for undamaged sample

List of abbreviations.

4WD	four wheel drive (vehicle)
BL	Bridge logger
CB	chevron bend
CMOD	crack mouth opening displacement
CRB	Columbia River basalt
CRBG	Columbia River basalt group
CSPF	closely spaced parallel fractures
FMIDR	full resolution mosaicked image data record
GRS	gamma ray spectroscopy
HPTA	high pressure technology association
IDT	inductive displacement transducer
ISRM	international society for rock mechanics
LEFM	linear elastic fracture mechanics
LVDT	linear voltage displacement transducer
MIDR	mosaicked image data record
MORB	mid-ocean ridge basalt
SAR	synthetic aperture radar
SEM	scanning electron microscope
SL	setup logger
SR	short rod
VI	virtual instrument
WR	wrinkle ridge
XRF	X-ray fluorescence

Acknowledgements.

Primarily, I would like to thank my supervisors, Peter Sammonds and Claudio Vita-Finzi, for their support and advice over the period of this PhD and to honestly say that I cannot see how their complementary strengths as advisers could be bettered. I would also like to show my respect for Phil Meredith, whose advice has been invaluable to me.

This project would never have been able to continue without the support of the Rock and Ice Physics experimental officers and I hope John Bowles, Neil Hughes and Steve Boon will remember me as fondly in years to come as I will them. Other past and present members of the Rock and Ice Physics Laboratory I would like to thank for their advice and friendship include Valentina Rocchi, Oswald Clint, Cathy Stafford, Colin Jones and Steve Covey-Crump. Friday football will also be sorely missed.

I would like to thank John Guest, Ellen Stofan and Chris Kilburn for their help with all things planetary or volcanological. Jim Davey, Andy Beard, Celine Murphy, Ron Dudman, Leisa Clemente, Toby Stiles, Danuta Kaminski and Richard Rabe and others are thanked for their frequent and good-natured assistance in a variety of fields.

I acknowledge the UCL graduate school and central research fund for funding essential to my research and NERC who sponsored me during this project.

I wish to acknowledge Francesco Stoppa for his guidance in Italy and Kirsty Langley and Haldor Torfason for their assistance during my expedition to Iceland. For help in my African adventure, I would also thank Matt Genge, Adrian Jones, Alex Magayane of the Tanzanian Ministry of Energy and Minerals, Tony Church of Safari's Unlimited and Burra Gadiye, the Lengai guide.

In the houmous eating planetary group I thank Antony Brian, Emma Bowden, Paula Martin, Dominic Fortes, Louise Bishop, Pete Grindrod and Veronica Bray for being tolerant and good-humoured work-mates and ex RPIF members Sarah Dunkin

and Dave Heather, who inspired me to venture into the world of scientific outreach. I would also like to say a huge thankyou to the whole UCL Geology department for the friendly and welcoming attitude displayed by staff and students alike. In particular, cheers to Dave Hodgson and Matt Phillips who I feel I have known longer than these few years.

Finally I would like to thank Naomi, Jon, Gayle, Ollie and Anne for putting up with me in one way or another over these last three years and my parents for putting up with me for even longer.

Chapter 1

Introduction.

1.1. Venus: background and current research.

Venus could almost be termed Earth's twin, so similar is it in size and mass. However, Venus has a much thicker atmosphere and is surrounded by a dense mass of clouds making visual observations of the surface impossible. There was much speculation about the nature of the Venusian surface prior to the space age, and the exploration of Venus by the NASA Pioneer Venus spacecraft and the Russian Venera and Vega missions increased our knowledge of the planet considerably. It was the spectacular radar imagery of the NASA Magellan mission in the early 1990s, however, that really captured the imagination of scientists and general public alike (see for instance Magellan at Venus special edition of Journal of Geophysical Research (1992) or Cattermole, 1994). Figure 1.1 shows a global topographic map of Venus generated from Magellan data and some important physical properties of Earth and Venus are shown in table 1.1.

Property	Venus	Earth
Mass /kg	4.87×10^{24}	5.98×10^{24}
Mean Density /kgm^{-3}	5420	5520
Surface gravity /ms^{-2}	8.87	9.78
Equatorial radius /km	6051	6378
Mean orbital radius /au	0.73	1.0
Orbital period /days	224.7	365.25
Sidereal rotational period	243 days	23.9 hours
Mean surface temperature /°C	468	15
Mean surface pressure /MPa	0.9	0.1
Atmospheric composition	CO_2	N_2, O_2

Table 1.1. Physical properties of Earth and Venus.

The surface conditions on Venus are very different from those of Earth, despite the similarities in size and mass. Because there is no water or vegetation to hide the geology of Venus and the atmosphere protects the planet from the regolith-forming action of small impacts, the geological record is almost pristine, thus spacecraft images are especially useful in unravelling the geological history of the surface. Probably the most important discoveries made by the Magellan mission are the fact that Venus has no plate tectonics (Solomon *et al.*, 1991) and that it has a paucity of impact craters (Schaber *et al.*, 1992), implying a relatively young surface (Nimmo and McKenzie, 1998).

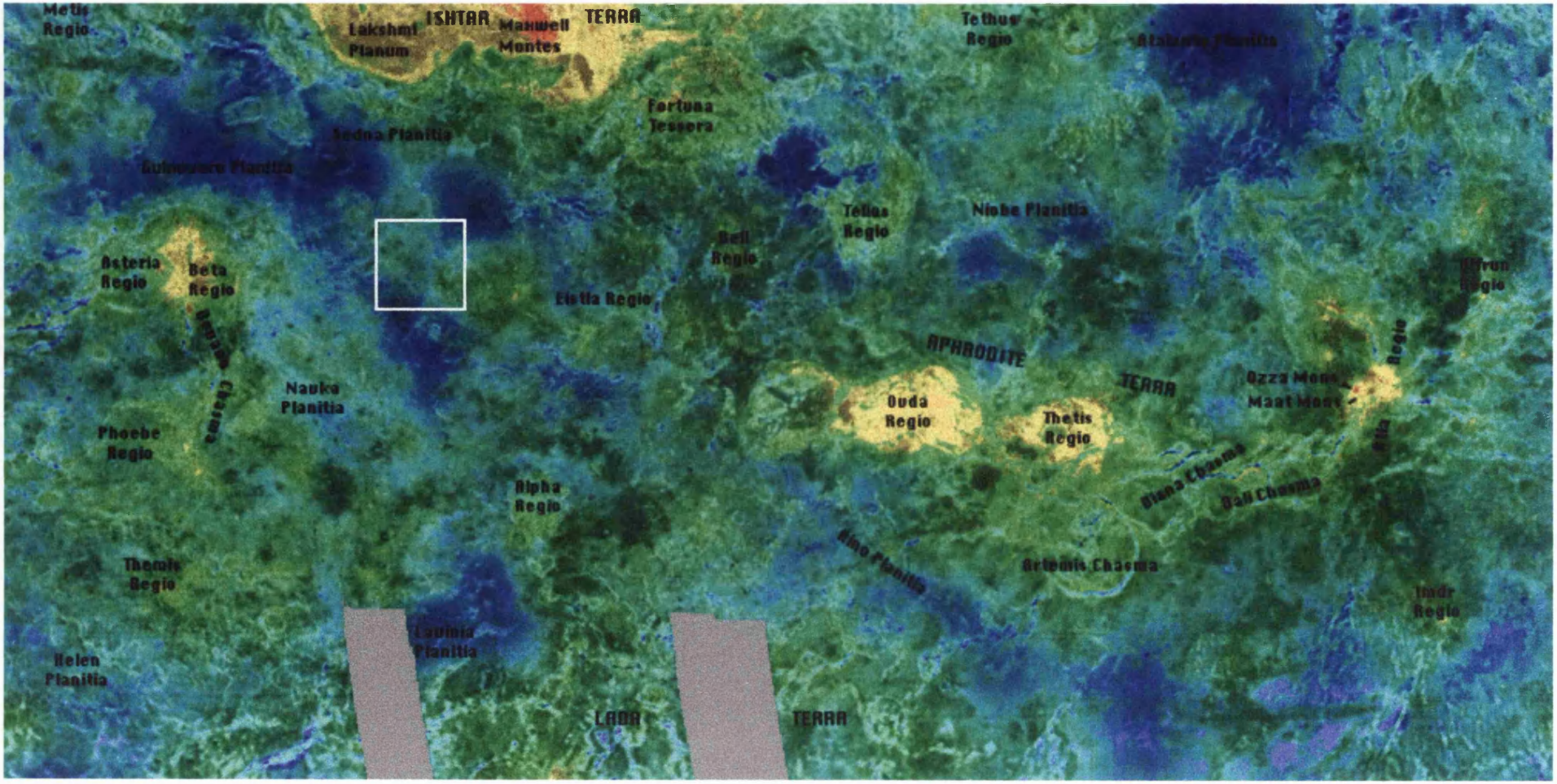

Fig. 1.1. Global topographic map of Venus produced by NASA. The height of the topography is represented by the colour (warm colours are high, cool colours low). Map is centred on 60°E and extends FROM 120°W to 240°E and 65°S to 65°N. The most dense occurrence of CSPF is found in the area boxed in white. This area is the study area of this project.

As Schubert *et al.* (1997) point out, plate tectonics is an important heat loss mechanism on Earth and the absence of such a mechanism on Venus has important effects on the thermal evolution of the planet. Recent work suggests that internal heat production of Earth and Venus is similar but scales directly with the mass of the planet. This means either that the mantle of Venus heating up, or that there are other sources of heat loss.

The low density and near random distribution of impact craters have been used to suggest that there was a global resurfacing event 400-700Ma (Strom *et al.*, 1994), although some authors (e.g. Phillips, 1992) suggest that resurfacing was more localised and not so temporally constrained (the equilibrium resurfacing theory). See Basilevsky *et al.* (1997).

1.2. The plains of Venus.

Plains units make up as much as 80% of Venus' surface (Masurky *et al.*, 1980). The plains of Venus are typically deformed by both extensional and compressional tectonism (Banerdt *et al.*, 1997) which can be found in localised deformation zones or distributed over larger areas. Rifting (Solomon et al, 1982), wrinkle-ridges (Mcgill, 1993) and coronae (Stofan *et al.*, 1997) commonly deform the plains and detailed observations of these features can be used as a tool to investigate the crust, lithosphere, geological relations and resurfacing history of the local area. Small scale tectonic deformation in the plains caused by rift areas or topographic rises are particularly useful because they constrain the formation times of these large features with respect to the surrounding plains.

One such example of small scale features are closely spaced parallel lineations, the best example of which forms one component of the 'Gridded-plains' of Guinevere Planitia (see fig. 1.1) and are described in Solomon *et al.* (1992) and Banerdt and Sammis (1993). These features are particularly mystifying because of their close spacing and large areal extents (fig. 1.2) which seem to defy explanation by common geophysical models (Solomon *et al.*, 1992).

1.3. Closely Spaced Parallel Fractures (CSPF).

The parallel lineations referred to above are found in an area centred at 30N 333E and are Synthetic Aperture Radar (SAR) bright, linear features 10s or hundreds of kilometres long in closely spaced, sub-parallel sets which can number hundreds. Because they are only one or two pixels wide, no subordinate features can be resolved.

As the features are bright in left and right-looking SAR imagery, they have been interpreted as rubble-filled mode I extensional fractures (Banerdt and Sammis, 1992). I accept this hypothesis and suggest that a suitable designation for these features is Closely Spaced Parallel Fractures (CSPF).

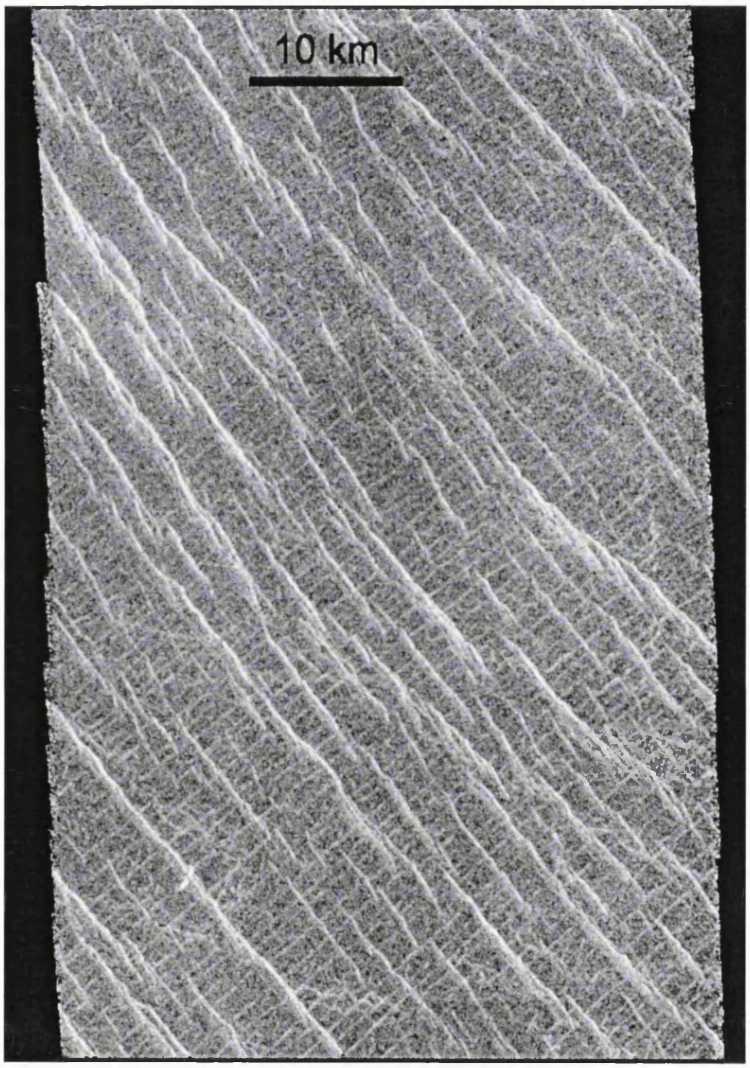

Fig. 1.2. The 'Gridded Plains' of Guinevere Planitia. Image centred at 30N333. North is up. The fainter, NE-SW trending lineations are very closely spaced and are very thin. The brighter, NW-SE trending features are interpreted as extensional features such as narrow graben or normal faults.

Anderson and Smrekar (1999) and Banerdt and Sammis (1992) have proposed models of formation for CSPF. Banerdt and Sammis (1992) favour a shear lag model where the driving force for the fractures comes from basal drag of a strong ductile layer beneath a weaker brittle layer. Anderson and Smrekar (1999) propose that global climate change causes sufficient stress in the crust to create these fractures.

1.4. A new methodology for investigating tectonic deformation in the Venusian plains.

In this thesis I describe a new methodology for investigating planetary tectonism. The methodology is based upon the principles of material science, geological modelling (incorporating fracture mechanics), and uses experimental data and interpretation of imagery. A similar methodology has been used successfully in the interpretation of crevassing on the Ronne Ice Shelf in Antarctica (Rist *et al.*, 1999) and is described in Sammonds (1999).

Description of CSPFs as extensional fractures initiated at the surface can be accommodated using a two-dimensional fracture mechanics model. The key unknowns will be the fracture properties of the crustal material at Venusian surface conditions and at depth. These are required to determine the initiation and spacing of the fractures and the depth where the crack becomes stable. The tensile strength of material cannot be used in such a model because of the well-known effect of scaling, whereby larger rock-masses are weaker owing to the inclusion of larger flaws. 'Fracture toughness' testing is accordingly used in this project. This critical fracture parameter is a material property and therefore independent of scale and experiments on laboratory-scale samples can be applied to the deformation observed in CSPF. The key physical properties have to be measured using Earth analogues of Venusian rocks. The choice of analogue rock type is constrained by the geochemical data of the Venera and Vega probes and by the conditions on the surface of Venus.

The apparatus used to measure fracture toughness at Venusian conditions is a key element of this methodology. The development of the apparatus itself is a new application of scientific and engineering techniques and, because measurements under demanding Venusian conditions are difficult to perform, considerable effort has been devoted to ensuring that the new apparatus functions correctly.

1.5. Aims of the project.

The primary aim of the experimental part of this project was to carry out a series of fracture toughness tests on basalt, the analogue Venusian rock, at a variety of temperatures and confining pressures. A secondary part of the project was to use carbonatite in these tests. Despite a successful sample collection trip to East Africa to collect carbonatite, the material was permeated with undetectable macroscopic flaws. This made measurement of fracture toughness impossible owing to pre-existing damage in any samples to be tested. (Details of the sample collection and some of the techniques

used prior to the discovery that the samples were unusable are still given in this thesis). The aims of the imagery study were to measure the spacing and orientations of the CSPF and to analyse the geological and stratigraphic settings of the units in which they occur. These two themes are then drawn together using fracture mechanics modelling, the aim of which is to construct a consistent model of fracture spacing that can be used to assess the criticality of variables such as material properties, atmospheric conditions and lithospheric stress.

1.6. Thesis plan.

Chapter two describes the plains of Venus and discusses the evidence that makes the assumption of their being largely composed of basaltic igneous rock so overwhelming. It also details some simple modelling work on carbonatites that I have performed which shows that some features on Venus are unlikely to be formed by basaltic volcanism and that some of the plains could consist of rocks of a more exotic composition. Chapter three presents the results of the imagery work performed in the Guinevere and Sedna Planitia regions of Venus, including details of fracture spacing, orientation and geological setting. Chapter four summarises the rock mechanics theory applicable to this project, specifically Linear Elastic Fracture Mechanics (LEFM) and describes experimental techniques for measuring fracture mechanics properties. Chapter five gives full details on the experimental apparatus used in this project and chapter six describes its evolution. The chapter is split into separate sections, each devoted to the different subsystems of the apparatus in approximately chronological order. Chapter seven gives details of the experimental methods used, not only in the fracture toughness tests but also in the calibration of the apparatus and in the measurement of additional parameters used to characterise the rock samples. Chapter eight presents details of the sample collection fieldwork in Italy, Tanzania and Iceland and describes the results from a variety of characterisation measurements made on the samples. Chapter nine presents the results from over 30 fracture toughness tests as well as full descriptions of error analysis. Alternative methods of data analysis are provided and compared with the standard methods from the literature. Chapter ten describes a new fracture mechanics model of crack spacing, which uses these experimental results. Chapter 11 presents a discussion of these results, the imagery measurements and the outcome of the experimental model. A key issue in the discussion is the reliability of the experimental data and the relative importance of variables in determining the spacing of CSPF. This

chapter also includes comments on possible future work on CSPF including improvements to the fracture mechanics apparatus.

Chapter 2

The Venusian plains.

2.1. Introduction.

In this chapter I introduce the different types of Magellan data used in this thesis and discuss the origin and composition of the Venusian plains. The arguments as to why the plains are assumed to be volcanic in origin and as to why these flood lavas have traditionally been thought of as having a basaltic composition are examined. Several criteria for the choice of a terrestrial analogue to Venusian basalt are then formulated. In addition, the results of numerical modelling that I have performed dealing with channelised flow of lava are presented. These results, together with imagery of channels, suggest that basalt cannot form all the morphological features found on the surface. The arguments for alternative lava types, and therefore, alternative Venus analogue rocks, are summarised.

2.2. Magellan Imagery and the plains of Venus.

Venus has a surface area about twice that of the continents of Earth making mapping of the surface a major undertaking. Despite the size of the task, the NASA Magellan mission mapped about 98% of the surface using Synthetic Aperture Radar (SAR) to view the surface through the cloud cover. The Magellan mission is described in Wall *et al.* (1995). The images returned by the mission have been assembled to produce Mosaiced Image Data Records (MIDRs) with a variety of resolutions. Full resolution data (FMIDRs) have been re-sampled to give 75m per pixel data products although the true resolution of the data is never better than 120m. The full resolution data has also been compressed and re-mosaiced to give C1-MIDRs, C2-MIDRs and C3MIDRs, which have pixel sizes corresponding to 225, 675 and 2025 metres respectively. The final type of SAR data product is the FMAP, a large format version of the FMIDR, which has the same pixel size but typically covers a 12° by 12° area of the surface. Other data sets from the Magellan mission include the topographic data that have a vertical resolution of about 50m but a horizontal resolution of about 5km and data products that display gravity, roughness, emissivity and slope. A comprehensive review of the theory and interpretation of SAR imagery is given in Ford *et al.* (1993).

This thesis mainly uses FMAP SAR imagery and topography data. Fig. 1.1 shows a global topography map of Venus.

The gravity data for Venus (fig. 2.1), based on either line-of-sight acceleration tracking of the spacecraft or Doppler data, show a greater spatial correspondence with topography than for any other planet (Sjogren *et al.*, 1997). This implies that almost all of the Venusian topography is actively compensated, either by lithospheric buoyancy or by dynamic support caused by density variation associated with convection in the mantle. The spatial resolution of the gravity data has improved greatly in recent years thanks to an increase in computing power and higher order gravity models are continually being generated (Barriot *et al.*, 1998 have produced a 180th order and degree model). Some authors (e.g. Smrekar *et al.*, (1997) have used the gravity data and the admittance (wavelength dependent ratio of gravity and topography) to infer whether large topographic rises are dynamically or isostatically compensated. Some rises, such as Western Eistla Regio, may be recently active, as shown by a bottom loading signature in the admittance plots (Smrekar, 1994).

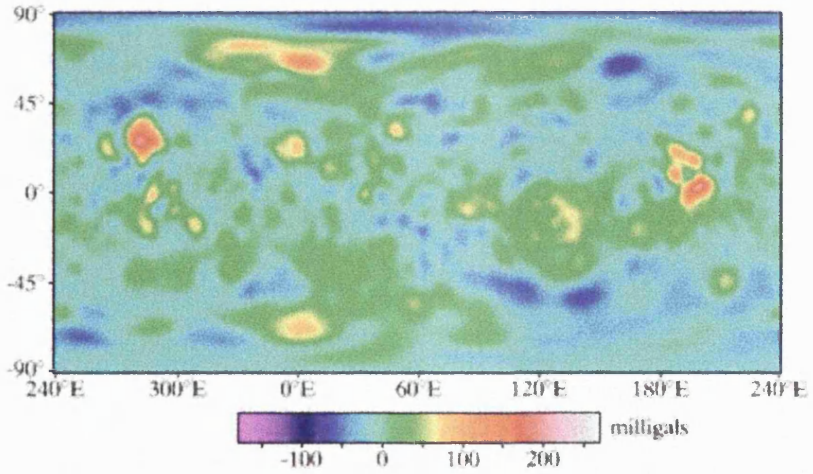

Fig. 2.1. Venus free-air gravity from Magellan cycles 4 and 5 from NASA Magellan web-page. Comparison with fig. 1.1 shows a high correlation between topography and gravity.

The Magellan SAR and topography data revealed that the majority of the surface of Venus is made up of extensive volcanic plains which range from approximately 1.5 km below the mean planetary radius of 6051.3km to about 2 km above it (Guest *et al.*, 1992). Plains units cover more than 80% (Masursky *et al.*, 1980) of the surface, and display numerous volcanic flow fields which are commonly greater than 50,000 km^2 in area (Lancaster *et al.*, 1995). The volcanic flows can often be resolved into individual

flows, but there are large areas of the plains, which appear homogenous when viewed by SAR. These homogenous areas are interpreted to be either older volcanic flows which have been weathered in such a way that their margins cannot be resolved, or flows so large that their margins are too widely separated to appear on adjacent SAR images.

2.3. The Plains of Venus: evidence for a volcanic origin.

Volcanic landforms dominate the surface of Venus and exist at all scales. Extensive lava flows can be seen in fig. 2.2 and it is easy to trace flows from source to termination hundreds of kilometres away. In figures 2.2 and 2.3, older features are embayed by younger ones.

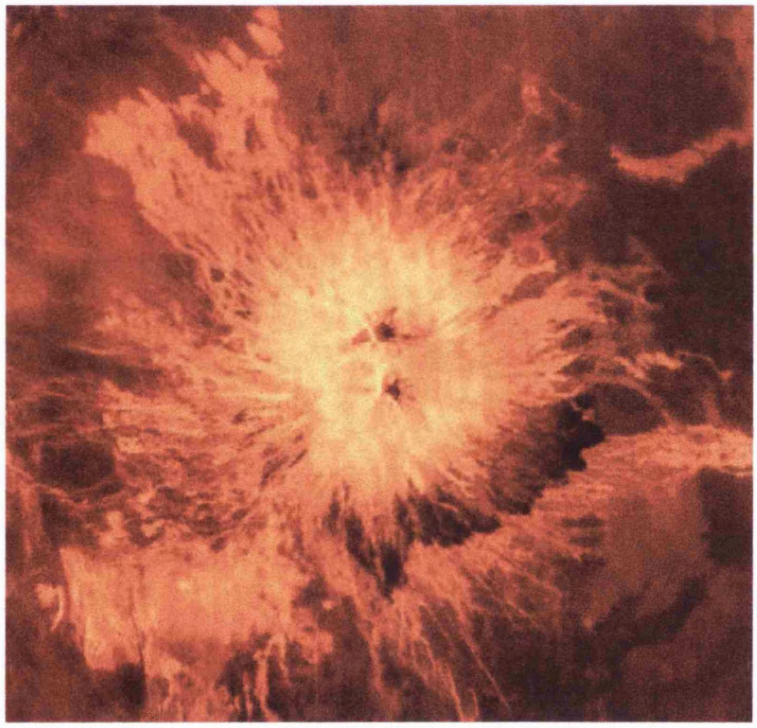

Fig. 2.2. Sapas Mons, a volcano approximately 400 kilometres in diameter and 1.5 kilometres high, located on a topographic rise in Atla Regio. The sides of the volcano show numerous bright overlapping flows that provide the edifice with a roughly radial outline. False colour.

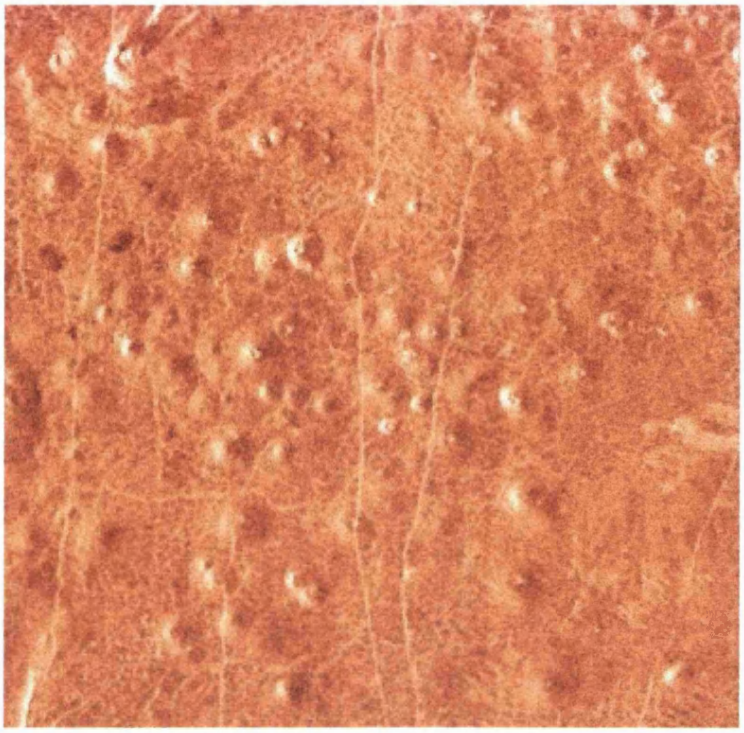

Fig. 2.3. A cluster of small cone volcanoes, each about 2 kilometres in diameter and 200 meters high, in Niobe Planitia. False colour.

The peculiarly low crater density on the surface of Venus suggests that there has been at least one large-scale resurfacing event which obliterated any trace of earlier impact events shared with the rest of the inner solar system. Some authors have suggested that the crater distribution is impossible to distinguish from a random population and have used this to suggest that the resurfacing was either global (Schaber *et al.*, 1992, Strom *et al.*, 1994) or continual and regional (Phillips at al, 1992). Huack *et al.*, (1998) found that the crater distribution is not completely spatially random and imply that resurfacing was less than catastrophic and may have occurred over 0.5Gyr. Despite disagreements over the timing and nature of resurfacing, all these authors agree that widespread volcanic activity occurred in the past and is responsible for the large plains units of Venus.

There is very little evidence to suggest that explosive volcanic activity is a significant mechanism in the emplacement of the plains, although, theoretically, there are instances where it might occur (Fagents and Wilson, 1995). The lack of explosive volcanism is explained by the inhibiting effect that the dense atmosphere would have on explosive devisiculation (Head and Wilson, 1992). This implies that the extensive flow patterns visible on the Magellan images are not pyroclastic deposits and that the plains are composed of dense extrusive rocks.

It is difficult to estimate the thickness of individual flows on Venus, but the vertical resolution of ≈50m of the altimetric data suggests that individual units are less than 50m thick. By association with graben and ridges whose heights have been clinometrically measured, however, an estimate of thickness of certain flows can be made (Guest *et al.*, 1992, Roberts *et al.,* 1992). Kreslavsky and Head (1999) used the embayment of small shields in a similar manner. All these authors produce estimates of the order of 50-200m for the thickness of regional plains units. Large flows with areas of around 50,000 km^2 could therefore have volumes of 10^3-10^4 km^3. It is important to note, however, that for the volume of individual flow fields to be estimated correctly, they must have roughness which contrast with that of the surrounding terrain. If underlying flows are of similar the volumes of flow fields be of the scale of kilometres thick.

The general conclusion that the plains of Venus are formed from large-scale volcanic flow is thus difficult to dispute, but we cannot know the composition, mineralogy or style of volcanism with the same confidence as we do on the Earth. Even so, large-scale volcanism on the Earth provides some basis for a discussion of flow genesis.

The most voluminous volcanic flows on Earth are the product of basaltic fissure eruption (Williams and McBirney, 1976). The best known example is the Columbia River Basalt Group (CRBG) in north-eastern Oregon, USA. These flows erupted from fissures between 17.5 and 6 Ma and cover an area of over 160,000km^2 (Reidel, 1998). They include over 300 flows with an estimated total volume of over 170,000 km^3. One flow, the Roza flow, has a volume of more than 1,200km^3 and is therefore comparable in scale to the large single flows seen on the surface of Venus. Another example of terrestrial flood volcanism is the early Palaeocene Deccan basalts of India, which cover 500,000km^2 with a total thickness of approximately 1 km. They are not single flows but a succession of activity that is thought to have lasted at least a million years. Other such flood basalts are found in South America, Siberia, Ethiopia and Northern Australia.

2.4. Composition and physical properties of Venusian basalt.

The composition of the volcanic material that makes up the volcanic plains of Venus can only be inferred from imagery using terrestrial analogues and comparisons with volcanism on other planetary bodies. Compositional measurements made by

Russian spacecraft which landed on the surface of Venus in the 1980's will be discussed in section 2.4.2. The physical properties of the material (grain size, density, porosity, etc) can only be estimated from Magellan data, imagery returned by the landing craft cameras and inference based upon the surface conditions.

2.4.1. Physical properties of Venusian rocks.

Fig. 2.4 shows the heat loss from a hot surface under a terrestrial and Venusian atmosphere using simple thermodynamic concepts (Khan, 1987, Incropera and DeWitt, 1996, Ozisic, 1985). At temperatures expected in a cooling lava flow, the heat loss under a Venusian atmosphere is about 1.5 times greater than under an Earth-like one. The added heat loss due to convection in the thick Venus atmosphere more than compensates for the reduced radiation in the hotter ambient surroundings. This implies that flows cool more quickly on Venus than on Earth and, at least near the surface of the flow, they will be finer grained.

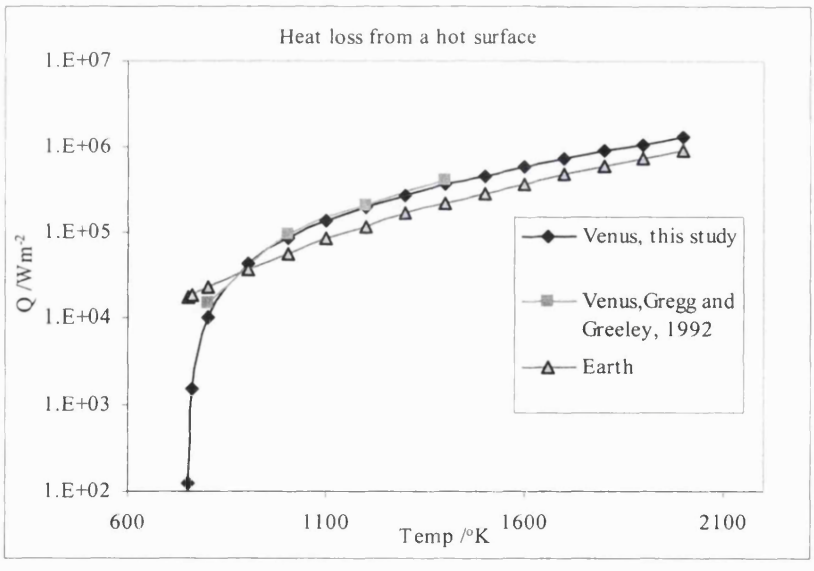

Fig. 2.4. Heat loss, Q, from a hot surface under Venusian and terrestrial atmospheres.

Another point to note is that the greater atmospheric pressure on Venus will suppress dissolution of volatiles. Thus, the vesicularity of Venusian igneous rocks will be lower than for those of Earth and hence the density of Venusian rocks will be slightly higher. I therefore conclude that whatever rock we use to simulate the shallow Venusian crust should be an extrusive igneous rock which is fine grained and with low porosity. The imagery taken at the surface by the Russian Venera probes provides constraining ground-truth evidence for these assumptions.

Fig. 2.5. Venera 9 and 10 panoramas in original perspective. The near field rocks in the top image are about 30-50 cm in dimaeter. The scale is the same in both images. Note the presence of many angular blocks and the platy bedrock, which is especially visible in the Venera 10 image (bottom).

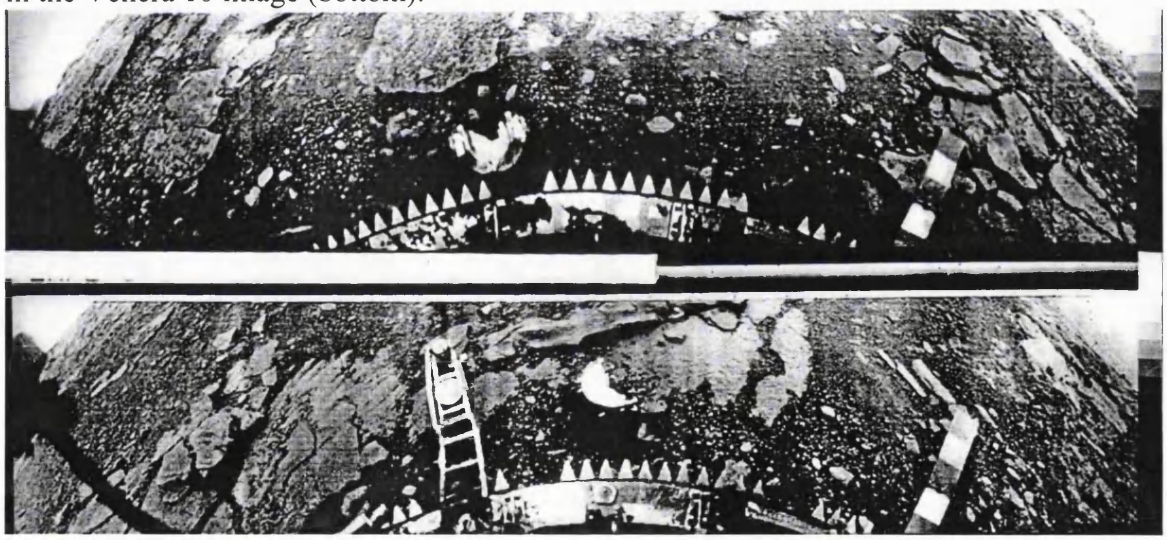

Fig. 2.6. Venera 13 panorama (left and right views). The arm to the left of the bottom (right) image is 60 cm long. The terrain appears to consist of almost equal parts of bedrock and fines.

Fig. 2.7. Venera 14 panorama (left and right views). The arm in the bottom figure is 60cm long. Note the platy and polygonal bedrock at this site.

The imagery obtained by the Venera landers (figs. 2.5, 2.6 and 2.7) although poor in quality, provides invaluable ground truth which agrees well with the assumptions made about the nature of the plains. Venera 14 appears to have touched down in an area of relatively undisturbed polygonally jointed rock. The other sites show smaller amounts of bedrock and Venera 9 imaged, fragments, blocks and fines and no bedrock. A detailed analysis of the photographic images can be found in Garvin *et al.* (1984). All four spacecraft landed (within 150 km) in regions that are classified as plains. Full-resolution mosaicked images have been prepared for each site, and geological maps of each landing site have been made from these mosaics (Weitz and Basilevsky, 1993). Table 2.1 summarises the landing site conditions.

Spacecraft	Site Location	Mean Altitude/km	General Description
Venera 8	10.70°S, 335.23°E	6051.85	East of Phoebe Regio. Mainly dark, old plains.
Venera 9	31.09°N, 291.64°E	6052.89	Northeast slope of Beta Regio. Mainly old fractured plains and tesserae.
Venera 10	15.42°N, 291.51°E	6052.02	Southeast edge of Beta Regio. Fractured plains and tesserae.
Venera 13	7.55°S, 303.69°E	6052.25	East of Phoebe Regio. Mainly dark plains with some fractured areas.
Venera 14	13.05°S, 310.19°E	6052.29	Southern Navka Planitia. On the flanks of a 75km shield volcano. Plains dominate surroundings.
Vega 1	8.10°N, 175.85°E	6051.32	Rusalka Planitia. Mainly dark, wrinkled plains.
Vega 2	7.14°S, 177.67°E	6052.1	Between Northern Dali Chasmata and Rusalka Planitia. Mainly fractured dark and bright plains.

Table 2.1. Venus probes landing sites.

2.4.2. Chemical composition of Venusian rocks.

In addition to the imagery obtained at the surface, the Russian probes were also able to make some compositional measurements of their landing sites using X-ray fluorescence spectroscopy (XRF) and gamma ray spectroscopy (GRS). The GRS measured underlying rocks up to cubic meters in volume whereas the XRF counter used drilled samples of only a few grams in mass. The GRS is, therefore, generally assumed to be more representative of the country rock than the XRF, which may have sampled aeolian material or other fragments rather than bedrock or large blocks.

The GRS measured only percentile abundance of potassium and parts per million abundance of uranium and thorium. The XRF measured percentile abundance of

10 different elements and compounds. These results are summarised in tables 2.2 and 2.3 with terrestrial basalt and nephelinite for comparison.

Element	Venera 8	Venera 9	Venera 10	Vega 1	Vega 2
Potassium %	4.0±1.2	0.5±0.1	0.3±0.2	0.45±0.22	0.40±0.20
Uranium PPM	2.2±0.7	0.6±0.2	0.5±0.3	0.64±0.47	0.68±0.38
Thorium PPM	6.5±0.2	3.7±0.4	0.7±0.3	0.5±1.2	2.0±1.0

Table 2.2. Compiled results revealed by Gamma Ray Spectroscopy. After Barsukov (1992).

Oxide %	Venera 13 *	Venera 14 *	Vega 2 *	Terrestrial basalt **	Terrestrial nephelinite.✞
SiO_2	45.1 ± 3.0	48.7 ± 3.6	45.6 ± 3.2	49.2	44.13
TiO_2	1.59 ± 0.45	1.27 ± 0.41	0.2 ± 0.1	-	1.05
Al_2O_3	15.8 ± 3.0	17.9 ± 2.6	16.0 ± 1.8	15.7	13.05
FeO	9.3 ± 2.2	8.8 ± 1.8	7.74 ± 1.1	7.1	3.83
MnO	0.2 ± 0.1	0.16 ± 0.08	0.14 ± 0.12	-	0.34
MgO	11.4 ± 6.2	8.1 ± 3.3	11.5 ± 3.7	6.7	0.80
CaO	7.1 ± 0.96	10.3 ± 1.2	7.5 ± 0.7	9.5	7.65
K_2O	4.0 ± 0.63	0.2 ± 0.07	0.1 ± 0.08	1.1	5.43
S	0.65 ± 0.4	0.35 ± 0.31	1.9 ± 0.6	-	-
Cl	< 0.3	< 0.4	< 0.3	-	-

Table 2.3. Compiled results from XRF spectroscopy with terrestrial igneous rock results for comparison. Table shows weight % of individual oxides. * Barsukov (1992), ** Hall (1987), ✞ Dawson, (1989).

These data are incomplete in that they only show the percentage of potassium and do not include the abundance of sodium, although this can be estimated from the

XRF results using the method of Barsukov (1992). Nevertheless, the results can be compared with terrestrial volcanic samples, and show that the rocks measured at the Venera 8 and 13 were similar to terrestrial nephelinites or trachytes, whereas the remainder of the samples are more like terrestrial mid-ocean ridge basalt (MORB). A fuller description of the implications of the results from the Russian landers is given by Barsukov (1992).

If we accept that the plains of Venus are composed of basalt, the terrestrial analogue rock should be a fine grained, low porosity basalt. Icelandic basalt taken from a large jointed flow was accordingly used in this study. Its mineralogy, composition and provenance are discussed in chapter eight.

2.5. Canali and the case for exotic lava compositions.

Nevertheless, one class of features has been identified from Magellan imagery which is difficult to explain in terms of basaltic volcanism as we know it. These features, termed 'canali', are channels with lengths of 1000's of km and morphology which appears almost fluvial in character. Some authors (William-Jones *et al.*, 1998) have asserted that, because of their morphology, the canali (singular: canale) cannot be the product of basaltic volcanism and must have a more exotic composition. Canali would then serve as indicators of composition for those areas of the plains where they occur. In addition, their great lengths and age would seem to make them important clues to the large-scale resurfacing of the planet.

2.5.1. Canali: physical description.

The canali are a class of channel feature thought to be unique to Venus, unlike sinuous rilles which are also found on Earth, Mars and the Moon. They are found most commonly in the plains of Venus, although they are more extensive in certain lowland areas than others. A useful sketch map of the distribution of canali can be found in Komatsu *et al.* (1993). Venusian canali are classified by most authors as simple channels which can be distinguished from lunar or Venusian sinuous rilles by their high meander wavelength (Baker *et al.*, 1992) and large radius of curvature. Canali are generally of constant width over their length and have a low depth/width ratio but their most spectacular feature is their length: some have been traced, virtually unbroken, for thousands of km and the longest measures approximately 6,800 km.

A 'typical' canale could be said to be >500 km in length with a width of 1-3 km and a depth of <50m. It may have radar-bright margins indicating that it has raised margins or levees, and will probably be radar-dark when compared to the surrounding areas. Venusian rilles tend to have a similar sinuosity but are shorter, tending to be of the order of 10's to 100's of km, and are generally 50 to 250m in depth (Baker *et al.* 1992, Komatsu *et al.,* 1993).

Kargel *et al.* (1994) noted that some canali have meander properties which indicate channel migration similar to that of terrestrial rivers on floodplains. They also note that some canali terminate in deltas similar to bird's-foot deltas on Earth and that there are many similarities between other Venusian channels and Martian outflow features. In general, however, terminations of canali are difficult to resolve, most of them appearing to end abruptly or to grade into the surrounding plains. The range of widths and depths of terrestrial rivers encompasses all those of Venusian canali but in lengths they cannot compete with the longest Venusian channels. Rivers on Earth are also more sinuous, indicating that their meanders are more developed (Komatsu and Baker, 1994), the conclusion being that canali were not formed by flowing water.

Canali are commonly embayed by lava flows and cut by fractures. There is evidence of post emplacement tectonic uplift in which the gradient of a canale is reversed (Baker *et al.*, 1992) and there are examples of canali being diverted by local tectonic features. Canali rarely cut through other tectonic features, although there are examples of canali cutting through coronae (Baker *et al.,* 1992) and through tesserae (see fig. 2.9). It is clear that canali are generally quite old in relation to the bulk of the Venusian surface.

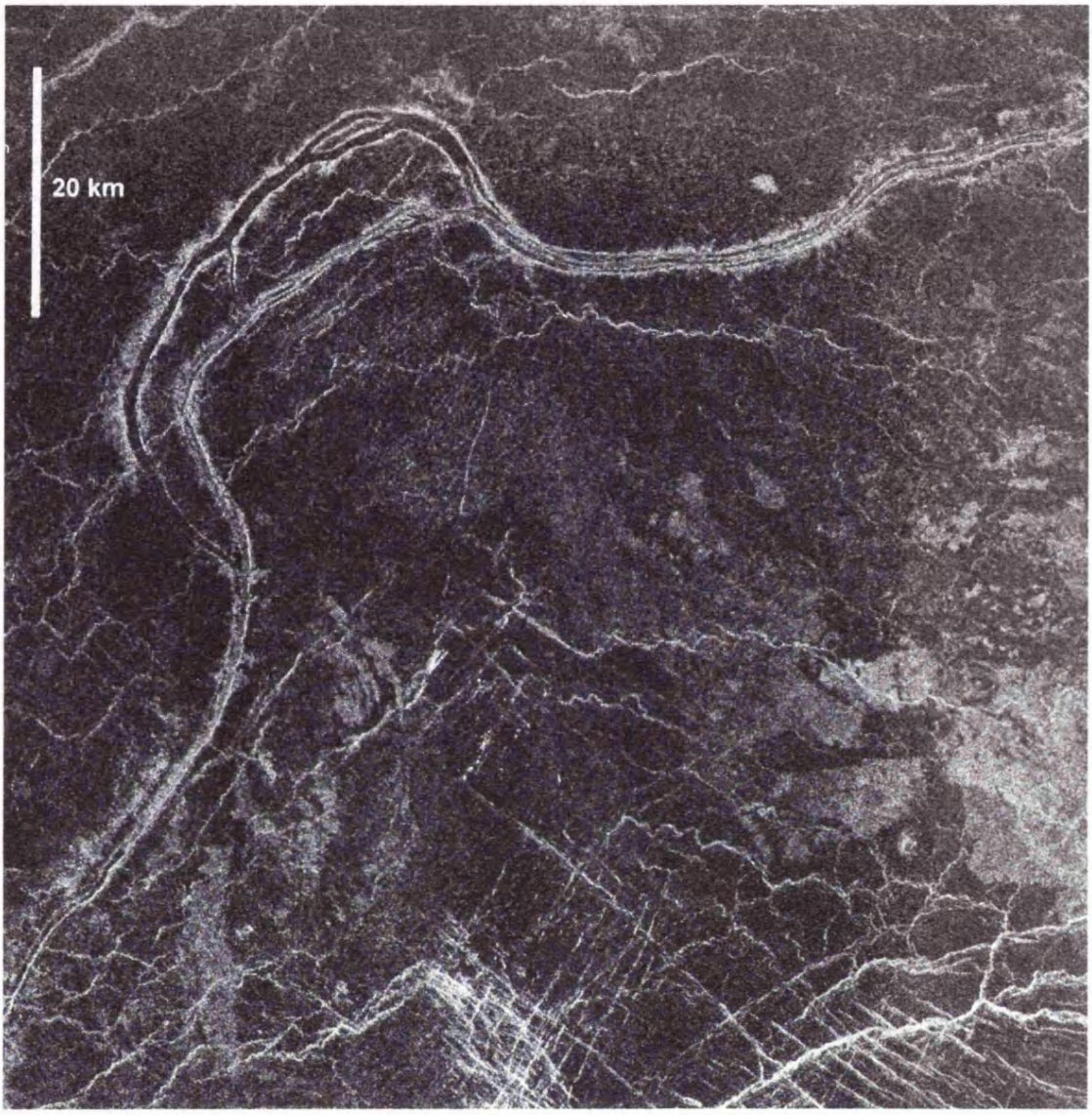

Fig. 2.8. Cut off loops in a canale. This figure shows part of an 800km canale situated at 45N 017E which displays a variety of unusual features. The branch of the channel containing the streamlined island appears to be cut off by a younger channel, which exists inside the bed of the older one. Note also the bright margins of the channel indicating a rougher area which, in places, extends over a kilometre from the channel. The linking branch of the cut-off loop implies that both branches of the channel were active simultaneously for a period of time. North is up.

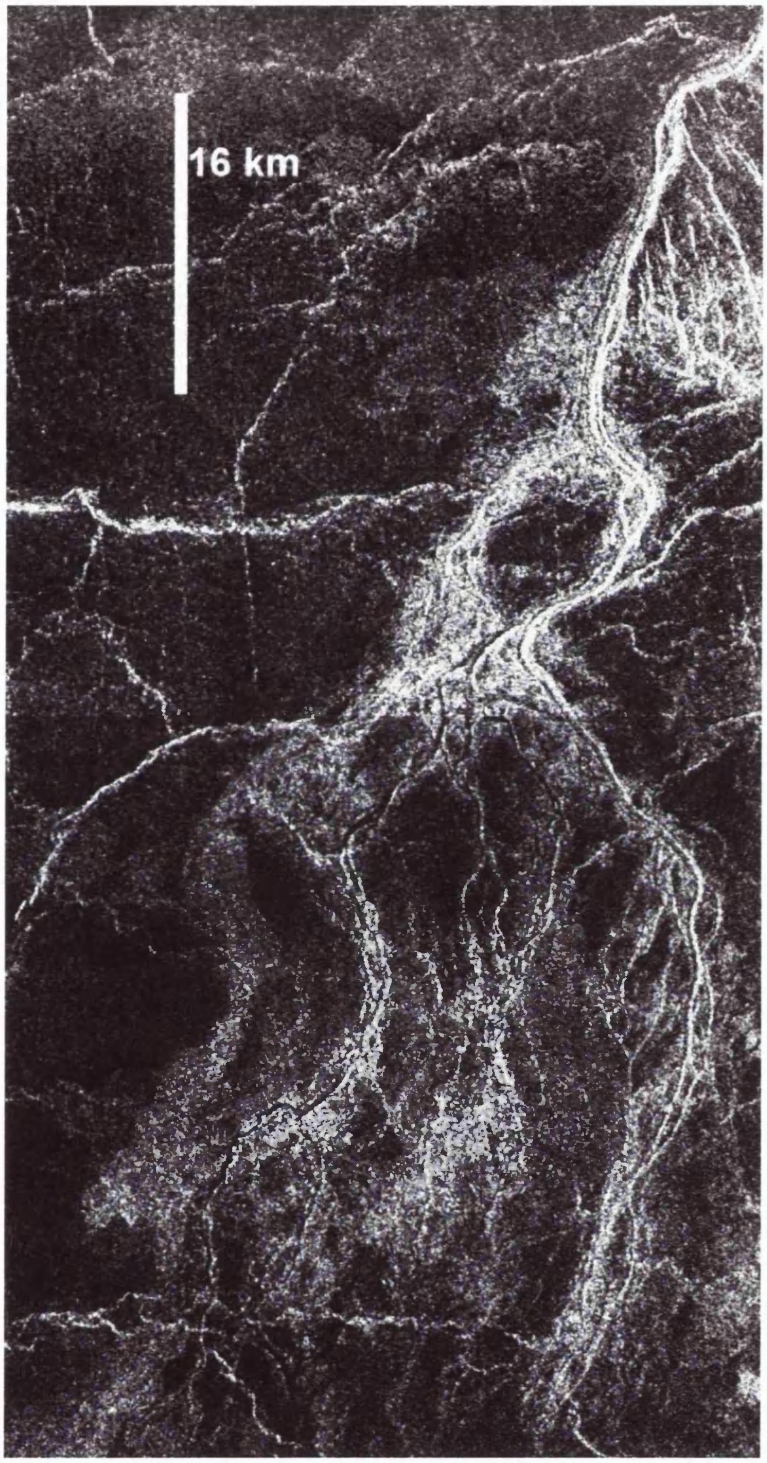

Fig. 2.9. Delta-like termination of a canale. This image, centred at 45N 015E, shows the termination of the canale in figure 2.8. The channel splits and then reforms before entering a delta-like dendritic network. Bright areas, possibly indicating deposition of solids from the channel-forming fluid, surround these small, braided, channels. North is up.

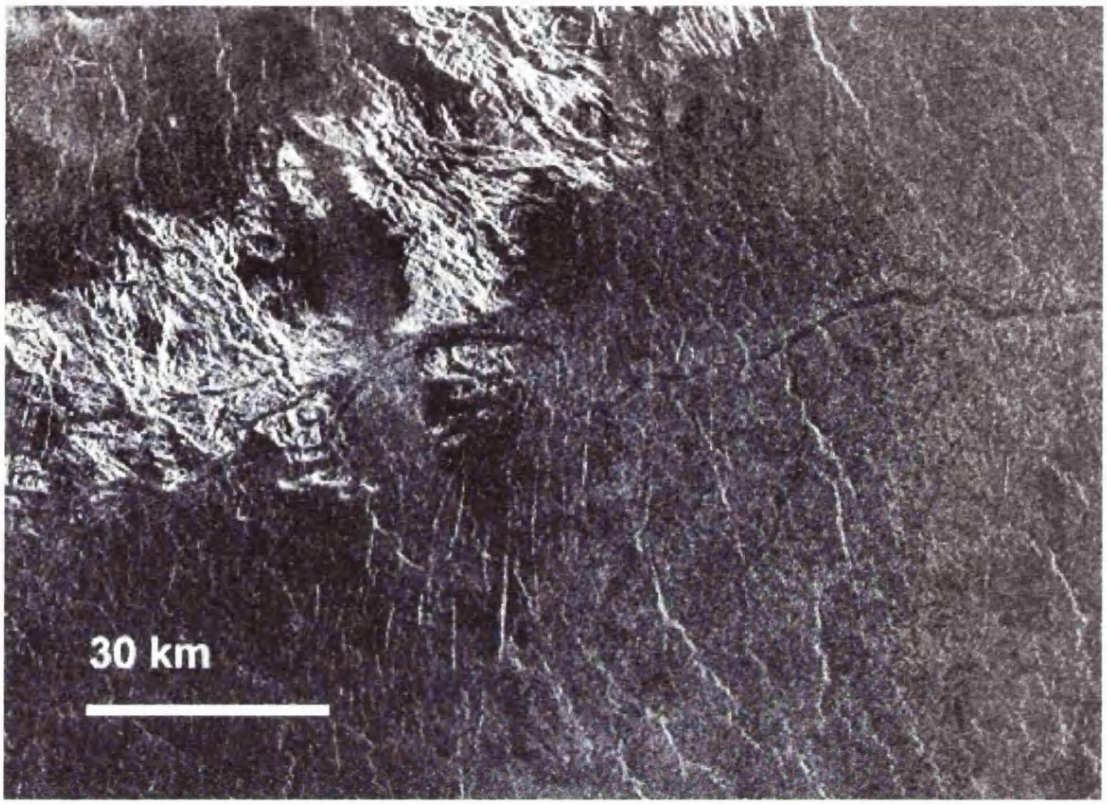

Fig. 2.10. Eroding canale. Centred at 49S265E, this image shows a canale crossing an area of bright terrain. Near their margins, old highlands embayed by lava plains are close to the elevation of the surrounding flows. Faults and valleys could be flooded with lavas that widen to form the features shown above. This image strongly supports the argument for canali formed by mechanical erosion of fluid lava rather than as feeder channels for large flows.

2.5.2. Canali: possible mechanism of formation.

A variety of mechanisms have been suggested for the formation of canali, not all of which are volcanic. Jones, personal communication (2000), has suggested that sub-aqueous erosion by bottom hugging sediment pulses, or water erosion under a water-saturated, high pressure atmosphere, may be responsible. Other authors suggest that canali are either giant constructional lava channels (e.g. Gregg and Greeley, 1993) or mainly erosional lava channels (William-Jones *et al.*, 1998).

Both the mechanisms involving water require lower temperatures than those of the present Venusian atmosphere, suggesting that the runaway greenhouse effect occurred late in the planet's history. These mechanisms also imply that a large amount of water was lost from the surface in the last 500-1000Ma. This could only be accomplished by atmospheric loss of hydrogen coupled with large-scale oxidation of the rocks at the planet's surface. Most atmospheric models for Venus exclude this scenario,

and, in view of the evidence from the crater record and from the extensive lava flows visible on Magellan imagery, this possibility will not be explored further here.

The constructional volcanic model (Gregg and Greeley, 1993) sees the channels as feeders for a huge lava flow, similar to a large aa flow on Earth, perhaps accompanied by lava tube formation, although this seems unlikely as the tubes would have had to be almost two orders of magnitude wider than their terrestrial counterparts. If canali formed in the same way as terrestrial lava channels, they would be up to 10 times larger (terrestrial lava flows are rarely more than 100kms in length). The corresponding cooling times, eruption rates and morphology of channels are explored in 2.5.3a.

The erosional model invokes scouring of the bedrock by a turbulent sediment-carrying fluid that incises a channel over a long period of time during repeated or prolonged eruptions. Figure 2.10 seems to supply evidence that canali formation involved erosion of the bedrock. Features such as those in figure 2.8 and 2.9 support this: an inner channel within a larger one indicates an erosional mechanism, whilst a delta formation shows that there has been deposition of solids. Section 2.5.3b deals with numerical considerations applicable to turbulent lava flow, especially cooling time, which will be much shorter than for the constructional model.

2.5.3. Canali: numerical considerations.

The formation of very long flows is constrained by two very basic concepts: 1) the flow must travel rapidly such that cooling is minimised or else cooling must be reduced through insulation of the flow, and 2) the volume of lava erupted must be sufficient to cover the large distance of the flow (Keszthelyi and Self, 1998). This leads to the idea that the flow of lava ceases as a result of either a cooling limit or a volume limit. We can apply these ideas to two simple models of canali formation to investigate the possible travel lengths and associated eruption parameters. In both cases we shall assume that the flow is cooling limited and comes to a halt when the whole thickness of the flow is solid.

The main differences between the models proposed for canali are the postulated physical properties of the lava. In order for substantial mechanical or thermal erosion to occur the liquid has to be in a turbulent flow regime, which enhances the cooling effects as laminar flows tend to cool much more slowly due to crusting and the limited efficiency of heat loss by conduction within the flow. If viscous forces dominate, the

liquid will flow in a laminar fashion, and have a low Reynolds number. If inertial forces dominate, the Reynolds number climbs until a threshold is breached and the flow becomes turbulent. By applying the Reynolds criterion we can therefore investigate both the laminar and turbulent flow of lava in channels.

Turbulent flow, Re > 12,500
Intermediate flow, 12,500 > Re > 2000 (French, 1994)
Laminar flow, Re < 2000

2.5.3a. Laminar flow model with an insulating crust leading to constructional origin of canali.

Simple steady laminar flow in a channel much wider than it is deep can be approximated by the Jeffreys equation

$$u \approx \frac{\rho g d^2 \alpha}{3\nu} \tag{2.1}$$

where u = mean flow velocity, ρ = density of lava, g = surface gravity (8.87 ms^{-2}), d = depth of flow, ν = kinematic viscosity of lava and α = slope (if small, otherwise sinα)

The equation for describing the turbulent to laminar transition in a fluid is

$$\mathrm{Re} = \frac{\rho u d}{\nu} \leq 2000 \text{ for laminar flow (French, 1994)} \tag{2.2}$$

By rearranging these formulae and eliminating the velocity, an expression for the minimum viscosity required for laminar flow can be obtained.

The generally accepted value for the slope of Venusian plains is α = 0.001 (Williams-Jones *et al.*, 1998, Gregg and Greeley, 1993, Kargel *et al.*, 1993). Assuming that d = 1-25m and ρ = 2000kgm^{-3} the viscosities required for the laminar/turbulent threshold would be of the order of 100-500 Pa.s for a 10-25m deep flow. Hence, for flows with depths similar to Venusian canali, even medium-low viscosity lavas such as basalt (v=100-1000Pa.s) could flow in the laminar regime.

If this were the case, then the resulting velocity obtained by substituting the value of ν back into the Jeffreys Equation (2.1) would be 6-10 ms^{-1} which would give travel times on the scale of 1-2 days per 1000km (i.e. 10 to 15 days for the longest canale). It should be noted that this time is associated with the advance of 'packets' of lava flowing in the feeder channel, not with the advance of the flow-front, which would

take orders of magnitude longer. Whether or not the lava could remain liquid whilst it was in the feeder for these times depends upon the rate of formation of crust and the conductive heat loss through it. This can be approximated using the Stefan equation, which applies to the formation of a crust on a cooling lava lake (Turcotte and Schubert, 1982).

For the conditions that we are interested in (i.e. a Venusian ambient temperature and basaltic type lava), we can use T_m, temperature of melt = 1350 K, T_o, ambient temperature = 750 K, c, heat capacity of lava = 1200 $J.kg^{-1}.K^{-1}$, L, latent heat of fusion = 400,000 $J.kg^{-1}$, k, thermal diffusivity = $8.0x10^{-5}m^2.s^{-1}$ to solve the Stefan equation and generate crust formation in the lava as a function of time.

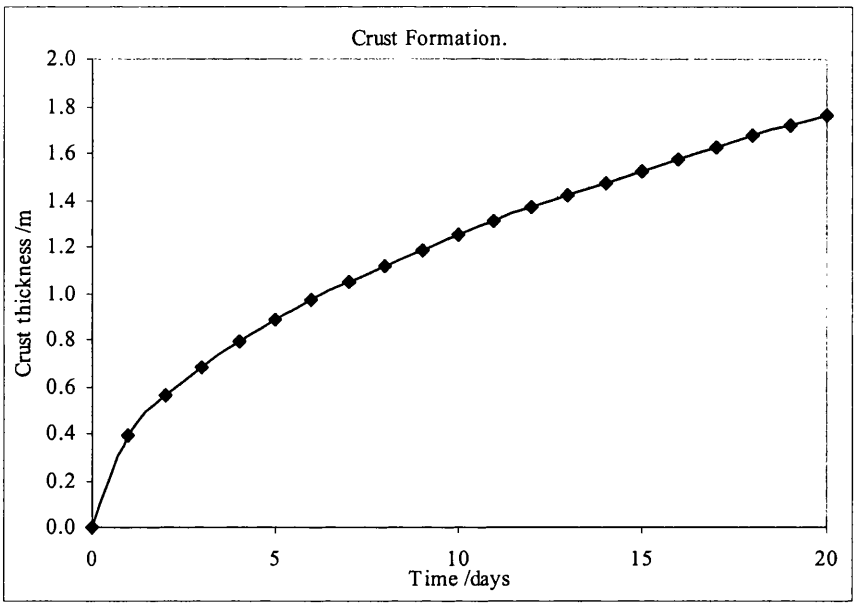

Fig. 2.11. Solution of Stefan equation applied to formation of crust on a lava flow.

Fig. 2.11shows that the crust thickness after 10-15 days would be substantially less than the lava depth of a typical canale, allowing continued channelled behaviour. In reality, this cooling would be faster due to continual cracking of the crust which would expose the hotter core material. Also, any crust that was reincorporated into the flow would cool the lava as it re-melted (although this would have much less effect than on Earth owing to the higher temperature of the reincorporated crust).

Hence it is physically possible for an aa flow to travel the distances seen in canali. This can be shown by multiplying the cooling times (>10 days) by the flow speed obtained from (2.1), 6-10m/s. If the cooling time was 15 days and flow velocity

was 6m/s, the length would be over 7000km, that is greater than the longest observed length of a canale.

The length of time and erupted volume required to emplace such a flow can be estimated by comparison with the Earth. The flow advance rate tends to be highest during the initial period of eruption: flows on Earth tend to reach 50% of their final length during the first 24 hours but can continue to advance for more than 10 days. (Kilburn and Guest, 1993). Rapid slowing is caused by shallowing terrain, decreasing discharge rate or increasing frontal resistance. Terrestrial flow advance rates are of the order of 0.01-2ms^{-1} for aa lavas from Etna, but channelised parts of the flow can move much faster. Hawaiian basaltic flows have been known to travel at over 10ms^{-1} in places. If we assume that a large Venusian lava flow front initially advances at 1ms^{-1} and reaches 50% of its total length in 10% of its eruption time (in a similar way to aa flows of Etna), then the total time taken to emplace a flow of 1000km would be around 50-100 days. Similarly, for the longest channel on Venus, the time taken to form a channel 6800km long would be over a year. Of course, some parts of the channelised lava would still move many times faster. For a canale with a width of 2000m and a depth of 10m, the flow speeds in the feeder channel would be of the order of 6-10 ms^{-1}. This implies an eruption rate of 1-2x10^5 m^{3}s^{-1}, which agrees well with the work of Reidel (1998) on the Umatilla member of the Columbia River Basalt Group. Also, the total volume of lava would be of the order of 2,000-10,000km^3, which is, again, of a similar order to terrestrial flood basalts.

2.5.3b. Turbulent flow model

Figures 2.8, 2.9 and 2.10 provide strong morphological evidence for turbulent, eroding lavas forming the canali. If the lava that formed the canali is turbulent and therefore has a high Reynolds number, some of its characteristics can be inferred. From (2.2) we can plot the Reynolds number against viscosity for a specimen canale and, assuming a density of 2000kg/m^3 applying a correction factor for different lava types. The same applies for the depth of the flow, a reference depth of 10m being be used as a starting point.

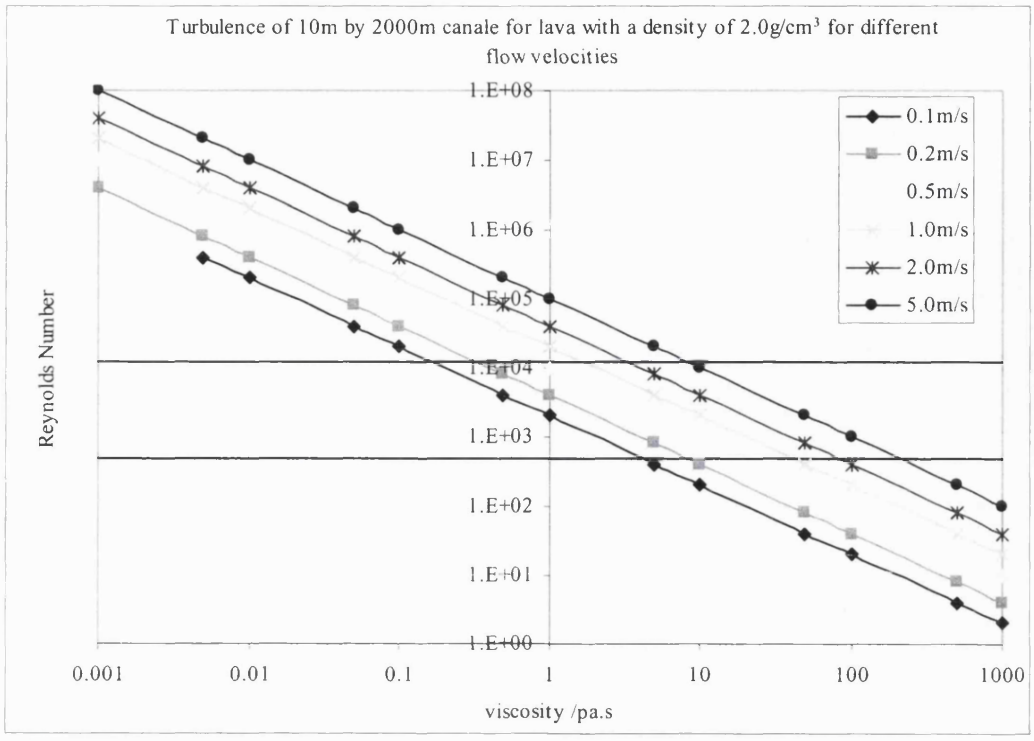

Fig. 2.12. Turbulence criterion for a typical canale with a variety of different velocities. Horizontal lines indicate turbulent/intermediate/laminar regimes with turbulent regime being the topmost region.

Typical viscosities and densities for lavas are

- Basalt (Hawaii) v = 50-500 Pa.s, ρ = 2,700 kgm^{-3} (Williams-Jones *et al.*, 1998, Kargel at al, 1994)
- Natrocarbonatite v = 0.01-0.1 Pa.s ρ = 2,200 kgm^{-3} (Williams-Jones *et al.*, 1998, Kargel at al, 1994, Dobson *et al.* 1996)
- Komatiite v = 0.01-1.0 Pa.s ρ =2,800 kgm^{-3} (Williams-Jones *et al.*, 1998, Kargel *et al.*, 1994)

As indicated by the high Reynolds number in fig. 2.12, carbonatite and komatiite are both turbulent in the regime proposed for the formation of canali. The least viscous basalts are only in the intermediate region even for deep, dense, fast-flowing lavas. Many of the morphological features of the canali appear to require slow moving turbulent flows. Delta-like features suggest mechanical erosion balanced by sediment deposition, either through crystallisation or sediment transit. It is also important to note that, by analogy to terrestrial fluvial forms, the flow speed should be < 0.5-1.5 m/s for braiding to develop (Williams-Jones *et al.*, 1998). Carbonatite or komatiite could be turbulent at these velocities even if the flow thickness were only 1m. The thickness of

the flow is important because the flow rate of a channelised turbulent flow depends upon its thickness assuming that gravitational forces acting upon the lava are balanced with the frictional forces. This relationship is represented by the Chezy equation

$$u = \sqrt{\frac{(2.g.d.\alpha)}{f}} \tag{2.3}$$

(Hulme, 1974 and French, 1994), where f is the friction factor and is given a value of 0.01 from a modified Moody Diagram (French, 1994).

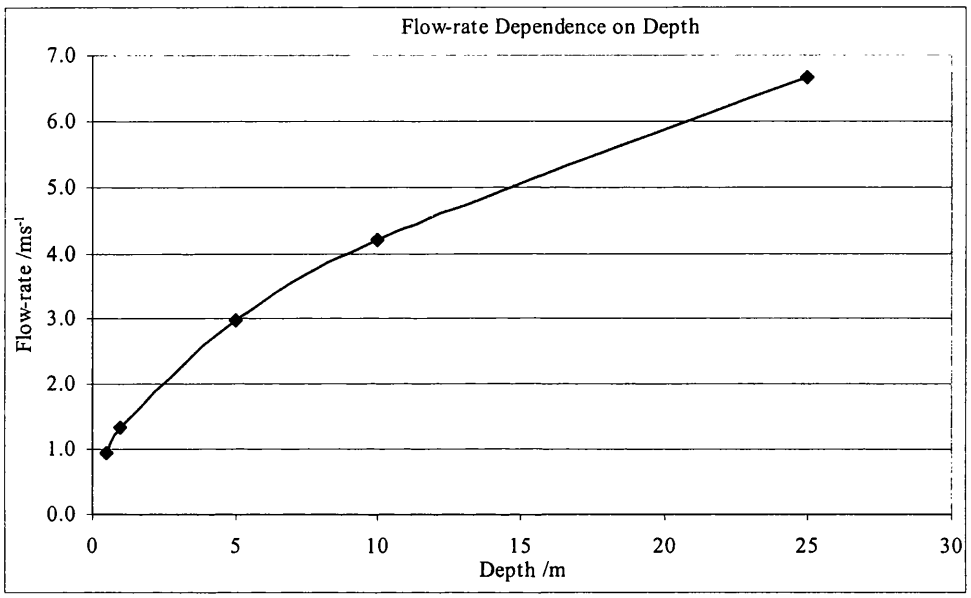

Fig. 2.13. Graphical plot of Chezy equation for 'typical' canale of width 2000m and Venusian gravity and slope.

These data can be combined with the heat loss data from a hot surface (fig. 2.4) and incorporated into a simple model giving the fastest heat-loss from the lava to the atmosphere, but ignoring heating of the bedrock. The model assumes that, on a small time-scale, the lava is turbulent enough to mix fully, from top to bottom, so there is no vertical thermal gradient. This model assumes that no crusting occurs and that the rheological properties of the lava are unaffected by the temperature change. Although this is unrealistic as some crusting occurs even in turbulent lava and the rheological properties of the lava depend upon the temperature, it serves as a first order approximation of the behaviour. The model also assumes that the loss in gravitational potential energy of the flowing lava is returned to the system as frictional heating of the lava and that the velocity is constant. Furthermore, the model does not consider the existence of the solidus or liquidus and merely seeks to describe how a liquid would lose heat. Arbitrary values can then be applied to obtain an estimate of the solidification

time for particular lava types. This may be unreasonable for silicate lavas but, as Kargel *et al.* (1994) point out, carbonate-rich melts have such low viscosities that precipitated crystals settle quickly, which means that carbonatite flows should remain fluid almost until the point of complete solidification. Dawson *et al.* (1989) confirmed this when describing a natrocarbonatite eruption of Oldoinyo Lengai in 1988.

Values for different lava types can be inserted into this model to investigate whether they can flow for protracted periods before solidifying. This would give an indication of the properties of lava required to erode a canale mechanically. The cooling time needs to be maximised and this can be accomplished by assuming that the lava erupted at a temperature well above the point at which it becomes solid or by considering a lava erupted near the Venusian ambient temperature. An example of the first is Komatiite lava, and natrocarbonatite or calciocarbonatite lava are examples of the second.

Figures 2.14 and 2.15 show the results of a simple numerical model that I have devised based on 5-second time steps between successive iterations. The model is independent of time step size below about 15 seconds. The results are shown for natrocarbonatite and komatiite. In both cases the width of the canale is assumed to be 2000m and the slope 0.001.

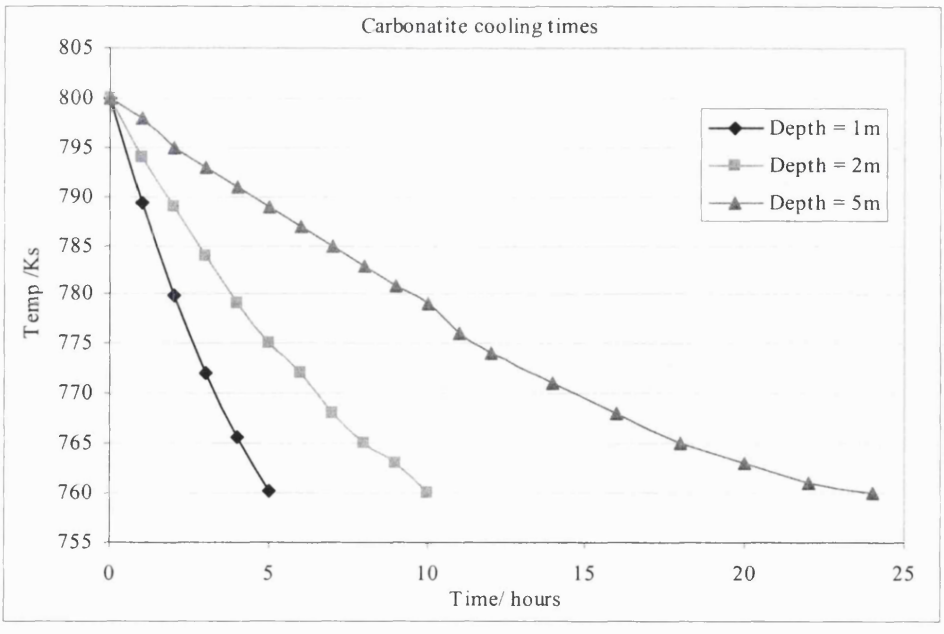

Fig. 2.14. Cooling times for natrocarbonatite flows assuming eruption temperature of 800K

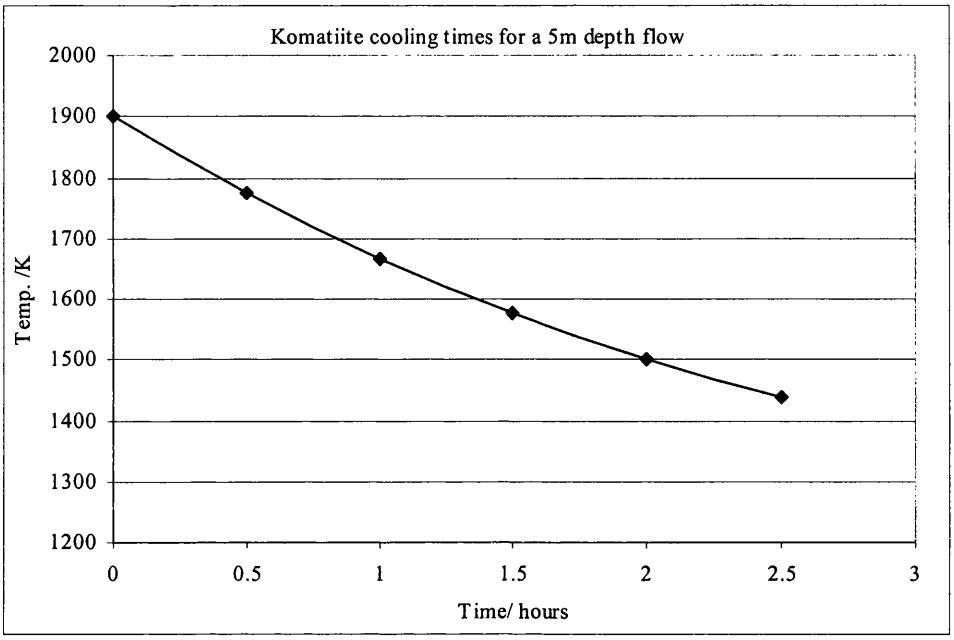

Fig. 2.15. Cooling times for Komatiite flows assuming eruption temperature of 1900K

Figs. 2.14 and 2.15 show that a minimum depth of 2m of carbonatite is required to remain fluid for more than 10 hours when flowing in a fully turbulent regime. This depth of flow would have a velocity of about 2m/s, a velocity slightly too high for formation of some features seen in the imagery to form. Locally, however, the channel may broaden, slowing the flow speed so that these features may form whilst at other points in the canale a faster flow speed would make the canale meander less and form straighter sections. Komatiite lava flowing in a turbulent regime loses heat far too quickly to flow great distances owing to its high eruption temperature and it can be eliminated as a potential canale forming lava.

Depth /m	Flow Velocity /ms^{-1}	Cooling time /hours	Flow distance /km	Approx. required eruption rate /m^3s^{-1}
0.5	0.9	2.5	8	9.0×10^2
1	1.3	5.0	24	2.6×10^3
5	3.0	25.0	268	3.0×10^4
10	4.2	50.0	758	8.4×10^4
25	6.7	125.0	2997	3.4×10^5

Table 2.4. Potential flow distances of carbonatites.

Table 2.4 shows that this first-order model rules out carbonatite as a canale-forming medium unless the channel is very deep, as it would cool too quickly. However, it must be stressed that this model gives a 'fastest cooling time' estimate for the flow. A real turbulent flow with some crusting and thermal gradients within the flow may cool an order of magnitude more slowly.

2.5.4 Discussion arising from numerical modelling.

This simple modelling highlights the difference between a turbulent flow and a laminar flow insulated by a quasi-stable crust. The turbulent flow cools much more quickly but needs to have a low flow velocity in order to agree with the morphological features seen in the imagery, which tends to rule out long distance flows. The laminar flow model resulting in constructional channels does not agree with the observed morphology but the slower cooling times made possible by crustal insulation can lead to flows sufficiently long to cover the lengths of canali.

If the heat loss were inhibited in the turbulent model (due to some degree of crusting, for example) by a factor of ten when compared with the simple model, then the distance for critical cooling would be ten times greater. Short canali, less than 1000km in length, could now be formed by very shallow flows forming complicated morphological structures (due to the low flow rate) whilst canali up to 7000km long could be formed only by flows of the order of 10m thick. This would enable canali to be formed by the eroding properties of cool, turbulent lava and would explain many of the morphological features which the laminar crust-insulated channel model fails to explain. An interesting future avenue of canali investigation would be to see whether only the shorter and thinner canali display complex morphologies or whether braiding, scroll bars and deltas are found even for larger canali.

In summary, both of the simple numerical models that have been outlined are inadequate to provide a first order approximation of the lengths, volumes and morphologies of the flows. The two mechanisms require radically different types of lava, one of which is associated with flood deposits on Earth (basalt) and the other which is rather rare (carbonatite). Laminar, constructional basaltic flows fail to explain the morphological evidence, but if we invoke carbonatites to scour the channels, rather like water filled rivers on Earth, we find that, at present Venusian conditions, turbulent flows lose heat too quickly to travel the required distances. The global climate change

suggested by Bullock and Grinspoon (1998), might of course be sufficient for carbonatites to become mobile on the surface of Venus indefinitely.

2.5.5. Carbonatites as channel forming fluids.

If carbonatite flows form canali morphology there must be an explanation for how such large amounts of carbonate melt could be concentrated in specific areas. This may be explained by surface-atmosphere interactions or by repeated climate change. The Venusian atmosphere could be buffered by reaction with carbonate on the surface in reactions such as

$$CaCO_3 + SiO_2 = CaSiO_3 + CO_2 \quad (2.4)$$

Hashimoto *et al.* (1996) conclude that, although the present surface temperature and pressure agree well with the equilibrium of this equation, the state is unstable for small perturbations in temperature or pressure. Small increases in CO_2 concentration could therefore result in runaway fixing of carbonate into the surface rocks and vice-versa and conclude that the CO_2 content of the atmosphere could formerly have been three times that of the present day.

A climate change that caused carbonatites to become permanently mobile would have the effect of ponding any carbonatites that were erupted in local depressions. As the atmosphere of Venus is very dry they would resist weathering and would solidify if the climate cooled. A further climate change may then re-melt these ponds of carbonatite, which would then be concentrated in sufficient volumes to form the features we now see as canali.

2.6. Analogue rock types for experiments on Venusian plains material.

In summary, the two end-member rock types that could represent the volcanic plains of Venus are carbonatites and basalt. The evidence for basaltic volcanism, however, is much stronger and basalt is considered the primary experimental sample type. Suitable basalt for these experiments would be high density, low vesicularity and very small grain size. In addition the rock samples should be isotropic and free of macroscopic fractures and joints and, preferably, unaltered by weathering or hydrous alteration. A suitable carbonatite sample should share these criteria. Chapter eight describes sample collection and characterisation measurements on rock samples used in this thesis.

2.7. Conclusion.

The volcanic plains of Venus contain many volcanic landforms at a variety of scales. Terrestrial style basaltic volcanism is sufficient to explain most of these features, and measurements made by the Venera and Vega probes support the assumption that basalt makes up most of the Volcanic plains of Venus. Therefore, the primary Venusian analogue rock type must be basalt.

There are features, however, that are difficult to explain in terms of basaltic volcanism. The hypothesis that these features are formed by carbonatites answers many of the morphological questions that basaltic volcanism cannot (although it must be stressed that this inference is purely speculative whereas the evidence for a basaltic composition is far more solid). Simple flow models applied to canali have shown that neither carbonatite nor basalt can fully explain these enigmatic features but carbonatite lava appears to be the most likely canali-forming fluid. It is therefore possible that extensive sheets of carbonatite lavas may locally overlie the plains of Venus. Rock mechanics tests on carbonatite samples are therefore a useful, but secondary, part of the experimental program.

Chapter 3

Observations of closely spaced parallel fractures from Magellan imagery.

3.1. Introduction.

As described in chapter one, the closely spaced parallel features found in plains regions of Venus are interpreted as being sets of extensional fractures and are termed CSPF (closely spaced parallel fractures). In this chapter, I describe a series of mapping and statistical studies on these fractures and describe their geological setting and stratigraphy. At the end of the chapter, previous work by other authors relevant to CSPF is examined.

The analysis described in this chapter is based almost entirely on the Magellan SAR (synthetic aperture radar) and altimetry data sets collected between 1990 and 1994. The Magellan mission is described in full by Wall *et al.* (1995) and a comprehensive review of the theory and interpretation of SAR imagery is given in Ford *et al.* (1993). A few major points should, however, be noted prior to detailed discussion of SAR imagery.

The brightness of pixels in a SAR image depends upon several variables: the decimetre scale roughness, the topographic angle of the target and the electrical properties of the target. The radar incidence angle also influences the brightness. Rough surfaces have a higher backscatter and thus appear brighter in the SAR images. Steep topographic slopes will also appear brighter if orientated towards the imaging sensor and darker if sloping away. Areas with high dielectric constants (due to composition and/or bulk density) will also have enhanced radar backscatter and hence appear brighter. It should also be noted that some areas of Venus have relatively little variation in backscatter and thus appear very uniform in the imagery. For images in this chapter where no quantitative measurements of backscatter are necessary, a contrast increase has often, therefore, been applied.

The topographic data set based on the altimetry measurements has far poorer horizontal resolution (pixel size of 5x5km) than the SAR data but a vertical resolution of about 50m (Ford and Pettengill, 1992). The topography data is also displayed in Mercator or global sinusoidal projection compared to the local sinusoidal projection of the SAR imagery. This leads to difficulties in displaying topography and SAR at the same resolution, and SAR data have to be overlain on lower resolution topography data

to make useful comparisons. This problem, together with that of overlaying imagery of different projections, is discussed later in the chapter.

3.2. Aim of imagery work.

The aim of the imagery work performed in this study was to assess several key issues relating to the formation of CSPF.

Certain aspects of the fractures cannot be determined by direct observation. For example, how deep do the cracks penetrate, and is this related to their length? Are they shallow fractures in a layer or semi-elliptical cracks in a homogenous crust? These secondary properties can only be inferred with knowledge of the mechanism of formation. In a recent review of the subject, Anderson and Smrekar (1999) identify several possible models of formation, including the shear-lag and stress shadow models of Banerdt and Sammis (1992) and extensional necking of a cooling lava flow. Furthermore, they suggest that thermal stress caused by global climate change may be the missing link in understanding how these features were formed. In order to test the validity of these models, certain questions were set which could be answered from detailed analysis of Magellan imagery.

- Do the azimuthal directions of the fracture sets follow any kind of trend? If so, can these trends be related to any local geological features?
- What are the relative ages and stratigraphic settings of the fracture sets?
- How many intersecting fracture sets are found in one region?
- What are the spacings of the fracture sets? Are they consistent over large areas or are there trends in the spacings

The main problem with answering the above questions is the paucity of data. Although the fracture patterns are widespread (Banerdt and Sammis, 1992) they are, in many cases, destroyed or overlain by later activity leading to a 'patchy' distribution of fractures which makes quantitative measurements difficult. For this reason, rather than making a global survey of occurrences and attempting to apply statistical methods to various small data sets, one area on Venus with a large, continuous set of fractures was chosen for detailed study. This area is to the west of Western Eistla Regio and contains several (non-orthogonal) intersecting fracture sets as well as the well-documented orthogonal 'gridded plains'. In this area, I mapped the azimuthal directions of the CSPF,

measured the spacings over a large area and ascertained whether regional geology exerted any influence over the morphology, spacing or direction of the CSPF.

3.3. Results from imagery work.

3.3.1. Mapping of azimuthal direction of CSPF.

The area under scrutiny is spread over four FMAPs from 12 to 36°N and 324 to 348°E. The names of these FMAPs are Sedna Planitia Southwest, Sedna Planitia Southeast, Aurelia and Benton. Each individual FMAP is broken up into 36 'framelets' each of 2° by 2°. The first stage in the mapping process was to scan through the hardcopy images to identify which framelets contained these features and then to mosaic these framelets in such a way that long profiles could be taken across the area and trends in direction could be identified. This meant that criteria for inclusion or exclusion of features had to be made based upon morphology.

The criteria used for including lineations in the study were as follows:

- The lineations had to be thin (i.e. one or two pixels in width) and straight (this means that features with definite curves such as concentric fractures around small coronae and braided *en-echelon* faults would be excluded). In addition, the extents of the fractures had to be longer than 10 times the spacing.
- The lineations had to be in virtually parallel sets with a spacing of less than 5km (equivalent to approximately 5mm on hardcopy and 65 pixels on FMAP framelet, full resolution CD-ROM images). A set can be as few as 5-10 fractures or contain hundreds.
- No structure was to be visible, i.e. the lineations were not to be *en-echelon* nor include any visible graben-like features (i.e. flat floors or obvious steep walls) although they could trend into graben at the limits of the area.

These criteria ensured that only numerous, long, thin, straight fractures in parallel sets were included in the study. The ideal fracture set can be seen in figure 3.2a. The fractures seen in figure 3.2b and 3.2c were included in the study whereas those in figures 3.2d, 3.2e, 3.2f were excluded.

The criterion that the fractures must be straight is the most flexible. Individual fractures should not be curved on an 10km scale although the trend of fields of

fractures is allowed to curve with a radius of 10s of km. This is, in fact, often the case and is an interesting aspect that demands further analysis.

The closely spaced parallel fractures are often observed to trend into polygonal fracture patterns. This leads to polygons with a dominant trend or parallel lineations with polygonal features. Some human interpretation must therefore be used to include or exclude certain features. Another problem with applying these criteria rigorously is that these features are faint and difficult to identify. With spacings of sometimes less than a kilometre and often poorly contrasting with the plains they deform, these lineaments are not easy to identify or measure. Human judgement is more suitable for identifying fractures than computer based profiles based purely on brightness because differentiating between spurious 'bright-spots' and bright fractures is easy for an observer but impossible on a brightness profile .

Applying these criteria to the CD-ROM images of the four FMAPS used in the study enabled a map of framelets containing these features to be constructed and is shown in fig 3.1.

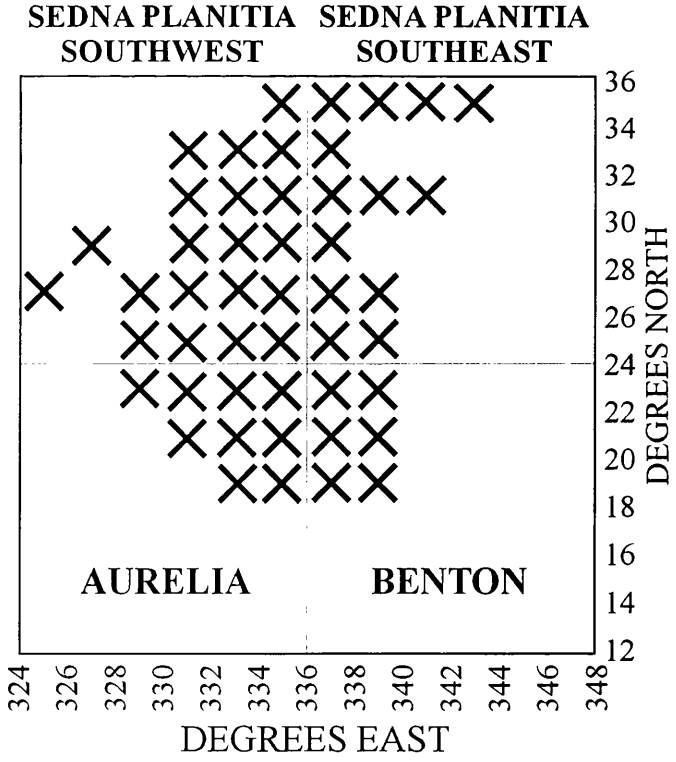

Fig. 3.1. Framelets containing linear features conforming to selection criteria (marked with X) in the four FMAPS used in this study. The study area is also shown on a global map as in fig 1.1.

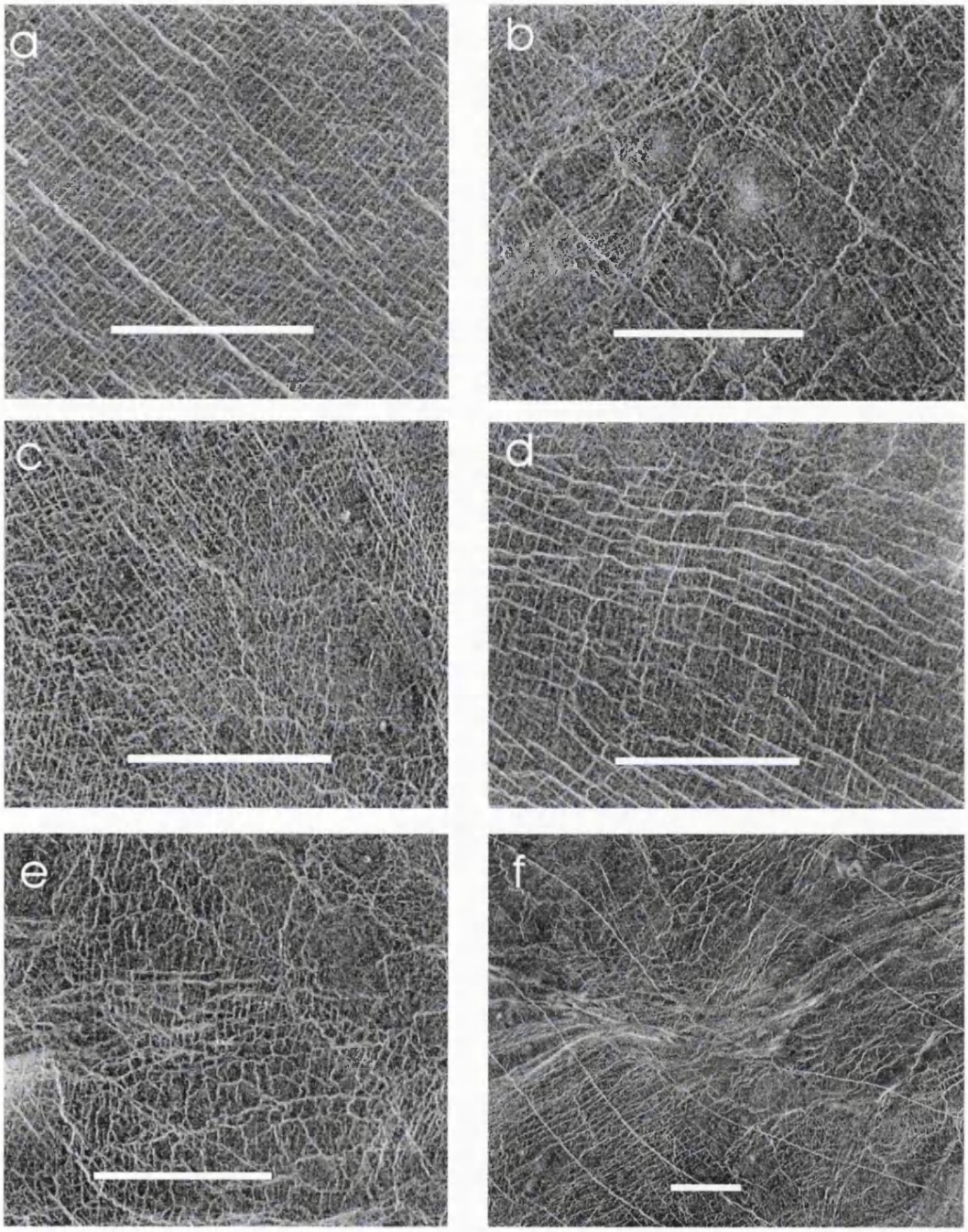

Fig. 3.2. Sample images from the study area. All scale bars 20km. North is up.
a) Ideal fracture pattern for mapping and statistical measurements. b) Fractures obscured by shields; acceptable for mapping but not for statistical measurements. c) Two intersecting fracture sets, both acceptable for inclusion. d) E-W set unacceptable due to irregular shape and graben-like 'structure'. N-S set borderline acceptable. e.) N-S trending polygonal set; unacceptable because too polygonal. f) NW-SE bright fractures unacceptable because irregularly shaped and too widely spaced.

Groups of five or six framelets were mosaicked together to form larger images. The azimuthal directions of the fractures were marked on each map with a large arrow for every 5-10 fractures, with different colours used to identify different sets. Where

fracture sets showed a consistent trend or were continuous over large areas, the same colours were used. Thus, individual sets could easily be identified and isolated from each other. An example of these maps is shown in fig. 3.3 below.

Angular error due to the sinusoidal projection of the data is not accounted for in these maps but only amounts to a few degrees at most. When all the framelets containing CSPF had been mapped, the images were reduced and remapped with one large arrow for every 2-5 smaller ones from the original maps. These new maps were then subjected to a skew transformation (in order to take into account the angular error induced by the sinusoidal projection of each FMAP), mosaicked together and then overlain on lower resolution (C2MIDR) SAR imagery and Magellan topographic data. In order to check that the skew was not distorting the image, craters were used as reference points and matched with both the fracture trend map and the topography and SAR imagery.

The overlain directions showed a distinct trend when compared with the topography, one set in particular following the edge of a topographic high very closely. The overlays were then further reduced in size and overlain upon a C2MIDR browse image that showed a wider area. The trend of the dominant set was concentric to the margins of the topographic rise of Eastern Eistla Regio. Another set appeared to have a similar trend but slightly offset whilst a third displayed a similar concentric pattern but around a smaller topographic high in the north-west of the region. Figure 3.4 shows these sets overlain on the topography and SAR data for the region.

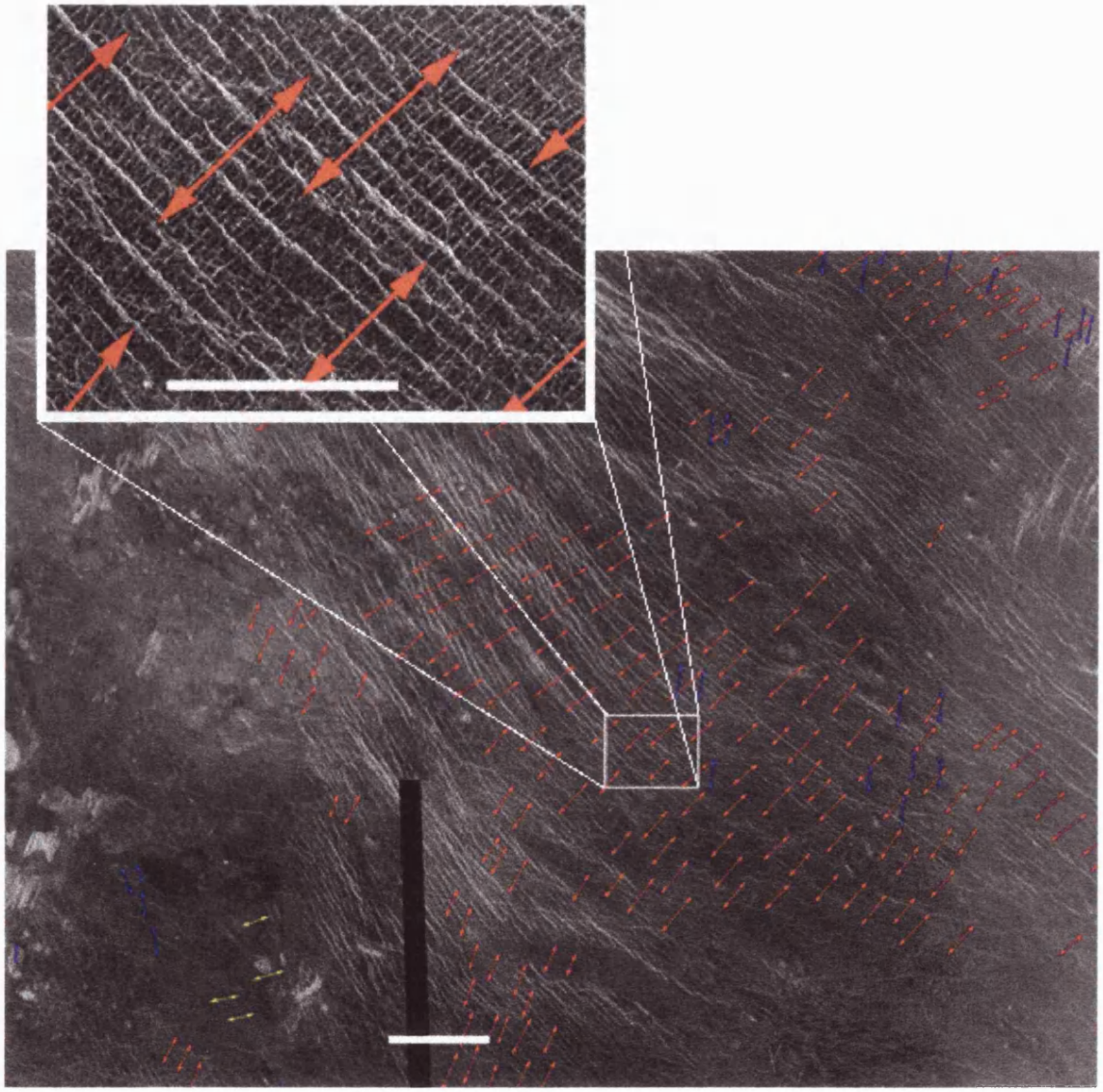

Fig. 3.3. Example of azimuthal direction mapping method. Scale bars are 50km (main image) and 20km (inset). North is up.

Fig. 3.4. (Next page) SAR and topography of Western Eistla Regio. Up to three separate sets of fractures can be identified from the initial mapping. The dominant set (red arrows) appears to follow the edge of the topographic rise closely. The set marked by pink arrows is just visible in the figure and consists of only a few areas of a small number of parallel fractures. The set marked by black arrows, which may actually be two separate sets (north and south), appears to show similar concentric trends to the red set, but where the deformation centre is situated is less obvious. Also marked on this image are the positions of several profiles described later in this chapter. The non-linear nature of the topographic scale should be noted.

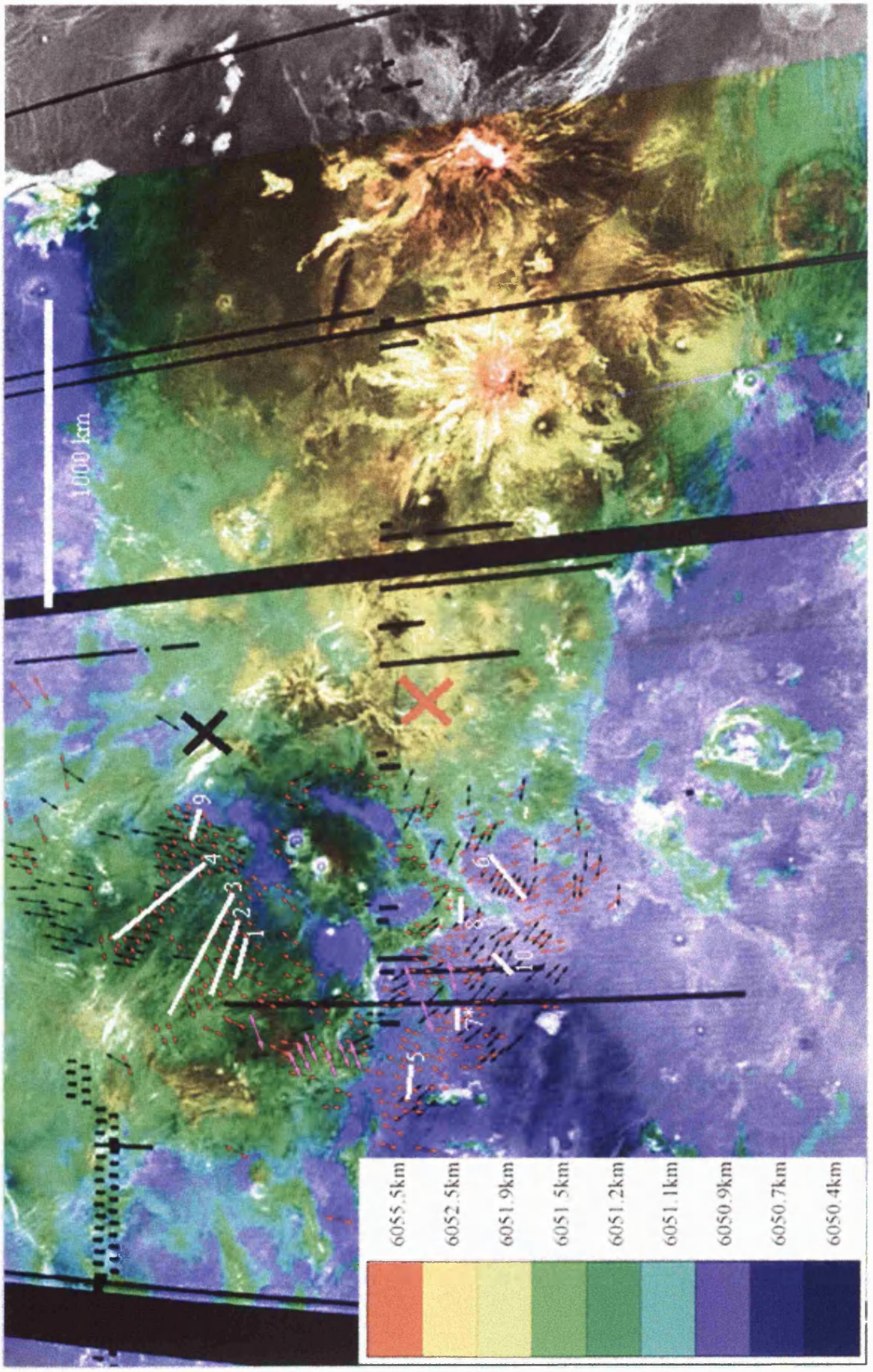
1000 km
6055.5km
6052.5km
6051.9km
6051.5km
6051.2km
6051.1km
6050.9km
6050.7km
6050.4km

3.3.2. Fracture spacing measurement: method

In order to characterise the variation of fracture spacing a large number of measurements over a large area should be made. Several methods were evaluated in order to choose the most efficient and statistically valid. The two most promising methods were identified as either splitting the area into grids or drawing profiles across large areas. The final choice as to which was used was based upon a trial run of each method.

The first method was attempted over a medium-dense fracture density framelet by splitting the area in 36 squares (6x6 equal areas) and attempting to measure 20-50 fractures for each fracture set in each square. It soon became apparent, however, that some grids had no fractures whilst others had many, and that choosing which fractures to measure was problematic. For example, an observer asked to measure 50 random fractures may choose the same pair twice, will have an unintentional bias towards the brighter features, and will find it difficult to take a realistically random sample. If a set of random points is projected on the grid, measurements can be made with higher confidence of statistical validity but the question then arises as to what happens if there are no fractures under the measurement point. Also, this method is very time consuming and inefficient: - many of the grids contained few fractures to be statistically valid but this could not be known until after the measurements had been made.

Drawing profiles across large areas had several advantages over gridding. Firstly, the sampling can be chosen so that the profiles are drawn over the areas with most fractures. Also, the profiles can be drawn radial to the topographic rise of Eistla Regio to test if there was any variation with distance from the rise. Secondly, missing data caused by other features obscuring the fractures or mysterious gaps in the fracture patterns (a common occurrence) would not damage the statistical validity of the data, it would merely make a gap in the distance/spacing plot, and could be avoided by careful placing of the profiles. Finally, the profiles used by Banerdt and Sammis (1992) to measure statistical fracture spacing would provide a check on the results from the same area. The profile method was therefore chosen and 10 profiles were constructed over a large area (fig. 3.4), eight in the dominant red set of fractures and two in the black set (the pink set was too sparse to provide data).

The mosaicked FMAP framelet maps constructed for the azimuthal direction mapping were also used for profiles. In each case, a long line (between 50 and 500km) was drawn through the area with most visible fractures approximately radial to the Eistla topographic rise. Using a line tool in the Adobe PhotoShop software, single pixel-

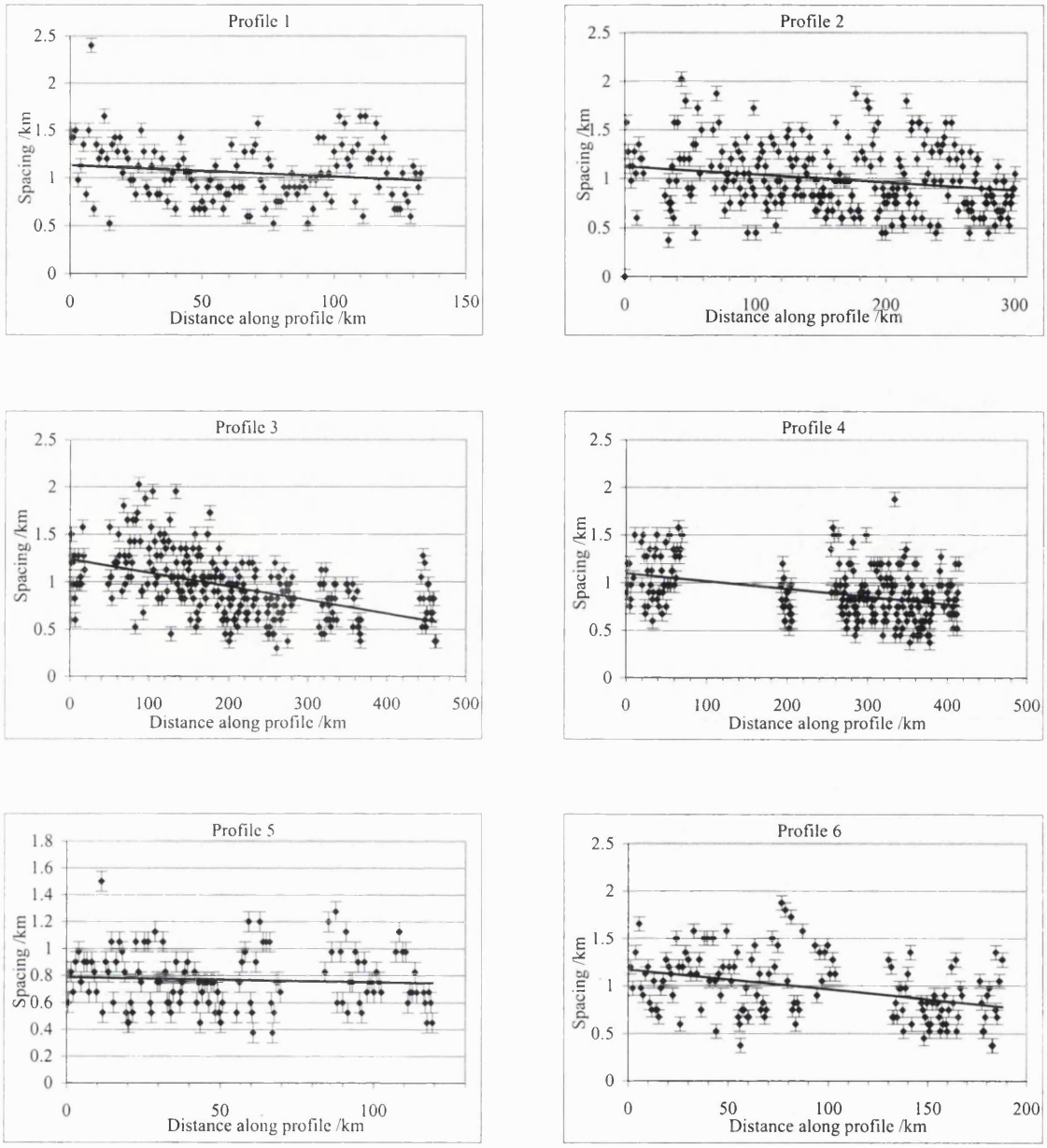

Fig. 3.6. Results from profiles 1-6. Note large gaps in data in some profiles where the features where locally obscured. See fig. 3.4 for location of profiles.

width lines were drawn along the fractures that intersected the profile. The distance along the profile from the start to each fracture could then be measured (in pixels) using the dimension tool. Spacing was measured, again with the dimension tool, in the most perpendicular sense between adjacent fractures and not merely as the distance between the points at which the fractures intersect the profile. An example of the profile method is shown in fig. 3.5. This method is preferable to that of Bowman *et al.* (1994) because it does not reduce the amount of data and makes use of human judgement rather than brightness profiles. This means areas with few fractures can be avoided and fractures that are locally obscured can still be included in the study if their position can be firmly established.

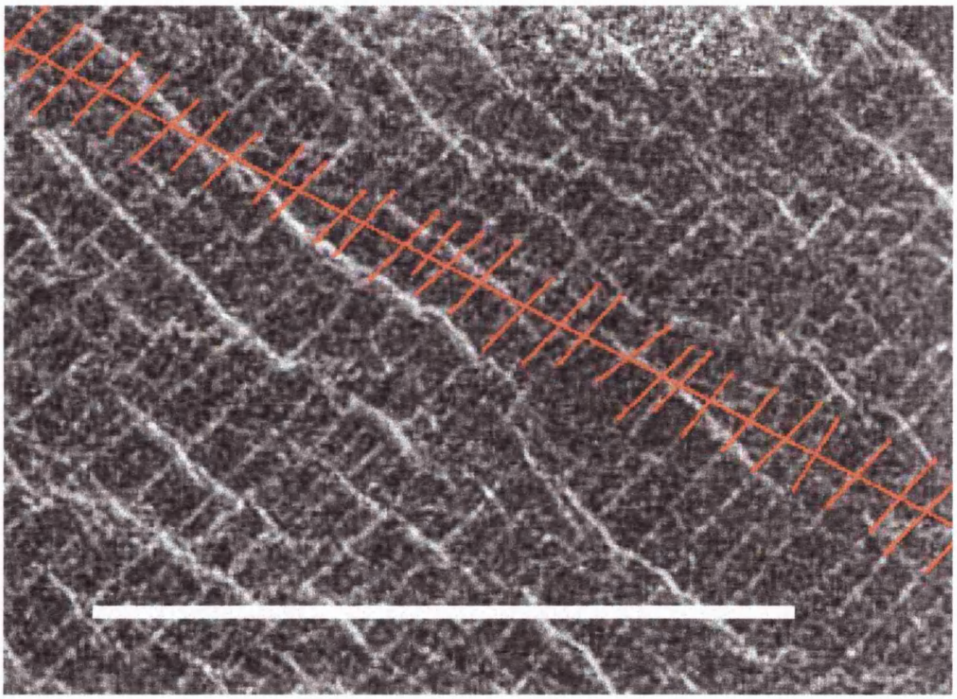

Fig. 3.5. Example of profile used for spacing measurements. Scale bar is 20km. North is up. Note that the profile need not be orthogonal to the fracture set because the spacing is measured for each individual pair of fractures.

3.3.3. Fracture spacing measurements: results.

The distance along the profile was measured in all cases to the second of each fracture pair (see fig 3.4 for location of profiles). Measurement error on the distance along the profile was small with respect to the distance and is omitted from the plots. Error on the spacing is taken to be +/- 1 pixel, which is equivalent to 0.075km. The zero point of all profiles is taken as the end nearest Eistla Regio. The results of the profiles are shown in figs. 3.6 and 3.7.

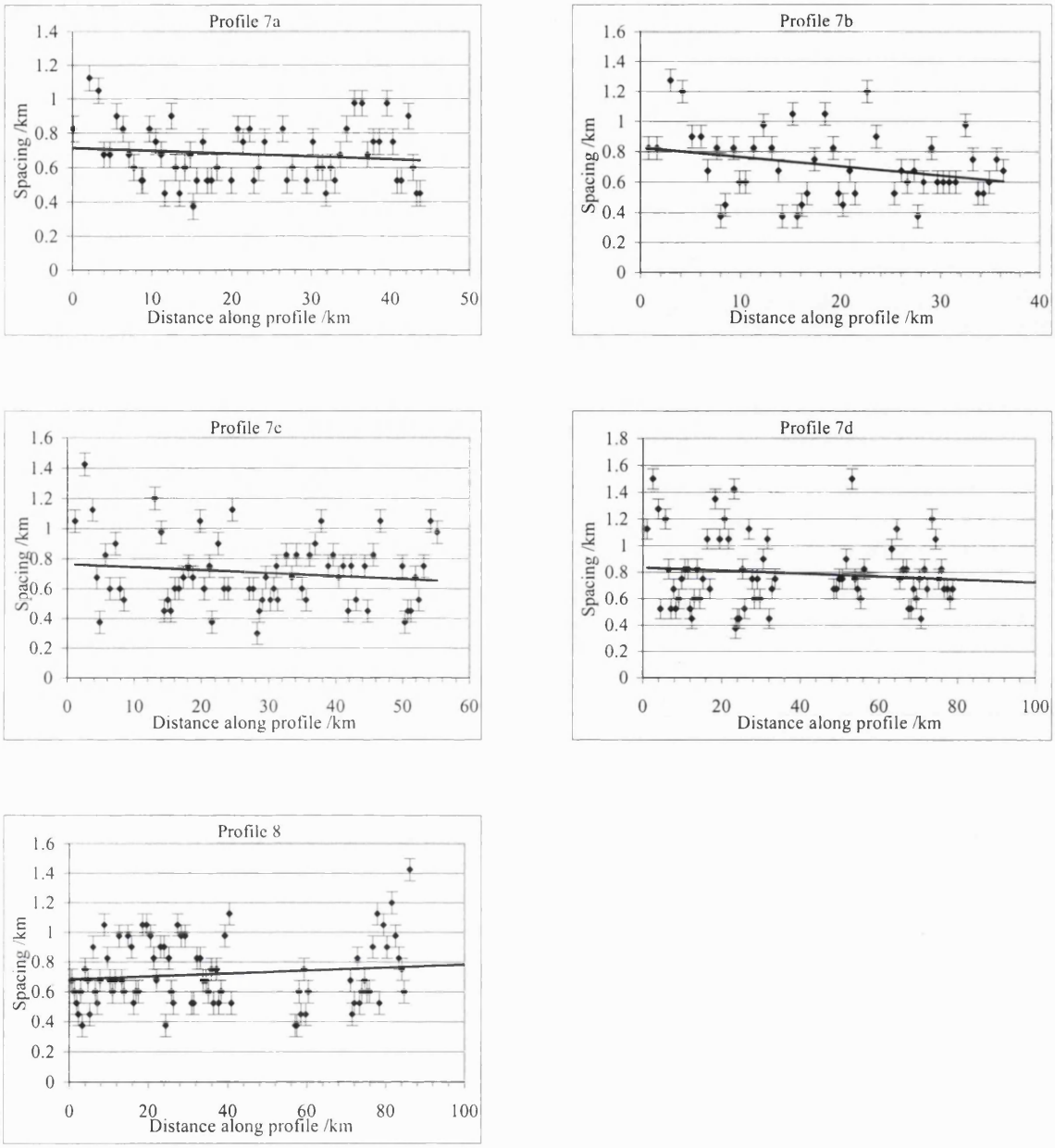

Fig. 3.7. Results from profiles 7 and 8. Profile 7 was made up of 4 separate profiles approximately parallel to one another over a width of less than 30km. This was done to check the transverse consistency of the profiles over the local area, i.e. to show that the profiles are typical of the area around them. See fig. 3.4 for location of profiles.

Profiles 9 and 10 were taken from the black set and, again, the start point is the end nearest Eistla Regio. The results of these profiles are shown in figure 3.8. Fewer profiles could be made because there were less easily measurable fractures in these sets.

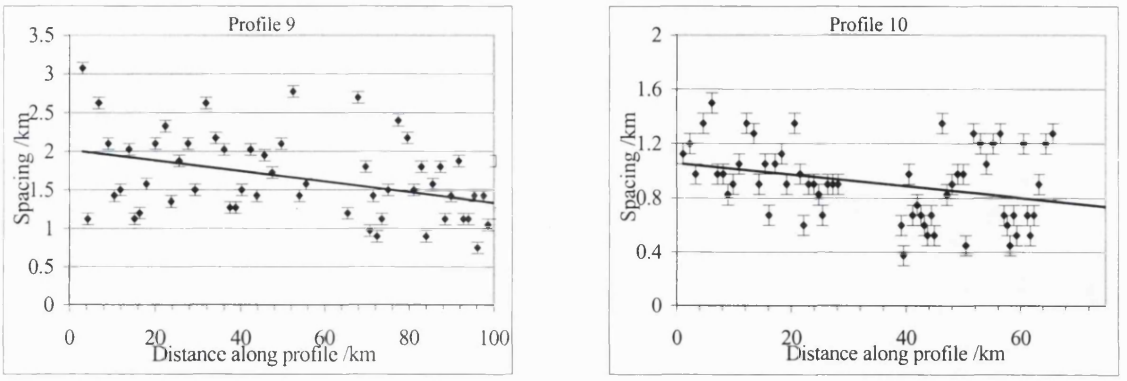

Fig. 3.8. Profile plots from black set of fractures. See fig. 3.4 for location of profiles.

3.3.4. Fracture spacing measurements: significance of trends.

The best fit lines of almost all these profiles show a trend of decreasing spacing with increasing distance from the rise. A correlation r-value was calculated for each set of data and compared to the 90% and 99% confidence values from standard tables (Bailey, 1959) to estimate the significance of the trend.

Profile	r-value	90%value	99%value	significant?
1	-0.13	0.16	0.25	NO
2	-0.2	0.16	0.25	MEDIUM
3	-0.52	0.16	0.25	YES
4	-0.38	0.16	0.25	YES
5	-0.06	0.16	0.25	NO
6	-0.37	0.16	0.25	YES
7a	-0.12	0.21	0.33	NO
7b	-0.29	0.23	0.35	MEDIUM
7c	-0.11	0.21	0.33	NO
7d	-0.13	0.2	0.3	NO
8	0.13	0.18	0.28	NO
9	-0.58	0.16	0.25	YES
10	-0.31	0.21	0.33	MEDIUM

Table.3.1. Correlation factor and significance for spacing profiles.

The overall impression that spacing is inversely proportional to distance from the topographic rise is supported by the fact that almost all the r-values are negative. However, only four of the profiles have a statistically significant deviation from a random population. These are profiles 3, 4, 6 and 9. Profiles 3, 4 and 9 are all in a similar area although profile 9 samples a different set of fractures. Furthermore, profiles 3, 4, and 6 are amongst the longest of the profiles and in dense regions of fractures, which means the data are more reliable.

3.3.5. Fracture spacing measurements: spacing number frequency distribution.

The spacing/frequency plots for each profile are shown in figure 3.9, 3.10 and 3.11 Most of them appear to diverge slightly from a normal distribution. However, the method used to measure fracture spacing may lead to weighting towards larger values. This would occur if a faint fracture was missed out from the profile and therefore not recorded as a 'gap' in the data. The missed fracture would effectively double one of the measured spacings and if this happened several times over a profile or section it could significantly alter the results. The opposite case where human error leads to 'seeing' a fracture where there is not one present is almost certainly much less likely, although still probably occurs in a data set with over 1000 measurements of fracture spacing.

This effect can be seen most clearly in profiles 1, 6, 7 (a, b, and c) and 8 where the mean of the normal distribution is to the right of the mode of the data and there are more bins to the right of the average spacing than the left. A change in mean fracture spacing along the profile would not have this effect, as it would merely widen the distribution.

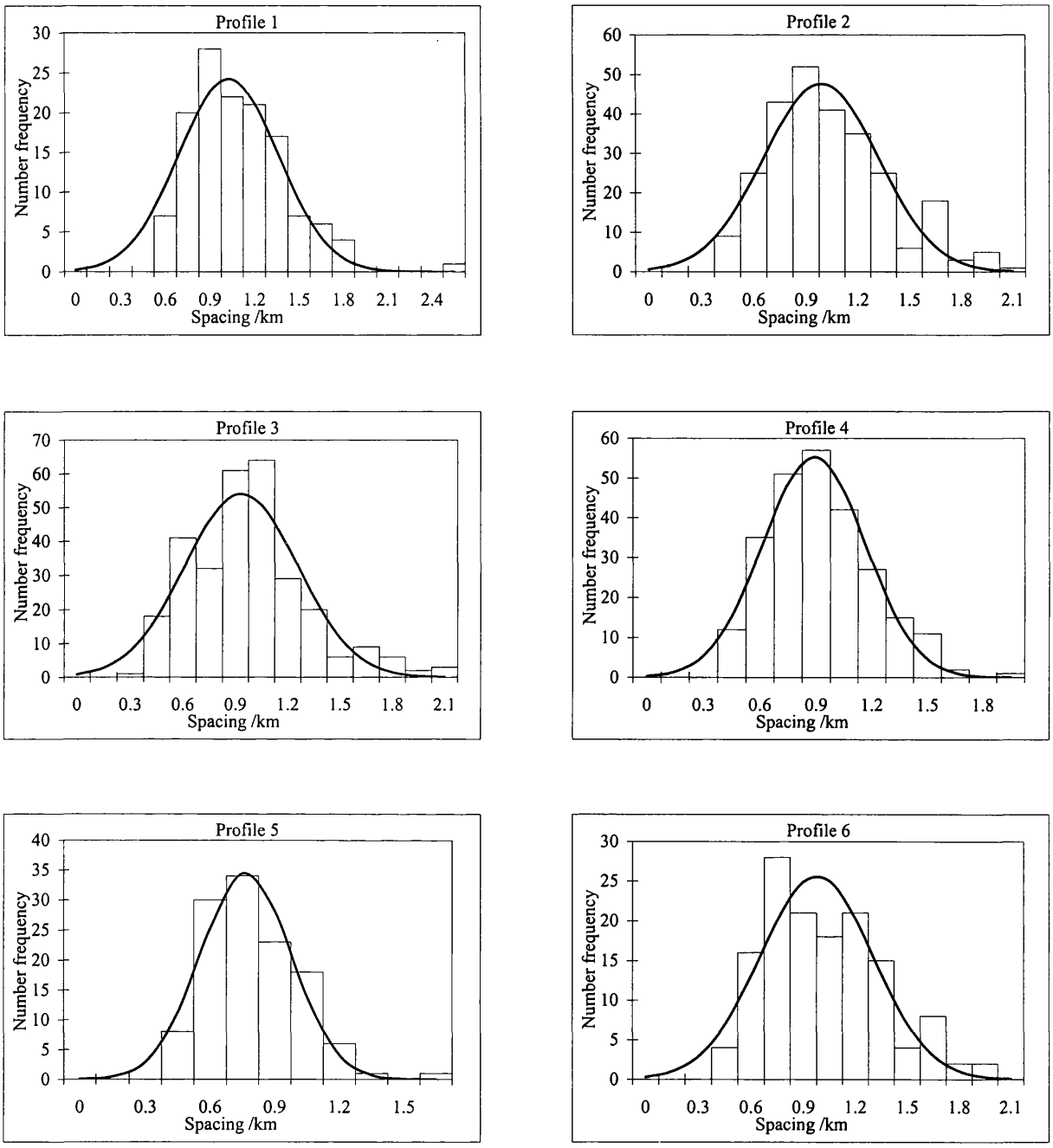

Fig.3.9. Number frequency distribution plots of fracture spacing for profiles 1-6.

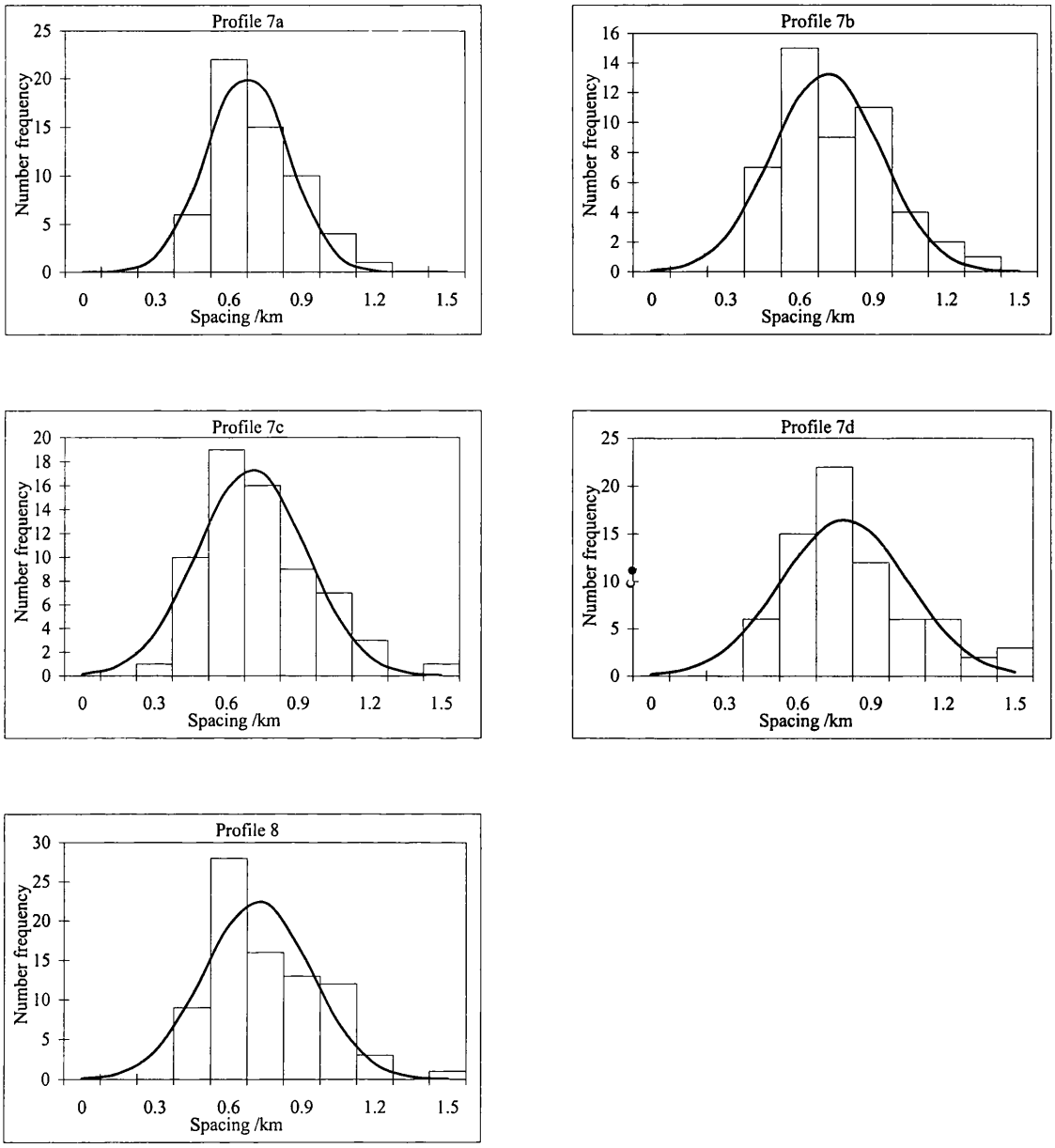

Fig.3.10. Number frequency distribution plots of fracture spacing for profiles 7 and 8.

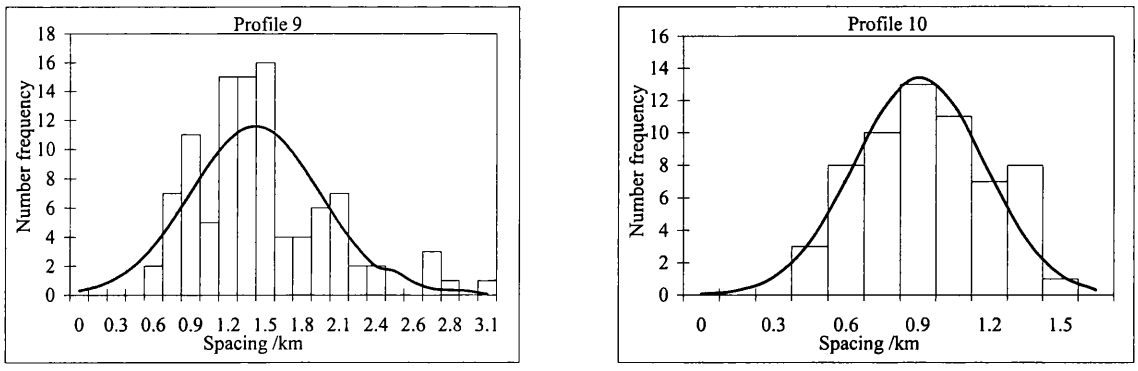

Fig. 3.11. Number frequency distribution plots of fracture spacing for profiles 9 and 10.

3.3.6. Fracture spacing measurements: further significance of trends.

Those profiles with lengths greater than 100km were broken up into approximately 50km sections, the mean spacing being taken for each individual section or profile. The results are shown in table 3.2, below.

Profile	Mean spacing /km	Std dev. /km
1a	1.08	0.31
1b	1	0.34
2a	1.08	0.36
2b	0.99	0.32
2c	0.93	0.31
3a	1.18	0.31
3b	0.87	0.27
3c	0.76	0.26
4a	1.01	0.27
4b	0.84	0.26
5	0.77	0.21
6	0.98	0.33
7a	0.68	0.17
7b	0.71	0.22
7c	0.71	0.23
7d	0.79	0.26
8	0.72	0.22
9	1.42	0.52
10	0.91	0.27

Table 3.2 Mean spacing of split profiles and standard deviations.

The standard deviations of these data conform to a linear fit of the form $\sigma = 0.36d$, where σ is the standard error. This is with close agreement with Banerdt and Sammis (1992), who found that $\sigma = d/3$ for the seven profiles that they measured.

The relationship shown in fig 3.12 does not give information on any physical property of these fracture sets, but it does show that the profile sets are consistent with one another and with those of Banerdt and Sammis, 1992.

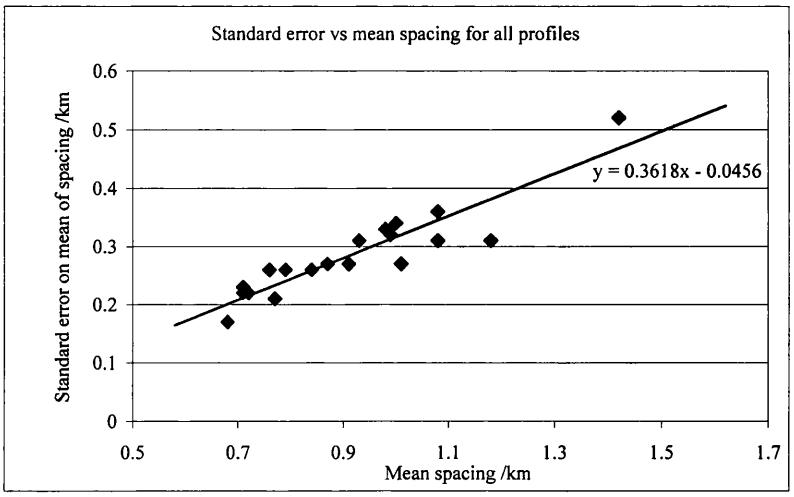

Fig. 3.12. Plot of standard error on the mean against the mean spacing of fractures for all profiles. The linear best-fit line is $\sigma = 0.36d$ where d is the mean spacing and σ the standard deviation.

3.4. Factors controlling spacing and azimuthal direction.

The mapping of the azimuthal directions of the CSPF shows that they form in concentric patterns which appear to follow the edge of the Western Eistla Regio topographic rise. The dependence of fracture spacing upon the position of the profile can be investigated by measuring the distance of the start of the profile (or segment of profile) from an imaginary line drawn around the extent of the topographic swell of Western Eistla Regio. Two lines have been drawn corresponding to the maximum and minimum interpreted extents of the topographic rise as shown in fig. 3.13.

The distance of each profile from the centre of the rise was also measured. Fig 3.14 and 3.15 show the plots of the dependence of mean spacing on distance from the edge and centre of the topographic rise. The error bars on fig. 3.14 correspond to the envelope of maximum/minimum distances obtained from fig 3.13. The error bars in fig. 3.15 represent an estimate of the uncertainty in choosing a centre-point for the rise.

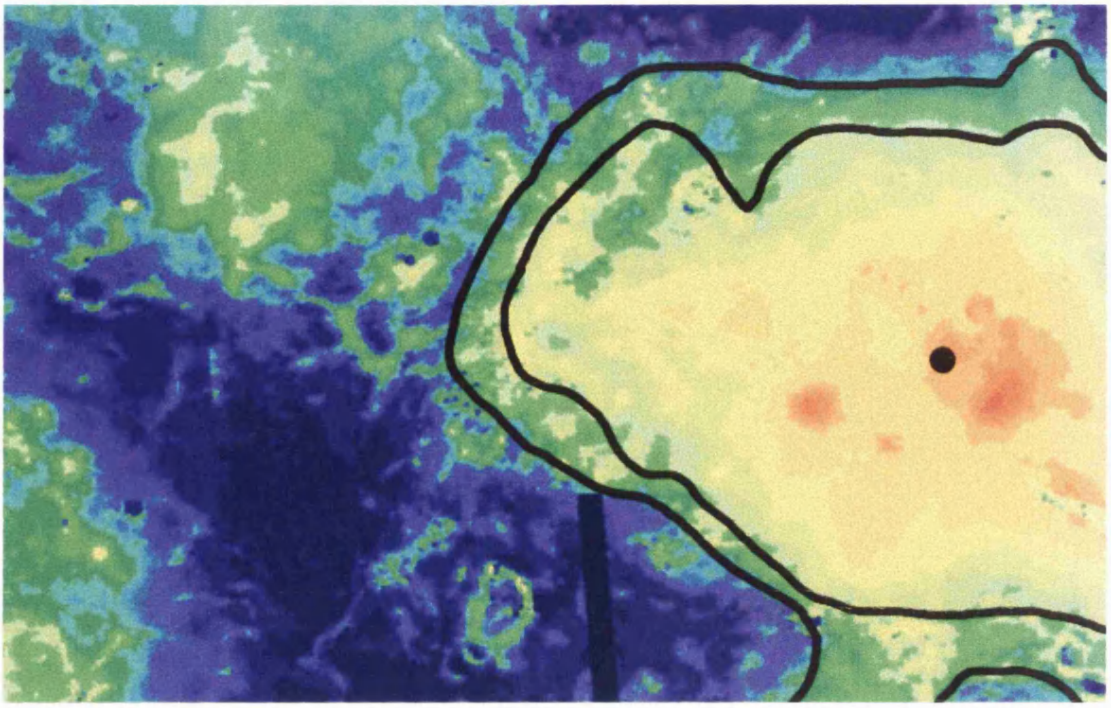

Fig. 3.13. Extents of topographic rise. This figure is as in fig. 3.4 but with most of the detail removed. Two interpretations of the maximum extent of the topographic swell are shown to give an idea of the possible maximum/minimum envelope of distances of profiles from the edge of the rise. Also marked is the rise "centre point". Scale bar and topographic scale as in fig. 3.4.

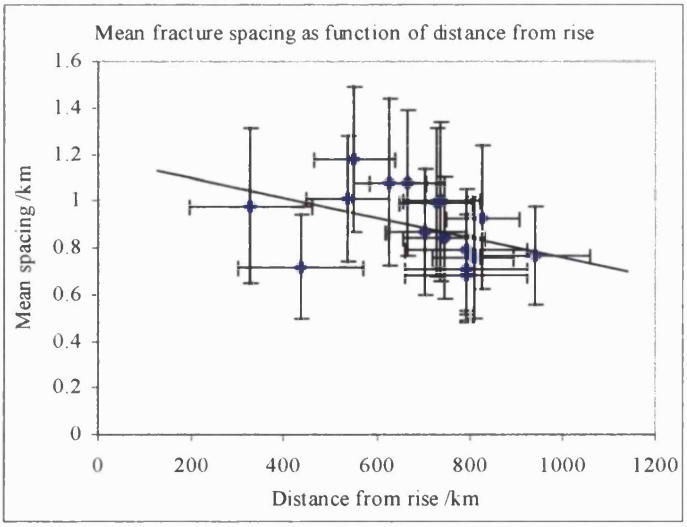

Fig. 3.14. Variation of mean fracture spacing with distance from edge of Western Eistla Regio topographic rise. X axis error bars correspond to maximum/minimum distances from fig. 3.13. Y-axis error bars are from standard deviation of data.

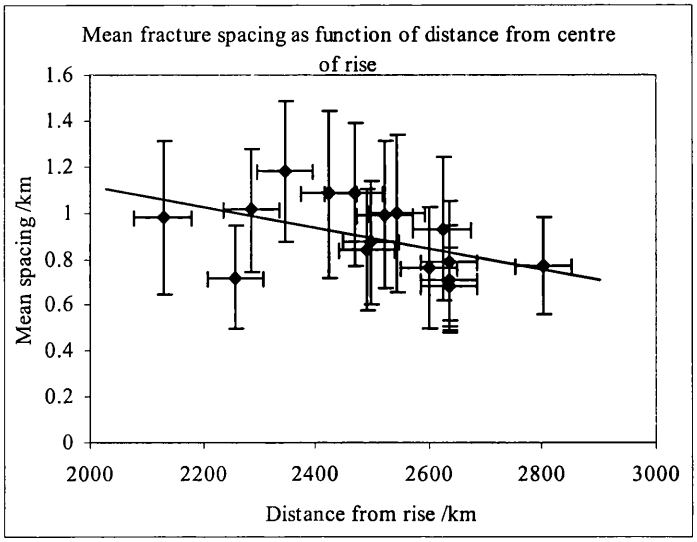

Fig. 3.15. Variation of mean fracture spacing with distance from centre of topographic rise. Error bars as in preceding figure plus estimate of uncertainty on position of centre.

Except for the two data points closest to the rise, there appears to be a steadily decreasing trend in fracture spacing with increasing distance from the rise, although the large spread of deviation of each data set makes this rather difficult to support. Nevertheless, the r-values for these measurements are –0.43 and –0.5 for distance from the centre and the edge of the rise respectively. The confidence r-values for both these data sets are 0.41 and 0.62 for 90% and 99% probability. Thus there is only weak statistical evidence for the inverse variation of spacing with distance across all of the profiles but it is reinforced by the fact that seven of the thirteen individual profiles showed some significant negative trend. The implications of these relationships between spacing and distance are discussed in chapter 11.

In addition, a centre of deformation for the red set was constructed by constructing lines perpendicular to the fracture trends (figs. 3.16 and 3.17) and the distance of the profiles segments plotted against distance from these local centres. The northern black set did not show a consistent central point and the southern black set had too few profiles Here too, there was a weak inverse relationship (fig. 3.18).

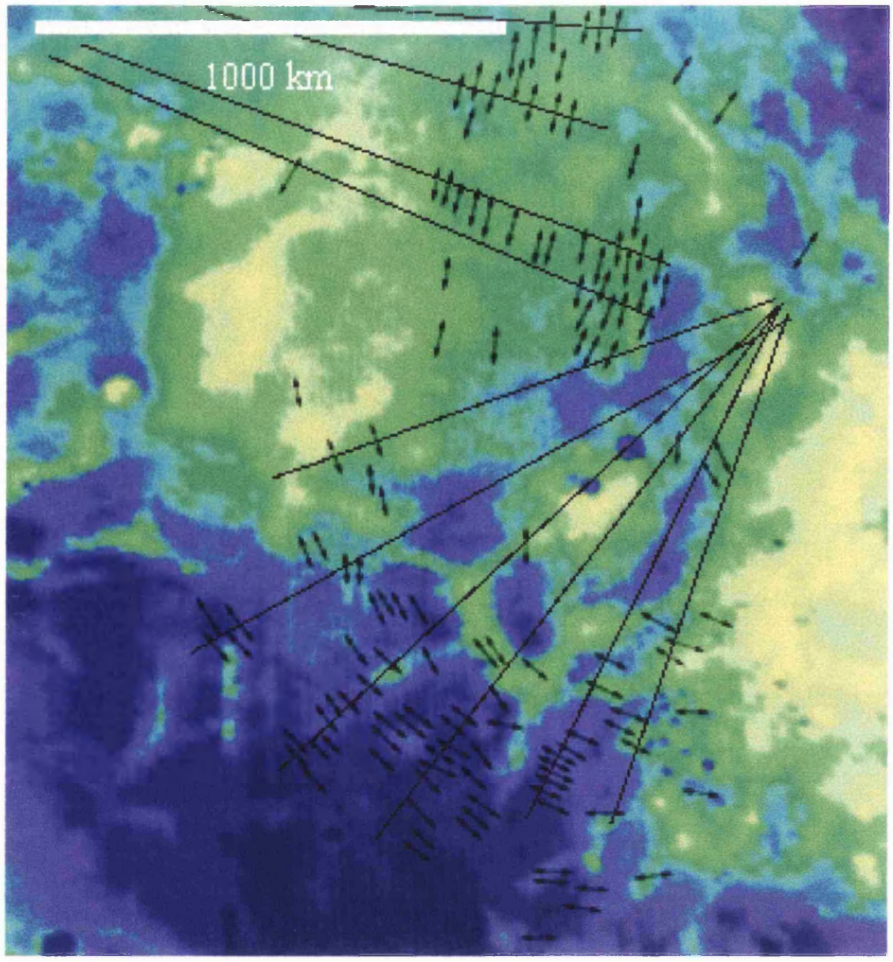

Fig. 3.16. Topographic plot showing how the centre of curvature was constructed for the black sets of CSPF. Note how the northern set has no clearly distinguishable centre. In contrast, the southern set has a discrete centre of curvature which is marked with a black cross on fig. 3.4.

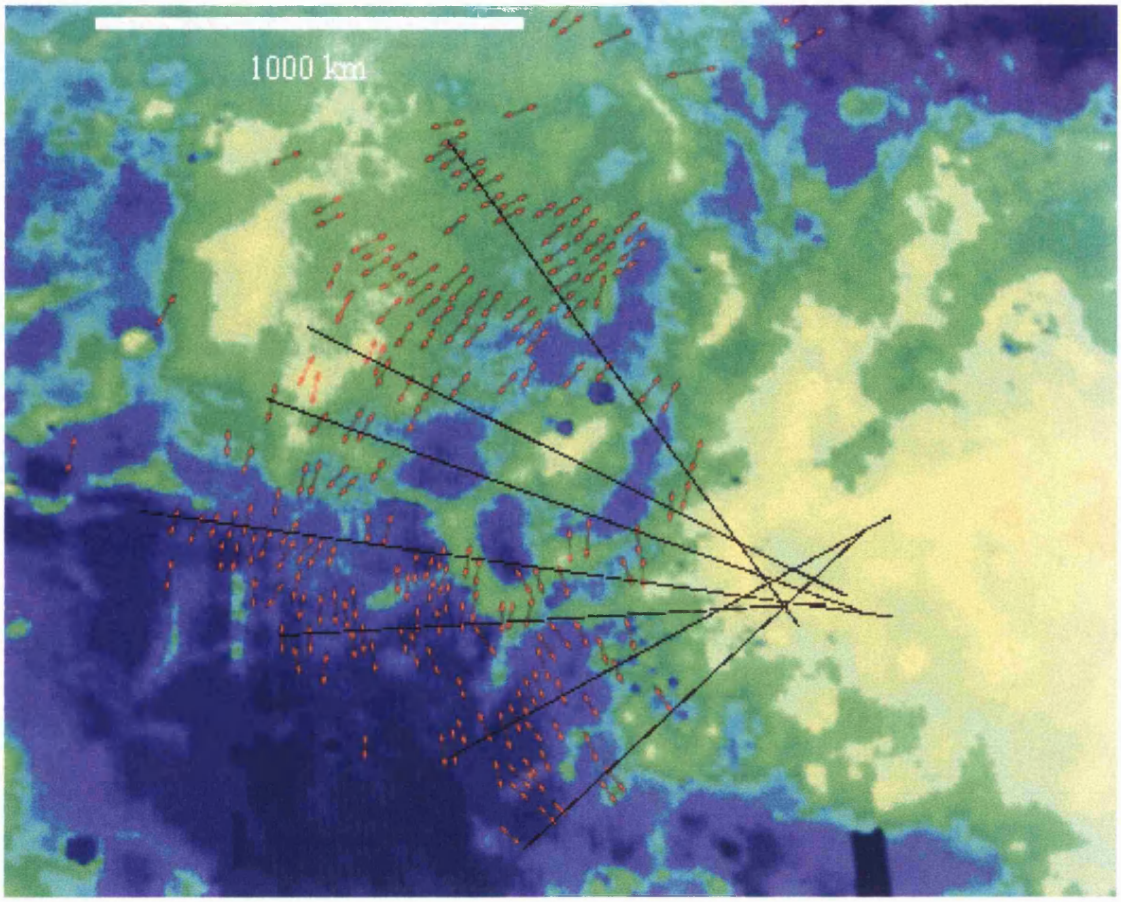

Fig. 3.17. Constructional lines for centre of radius of red set of CSPF. The centre point is not as well defined as the southern black set but may be associated with the faint, circular topographic feature at centre right of the image. Centre marked with red cross on fig 3.4.

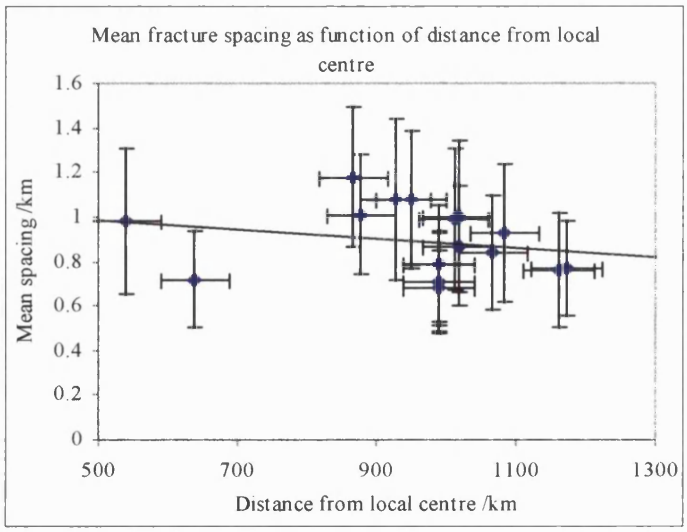

Fig.3.18. Variation of mean spacing of red set of CSPF with distance from the local centre of curvature. See figs. 3.4 and 3.17. r-value for this plot is–0.22

3.5 Length distribution of CSPF.

The final numerical observation made in this region is the length distribution of the fractures. This is complicated by the fact that no pristine set of data can be found. Nearly all CSPF are obscured to some extent by volcanism, deformed by later tectonism, or present in multiple, intersecting sets which make length measurements difficult. In addition, as has been noted before, the features are at the limit of the image resolution. As an example, over 250 measurements were made of fractures centred at approximately 29N333 (probably the best region for this kind of measurements), giving a mean length of just over 20km. The measurements are almost certainly biased towards shorter fractures, because the longer the fracture, the more likely it is to be partially obscured by volcanism or tectonism. The results of this survey are shown in figure 3.19.

Figure 3.19b shows no specific break in slope at any length, implying that no change in propagation style occurs as the fractures develop. This is in contrast to the results from the orthogonal set of brighter fractures described in Bowman and Sammis (1995) which have a distinct break in slope indicating that the fractures penetrate to a mechanical boundary. The smooth shape of Fig 3.19b shows that the CSPF formed at a time when the depth to the mechanical boundary was different, or that they do not penetrate as deeply as the brighter orthogonal fractures, or both. That they do not penetrate so deeply is supported by the graben like morphology of the brighter set and their greater lengths. The implications of this are discussed further in chapter 11.

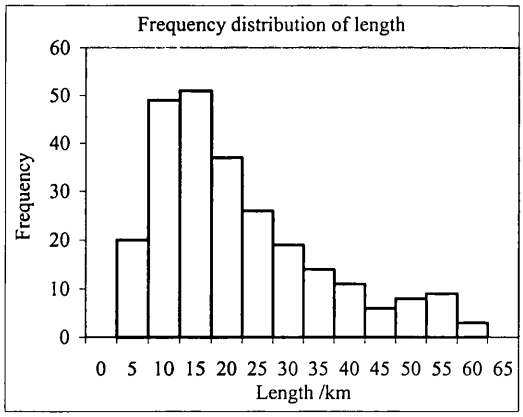

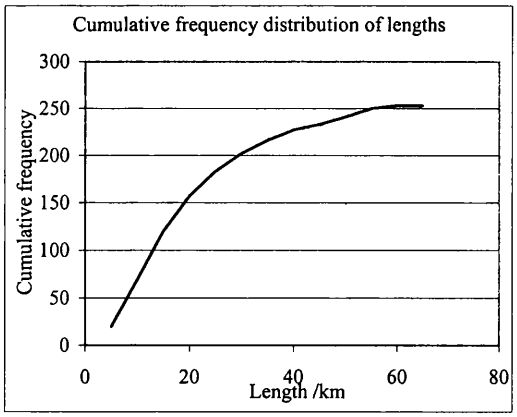

Figs. 3.19a and 3.19b. Length frequency distribution plots for CSPF.

3.6. Geological and stratigraphic setting of CSPF.

Fig.3.20 shows a geological sketch map of much of the area shown in fig 3.4. Superimposed on this map are the trends of CSPF. The units shown are simplified from those of Copp (1997) and are summarised below:

spr/gpr. **Sedna/Guinevere regional plains material.** Extensive unit covering the largest area of the units described. Low SAR backscatter gives the unit a dark appearance in imagery. Deformed by wrinkle ridges, the unit is deficient in small edifices and contains few identifiable flow features. The backscatter is modified (both increased and decreased in various areas) by superficial deposits from impact craters thought to be fallout materials. The unit generally occurs below mean planetary radius (mpr), except where uplift from the Western Eistla topographic rise has raised it.

The Unit is interpreted as extensive volcanic plains with surfaces smooth at the decimetre scale of the radar, later deformed by compressive stresses. The unit is relatively young although it is embayed by even younger volcanic flows as described below. Copp (1997) suggests thatmost of the uplift at Western Eistla Regio occurred prior to emplacement of spr/gpr because the plains embay the rise, although some evidence contradicts this idea. For example, volcanic deposits, overlying the regional plains, appear to flow 'uphill' (Copp, 1997). This suggests that there has been continued uplift since the emplacement of the regional plains.

Fig. 3.20 (Next page). Geological sketch map of Sif Mons (V31) and Sedna Planitia (V19) mapping quadrangles. North is up. After Copp and Guest (2000) and Copp and Guest (1997). See text for description of units. Note orientation of CSPF. Sif Mons quadrangle uses a Mercator Projection and covers an area of approximately $3x10^9 km^2$ whilst the Sedna Planitia quadrangle uses Lambert Conformal Conic Projection and has an area of approximately $6.6x10^9 km^2$. The CSPF have been superimposed on the map by using impact craters and other geological features as markers and applying skew and rotation transformations to alter the projection using Adobe PhotoShop software.
A full description of the geology of these quadrangles can be found in Copp (1997).

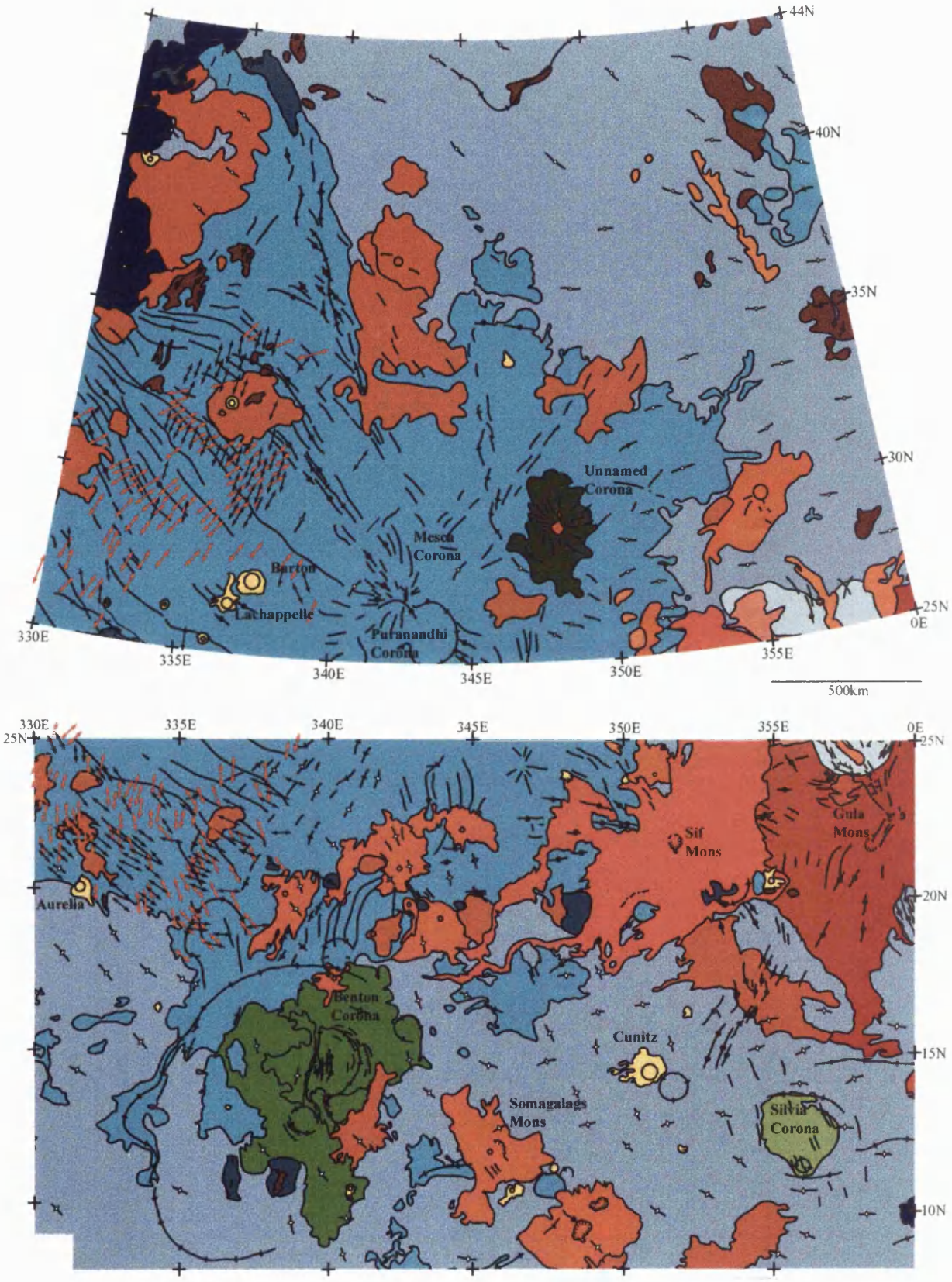
44N
40N
35N
30N
25N
0E
330E
335E
340E
345E
350E
355E
Unnamed Corona
Mesca Corona
Barton
Lachappelle
Puranandhi Corona
500km
Sif Mons
Gula Mons
Aurelia
20N
Benton Corona
Cunitz
15N
Somagalags Mons
Silvia Corona
10N
Impact crater rim or volcanic centre
Thrust fault or ramp
Graben (with mappable boundary faults)
Depression
Lineament or unit boundary
Graben (non-mappable boundarys)
Ridge crest
Wrinkle-ridge crest
pd
splm /gplm
pre
spr / gpr
sph / gph
s
g
vc
f / fd
ef
t
nf
c
cu
cb
cs

splm/gplm **Sedna/Guinevere lineated and mottled plains.** The second most aerially extensive unit found in quadrangles V19 and V31, characterised by a moderate, locally variable radar backscatter. The unit contains many small volcanic edifices and is deformed by wrinkle-ridges, graben and larger scale tectonic features. Linear and mottled plains appear to be the sole unit containing CSPF. Other small-scale deformation styles include polygonal and reticulate fracture patterns which do not fulfil the criteria established above for CSPF. Again, SAR brightness is changed by local fallout from impact craters. One set of wrinkle ridges is confined to this unit implying that the unit is older than the regional plains. Also, supporting this suggestion, the regional plains are seen to embay the s/gplm unit at all boundaries. The unit sits at or slightly above mpr. The lineated and mottled plains units are interpreted to be volcanic in origin but although small volcanic edifices are abundant the source of such a large amount of material cannot be readily identified. Continued small-scale volcanism and tectonic deformation may have been responsible for the mottled appearance, with the presently observable volcanic and tectonic features representing the last stages of formation. The unit shows no evidence of rapid emplacement and was probably formed over different time periods depending on the level of geological activity.

pd and t **Deformed plains materials and tessera.** Small outcrops of material with strong backscatter. Both units are embayed by plains units and thus considered relatively old and are extensively deformed by tectonic features. Tessera units show intersecting ridge and groove structures and are topographically high with respect to surrounding material. Deformed plains units are typically deformed by both extensional and compressional features and similar to, although generally smaller than, the tessera units. These units are thought to be the remnants of a highly deformed crust and are interpreted as being the oldest units in the mapping area.

sph/gph **Sedna/Guinevere homogenous plains.** A moderate backscatter plains unit, similar in morphology to regional plains, but less extensive and generally brighter in SAR imagery. Wrinkle ridges are more difficult to

identify as they are similar in radar properties to the plains they deform. The boundaries are unclear although the unit does appear to be embayed by regional plains, and overlies both lineated and mottled plains.
This unit is interpreted as a set of volcanic plains. It probably formed in a similar way to the regional plains although the brighter backscatter may imply a greater surface roughness and a difference in flow style of the lava.

pre **Relic plains.** A small unit with moderate backscatter found north of Gula Mons. It shows some deformation by compressional and extensional features. The unit is embayed by rp and overlain by nf and f units. This unit is thought to consist of older plains material that has undergone uplift and deformation during the formation of Nissabra Corona, a 300km wide feature to the north of Gula Mons.

s and g **Sif and Gula Mons material.** Flow like materials associated with Sif and Gula Mons. The units are comprised of individual flows with varying backscatter and morphologies. Individual flows may extend for up to 400km from the summit calderas. The Sif Mons material is superimposed on the local regional plains material and is seen to flow around 'islands' of gplm/gpr/pd on the south-western flank of the volcano. The Gula Mons material also embays regional plains.
The interpretation of these units is that they are the volcanic flows associated with the large shield volcanoes Sif and Gula Mons. The volcanoes appear to have formed during numerous eruptive events and there is evidence of flank eruptions especially on Sif Mons.

vc **Volcanic centre material.** Flow materials and edifices associated with intermediate scale volcanism. Summit pits or calderas may be visible surrounded by flows with variable backscatter. Individual flows are recognisable in many of these units. These units generally superimpose regional and linear and mottled plains.

f/fd **Isolated/dissociated flow material.** Small isolated outcrops characterised by low/medium backscatter. Observed to overlie splm and

pr. Some appear to emanate from small pits or lineaments. Control of flow by wrinkle ridges is observed and the source vents and flows are not topographically distinguishable from the surrounding plains.
These units are interpreted to be small-scale, local volcanic flows from vents or fissures. The lava is thought to be fluid owing to control of flow direction by ridges and lack of edifices.

ef **Edifice fields**. These units are manifested as local concentrations of small volcanic edifices. The morphology is predominantly shield-like although variation through cone morphology is observed. Most edifices are <10km in diameter with a concentration of 4-10 edifices per km^2. The unit is observed to overlie pr, lpm, ph and vc but is also seen to be embayed by vc. The units are often seen to be associated with local graben or lineaments and overlie CSPF.
These units are thought to be formed by local melting, with the area of the unit controlled by the extent of a shallow reservoir. The range of morphologies and complicated stratigraphic relations indicates that these features may have been formed at a variety of different times, or that the process which gave rise to them was active over a long period of time.

nf **Neago fluctus materials.** This unit is comprised of various flows with a wide range of morphologies and backscatters. Although some flows are observed to be deformed by wrinkle ridges, the brightness of parts of this unit are close to that of the ridges themselves making it difficult to identify them. Thus they may exist in more flows than can be observed The bulk of flows associated with this unit emanate from a N-S trending graben (Lancaster *et al.*, 1995). The unit is interpreted as a great flow field. These units are common on Venus and are closely associated with rifting and lithospheric extension.

c **Impact Craters.** These units comprise the ejecta, crater floor and crater peak materials. The floors are often dark in SAR imagery, whilst ejecta and central peaks are amongst the brightest areas in Venus SAR imagery. Ejecta margins are often lobate and asymmetrical.

cu, cb, cs **Coronae material (Unnamed, Benton and Silvia coronae respectively).** Silvia corona material has moderate backscatter and has undergone greater tectonic deformation than the regional plains that embay it. It is thus interpreted to be early plains deformed and uplifted by the formation of the corona. Benton corona material has a variety of morphologies and contains volcanic flow fields, edifices and concentric and radial tectonic features. There are several stratigraphically distinct units ranging from early flood lavas to late stage effusive volcanism. The cu unit has moderate backscatter similar to the splm plains that it superposes. Radial graben deform the flows, which are interpreted to be volcanic flows associated with the corona.

These units have a definite stratigraphic relation (although some cannot be constrained in time) as shown in figure 3.21. The ef and vc units in particular are ubiquitous throughout much of the stratigraphic record.

The CSPF are only found in the gplm and splm units (although they also appear in ef units that embay them) and are thus older than the regional plains and Sif and Gula Mons shield volcanoes. There is some evidence of CSPF deforming small shields (Guest and Stofan, 1999) although it is very difficult to say whether this is a false interpretation caused by the deformation showing through underneath the flow.

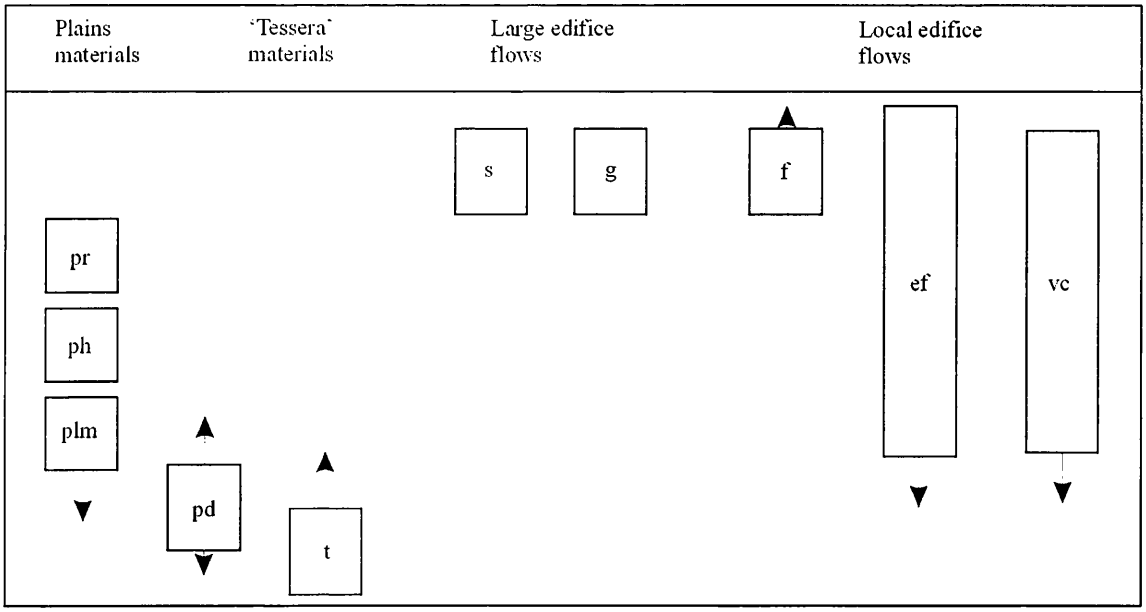

Fig. 3.21. Stratigraphic relationship between major units in V19 and V31 mapping quadrants. CSPF occur in the same stratigraphic position as plm units. Note that ef and vc appear as a continuous range and cannot be tied down to a particular stratigraphic time period. Arrows indicate uncertainty in the stratigraphic record.

The CSPF are post dated by the larger scale linear tectonic features such as the graben/en echelon faults to the north-west of Mesca Corona. This age relation is shown in fig. 3.22.

The CSPF in fig. 3.22 predate the larger extensional features, as shown by the fact that a small shield overlies the CSPF, but are deformed by the NW-SE trending extensional features. This stratigraphic relation is common throughout the area studied. Also, the larger scale features commonly start or terminate at CSPF, indicating that the smaller fractures act to arrest the larger faults. This often gives the appearance of shearing along the CSPF, but this is ruled out by the lack of consistent lateral strain in the local area. The relative ages of different sets of CSPF are more difficult to determine. The features are at the resolution limit of the imagery and it is very difficult to find examples of crack arrest or sequences of deformation as in fig. 3.22. These features are, therefore, interpreted as forming within a time scale that is after the emplacement of plm units but before the emplacement of regional plains. No precise position in the stratigraphic record can be established.

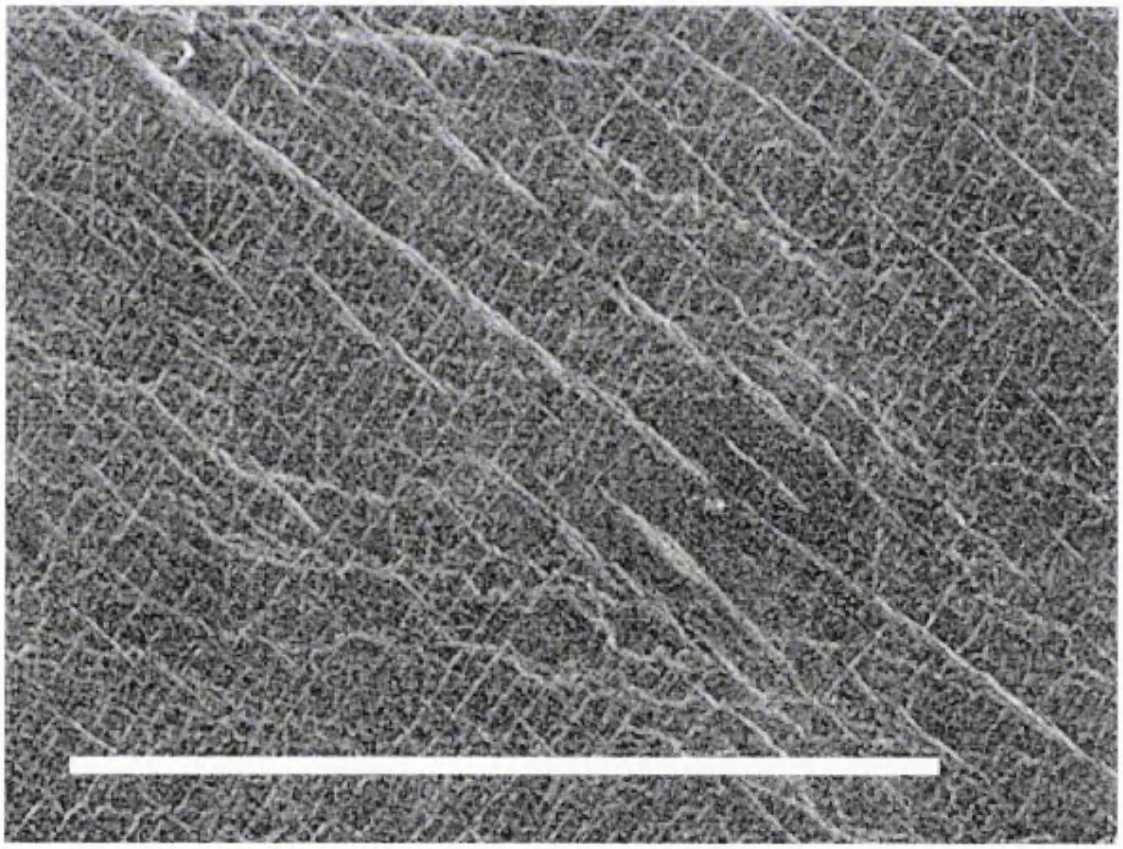

Fig. 3.22. Age relationship between CSPF and other extensional features. Scale bar is 50 km. North is up. This image is from FMAP framelet 31N339.

Copp (1997) interprets the plm units as early plains modified by continuous small-scale volcanic events and continued tectonism. If this is the case, then the

different sets of CSPF may be the fingerprints of the last few major tectonic events in the region and thus useful stratigraphic markers. For example, the concentric nature of the 'red' set of CSPF appears to associate them closely with the Western Eistla Regio topographic rise. The plains they are deforming, however, predate the formation of either Sif or Gula Mons, strongly implying that there was local extensional tectonism associated with the rise well before the currently visible large-scale edifices were formed.

Structures caused by compressive deformation are widespread thoughout the region under study and are most clearly manifested as wrinkle ridges (WR). Several workers have mapped these features (McGill, 1994; Basilevsky, 1994; Bilotti and Suppe, 1999) and have reached the conclusion that Western Eistla Regio is surrounded by a concentric pattern of WR which appear in both the plm and pr units (although they are much clearer in pr units). This begs the question as to which came first, CSPF or WR? The fact that some WR form in pr units and also extend into plm units implies that they must post-date CSPF, which formed prior to pr terrain. WR can also be shown to post-date CSPF by analysing the morphology of the ridges. Figures 3.23 and 3.24 show examples of WR that formed after CSPF. There are many WR for which the stratigraphic association with CSPF cannot be determined. Examples of WR from each of the four FMAP used in the study have been observed, however, and this evidence strongly implies that the concentric WR formations mapped by McGill (1994) and Bilotti and Suppe (1999) post date CSPF.

Because many of the WR are concentric to the Western Eistla Regio topographic rise, they are almost certainly due to tectonic forces associated with the evolution of the rise. As CSPF are also concentric to the rise, or to local centres that are part of it, but are amongst the oldest features in the area, the rise must have been active over almost all of the stratigraphic history of the area. CSPF are therefore a useful stratigraphic marker when, as has been shown in this chapter, they are associated with regional geology.

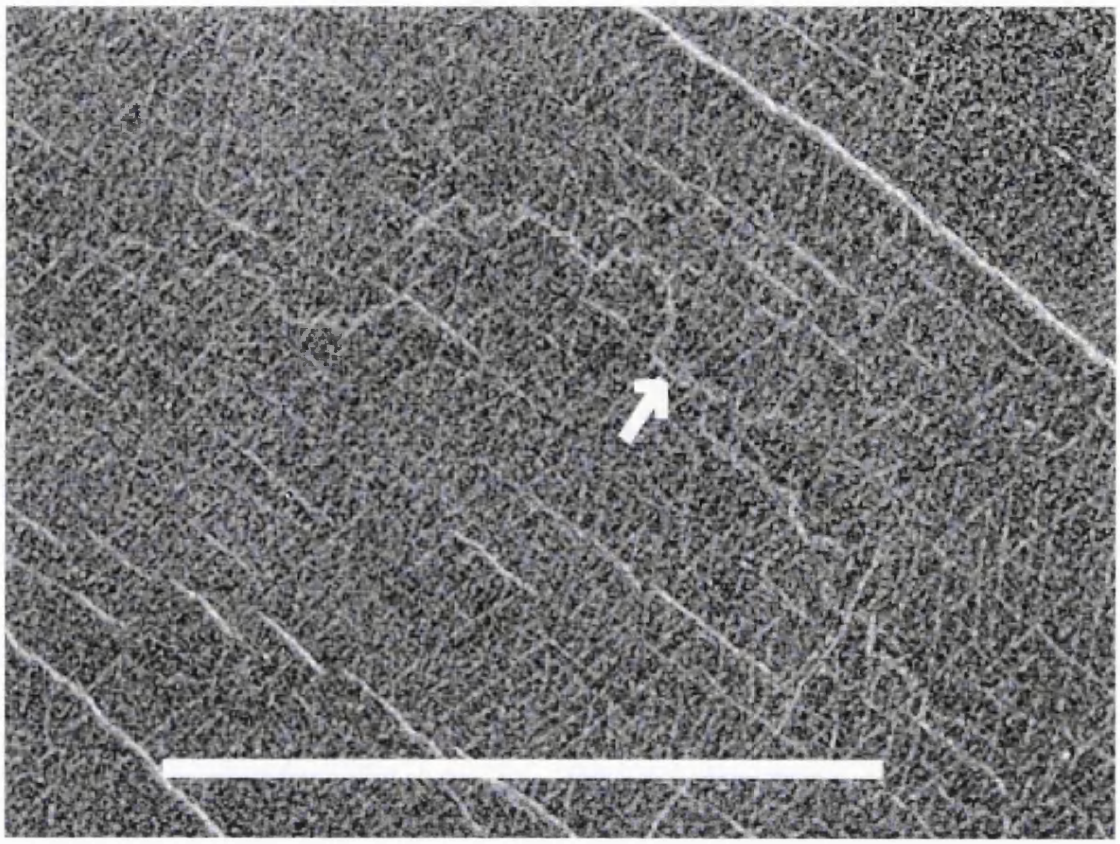

Fig. 3.23. Wrinkle ridge (arrowed) showing morphology controlled by NE and NNE trending CSPF which it obviously post-dates. Scale bar is 30km, image taken from FMAP framelet 33N 335E. North is up.

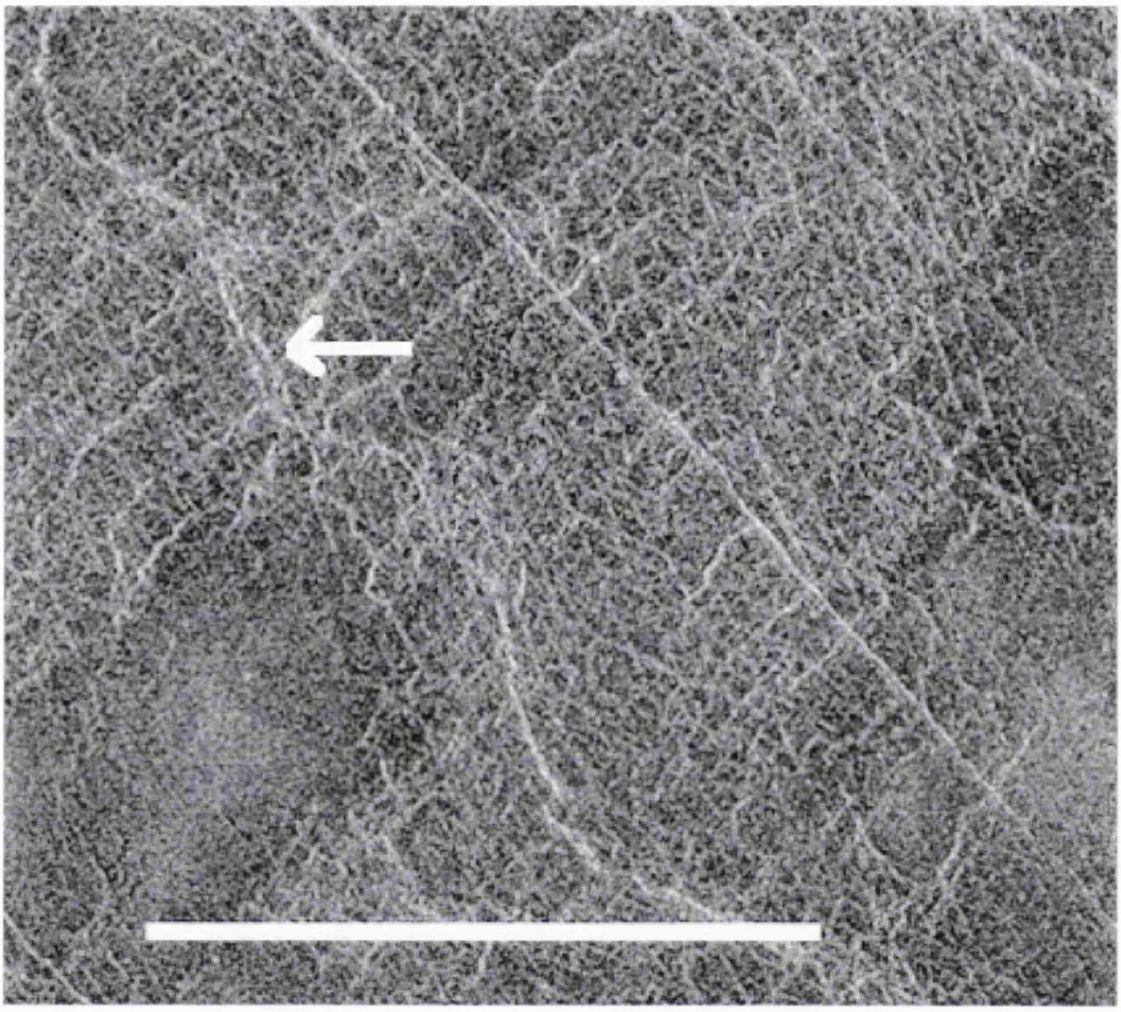

Fig. 3.24. Image showing wrinkle ridge (arrowed) controlled by CSPF. The image also shows a long lineation that deforms shield deposits, which in turn overlie CSPF. The shield to the left appears to be deformed by CSPF at the margins, showing how fracturing can show through later deposits, causing confusion in mapping and stratigraphic interpretation. Scale bar is 30km and image is from FMAP framelet 21N 337E. North is up.

3.7. Previous models of CSPF.

The statistical and mapping results used in this study are useful but cannot explain how the CSPF formed. Here, I examine previous work by other authors who have proposed quantitative models for CSPF formation.

The three models summarised here are the stress shadow and shear lag models of Banerdt and Sammis (1992) and the thermal model of Anderson and Smrekar (1999). All will be shown to be inadequate, in the form they have been presented, for description of the CSPF.

3.7.1. Comments on observations by Banerdt and Sammis (1992).

Like the study of Banerdt and Sammis (1992), the observations of CSPF from this chapter showed little variation in spacing over large areas. The observation from Banerdt and Sammis that there are "no good examples found with a spacing significantly smaller or larger spacings than 1.0-2.5km" is probably quite easy to explain. Many of the patterns measured in this study have spacing from 0.7 -1.0km but it would be very hard to spot fractures with spacing <0.5km. These would appear to be separated by only 6-7 pixels or, as is more realistic (if we assume the actual fracture to have a width of 1-2 pixels) only 2-4 pixels. Also, by analogy to the shatter zone of Nur (1982), the area surrounding a fracture that is broken and disturbed and therefore rougher than the surrounding areas, closer spaced fractures would, presumably, have smaller widths themselves and thus a smaller shatter zone. The radar return from the fractures would consequently be weaker and hence more difficult to distinguish from the background plains. Thus, the closer spaced the fractures, the more unlikely they are to be visible from the SAR images.

This study, although confined to a limited area, agrees with that of Banerdt and Sammis (1992) in that there appear to be few examples with larger spacings. This may be due to the nature of the deformation and is an important point to note in formulating a model.

3.7.2. Stress shadow model as described in Banerdt and Sammis (1992).

Using the well known principle that tensile stress is relieved near to a vertical fracture (fig 3.25), Banerdt and Sammis suggest that new fractures will not form within the stress shadow of a pre-existing fracture and will therefore have spacing that scales with the depths of the cracks. They specifically note the case where the depth of fracturing is controlled by layering, and reject the model because it would rely upon a relatively constant layer thickness over a large area. This is probably unlikely, although it should be noted that repeated emplacements of very fluid lava may form topographically flat layers which, when overlain by other fluid lavas, may generate thin, constant depth layers over large areas.

What is more important, though given a subordinate role by Banerdt and Sammis, is that a horizontal layer is not vital for the stress shadow model. If the cracks penetrate to an approximately similar depth, for whatever reason, the spacings will be similar. For this reason the stress shadow concept is a viable model for explaining CSPF although not in the form described by Banerdt and Sammis, 1992.

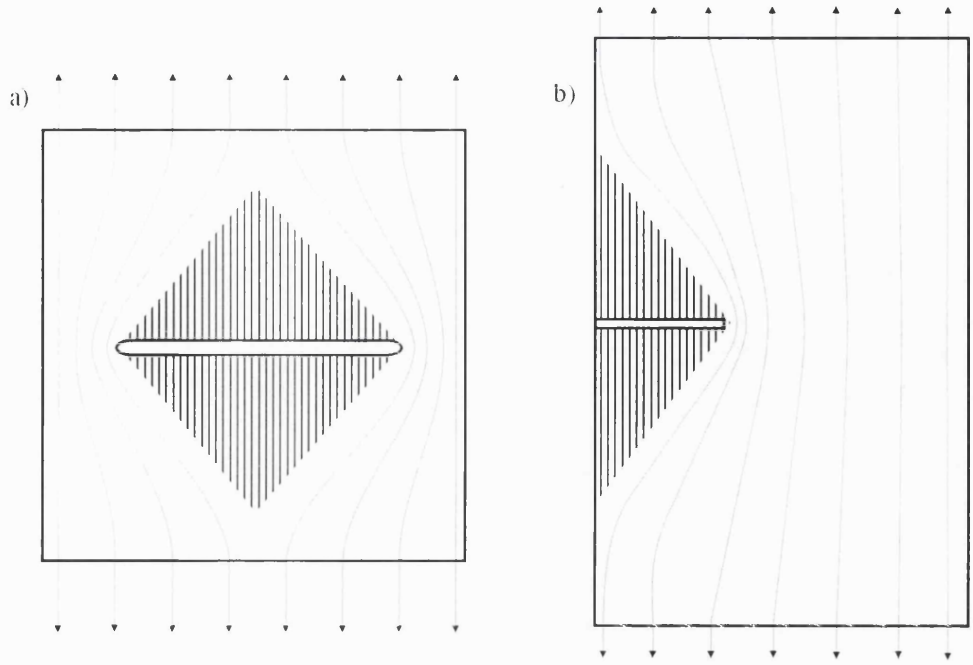

Fig. 3.25. Stress shadows (shaded area) around a crack in a plate (a) and an edge crack (b). The stress is relieved for a certain distance from the defect.

3.7.3. Shear-lag model.

Banerdt and Sammis identified the shear lag model, adapted from materials sciences (Hu and Evans, 1989) to describe a brittle film, ductilely coupled to an elastic substrate, as a possible mechanism for the formation of CSPF. In this model, a brittle layer with a thickness of less than a kilometre is coupled to a stronger layer underneath and subjected to a tensile stress greater than the tensile strength of the brittle layer (see fig 3.26). The tensile stress around an initial vertical fracture is relieved by the stronger substrate through a coupling traction at the base of the brittle layer. In this way each fracture has a zone of stress relief around it in a similar way to the stress shadow model of 3.7.2. Banerdt and Sammis (1992) suggested frictional sliding (of a flood basalt deposit on a stronger bedrock substrate) as the plastic coupling mechanism and thus generated an expression for the critical spacing that is, within certain conditions, independent of the thickness of the layer. The brittle layer thickness must be some factor less than the fracture spacing such that the maximum principal stress approximates the horizontal stress σ_{xx}. For thicker layers this is not the case and the predicted fractures would be less steeply dipping and thus more likely to form horst and graben features than tensile cracks. With the assumption that the layer is about a kilometre thick the model is independent of layer thickness and gives an average spacing d where $d = \frac{3T_0}{2\mu\rho g}$. T_0 is the tensile strength of the brittle layer, μ is the

coefficient of friction and g the acceleration due to gravity. The strength of the rock mass is, however, difficult to assess and depends upon the degree of jointing in the rock mass but it can be assumed to be of the order of 1-40MPa. If the mean spacing is 1.0km then this translates to a tensile strength of the rock mass of around 35MPa. Although this value is lower than that of some intact basalts, which is 40MPa, it is still larger than would be expected for a rock mass with even a very small amount of pre-existing damage. In fact, according to Schultz (1993), the values of tensile strength for the rock mass on Venus are likely to be between 0.2 and 2.0 MPa based on the empirical Hoek-Brown envelope (Brown and Hoek, 1988).

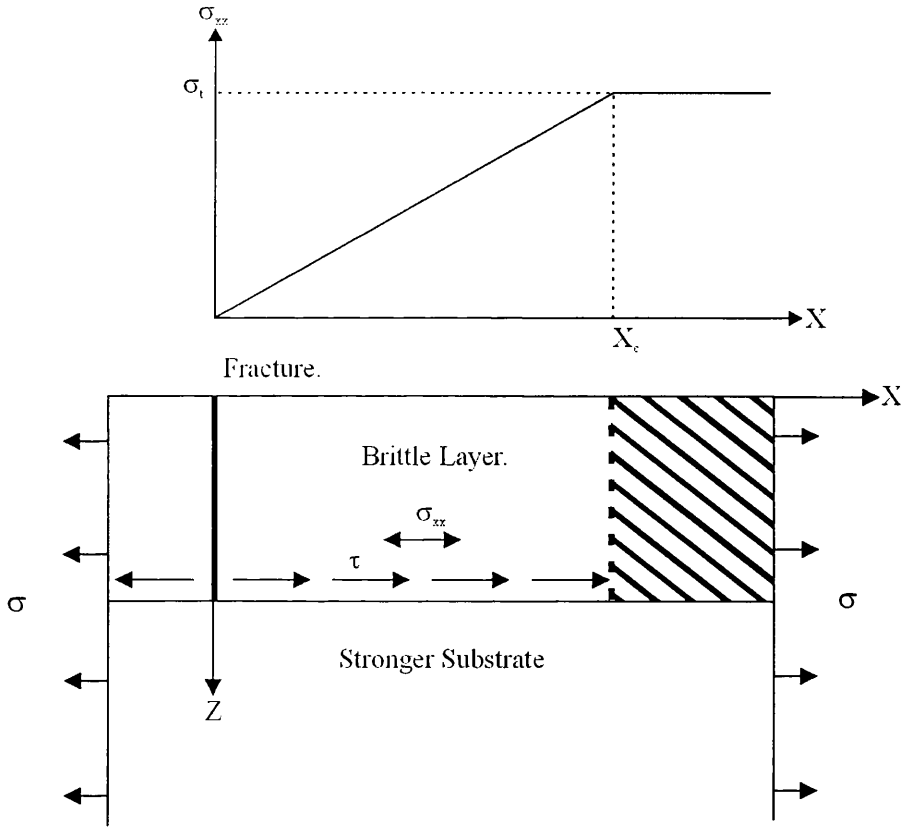

Fig. 3.26. Active case of shear lag model (after Banerdt and Sammis, 1992) where the upper brittle layer is ductilely coupled to the stronger substrate. The system is loaded by a tensile force, σ, greater than the tensile strength of the upper layer σ_t, causing the layer to fracture. The amount of elastic recovery is limited by the basal traction, τ, and stress is relieved only for a distance X_c from the fracture after which (hatched area) a new fracture can form. With time, more fractures develop and the areas of possible fracture forming are used up leading to a 'saturated' fracture pattern.

Using the same values as Banerdt and Sammis (1992), the lower values of tensile strength give a mean fracture spacing of between 15 and 150m. These values do not agree with the observations of the plains; in fact they are an order of magnitude too small. However, the model ignores any horizontal component of overburden pressure, which could rectify the problem (e.g., for a 500m thick layer the mean spacing would be

1.0km if overburden were added to the model): for, at depths greater than a few hundred metres the tensile strength of the layer becomes mathematically insignificant and spacing is approximated by $d = \frac{3z}{2\mu}$. This would make the model depend explicitly upon the thickness of the layer, negating the key advantage of the Shear-Lag model. But, for values of μ between 0.6 and 0.85 (as used by Banerdt and Sammis, 1992) the mean spacing would be approximately 2z, where z is the layer thickness- a result very similar to that predicted by the Banerdt and Sammis formulation of the stress shadow model.

For this reason, the shear lag model would appear to be a viable model of deformation, although the implicit assumption that the substrate layer is separate from, and stronger than, the brittle upper layer is difficult to justify. At depths of 3-4km or more, this may be more realistic as the plastic behaviour of the rocks results in ductile failure (Solomon *et al.*, 1992), but at shallow depths there seems little to prevent faulting and fracturing if the tensile stress is large enough. Furthermore, the observation that CSPF follow concentric patterns is difficult to reconcile with the shear lag model, and appears more consistent with a simple concentric stress field.

3.7.4. Thermal model.

The thermal model of Anderson and Smrekar (1999) seeks not to explain the mechanism that formed the CSPF, or the spacing of the features, but rather to offer an explanation for the source of the tensile stress that formed them and to analyse the depths to which such stresses can propagate failure. Anderson and Smrekar propose that thermal changes in the atmosphere are the source of this global tensile stress. The model is based upon several assumptions. Firstly, that Venus underwent a global resurfacing episode 300-700MY ago that was accompanied by a huge outgassing of SO_2 and H_2O, thus altering the Venusian climate (Bullock and Grinspoon, 1998). Secondly, the assumption is that the climate change followed the pattern of cooling-heating-cooling where the magnitudes of temperature change are 100K, 200K and 100K respectively. Thirdly, these changes are geologically instantaneous and the timescale over which temperature changes penetrate the lithosphere is critical. From these assumptions, Anderson and Smrekar show that the depth of thermal penetration into the lithosphere can produce stresses large enough to cause failure.

The first assumption depends entirely upon the validity of the argument of whether Venus was globally or regionally resurfaced. This is a contentious and important issue, with some authors favouring a directional, stratigraphic model

(Basilevsky et al., 1997 for example) with different units forming globally at specific times whilst others (e.g. Guest and Stofan, 1999) favour a non-directional model more consistent with 'equilibrium resurfacing' whereby some units form throughout the geological record. The arguments involved in this issue are complex and depend somewhat on personal methods of stratigraphic mapping. As such, the debate is outside the scope of this thesis. What can be highlighted, however, is that the CSPF are found almost solely in the unit designated plm by Copp (1997). This is the stratigraphically oldest unit in the area and overlain by the regional plains (pr), the most aerially extensive unit. The plm units are deformed by CSPF whereas the younger, but more widespread, pr, are not. Thus the global resurfacing event must have occurred before the emplacement of plm in order for climate change associated with it to be responsible for the CSPF. For this reason, rp units must have been emplaced after the climate change step that caused the CSPF or withstood deformation for some reason. The fact that there are two cooling stages makes this unlikely, especially as the model suggests that the middle 'heating' phase is responsible for wrinkle ridging which is found extensively on the rp. The second cooling phase (over 500MY after the first cooling phase) should, in the model of Anderson and Smrekar, have deformed the rp units as the model does not depend upon the tensile strength of the material and the thickness of the regional plains spans 50-500m (Kreslavsky and Head, 1999). Thus the stratigraphic setting of rp and plm units, together with the fact that CSPF are only found in plm, units undermines the idea that global climate change (at least, in the sense of Anderson and Smrekar, 1999) is the source of the stress that formed them

Also, some observations of the CSPF make the thermal model difficult to accept. The fact that the CSPF in the region studied are associated with the topographic rise of Eistla Regio implies that stresses caused by the formation of the rise, rather than isotropic stress caused by thermal contraction, are the source of CSPF. The simple fact that the fractures are in linear sets also seems at odds with this model. The polygonal features mentioned earlier in this chapter and described by Anderson and Smrekar (1999) and Johnson and Sandwell (1992) seem much more likely candidates for formation by isotropic stress.

In conclusion, although the physical model proposed by Anderson and Smrekar is valid, it is based upon an assumption of global, volcanic resurfacing which has yet to be accepted. Also, the CSPF are linear features that have localised centres of deformation and therefore seem incompatible with the isotropic stress field that would be expected from a global climate change.

3.8. Conclusions.

The main conclusion of the work described in this chapter is that there are distinct trends in the azimuthal direction of the features identified as CSPF. The clearest and most aerially extensive set appears to trend concentrically to the large topographic rise of Western Eistla Regio, which is centred at 355E 25N. Two other sets of fractures can be identified, one of which (pink set of fig. 3.4) is only localised and very faint. The black set is better interpreted as two separate sets with distinct centres of curvature as the north and south regions cannot be linked together on the imagery unlike the majority of the fractures of the red set. These concentric trends can also be interpreted as being due to local uplift which has now subsided and has no topographic signature. The possible centres of uplift are marked on fig. 3.4 with a large 'X'.

The fractures are also shown to have a mean spacing consistent with the results of Banerdt and Sammis (1992), and display a trend of mean spacing versus standard deviation similar to that of Banerdt and Sammis (1992). Banerdt and Sammis (1992) note that there are changes in spacing and orientation of the CSPF over the area studied. There is now evidence that the spacing decreases slightly with increasing distance from the topographic rise or local centre of uplift.

CSPF occur only in lineated and mottled plains units, a plains unit that (with the exception of tesserae) appears to be the stratigraphically oldest in the region. CSPF have been shown to be older than most other tensional features such as graben and lineaments. The extensional event that formed the CSPF is also shown to predate regional compression as CSPF predate wrinkle ridges. Other authors (Anderson and Smrekar, 1999) have stated that the CSPF appear to be independent of regional structure and topography, although they appear to have misquoted Banerdt *et al.* (1997) who merely state that the source of regional tension has yet to be identified. Banerdt and Sammis (1992) also state that some sets of CSPF have "a slight, but apparently significant gradient in average spacing from one end to the other", which they interpret as possibly being due to variation in mechanical properties of the plains material.

The shear lag model of Banerdt and Sammis (1992) is insufficient to explain the spacing of CSPF, owing to their assumption that the rock mass is as strong as intact basalt, or the morphology, as the concentric patterns are unlikely to result from a shear lag system. The work of Anderson and Smrekar (1999) does not explain the spacing but does estimate the depth of penetration depths of cracks due to thermal stresses. However, the stratigraphic relationship between CSPF and WR and the concentric patterns of CSPF make global thermal stress an unlikely cause of CSPF.

The final conclusion of the work described in this chapter is that there are slight trends in average spacing (implying a trend in the spacing controlling factor), although at the limit of statistical analysis, and that the CSPF are controlled by regional geology, in this case, the topographic rise of Western Eistla Regio. Any quantitative approach to modelling the CSPF must explain the close spacing, the concentric patterns and the slight trend in spacing whilst using appropriate physical parameters for the rock mass to constrain the model.

Chapter 4

Application of rock mechanics theory to shallow crustal conditions on Venus.

4.1. Introduction.

The behaviour of materials that make up the terrestrial planets depends upon intrinsic factors, such as structure and composition, and extrinsic factors, such as temperature, pressure and the rate of deformation to which they are subjected. The aim of rock physics is to understand how materials behave is and this is done through experiments and theoretical and numerical methods. This chapter sets out the basics of rock mechanics theory and discusses the physics and mechanics applicable to shallow crustal conditions of Venus, focusing on the theory of normal faulting and jointing.

This thesis uses material science concepts and fracture mechanics theory to form a quantitative geophysical model for CSPF formation. The general methodology is described in Sammonds (1999) and a specific example of the application of this approach to crevassing in ice-shelves is Rist *et al.* (1999). The theory presented here, specifically the elasticity theory, forms the basis of this methodology.

4.2. Rheology of rocks.

Crustal rocks are invariably under stress. We can consider these rocks to be behaving as continua on a scale much larger than the atomic level and that they respond to stress by deforming. Stress and strain can be described in three dimensions by tensors and linked by a constitutive relation (Ranalli, 1995)

$$R(\varepsilon, \dot{\varepsilon}, \sigma, \dot{\sigma} .... \{M\}) = 0 \qquad (4.1)$$

where R is the rheological function, ε and σ are strain and stress and M represents the intrinsic material parameters. Dotted quantities represent the time derivatives. Materials that have the same form of constitutive equation are said to belong to the same rheological class (e.g., elastic, plastic, viscous). The material parameters represent rheological properties such as rigidity, compressibility, etc and, although they are intrinsic material properties, they can be affected by extrinsic conditions. Temperature, pressure and time can cause changes in these parameters even when the actual composition and form of the material itself is unchanged. These extrinsic factors can

even change the rheological class of the material, for example, the change in behaviour of metals from elastic to plastic upon heating.

Understanding the behaviour of rock before, during and after failure is central to the theory of faulting and fracture and therefore essential for describing the features observed on the surface of Venus. The history of the development of rock physics and rheology of rocks can be found in standard texts such as Ranalli (1995) and Gueguen and Palciauskas, (1994) and a review of the applications of rock physics can be found in Sammonds (1999).

4.3. Formulation of stress as components.

Stress is the fundamental dynamic quantity of rheology and is a 2^{nd} rank tensor. We can express stress in three dimensions in various ways. Here, I shall describe stress in terms of Cauchy's formula (Lawn, 1993), isotropic and deviatoric parts and finally using principal axes.

4.3.1. Stress tensor.

Considering rocks as continua, we can set up a Cartesian co-ordinate system to define the stress acting upon a body in three dimensions. If we consider an infinitesimal parallelepiped (fig. 4.1) with faces in the Cartesian planes, any body force acting on the whole system will exert a traction on each of the surfaces of this infinitesimal block. Of these six tractions, there will be three pairs of equal and opposite forces and thus we need only consider one of each pair. These tractions can then be written in their Cartesian components as shown in fig. 4.1 giving the stress tensor σ_{ij}:

$$\sigma_{ij} = \begin{pmatrix} \sigma_{11} & \sigma_{12} & \sigma_{31} \\ \sigma_{21} & \sigma_{22} & \sigma_{23} \\ \sigma_{31} & \sigma_{32} & \sigma_{33} \end{pmatrix} \tag{4.2}$$

where i represents the coordinate and j represents the direction of the component acting on the face of the element. The stress tensor is a tensor of rank two with units of force per area. For a continuous body in equilibrium the sum of all moments about any given axis will be zero and the tensor becomes symmetric such that $\sigma_{ij} = \sigma_{ji.}$, thus eliminating 3 unknowns.

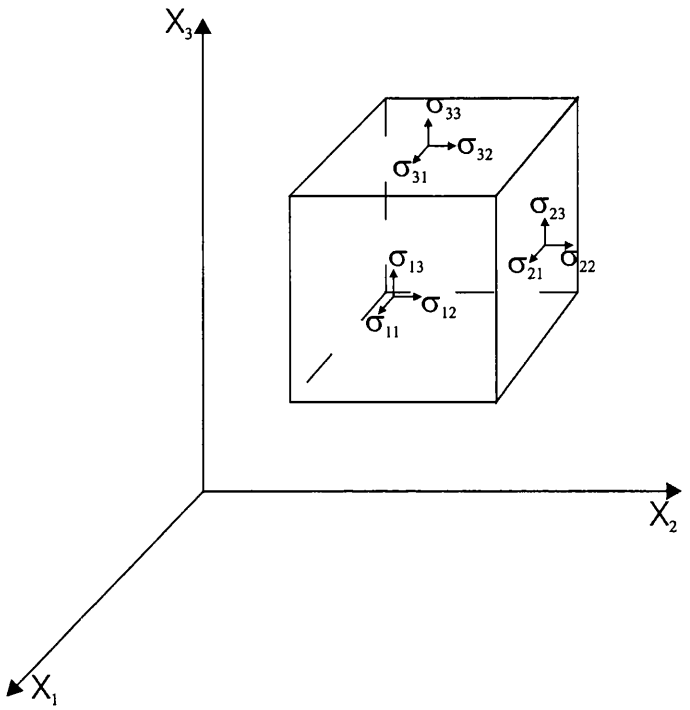

Fig. 4.1. Stress components on the faces of an infinitesimal parallelepiped.

Thus we can now specify a state of stress by specifying the six components of the stress tensor. Specifically, for an equilibrium state, the stress tensor symmetry leads to

$$\frac{\partial \sigma}{\partial x_j} + \rho X_i = 0 \tag{4.3}$$

where ρ is the density and X_i are the body forces per unit mass. σ is the stress.

4.3.2. Cauchy's formula.

Using the stress tensor to gain knowledge of the stress at a point in a body allows us to consider the stresses at a surface containing that point. This is important for many geological problems such as faulting. We can derive the normal and shear components of the stress tensor on the surface, the relationship between which is known as Cauchy's formula. If the unit normal to the surface is n_j then Cauchy's formula may be written as

$$T_{(n)i} = \sigma_{ij} n_j \tag{4.4}$$

where $T_{(n)i}$ are the tractions on the surface. This allows us to specify exactly the normal stress at the surface, τ, and the normal stress, σ, as

$$\sigma = \sigma_{ij} n_j n_i \text{ and } \tau = \sigma_{ij} n_j t_i \tag{4.5}$$

where t_I are the unit vectors tangential to the surface.

4.3.3. Isotropic and deviatoric stress.

Consider the stress tensor of (4.2). The tensor is symmetric with only six unknowns. Those diagonal parts are known as the isotropic parts whereas the off axis terms are called the deviatoric parts. The isotropic stress is defined as

$$\sigma_{ij}^{0} = \frac{1}{3}\sigma_{kk}\delta_{ij} \tag{4.6}$$

where δ_{ij} is the Kronecker delta and σ_{kk} is the sum of the diagonal parts of the stress tensor. This leaves the deviatoric stress to be written as

$$\sigma_{ij}^{'} = \sigma_{ij} - \sigma_{ij}^{0} \tag{4.7}$$

i.e., the remainder of the stress tensor with the isotropic part removed. Thus the stress tensor can always be written as

$$\sigma_{ij} = \sigma_0\delta_{ij} + \sigma_{ij}^{'} \tag{4.8}$$

where σ_0 is the mean normal stress. The deviator is thus the part of the state of stress that exists in addition to, or deviates from, hydrostatic pressure.

4.3.4. Principal axes.

When the diagonal, isotropic stress components are equal and the deviatoric components are zero, the body is in a state of hydrostatic stress. Similarly, if the co-ordinate system is chosen specifically (or transformed) such that the deviatoric parts are zero then the six non-zero components of the stress tensor reduce to only three. These are called the principal stress axes. It is convention in geophysics to label the σ_{11} term σ_1, the σ_{22} term σ_2 etc., with $\sigma_1 \geq \sigma_2 \geq \sigma_3$.

4.4. The brittle-plastic transition.

In general, rocks behave elastically for short timescales and under moderate conditions of temperature, pressure and stress. Plastic deformation, occuring at long timescales or higher temperature or pressure, is the manifestation of dislocation movement in the crystal lattices of the minerals that compose the rock and depends upon the number of easy-glide slip systems available. Silicate rocks, having only 2 easy slip systems, are therefore generally brittle (Murrell, 1989, Frost and Ashby, 1982).

Plastic deformation is characterised by a non-recoverable strain in the manner of a viscous fluid. Elastic behaviour is generally characterised by infinitesimal strain whereas plastic deformation can develop (large) finite strain. If failure occurs following

elastic behaviour it is termed brittle failure whereas failure after plastic behaviour is termed ductile or plastic failure. The transition between elastic and plastic behaviour for pure materials is well defined but, in the crust, the brittle-plastic transition occurs in a broad zone of environmental conditions where both kinds of deformation processes occur simultaneously. At low temperatures and pressures, brittle failure mechanisms dominate failure of the crust but at more extreme conditions, viscous flow occurs. Between these two lies the region of brittle-plastic behaviour and it has been shown that this transition occurs at lower temperatures and pressures for lower strain rates (Ranalli, 1995). Fig. 4.2 shows how the brittle-plastic transition is affected by pressure and temperature.

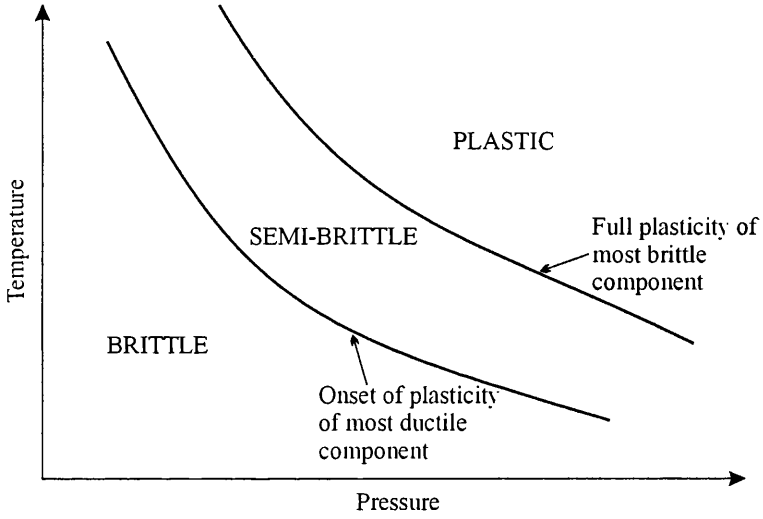

Fig. 4.2. The brittle-plastic transition in P-T space. After Odedra (1998).

The behaviour of rocks in the transition zone is complicated but, on Earth, brittle fracture is the dominant mechanism in the upper 10-20km of the crust. Silicate rocks tend to deform plastically for temperatures greater than a factor of 0.6 of their melt temperature (Frost and Ashby, 1982). Experiments on igneous rocks have shown that the transition from brittle to semi-brittle behaviour occurs above the pressures and temperatures found in the upper Venusian crust (Evans *et al.*, 1990), and the depth to the brittle-ductile transition on Venus is likely to be at least 2-4km (Solomon *et al.*, 1991). The CSPF are amongst the oldest features in the region mapped in this study (chapter three, Banerdt and Sammis, 1992) and are interpreted as extensional features. Another example of extensional features formed under high pressures and surviving for timescales of the order of 10-100Ma are mode I cracks found parallel to oceanic spreading ridges.

Thus the timescale of deformation and environmental conditions on Venus for formation of CSPF are consistent with brittle failure, at least in the shallow crust. We can therefore confidently describe the upper few kilometres of the Venusian crust using brittle faulting or fracture mechanics theory.

4.5. Failure under triaxial stress.

Having stated previously that the state of stress in the crust can be described in terms of principal axes and, in general, these are non-zero, we must summarise the theory of failure under triaxial stress conditions. Under various stress conditions, different types of failure occur. Figure 4.3 shows the different types of failure.

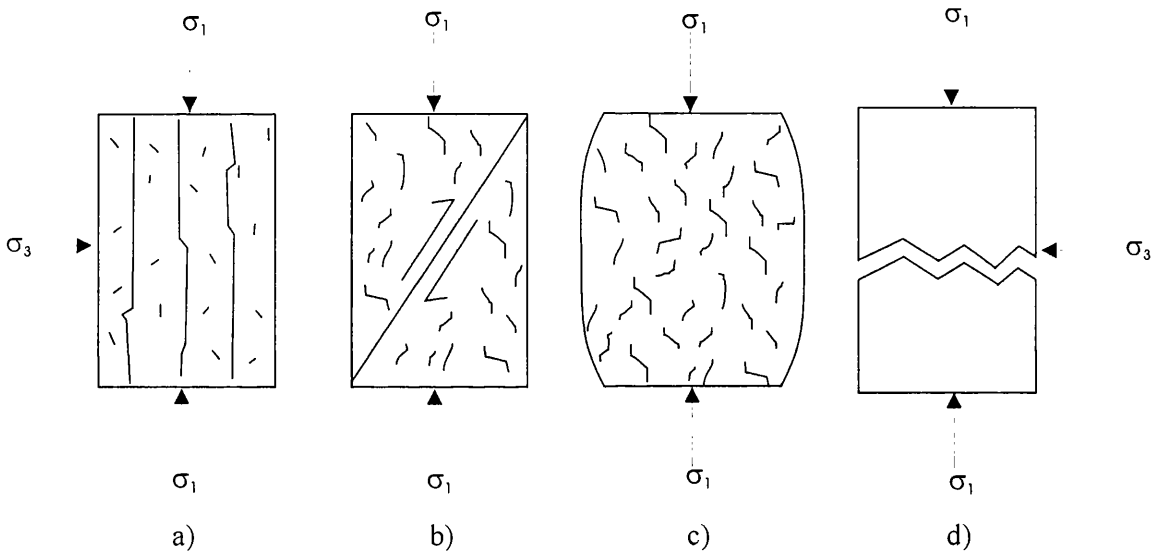

Fig. 4.3. Failure modes under triaxial conditions from Paterson (1978).

a) Longitudinal tensile splitting caused by uniaxial compression. σ_1 = large, σ_3 = small.
b) Shear fracture observed at approximately 30° angle to the maximum principal stress axis caused by linkage of smaller cracks. σ_1 = large, σ_3 = moderate.
c) Semi-brittle fracture and cataclastic flow (barrelling). A network of tiny shear fractures is formed but not one obvious fault. Although the failure mode appears to be plastic, in reality the processes involved are brittle with individual rock grains fracturing and sliding in a microscopic version of b). At high temperatures and pressures there is a transition to plastic flow of individual grains. σ_1 = large, σ_3 = large.
d) Tensile failure. Simple extension fracture with low strain and no shearing. σ_1 = large and negative, σ_3 = small.

4.5.1 Plastic failure criteria.

A number of empirical failure criteria have been formulated to explain both ductile and brittle failure. The Tresca maximum shear stress theory, for example, states that

yielding occurs when the maximum shear stress reaches a critical factor which is characteristic of the material. Only substantial deviation from hydrostatic pressure can cause yielding and the yield surface in stress space is a hexagonal prism for the Tresca criterion and a cylinder for the related Von Mises criterion. These are essentially ductile failure criteria and although they have some applicability to certain brittle problems (Ranalli, 1995), they are not relevant to this project.

4.5.2. Brittle failure criteria.

The empirical failure criteria of Mohr and Coulomb are generally used to describe brittle failure. The Coulomb criterion is based upon the projection of the stress tensor onto a plane as a normal and a shear component (see fig. 4.4). For failure the shear component must exceed the cohesion of the material plus a factor proportional to the normal stress. This criterion is expressed as

$$|\tau| = s_o + \mu\sigma_n \tag{4.9}$$

where s_o is the inherent shear strength, μ the coefficient of internal friction and σ_n the stress. The criterion can be used not only to find the failure point but also to calculate the conjugate angles of faulting at failure, θ. The Mohr criterion is similar to that of Coulomb, but uses an experimental approach to determine a failure envelope such that

$$|\tau| = f(\sigma_n) \tag{4.10}$$

In general, the shape of the Mohr envelope is a slightly downward turning version of the linear Coulomb criterion, which can be said to be the linear approximation of the Mohr criterion.

Despite the immediate utility of these criteria, they are merely empirical failure envelopes based on experimental data. The coefficient of internal friction has no real meaning because, prior to failure, there is no fracture face yet formed on which a frictional force can act. The internal friction can, however, be related to sliding on microcrack faces using the modified Griffith criterion as discussed in section 4.6.3. The real value of the Mohr and Coulomb criteria is that they are simple and easy to apply.

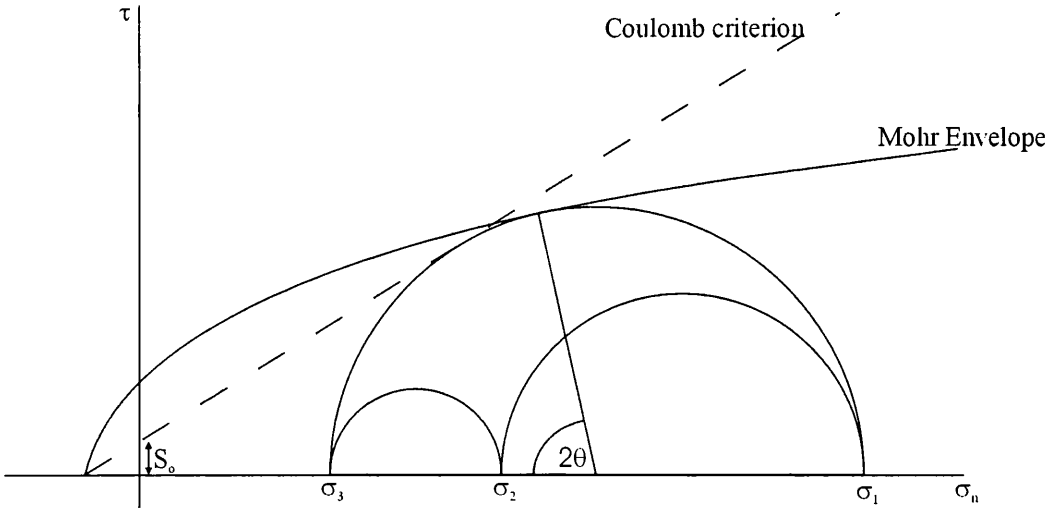

Fig. 4.4. Coulomb and Mohr failure envelopes in normal and shear stress space.

4.6. Griffith crack theory.

As was noted late in the nineteenth century, the 'critical applied stress' required for failure of a sample was often observed to show poor repeatability. Results could fluctuate by an order of magnitude and were always lower than predicted by theory. Griffith (1920) attempted to explain the low strengths measured in experiments compared with the theoretical strength based on bond energies. His experiments with glass bulbs and fibres showed that thinner samples were stronger and that newly formed samples were much stronger than older ones (even samples a few minutes old were measurably weaker). The hypothesis used to explain these findings was that microscopic cracks in the material weakened the structure and that these became increasingly stressed with time due to random movement in the molecular structure. In fact, Griffith stated that all solids contained these tiny defects which became known as microcracks.

Griffith made use of the stress concentration work of Inglis (1913), who showed that the maximum stress concentration near a defect in a solid was always found at the point of minimum radius of curvature. Griffith (1920) based his mathematical description of failure on the stress raising effect of a population of microcracks and applied a reversible energy balance concept to describe why large cracks propagated more easily than small ones.

4.6.1. The Griffith crack in uniform tension.

Below is a summary of the derivation of the result for a crack in uniform tension based on that of Lawn (1993). The concepts are used to derive the Griffith failure criterion describing depth of fracturing in the crust and also as the basis of linear elastic fracture mechanics, on which the experimental and modelling work in this thesis is based.

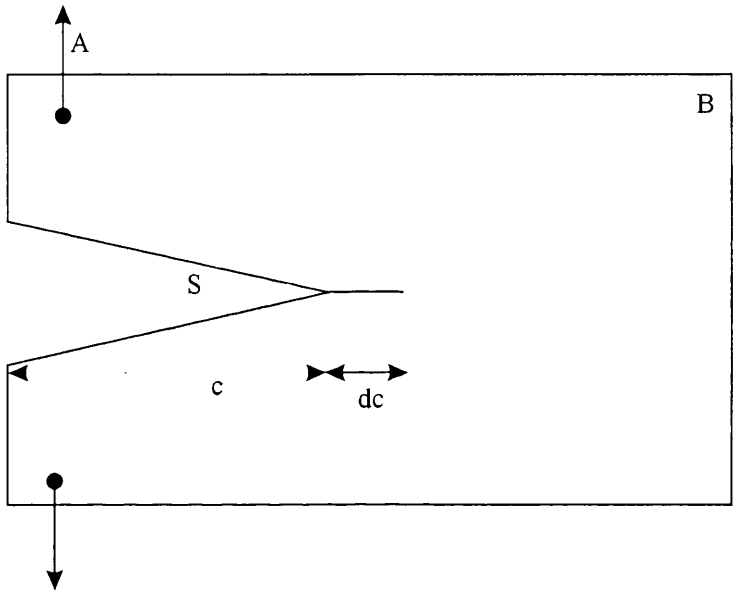

Fig. 4.5. Equilibrium plane crack system. Crack length c; extension, dc; elastic body, B; applied loading force, A; crack surface, S. After Lawn, 1993

The system is thought of as being in equilibrium; i.e. the crack is on the verge of extension. The total energy of the system U, can therefore be divided into a mechanical term (U_m) and a surface term (U_s). U_m is in turn made up of two components: the strain potential energy U_E and the potential energy of the loading system, U_A (where U_A is equivalent to the negative of the work done in displacing the load points) such that

$$U_M = U_E + U_A \tag{4.11}$$

For thermodynamic equilibrium, the mechanical and surface terms balance over an infinitesimally small crack extension, dc, giving

$$U = U_M + U_S \tag{4.12}$$

U_M can be said to increase with crack extension since the molecular forces across dc must be overcome during the creation of the fracture surfaces and hence can be said to oppose the formation of fractures. U_S, however, will decrease as the crack extends, favouring the extension of the crack. Griffith stated that the energy balance of (4.12) would be satisfied for a stable crack and thus there is an equilibrium requirement

$$\frac{dU}{dc} = 0 \tag{4.13}$$

Thus a crack would extend or retract reversibly in accordance with the sign of the left-hand side of (4.13) and small increases or decreases would lead to corresponding extension or retraction of the crack. Note that retraction of the crack is equivalent to complete healing with full joining of the molecular bonds.

If the Inglis analysis is now considered, the above criterion can be applied to a physical model. Consider an infinitesimally narrow elliptical cavity of length 2c in a large, elastic plate under uniform tensile stress σ_A as in fig. 4.6. Linear elasticity theory states that, for a body under constant stress during crack formation,

$$U_A = -2U_E \tag{4.14}$$

which implies that $U_m = -U_E$ from (4.11).

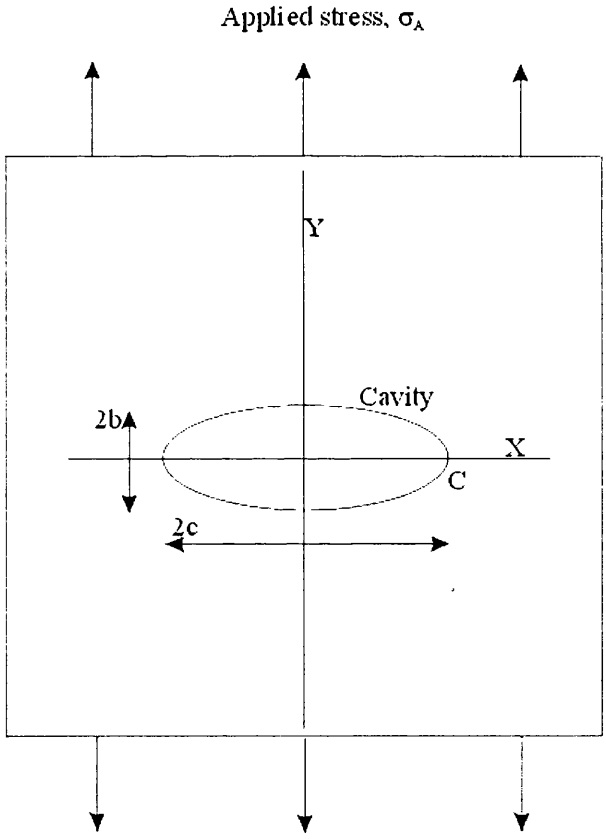

Fig. 4.6. A uniformly loaded elastic plate, C, with an elliptical flaw occupying –x<c<x.

By applying Inglis' stress analysis for an ellipse and the free energy per unit area of the crack surface, γ, we can find the total energy of the system

$$U(c) = -\frac{\pi c^2 \sigma_A^2}{E'} + 4c\gamma \tag{4.15}$$

Applying the Griffith criterion, (4.13), by differentiating (4.15) we can describe the point at which failure occurs. At this point $\sigma_A \rightarrow \sigma_c$ and $c \rightarrow c_0$ giving

$$\sigma_c = \left(\frac{2E'\gamma}{\pi c_o}\right)^{\frac{1}{2}} \tag{4.16}$$

The value of σ_c can be found experimentally and the product $\sigma_c c_0^{1/2}$ is known as the fracture toughness. This value is useful in that, given a known flaw and experimental knowledge of the fracture toughness of the material, one can predict the critical stress of the system. Conversely, if the stress field is known, the fracture size for failure can be predicted.

4.6.2. The plane Griffith criterion.

Griffith (1924) extended these ideas to develop a two-dimensional failure criterion in terms of the energy balance and stress concentration model. He based this model on several assumptions:

- The material is linearly elastic i.e. obeys Hooke's law and restricted to a two-dimensional problem.
- The material is pervaded by microcracks with random orientations and the most deleterious crack (that most likely to cause failure) is the longest, thinnest and most favourably oriented with respect to the stress field.
- Fracture occurs when the stress field at the tip of this crack reaches a critical stress.
- The cracks in the body are sufficiently spaced that they do not perturb the stress fields of their neighbouring defects.
- There are no forces along the crack walls.

The failure criterion is written in the form of a stress difference and is scaled in terms of the uniaxial tensile strength, T_0, such that the criterion for failure (where compressive stress is positive, tensile stress is negative) is

$$(\sigma_1 - \sigma_3)^2 = 8T_o(\sigma_1 + \sigma_3) \quad \text{if } \sigma_1+3\sigma_3 > 0 \tag{4.17}$$

$$\sigma_3 = -T_0 \quad \text{if } \sigma_1+3\sigma_3 < 0 \tag{4.18}$$

By analysing the stress fields around microcracks, it can be shown that internal cracks can lead to high tensile stresses near their tips even when both applied stresses are compressive, provided that they are not equal. These stresses can be sufficient to

cause failure (Murrell, 1970) and lead to the failure envelope fully derived by Murrell (1958)

$$\tau^2 + 4T_0\sigma - 4T_0^2 = 0 \tag{4.19}$$

where T_0 is the tensile strength and τ the shear stress. The failure envelope is a parabola in Mohr stress space. The great achievement of this criterion is that it is based upon the stresses acting on microscopic cracks yet predicts the failure point and direction of cracking of a macroscopic system. It also predicts that the compressive strength is an order of magnitude higher than the tensile strength of a material, in agreement with experiments.

4.6.3. The modified Griffith criterion.

The plane Griffith criterion does not take into consideration crack closure at high compressive stresses. In these cases, the frictional resistance of the crack walls reduces the stress concentration near the tips of the Griffith crack, strengthening the rock. The degree of strengthening depends upon the frictional resistance of the crack faces. The Mohr stress envelope for this criterion can be written as (Murrell and Digby, 1970)

$$\tau = 2T_0(1 + \frac{\sigma}{T_0})^{1/2} + 2\mu(\sigma - \sigma_c) \tag{4.20}$$

where σ_c is the stress required to close the crack. If this value is small the criterion reduces to

$$\tau = 2T_0 + 2\mu\sigma \tag{4.21}$$

which is equivalent to the Coulomb criterion of 4.5.2, with τ_0 equivalent to $2T_0$ and μ now identifiable as the frictional resistance of the opposing walls of a closed Griffith microcrack.

4.7. Fracture mechanics.

4.7.1. Introduction.

Linear elastic fracture mechanics (LEFM) is a method of analysing the behaviour of cracked solids by treating them as infinitesimally narrow slits in an isotropic linear elastic continuum (Lawn, 1993). CSPF are thought to be vertical

tension cracks and can therefore be described by LEFM. The effect an applied stress field has on the crack is calculated by first deriving the stress concentration for the particular geometry of the crack (or cracks in a multi-flaw system) and then applying a failure criterion based upon an intrinsic material parameter that expresses the resistance to fracture of the material. The macroscopic strength of the body is then related to this intrinsic fracture resistance parameter through a combination of the applied stress and crack geometry.

We can identify three modes of crack propagation as shown in fig. 4.8. Mode I (opening mode) is the response to purely tensile stress. Mode II (sliding mode) corresponds to longitudinal shearing in a direction normal to the crack front in response to purely shear stress. Mode III (tearing mode) is the response to purely shear stress and corresponds to lateral shearing parallel to the crack front.

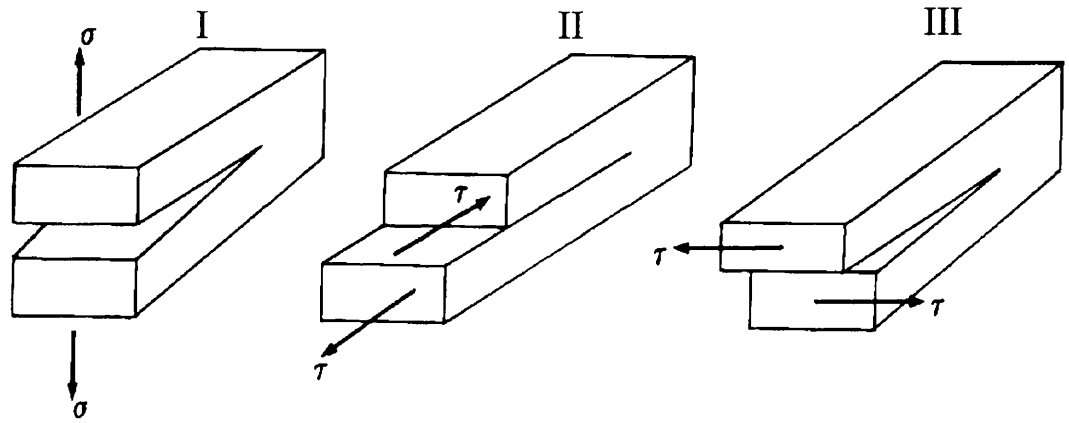

Fig. 4.7. Modes of crack propagation.

Mode I cracking is by far the most important when considering propagation of fractures in brittle solids because there is a tendency for cracking to occur so that shear stresses are minimised. Extension of the crack takes it away from the plane of the original fracture until it exists in a plane normal to the applied stress. We will, therefore, consider only mode I cracking.

4.7.2. Stress near the crack tip

The stress near the tip of a crack in uniform tension can be calculated using standard elasticity theory assuming that the crack walls are traction free and the material follows Hooke's law. The stresses in the near field can be identified using the conventions shown in fig. 4.8.

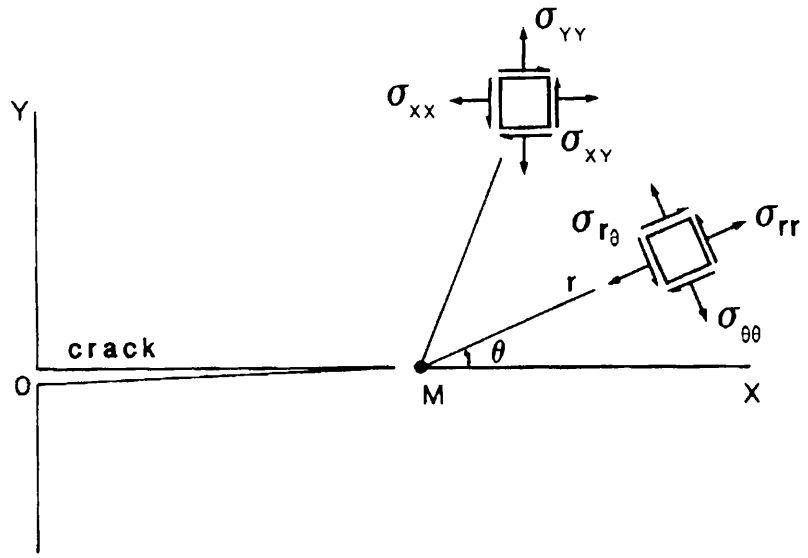

Fig. 4.8. Stress field near the tip of a crack in rectangular and polar co-ordinates. After Lawn, 1993.

Lawn (1993) gives a full set of solutions for the well known near-field stresses (Irwin, 1958) but here we shall just note some of the key features of the stress distribution.

- The stress field may be reduced to a simple form

$$\sigma_{ij} = K(2\pi r)^{-1/2} f_{ij}(\theta) \tag{4.22}$$

  comprised of three separate factors. The K factor is known as the stress intensity factor and depends only upon the specimen and loading geometry. The other components are a radial part with a characteristic $r^{-1/2}$ dependence, and an angular component, which has a more complex form.
- Owing to the nature of the radial part of (4.22), there is a singularity in this equation at r=0. This is a flaw in the simple LEFM equations which is discussed in section 4.7.5.
- For a given mode, the K terms that define the system are additive. This greatly simplifies calculations for complex loading systems.

In mode I cracking, the stress intensity factor, K, becomes

$$K = \Psi \sigma c^{1/2} \tag{4.23}$$

where σ is the applied tensile stress, 2c the crack length and Ψ a dimensionless term whose value depends upon the geometry of the particular crack problem. Some examples of this geometry term are

$\Psi = \pi^{1/2}$ straight crack length 2c, infinite specimen (4.24)

$\Psi = \alpha\pi^{1/2}$ ($\alpha = 1.12$) edge crack of length c (4.25)

$\Psi(c/w) = [(2w/c)\tan(\pi c/2w)]^{1/2}$ crack length 2c, specimen width 2w (4.26)

The stress intensity factor for an edge crack loaded in tension is therefore proportional to the applied stress and to the root of the crack length.

4.7.3. Fracture energy or mechanical energy release rate

Differentiating (4.11) with respect to the change in crack area gives us a value identified with the rate of release of mechanical energy with respect to the crack area. For the specific case of a straight crack this quantity is labelled G, the fracture energy

$$G = -\frac{dU_m}{dc} \tag{4.27}$$

where c is the crack length and U_m the mechanical energy as for (4.11). G is independent of loading type and, using the method of Griffith's energy balance, can be shown to be equivalent to the stress intensity factor, K, for mode I only

$$G = K^2 / E' \tag{4.28}$$

where E' = E for plane stress and E' = E /(1-v^2) for plane strain. Thus G and K are equivalent fracture mechanics parameters.

4.7.4. Critical values of fracture mechanics parameters

At failure, the values of G or K are equal to or greater than some critical values that are material properties labelled G_c or K_c. The critical value of K, K_c is known as the fracture toughness. These conditions are not sufficient for catastrophic failure to occur as the energy of the system must also be a maximum allowing the crack to extend at high speed. If the crack enters a region where the energy is a minimum, crack advance may arrest and form a stable crack but if conditions change, it may extend again.

4.7.5. Non-linear fracture mechanics.

Because LEFM predicts a stress singularity at the crack tip it is a fundamentally flawed theory. Near the crack tip there must be some kind of non–linear process. A

major step in describing this non-linear region was made by Irwin and Orowan in the 1950s (Irwin, 1958). They independently proposed that the crack system be divided into two mathematical zones. The outer or elastic zone transmits the applied load to the inner zone where the energy absorption processes take place. The inner zone is surrounded by a K-field governed by the external loading conditions. The work of separation required for crack propagation is therefore insensitive to the nature of the loading conditions. The outer zone configuration governs the mechanical energy release rate, and so LEFM is retained for dealing with the outer zone. The major assumption of the Irwin-Orowan concept is that the inner zone is small relative to the outer zone although, in practice, this assumption may not always hold true.

In the Irwin-Orowan extension of Griffith's theory, the rate of change of surface fracture energy in the inner zone is given the name R, the crack-resistance energy, and can be seen as the equivalent of the critical value of the fracture energy G_c, (Equations 4.32 and 4.33). R is a commonly used material property for describing the toughness of materials. In the limit of a purely brittle material R tends to R_0, which is twice the value of γ, the free surface energy ($R_0 = 2\gamma$ because both sides of the crack are taken into account). The crack-resistance energy in non-brittle materials is thus

$$R = 2\gamma + R_p \tag{4.29}$$

where R_p is a 'plastic-work' term describing the dissipative plastic energies and is difficult to quantify. R is therefore not a well-defined value.

Barenblatt (1962) introduced an atomic perspective to the field of fracture mechanics whilst retaining the powerful continuum approach. Recognising that fracture is essentially an extension of atomic bond rupture, he specified the resistance to fracture as a non-linear cohesive force function. However, by assuming that this force acted on a scale much larger than the atomic bonds it represented, he ensured that the continuum basis of LEFM could be retained. In a sense, Barenblatt replaced the Irwin-Orowan inner zone with a cohesion zone. This leads to the removal of the singularity, but implies a lack of knowledge of the exact position of the crack tip.

The aim of non-linear fracture mechanics is to describe the inherently non-linear behaviour of fracturing materials. Whether the material is behaving in this manner owing to actual plastic deformation or microcracking near the macrocrack tip is unimportant, as the methods outlined briefly above are applicable to both processes.

4.7.6. Experimental methods for determining fracture mechanics parameters.

A variety of experimental methods and sample configurations exist for measuring the critical values of the fracture mechanics properties described above. For this study, the important considerations of high temperature and pressure had to be taken into account when choosing the appropriate technique. Also, as high temperatures and pressures were to be used, a technique that could infer the degree of anelastic deformation in the behaviour would be advantageous. Furthermore, as the nature of extreme environment experiments makes in-situ observations nearly impossible, the method used could not rely on measuring the crack length in any way.

Commonly used test configurations for rock fracture mechanics, specifically for the measurement of fracture toughness, include the double torsion specimen, the double and single edge-notched specimen and the double cantilever beam specimen. A summary of many rock testing configurations may be found in Ouchterlony (1980). The configuration used in this project is the short-rod (SR) specimen, which has a variety of advantages:

- The specimens are in the form of notched cores and thus require little machining. This also makes the specimen compact so that it can be easily accommodated in a pressure vessel. In addition the vertical symmetry of the sample makes heating the sample without creating 'hot-spots' easier.
- Crack growth is initially stable owing to the chevron shape of the unnotched ligament in the sample. This not only makes control of crack growth relatively easy, but also means that the sample is essentially self pre-cracking.
- There is no need to measure crack length, only the compliance of the sample, because the dimensionless compliance of the sample depends only upon crack length and is independent of material. Thus knowledge of the compliance during the test allows crack length to be determined (Shannon *et al.*, 1982; Bubsey *et al.*, 1982 and Matsuki *et al.*, 1991b)
- The testing method has two levels. Level I tests only require measurement of failure stress and are useful for rapidly screening many samples, Level II tests require measurement of crack mouth opening displacement (CMOD) but gives information on the degree of non-linearity (anelasticity) of the sample. This information can be used to correct the Level I results for anelasticity.

- The testing methodology is the recommended technique for measuring the fracture toughness of rocks as suggested by the International Society for Rock Mechanics (ISRM, 1987). There therefore is a large body of literature detailing comparative tests and apparatus.

The basis of the test methodology is that the stress intensity factor for the sample geometry is known as a function of crack length. This means that, as the stress increases to the critical point where failure occurs, the stress intensity factor is always known and thus the critical value, the fracture toughness, can be easily extracted.

The detailed experimental methods and description of samples and apparatus for this type of test are described in chapters four and six.

4.7.7. Summary of LEFM.

By considering geological materials as continua, we can calculate the stress required for failure for a given pre-cracked system using the equations and methods of LEFM. These methods rely on knowledge of the material properties of the rock, which can only be gauged by carefully chosen experiments. Furthermore, the behaviour of rocks that contain a macroscopic flaw is also relevant to the surface of Venus because this will influence the morphology of surface features.

4.8.1 Fracture vs. faulting.

The difference between mode I cracking with virtually no displacement and faulting with movement on the crack faces is an important aspect of brittle deformation. Vertical cracks such as those hypothesised to form CSPF will initiate at the surface owing to the inhibiting effect of overburden. According to the Griffith criterion, (4.17) and (4.18), there will be a maximum depth to which vertical cracking occurs, beyond which the effects of shear stress cause the failure plane to move away from the vertical. The depth to which vertical cracks propagate can be derived from (4.17) to give

$$Z_{max} = \frac{3T_0}{\rho g} \tag{4.30}$$

where Z_{max} is the maximum depth of penetration at which cracks can still be vertical, ρ is the density of the material, g the gravitational strength and T_0 is the uniaxial tensile strength of the intact rock. Typical values for basalt are ρ = 3000kgm^{-3} and σ_t = 10-

40MPa (Schultz, 1993; Schultz, 1995) which give a maximum depth of 1.1-4.5km. The maximum depth of penetration is an important result because it shows that CSPF cannot penetrate very deeply into the crust and still retain their mode I morphology.

4.8.2. Anderson theory of faulting.

A more detailed method of examining faulting can be made by analysing the frictional behaviour of a rock mass and calculating the stress necessary to overcome frictional resistance in any given orientation. This analysis is useful when describing high tensile stress regimes above the purely tensile stress limit (4.30) or at depth where the overburden pressure becomes high can be used to calculate the type of faulting that will result. There are three generally accepted types of fault: thrust, strike slip and normal. They each have differing morphologies where exposed at the surface and can be identified on planetary surfaces by careful image interpretation. The three main types of fault were first noted by Anderson (1951), the type of faulting being controlled by the stress orientation. Fig. 4.9 shows Anderson's classification of faulting, which makes use of the principal stress axes and the fact that these axes are mutually orthogonal and that one of them is vertical. Anderson's theory was expanded by Sibson (1974) and can be summarised from Ranalli (1995) as follows:

The criterion for failure is that the stress difference rises until it is large enough to overcome the friction on the fault or to form a new fault. The two are seen as identical by assuming that internal friction is the same as sliding friction and also that the normal stress is much greater then the cohesive strength of the rock. Sliding on a pre-existing fault or creation of new faults are therefore described by the same equations. For most crustal conditions these assumptions are justified.

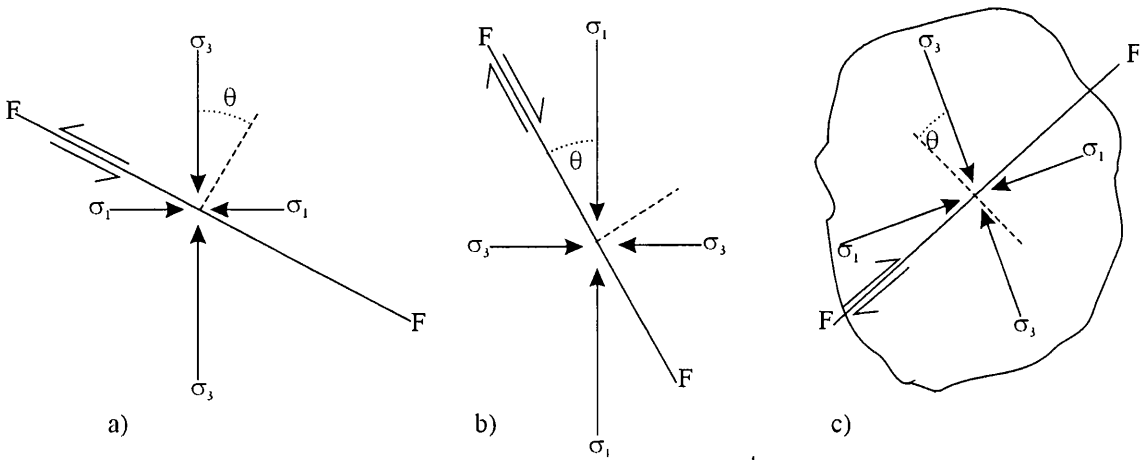

Fig. 4.9. Anderson's classification of faulting for a) thrust, b) normal and c) strike-slip faults. σ_1, σ_2 and σ_3 are the maximum, intermediate and minimum principal stress axes. Length of arrows do not represent magnitudes of stresses. σ_2 is in the plane of the fault and is therefore not included in the two dimensional representations above. a) and b) are side views whereas c) is a plan view. θ is the angle the principle stress axis makes with the normal. After Ranalli (1995).

By assuming the vertical stress is lithostatic, and equating fluid pressure in the rocks to a factor, λ, of the lithostatic pressure, the general equation for failure of the rock by one of these modes of faulting is given by

$$\sigma_{max} - \sigma_{min} \geq \alpha\rho g z(1-\lambda) \tag{4.31}$$

where α is a factor depending upon the type of fault (α = 3.0, 1.2 and 0.75 for thrust, strike-slip and normal faults respectively for typical values of the friction coefficient), ρ is the density of the material (assumed to be constant in the upper crust), g is the acceleration due to gravity, z is the depth beneath the surface and λ is the fluid pressure factor.

On Venus, with its dry crust and lithosphere, $\lambda = 0$ and $g = 8.87 ms^{-2}$ and we will assume that $\rho = 3{,}000 kgm^{-3}$ to the first approximation. This means that the stress difference for normal faulting will be around 20z MPa, where z is the depth in km. But if we assume that the rocks are bounded and the overburden is hydrostatic then

$$\sigma_{min} = (\sigma_{max} - T). \tag{4.32}$$

where T is the modulus of an applied horizontal tensile force and acts in the opposite sense to the hydrostatic overburden pressure. Thus the condition for normal faulting becomes

$$T \gtrsim 20z \text{ MPa}. \tag{4.33}$$

The criteria for other types of faulting are similar and can be approximated by applying extra stresses (either compressive or tensile) to the lithostatic state in the same manner. Note that this expression is inapplicable to shallow conditions where the normal stress is similar to the cohesive strength of the rock mass. Schultz (1993) estimates that the cohesion of a Venusian rock mass will be 0.5-5MPa and it is therefore inapplicable to apply (4.33) for horizontal stresses smaller than ~5 MPa.

4.9 Sub-critical cracking.

Classical fracture mechanics assumes that a solid with a flaw subjected to an opening stress field will fail suddenly when the fracture parameters (K, G) reach a critical material specific value (K_c, G_c). At this point, the system will fail catastrophically. However, for long term loading, crack extension can occur at values of K and G much lower than K_c or G_c (Atkinson and Meredith, 1987).

Various mechanisms exist to explain this behaviour, termed sub-critical crack growth, and although the presence of an active chemical species is required for all of them, there is some evidence that limited sub-critical activity can occur even in a vacuum (Wierderhorn *et al.*, 1974). The dominant mechanism for sub-critical crack growth in geological materials is stress corrosion (Atkinson, 1982). This is a two-stage process, the rate of which is controlled by the slower of the two stages:

a) Transport of the corrosive medium to the crack tip.

b) Reaction of a chemical fluid (commonly water) with the strained chemical bonds at the crack tip, weakening the bonding and lowering the stress required for failure.

Experimental work has shown that the presence of a corrosive fluid is important for sub-critical cracking. In particular, the rate of sub-critical behaviour increases with

- Increasing temperature and pressure of the corrosive fluid.
- Increasing pH of the active species (Atkinson and Meredith, 1981).

In summary, the most favourable conditions for stress-corrosion are those that promote hydrolysis reactions of Si-O bonds at crack tips. On Venus, because of the high temperature at the surface and sub-surface, there is no water available to partake in hydrolysis reactions. The action of the carbon dioxide atmosphere penetrating deep into the crack system can also be excluded as it is unlikely to react with the rock mass and

to disrupt the Si-O bonds at a rate significant enough to cause sub-critical crack growth. Some oxidation of the material by the CO_2 in the atmosphere will occur (Fegley *et al.*, 1997) but the CO_2 atmosphere will be largely inert if the rock mass consists of silicates. The role of stress corrosion, and therefore subcritical crack growth as a whole, can be considered secondary to dynamic rupture of the crust although future experimental work to monitor slow crack growth in basalt under a Venusian atmosphere would be required for full justification of this assumption.

4.10. Carbonates, fluids and pore pressure.

Throughout this chapter we have ignored the role of pore-fluids in view of the dry nature of the Venusian crust. However, some arguments (see chapter two) for the existence of carbonates on Venus also apply to pore-fluids. Carbonatites can have very low viscosities and very low melting temperatures, so that, at even shallow depths, melting of carbonate deposits may liberate enough fluid to form reservoirs of high-pressure fluid in the rock mass. Summarised below are some possible effects that this carbonate pore-fluid might have on the physical behaviour of the rocks.

The pressure of pore fluid in a system is described by the ratio of the fluid pressure to the lithostatic pressure of the rock mass overburden. This quantity, λ, was introduced in (4.30) and, for Earth, with a hydrostatic fluid pressure is around 0.4. On Venus, with a denser, carbonate fluid the value would be much higher, even approaching 1.0. Thus (4.33) becomes

$$T \gtrsim 20z(1-\lambda) \text{ MPa.} \qquad (4.34)$$

This means that for shallow crustal conditions with high fluid pressures, faulting can occur at very low stresses. A simple way of visualising this effect is to shift the Mohr stress circle representing the stress-state on a diagram such as fig. 4.4 to the left by an amount equivalent to the pore pressure, thus initiating fracture at lower differential stress. The critical porosity necessary for free transport of carbonate melt fluid will govern the effective pore pressure, although these considerations are outside the scope of this project. Nevertheless, it should be noted that fluid pressure may be important in investigating the mechanical behaviour of intensely deformed areas.

As described in section 4.9 above, fluids can also have an increasing effect on the rate of sub-critical crack growth by transporting active species to the crack tip. Thus the presence of pore fluids would increase the effects of slow, equilibrium crack

growth. Again, the quantitative effects of this are difficult to measure but are likely to be less than those on Earth, where hot aqueous fluids can drastically reduce the strength of the rock mass.

4.11. Conclusion.

The theory of rock mechanics has application to the small-scale deformations observed on the surface of Venus in that it enables us to apply appropriate theory quantitatively to the measurements made from the Magellan imagery. Specific results from theoretical rock mechanics applicable to CSPF are:

- The upper crust of Venus is likely to deform in a brittle fashion.
- Failure of the rock will probably be dynamic failure rather than slow crack growth due to sub-critical cracking.
- As CSPF are interpreted to be vertical tensional fractures, due to their simple morphology and brightness independent of look-angle, the application of linear elastic fracture mechanics theory is appropriate to investigating their mode of formation.
- Beyond a certain depth, described by the Griffith criterion, and dependent on the level of stress, faulting will occur. The cracks will therefore begin to have a horizontal component of extension, which will lead to normal faulting morphologies. As this is not observed for CSPF, constraints on the stress field and depth of penetration of these features can be made.
- The absence of pore-fluid pressure on Venus means the rocks can support higher stress differences without undergoing normal faulting. Conversely, the presence of a high density, carbonate pore fluid would decrease the strength of the rocks with respect to those of Earth, making normal faulting much more likely.

Chapter 5

Experimental apparatus.

5.1. Introduction.

As described in chapter four, the fracture behaviour of rocks can be described by the material parameters pertaining to the resistance to fracture of a material. The most commonly used of these parameters in rock mechanics is the critical value of the stress intensity factor, K_c, which is also known as the fracture toughness. This chapter describes the experimental apparatus used in this study to measure the fracture toughness of rocks under high temperatures and pressures. Chapter seven describes how the apparatus is used and calibrated.

The apparatus used in this research programme was originally constructed to measure fracture toughness under hydrothermal conditions. The results from this program are described in Jones *et al.* (1996). At the start of the project the apparatus was nearly complete but in need of many modifications to make it usable in this study. The apparatus functioned in an extremely unreliable manner and was uncalibrated. It could not reach the temperatures required for hydrothermal conditions and could only perform level I tests.

The main changes to the apparatus were to modify the rig for use with gas and to enable the measurement of displacement accurately enough to make level II testing possible. Level II testing is advantageous because it accounts for anelasticity effects. Level I testing tends to give results that are lower for smaller samples, whereas level II results are far less sample-size dependent. Almost all of the first and second years of the research project were therefore allocated to modifying the rig, perfecting the experimental methods and obtaining results. This chapter describes the whole system and not just the elements in which the author had an active part in designing or constructing. The evolution of the apparatus and the many modifications it underwent are described in chapter six which also serves as a log of the actual work performed by the author.

5.2. Design parameters

The criteria set for analysis of specimens under Venusian conditions were fixed at the beginning of the project. The samples had to be tested at 0-450° C under 0-20MPa of carbon dioxide to simulate present and past Venusian atmospheric conditions. The apparatus had to be capable of performing fracture toughness tests on a variety of samples using a sample size that does not effect the data (i.e. the sample size must be much greater than the grain size of the material). In order to provide comparative data the samples also had to be tested at the same temperatures and pressure using an alternative confining medium such as water. In addition, the data had to be logged in a way that facilitated the complex data analysis necessary for level II testing. In summary, the apparatus had to be able to operate at a variety of temperatures and pressures using both liquid and gaseous mediums whilst remaining simple to operate and capable of producing scientifically valid results.

5.3. Apparatus overview.

The major element of the apparatus used in this study is an environmental cell originally constructed for fracture mechanics measurements under hydrothermal conditions. The original hydrothermal design required the vessel to be constructed from a corrosion-resistant material and to be capable of containing pressures of 70MPa of liquid (water or brine) at 450°C. These features were of great value when simulating the Venusian atmosphere.

The cell is constructed of Hastelloy C-22; a nickel-alloy developed by the United States Navy with excellent corrosion resistance. The cell is designed for 60mm diameter ISRM standard short-rod samples. The specimen is located over two machined knife-edges which are forced apart by a small hydraulic actuator whilst, the transverse displacement of the knife-edges is measured by an inductive non-contacting displacement transducer.

Both the pressure in the actuator and the confining pressure are measured accurately using pressure transducers. Pressure dials are used to approximately monitor these variables during experiments. Thermocouples are located in the apparatus to monitor the temperatures of important elements of the system. All the sensors mentioned above are logged using a computer.

The pressure in the actuator is controlled using a servo-controlled intensifier system whilst the confining pressure is provided by a CO_2 gas booster pump. For safety

reasons, the pressure vessel is shielded within a thick dural cubicle and the other parts of the system are boxed in with steel plate. The components of the pressure vessel are shown in fig.5.1 and a photograph of the whole apparatus in fig. 5.2.

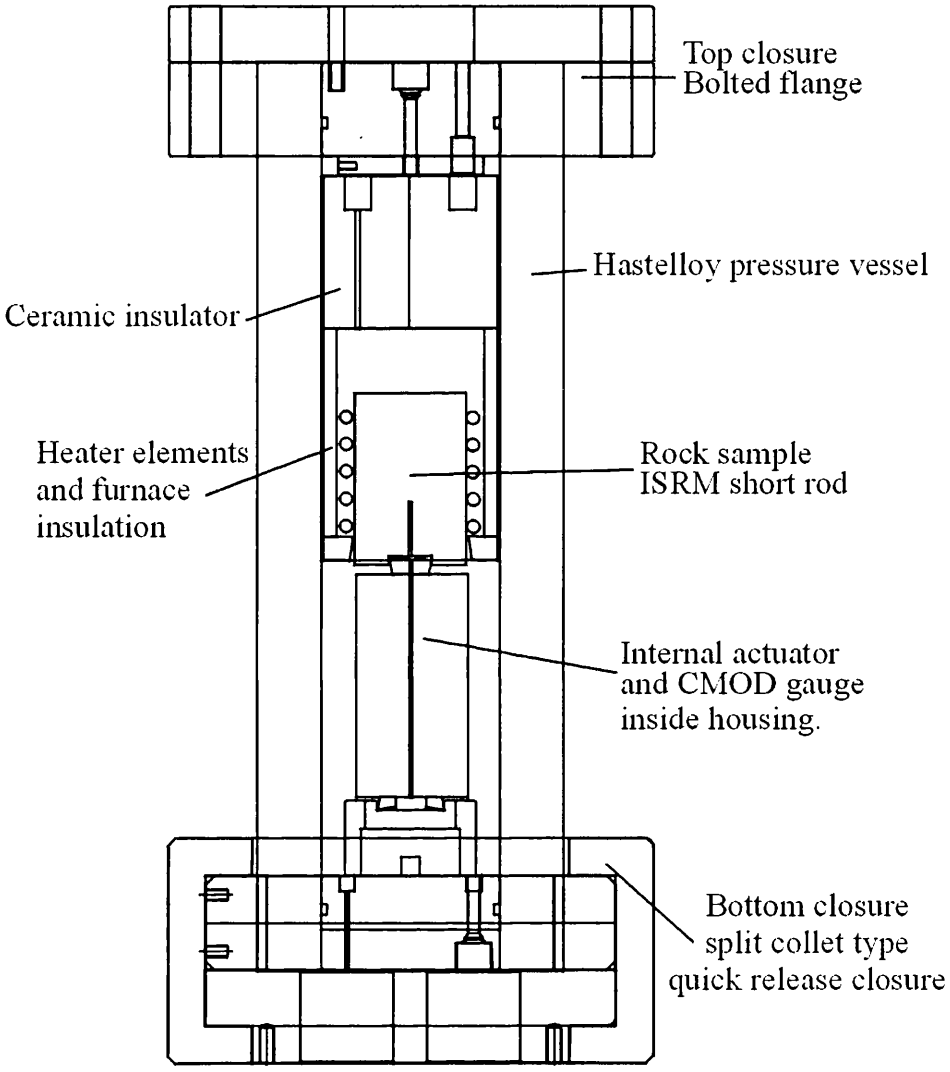

Fig. 5.1. Schematic overview of Hastelloy pressure vessel, heating system, force transfer system and closures.

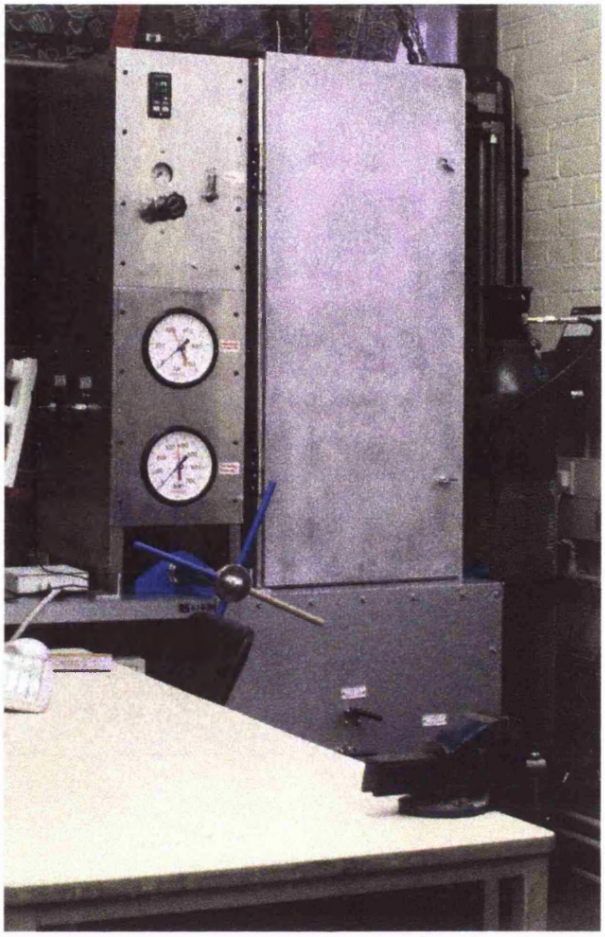

Fig. 5.2. External view of the apparatus showing safety barricades, actuator hand-pump and pressure gauges.

5.4. Pressure vessel specifications.

5.4.1. Vessel size and working pressure.

Although fracture toughness is an intrinsic property of a material, there is some scaling effect due to the increased effects of finite grain-size on smaller samples. The effect of sample size becomes smaller with increasing size until a plateau is reached (Matsuki *et al.* 1991). This is characterised by the K-resistance curve, the relation between fracture toughness and crack extension. A 60mm sample is sufficiently large for crack extension with a maximum value of approximately 30mm. This value is larger than the K-resistance plateau for most of the rock types tested in Matsuki *et al.* (1991). Discussion of the K-resistance curves for the samples used in this study can be found in the section devoted to experimental results, chapter nine.

The pressure vessel has an internal diameter of approximately 96mm and an external diameter of approximately160mm and can therefore contain a 60mm sample

together with the required heating elements. It is constructed from Hastelloy C22 alloy. By application of High Pressure Technology Association guidelines, (HPTA 1975) the working pressure of such a vessel can be estimated as shown in fig. 5.3.

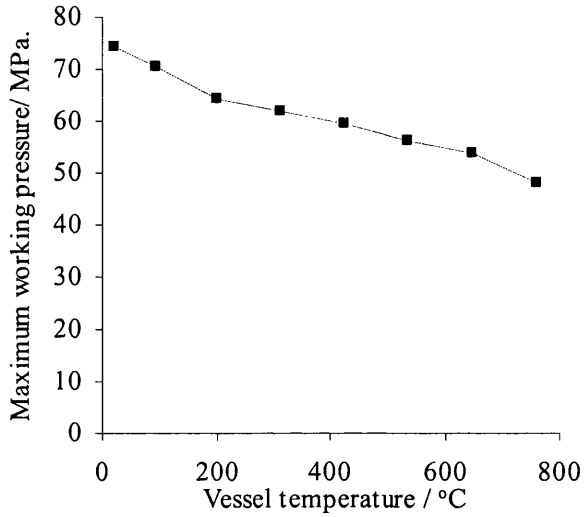

Fig. 5.3. Working pressure of fracture mechanics apparatus pressure vessel as a function of temperature. Full details on the derivation of this graph can be found in Appendix I, which deals with the safety aspects of this apparatus.

The pressures and temperatures required for this investigation are well within the safe working limit of the apparatus. Nevertheless, the use of gas as confining medium is a dangerous undertaking and so safety precautions have been of prime concern in this investigation. Appendix I covers the work done to assess and minimise the risk in the unlikely event of pressure vessel failure.

5.4.2. Vessel closures and fittings.

The vessel is designed so that the specimen can be placed on the actuator jaws and the vessel lowered down over it. The top closure is sealed using a bolted flange with 12 16mm steel bolts, a large o-ring with a PTFE backing ring providing the pressure seal. The reason why there are so many bolts, and also why they are so large is that, at a pressure of 20MPa, they are required to resist a force equivalent to 15 tons of weight. It is therefore essential that there is sufficient resistance to prevent the top closure from being ejected at high pressure. The centre of this closure is drilled out and a pressure release valve has been fitted. This valve is not used when gas is the confining medium (i.e. in most of this project) but is included to control the excess pressure should a liquid medium in the vessel change phase.

In addition, the top closure has holes for four high-pressure feed-through plugs. Two of these are used for the heating elements and two for thermocouples. All of these feed-throughs are drilled out Hastelloy plugs with grooves to accept high temperature o-rings. Although originally made of nitrile, all the upper seals (both the feed-throughs and the main closure) were later replaced with Viton o-rings when it was discovered that the vessel failed to hold pressure satisfactorily. These have a far superior resistance to temperature and are not markedly weaker. The heating elements and thermocouples are soldered into the feed-throughs to provide a pressure resistant seal.

The bottom closure of the vessel is of the split-collet type to allow fast and easy access. Three large C-shaped extrusions clamp over the flange of the vessel and under the actuator base and are held in place by steel pegs. The inner bore of the vessel fits snugly over the pressure seal around the actuator base. The result is a highly effective seal that takes only minutes to assemble. Fig. 5.4 shows a schematic of the bottom closure. The three C-shaped clamps each extend slightly less than a third of the way around the circular flange of the vessel, leaving room for three upright supports. The vessel slides up and down on these supports for access to the sample when the clamps are removed. Both the main seal and the lower feed-throughs use standard nitrile o-rings with PTFE backing rings. Viton seals are not necessary because the temperature never exceeds 50°C. There are six lower feed-throughs, one for the displacement transducer supply, one for the actuator pressure line and four thermocouple feed-throughs. The displacement transducer feed-through is electron-beam welded onto the mineral insulated cable but all the others were brazed on to the cable like the upper feed-throughs.

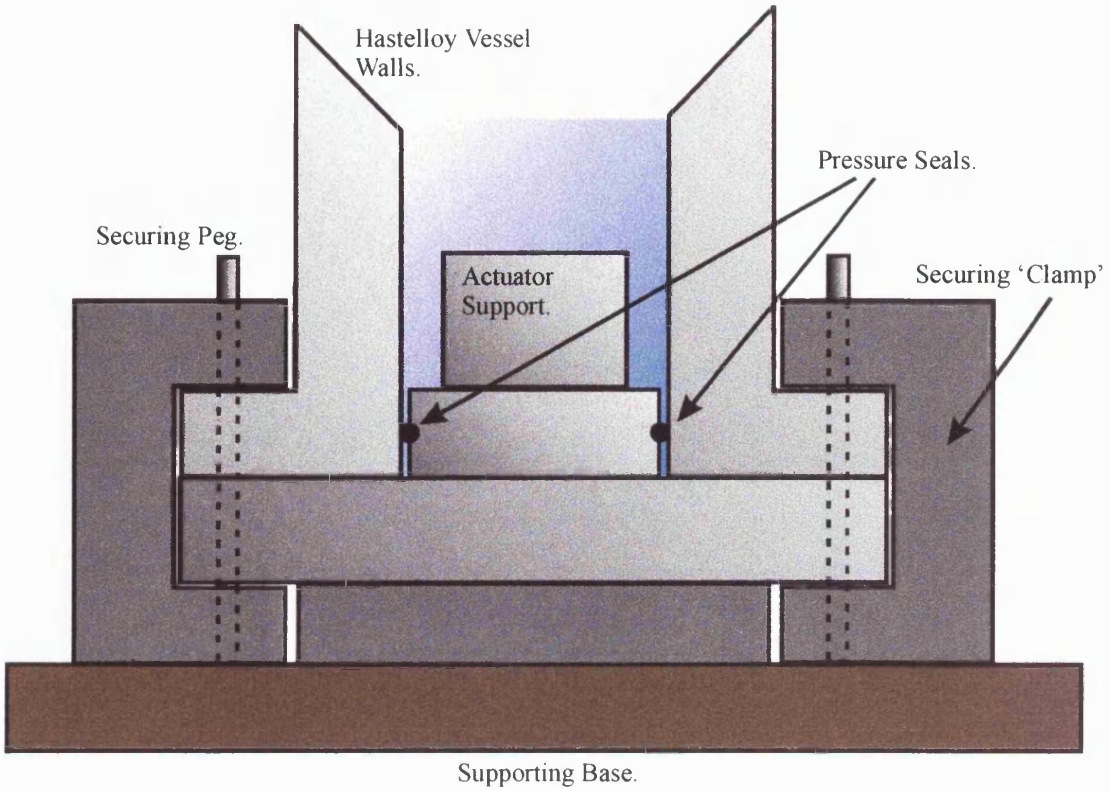

Fig. 5.4. Schematic of bottom closure.

5.5. Confining and actuator pressure system.

Unless otherwise stated, all piping and fittings for the confining system are rated at 10,000 psi (70MPa). The piping is standard stainless steel 3/8" (9.5mm) inner diameter (i.d.) pressure tubing and all fittings are of the taper-seal type. This makes the apparatus quick and easy to modify as taper-seal fittings are easily assembled. The displacement pressure system uses similar piping with 1/16" (1.6mm) i.d. which has a pressure rating of 30,000 psi (210MPa) and a coned pressure fitting. It less easy to modify but provides a greater margin of safety, and it reduces the volume of fluid required, which in turn, makes the pressure in the piston more responsive to the control system. Fig. 5.5 provides a schematic of the entire pressure system.

5.5.1. Confining pressure system.

To achieve elevated pressures when a liquid is used as confining medium, a small air-driven Haskel pump type M188 is used. This is capable of pressurising the vessel with a liquid to 100MPa or more. When a gas is used as confining medium, a large Haskel AG-152 air-driven gas-booster provides the pressure. The gas pump is integrated into the system alongside the liquid pump in such a way that either liquid or

gas can be used by simply isolating the pump that is not required. The gas pump has special seals to allow the use of carbon dioxide, which can liquefy under high pressures.

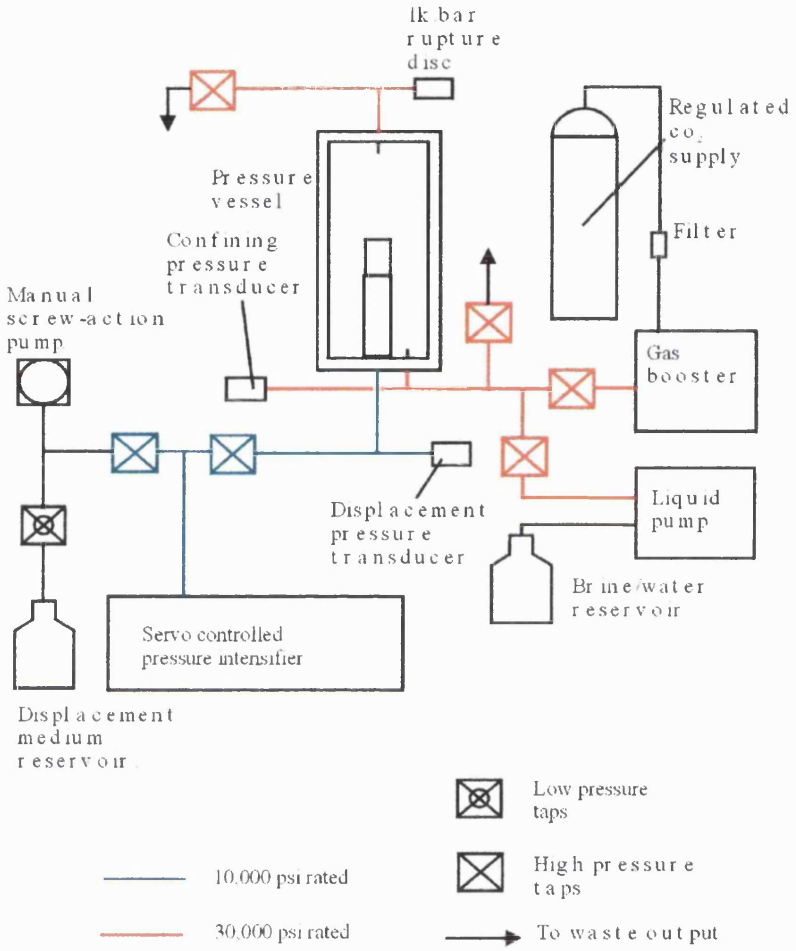

Fig. 5.5. The high-pressure system (for both confining and actuator pressure) used in the fracture mechanics apparatus.

The AG-152 has a maximum pressure output of 140MPa by boosting the bottle pressure of around 5-6MPa. The pump is contained within a sturdy steel enclosure mounted on wheels to make it mobile. Connection to the gas bottle is by reinforced flexible tubing through a bulkhead in the pump housing. The pump is hard-piped to the pressure system through another bulkhead. Both pumps are driven from the laboratory compressed air-line which, with a pressure of 1MPa, can ensure an excellent maximum pressure output for both pumps. The smaller liquid-pump is connected via a small-bore (2mm) tube whilst the larger gas booster uses 10mm bore reinforced plastic tubing to allow for greater airflow. The smaller pump cycles at approximately 5Hz whilst the gas booster cycles slower at around 1-2Hz. Both pumps are very noisy when operating and

every effort has been taken to mount them solidly to prevent resonant 'sounding-board' effects.

When the vessel has been pressurised, it can be isolated from the pumps. At the end of the experiment, gas is released through the waste tap. If the isolation taps are opened, pressure is released throughout the system, including the hose to the gas bottle. This is because the gas-pump only seals when the output pressure is equal to the input pressure. This built in safety feature ensures that the bottle-hose is not left under pressure for long periods.

There is no need to expel air in the vessel before charging with CO_2. The mass of air at 1atm pressure is insignificant compared to that of CO_2 at 10MPa.

The waste output tubes are all extended outdoors so that there is no risk of pockets of CO_2 causing an asphyxiation hazard in the laboratory. For the benefit of the operator, the confining pressure is displayed on a large dial on the front panel of the apparatus whilst a pressure transducer logs the pressure accurately.

5.5.2. Actuator pressure system.

The actuator pressure system is similar in construction to that of the confining system except that the tubing is rated at 30,000 psi (≈200MPa) with a 1/16" i.d. The fittings are different from the type used in the confining system in that they have a tapered thread to which a gland is attached. This seats against the joining nut creating a pressure-tight seal. The final connection to the actuator, along with some of the tubing in inaccessible areas, is flexible high-pressure tubing with 1/32" (0.8mm) i.d.

The pressure in the actuator is controlled in two ways. For accurate measurements, a servo-controlled intensifier is used. This adjusts the pressure in the actuator by constantly monitoring the feedback from the displacement pressure transducer and moving a piston until the set pressure is matched. The set point is controlled either using a simple ramp-generator, included as part of the servo-controller electronics, or direct control of the pressure set point by the operator. The latter method gives better results but requires some skill when turning the pressure dial to give accurate control of the rate at which the pressure changes. Level II tests use this system because the controller can instantly reverse the pressure in the actuator, thus ensuring excellent control of the force applied to the sample. The system used here is a Servo-

technique, two-channel intensifier controlled by a servo-technique dual control/display system.

For ease of use during commissioning of the apparatus, a simple screw pump was installed which can perform the same function as the intensifier. It also doubles as the priming system for the intensifier. The hand pump has been retained to provide a back up for the more complicated servo-controlled system.

5.6. Force transfer system.

The pressure build up in the actuator is converted to a tensile force in the sample using a novel design based upon precisely machined knife-edges. A sketch of this part of the apparatus is shown in fig. 5.6. The actuator itself sits inside a cylinder of Hastelloy that has been cut in half along the plane perpendicular to the axis of the actuator. At the base of each of these halves the cylinder has been machined to a knife-edge which sits in an accurately machined saddle. Two more knife-edges are situated at the top of the actuator housing and sit in a groove in the sample. As pressure builds up in the actuator, the top knife–edges are forced apart loading the sample in tension. Simultaneously, the bottom knife-edges are forced into the sharp corners of the saddle, causing the apparatus to seat in a repeatable fashion. Since the grooves in the sample and the shape of the saddle are precisely machined, rotational forces are minimised. Rotational forces are further restricted because the actuator acts on points further from the vertical axis than the knife edges that transfer the force to the sample. Also situated in this part of the apparatus are the inductive displacement transducer (IDT) used to measure the CMOD and several thermocouples. The calculations for conversion of pressure in the actuator to force on sample can be found in chapter seven.

The actuator itself is a simple piston, with back-to-back step seals to provide a tight seal. The back-to-back seals separate the actuator and confining fluids (see section 6.7). The ends of the piston and barrel have slightly convex locating lugs which sit in matching seats on the inside of each half of the housing. In this way, the force exerted on the housing is exerted on the same point as the two halves are moved apart and is consistent between tests. There is some frictional force retarding the pressure in the piston, which adds to the hysteresis in the results. The method used for correcting this is described in the data analysis section of chapter seven.

The design of the actuator housing was an ongoing process throughout this project. Knowledge of the behaviour of the knife edges and the actuator housing under

load is vital to the correct interpretation of level II results. The evolution of this part of the apparatus is discussed at length in Chapter six.

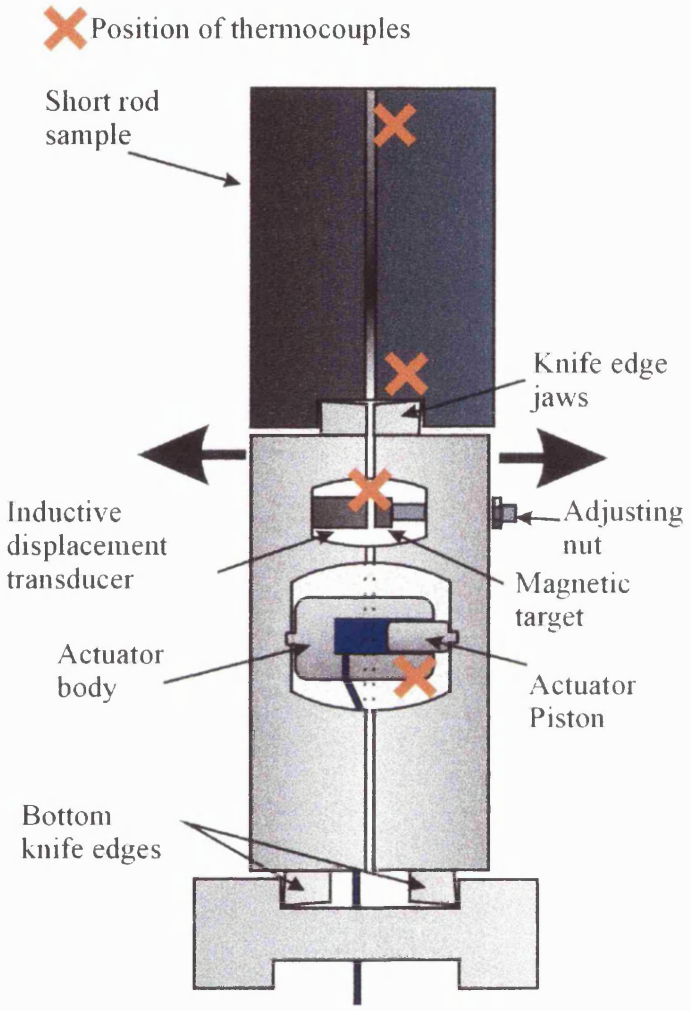

Fig. 5.6. Schematic of force-transfer system.

5.7. Sensors.

There are three types of sensors used in this apparatus: Druck pressure transducers, K-type thermocouples and the PY106C inductive displacement transducer.

5.7.1. Pressure transducers.

The pressure transducers are capable of measuring pressures up to 70MPa. They are situated near the indicating pressure dials behind the front panel of the apparatus and isolated from high temperatures which could affect the output. Amplification and excitation are provided for these transducers by a Eurocard-mounted amplifier. Supplied by RDP electronics, this piece of apparatus consists of a frame which supplies a stable

power source for several individual cards which can be purchased separately according to the required specification. Two cards are used in this apparatus: the 611 module and the 626 module. The 611 has two channels which provide excitation and amplification for two pressure transducers. The output gain and zero-point can be adjusted as well as the excitation voltage. The other card, the 626, is specifically designed for LVDTs (Linear Voltage Displacement Transducers) used in calibration (see chapter seven).

The amplified output of each transducer then passes to the computer logging system. Calibration is accomplished using a dead weight tester and is described in chapter seven.

5.7.2. Temperature measurement.

Thermocouples are used to provide temperature measurement throughout the apparatus. K-type thermocouples were selected because of their good corrected-linearity in the temperature range used. Four thermocouples are set in pressure feed-throughs in the top closure of the vessel. It is essential to monitor the temperature at the top of the vessel because the Viton o-rings in the vessel are constructed to resist temperatures only up to about 250° C, after which they become glassy and seal inefficiently. Therefore, one of these thermocouples is set in the top closure itself to protect the seals. Also at the top of the vessel is a thermocouple used to monitor the temperature at the inside wall of the cell and two control thermocouples which sit against the heating coils to provide feedback for the temperature controllers.

At the bottom closure there are feed-throughs for four thermocouples. Two are used to monitor the temperature of the sample: one at the top and one at the bottom. The third thermocouple monitors the temperature of the actuator, to protect the seal inside. The final thermocouple is attached to the IDT. As the output of the IDT changes with its temperature, it is essential for this to be closely monitored. Calibration of the IDT at high temperatures is described in chapter seven.

Finally there is a thermocouple mounted on the outside wall of the cell which, along with the inner wall thermocouple gives an idea of the thermal gradient across the wall of the cell. All thermocouples are directly connected to the data-logging card of the computer without pre-amplification. In addition, the top closure thermocouple is connected to a temperature controller which shuts off the heating system if the temperature exceeds the safe working limits of the top o-rings.

5.7.3. Displacement measurement.

The inductive displacement transducer, or IDT, is sealed inside a small cylinder, open at one end, 14mm in diameter and 35mm long. It is a very sensitive and sophisticated sensor capable of withstanding great pressures and temperatures. The input/output cables are contained within a mineral-insulated cable which is electron-beam welded onto the case of the sensor. The PY106C type IDT used here has a working temperature of 600°C and can withstand 20MPa of pressure. The PY106C has a maximum range of 1.5mm (failure of specimens usually occurs at approximately 30% of this total range) and is only 37.5mm in length. This makes it an ideal sensor for the environment used in this project. Disadvantages of using this kind of sensor include lack of thermal stability and a non-linear output. To correct for the variation of output with temperature, the sensor was factory calibrated at a variety of temperatures. These results are shown in chapter seven.

Non-linearity in the sensor complicates the calibration procedure. Although only a differential displacement is required for the experiments, the calibration cannot be differential and must be absolute. This is because any linearity correction cannot start at an arbitrary point unless the response is linear.

A stand-alone S7AC amplifier module provides amplification and excitation for the PY106C. This is a single-channel signal-conditioning unit that has been factory modified to increase the gain by a factor of three. Other slight modifications were also necessary for the unit to operate correctly with the PY106C and were made by the supplier.

5.8. Heating system.

The heating system is in the form of a stand-alone furnace comprised of two heating elements wrapped in insulation attached to the upper closure of the cell. The upper closure also has feed-throughs for three thermocouples as described above. This furnace can be removed from the cell in one piece and is lowered into place using the hoist that raises or lowers the whole cell.

The sample is heated by simple ohmic heating elements coiled around it. There are two such coils, one for the top of the sample and one for the bottom. This gives good control of thermal gradients. A full description of the evolution of the furnace can be found in chapter six.

Insulation is provided by a 1.5cm thick layer of alumina blanket. The blanket was cut to the correct length and placed inside a copper sheath. The copper sheath was tightened around the coils, compressing the insulation material until the whole assembly was small enough to fit into the barrel of the vessel. The sheath was screwed into the support ring and the whole furnace lowered into the vessel. Heat resistant filler was used to secure the alumina blanket in place and to block any holes which could allow convection currents. The bottom sheath support also acts as a guide for the sample and prevents insulation material falling out of the bottom of the furnace.

In order to restrict convection and heat loss upwards towards the top closure, a cylindrical ceramic spacer is used to reduce the volume of the vessel and to provide a degree of insulation for the top closure. This cylinder is machined in two parts and with four holes for the thermocouples and the heating element to pass through. This piece is attached to the top plug using a ceramic bolt. Avoiding high temperatures at the top closure is important because, as described above, the o-rings become inefficient at 250°C or above. The heating element is 'cool' for the first 8" of its length, so that the heat is delivered only to where it is needed.

The heating system required a considerable amount of power and is designed in such a way that three separate heating elements can be incorporated into the design. The fracture mechanics incarnation of the apparatus only uses two elements but further modifications to the apparatus are envisaged and the heating system was designed with this in mind.

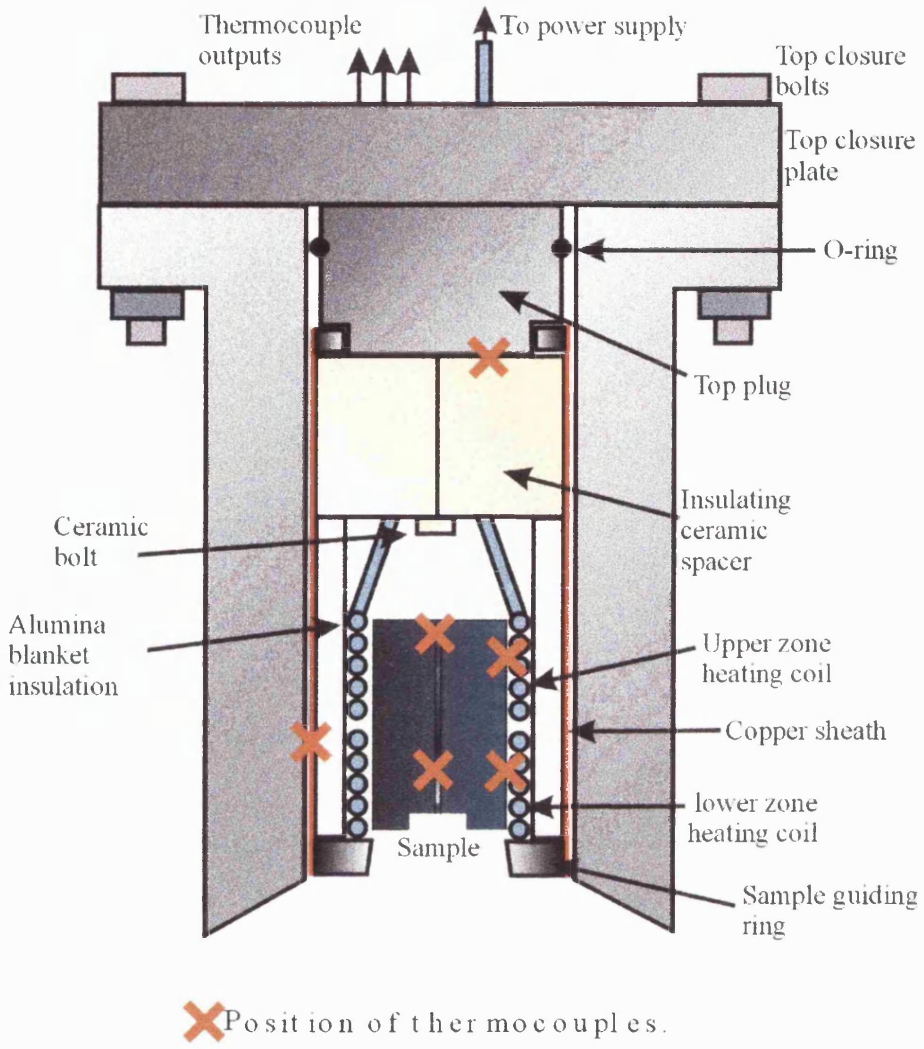

Fig 5.7. Sketch of the furnace showing all elements described in text. There are two thermocouples per heater zone, one for control and one for measuring sample temperature.

The temperature of the sample is controlled using Eurotherm 2408 and 2208 controllers. The controller is set to the desired temperature set-point and sends a logic signal to a diode which in turn allows a certain current to flow to the heater depending upon the proximity to the set-point and the configuration of the controller. The controller tunes itself automatically to ensure that over and under-shoot are minimised and that the temperature reaches the set-point quickly and remains stable. Both channels can be controlled separately but one controller can be slaved to make the entire system run from one set-point.

Safety is an important issue when designing an electrical circuit carrying 10's of amps at 100 volts. In addition to the solid state relay used to switch off the power if the top-plug gets too hot, there are three other important safety features in the heating

system. Firstly, there is a 15 amp circuit breaker set before the transformer for each phase used. This serves as protection for the mains system if the transformer becomes short-circuited. Secondly, there is a fast-blow 20 amp protistor after the transformer to protect the transformer and the diode if the heating element becomes short–circuited. Finally, every element of the system and the apparatus itself are grounded.

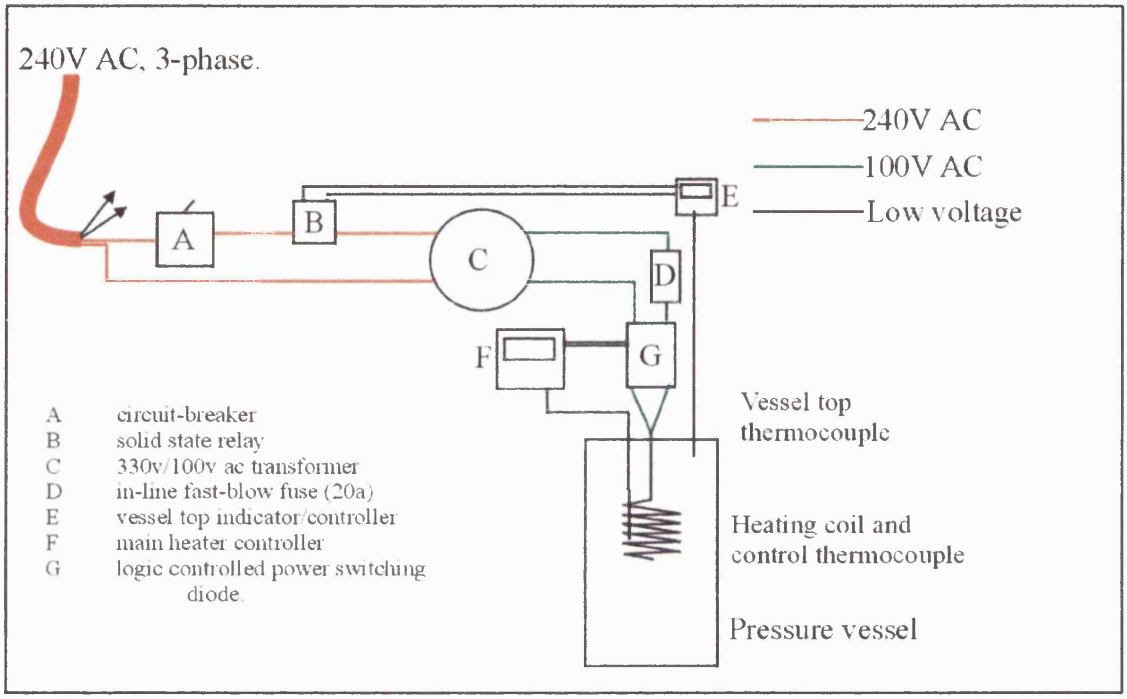

Fig. 5.8. Heater control system showing one of three possible channels. Each other channel is identical except that the same controller is used for both the second and third channel. Only two channels are used for this project. The other channels run from the spare phase of the supply cable indicated by arrows in the above diagram. There is, obviously, only one vessel-top protection controller, but the relay connections are made in parallel so all channels are disconnected if the vessel top becomes too hot.

The methods used in the testing and commissioning of the heater are described in chapter six.

5.9. Data logging system

In order for the results produced using this apparatus to be scientifically valid, certain variables must be monitored throughout each experiment. The most important fixed variables are the temperature and pressure, and these must be kept constant over the duration of the test. A level II test may take several minutes to perform and so these variables should be monitored approximately once a second. The direct variables are force and displacement and these must be measured many times a second in order to obtain an accurate plot of displacement as a function of force. Although an XY plotter

would be ideal for the display of the force/displacement data, a computer-based logging system has the advantage that it can store these data alongside the temperature and pressure data. A computer can also display other variables such as the vessel-top temperature, and be programmed to give a warning if it exceeds a given value. Hence the logging system used with this apparatus is computer based.

5.9.1. Data logging system- Hardware

The outputs from the various sensors pass through a range of conditioning systems before they are sampled by the computer. The output from the confining pressure transducer is amplified to a +/- 5V signal by an RDP series 600 conditioning unit. The same unit was used in initial LVDT calibration of the displacement sensor (see chapter six). The displacement transducer output is amplified by an RDP S7AC amplifier, which has been calibrated with the sensor by RDP themselves. This gives an output of 0-5V. The thermocouple outputs are not conditioned at all. The final signals are all gathered in a National Instruments SCB-68 screened multi-channel input box before passing along a screened cable to a National Instruments AT-MIO-16-XE50 I/O logging card within the computer. The computer used in this project is a 233MHz Pentium PC with a high-resolution screen and high quality video-card (for ease of use of the graphical programming interface).

The data logging card is capable of a total sampling rate of 500kS/s over 16 channels with a resolution of 16 bits over a –5/+5 volt range. The input channels are named:

- Ambient (Output from ambient temperature cold-junction compensator in SCB-68 box)
- Sample Hi (Output from thermocouple at top of the sample)
- Sample Lo (Output from thermocouple at bottom of the ligament in the sample)
- Wall (Output from thermocouple on outer wall of vessel)
- Actuator (Output from thermocouple at the actuator)
- PYC temp (Output from thermocouple at PYC displacement transducer)
- Vessel top (Output from thermocouple at vessel top)
- Displacement pressure (Output from displacement pressure transducer)
- Confining pressure (Output from confining pressure transducer)
- Displacement (Output from PYC displacement transducer)

Each of these is logged at between 5 and 50Hz depending on the settings specified by the operator in the front panel of the Bridge-logger virtual instrument (VI).

5.9.2. Data logging system- Software

The software used to record, manipulate and display the data is LabView Version 4.01 This is a modular programming system that allows the user to build 'virtual instruments' (VIs) that have read-outs, buttons and controls similar to traditional rack-mounted instruments but displayed on the computer screen. 'Behind' this front panel the user can program how the data are manipulated using the powerful graphical language 'G'. This allows almost unlimited freedom to combine the data from different channels and display it on the screen in a variety of formats. Combined with the huge library of ready-made VIs supplied with the program this flexibility makes Labview an ideal program for data-logging.

The two main VIs used with this apparatus are called 'Setup-logger' (SL) and 'Bridge-logger' (BL). SL is used to monitor the temperatures of all the thermocouple locations whilst the apparatus is reaching working temperature. The data are displayed on the screen both as an updating graph of temperature against time and as a digital readout for each thermocouple (See fig. 5.9). There is no facility to save the data in SL.

When the sample has reached working temperature, BL is run. BL displays a plot of force against displacement with a sample rate of 20 Hz. It also displays the sample temperature, force and displacement as a digital reading (see fig. 5.10).

When the test is completed the stop button activates a save dialogue which stores the buffer of raw data (sample Hi, sample Lo, displacement, displacement pressure, ambient, time) on the computer's hard disk. Raw data are saved because manipulated data contains the risk of error in the processing. The time value saved is merely the output from LabView's millisecond timer but allows stress/strain rate to be estimated from the data.

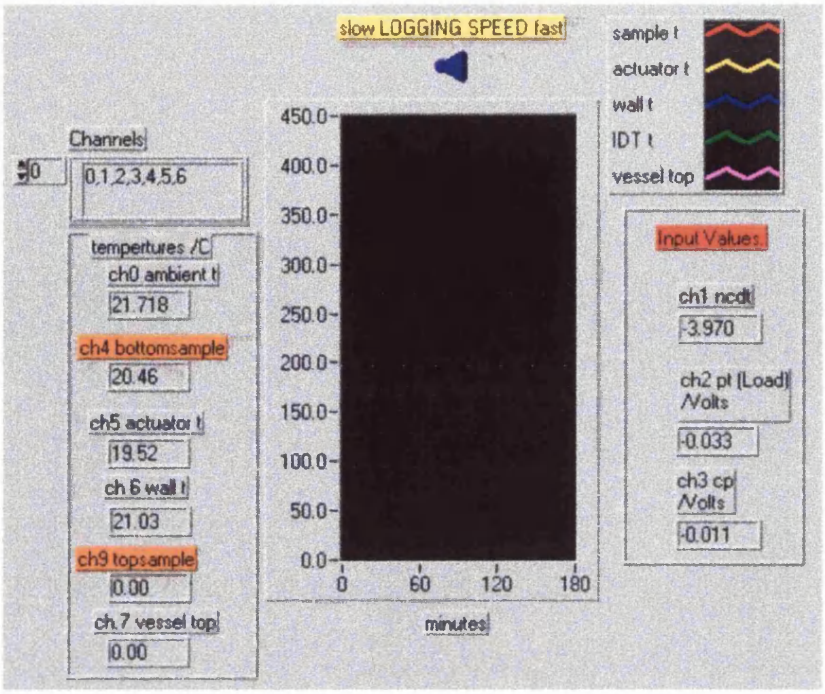

Fig. 5.9. Front panel of Setup-Logger VI showing readouts and controls.

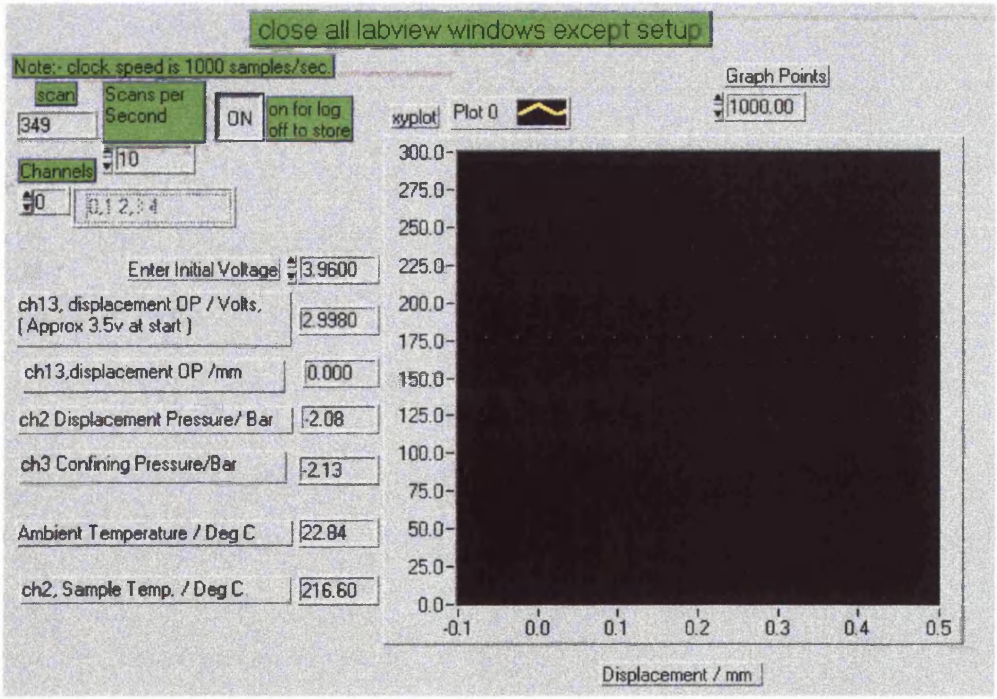

Fig. 5.10. Front panel of Bridge-Logger VI showing readouts and controls.

5. 10. Conclusions.

The apparatus described above is used to make measurements of the value of fracture toughness for the samples used in this project. Other apparatus used in this project is described in chapter six and seven detailing the evolution and methods of the apparatus respectively. Important aspects of this apparatus are:

- Ability to measure fracture toughness of rocks using 60mm SR samples according to standard test methods (ISRM, 1988). Level I or II testing may be used.
- Gas or liquid can be used as confining medium at pressures up to 50MPa.
- Self-tuning furnace can control temperatures of the samples to better than $\pm$ 1°C.
- Sample temperature can exceed 600°C.

The apparatus fulfils the design criteria set at the outset of the project and is safe and robust. A discussion of the efficacy of the design and a summary of further modifications to the apparatus can be found in chapter 11.

Chapter 6

Development of Experimental apparatus and techniques.

6.1. Introduction

At the start of this project the apparatus was incomplete and uncalibrated. It had the ability to perform level I fracture toughness tests at ambient conditions or with water as confining medium up to a pressure of 20MPa. The temperature levels the apparatus could achieve depended upon the confining medium: 400°C for ambient pressure or 200°C for water at 10MPa. The apparatus had not really been fully commissioned.

This chapter describes my development of the apparatus into the state described in chapter five. It also records some early results and measurements in order to highlight the decision-making and problem-solving processes required when carrying out an experimental redesign of this scale. The evolution of the experimental methods is described in tandem with that of the apparatus.

The chapter is divided by process, with each section referring to a different subsystem of the apparatus. Each section begins with a short description of the starting configuration of the subsystem followed by an approximately chronological account of the development. The main areas of modification were:

- The pumping and confining systems were modified to use gas as confining medium whilst retaining the ability to use water.
- The displacement medium system was upgraded to use a servo-controlled intensifier.
- The actuator housing was changed to use a one-piece, low compliance design.
- The furnace and heating systems were completely replaced.
- The logging hardware and most sensors were completely replaced.

6.2. Confining-pressure system.

The initial layout of the confing pressure system remained essentially unchanged but was supplemented by the addition of a gas pump. Fig. 6.1 shows the original and final pressure system.

The main concern when switching from a liquid to a gas for confining medium is one of safety. The compressibility of liquids is very small and hence the stored energy in a high-pressure liquid is also low. Gases, however, can store a great deal of elastic energy when pressurised and so a great deal of care must be used in the implementation of a system utilising pressurised gas. As the apparatus was not originally intended for use with gases, a prerequisite for any design work was a safety analysis of the pressure vessel and fittings. This work is described in detail in Appendix I. In addition, a burst disk was included to prevent possible vessel failure.

The choice of which gas booster to install was made on the basis of cost and suitability. The primary specifications for the booster were that it should be able to:

- provide a gas pressure of 100MPa.
- fill the pressure vessel (volume approximately 1 litre) within a reasonable time scale (minutes as opposed to hours).
- retain the ability to pump gases other than CO_2.

Two gas booster pumps fulfilled the criteria above. The first was a Haskel air-driven pump similar to that being used already to provide the pressure with liquid as confining medium, the second was an electrically powered pump made by Stanstead Fluid Power. The pumps had similar performance but the Stanstead pump was felt to be superior in convenience and quietness. This pump was, however, approximately 50% more expensive and the final choice was the Haskel air-driven booster described in the apparatus chapter.

When the pump was integrated into the system it was discovered that, although volume flow rate was high in the first minute of operation, the pump virtually ceased to cycle after 2-3 minutes. This problem was traced to the compressor supplying the air pressure to the laboratory. The output air flow rate of the compressor was not high enough to power the gas booster once the reservoir had been exhausted, leading to 'stalling' of the pump. This problem was fortuitously solved when the whole apparatus was moved to a different laboratory, which had an airline powered by a much larger compressor.

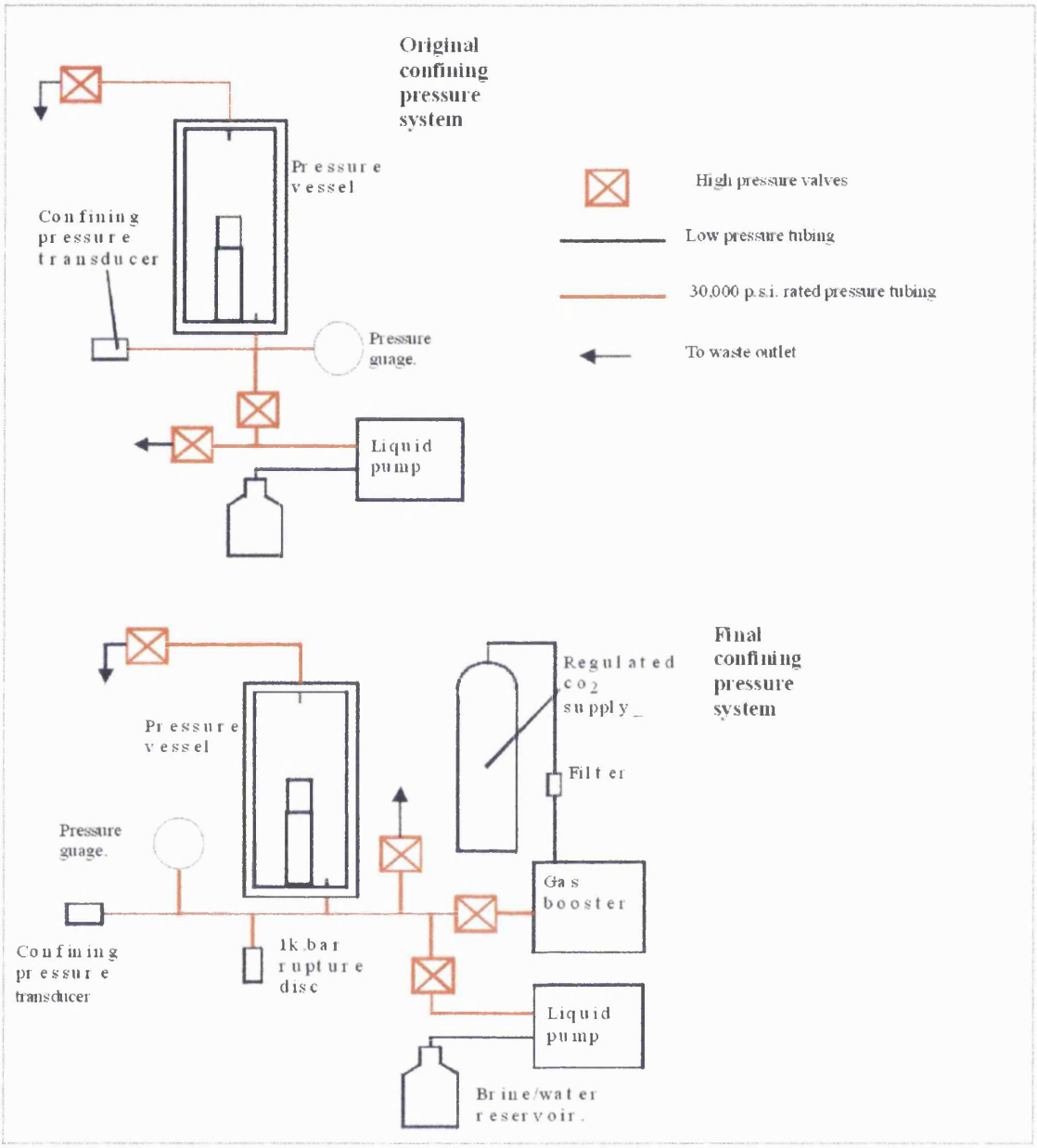

Fig. 6.1. The original and final confing pressure system.

6.3. Displacement pressure system.

The displacement pressure system was initially based upon a simple screw pump design in which the operator could control the pressure by winding the handle manually. The pump was filled from a reservoir and, initially, water was used as the actuator fluid. The initial and final configuration are shown in fig. 6.2.

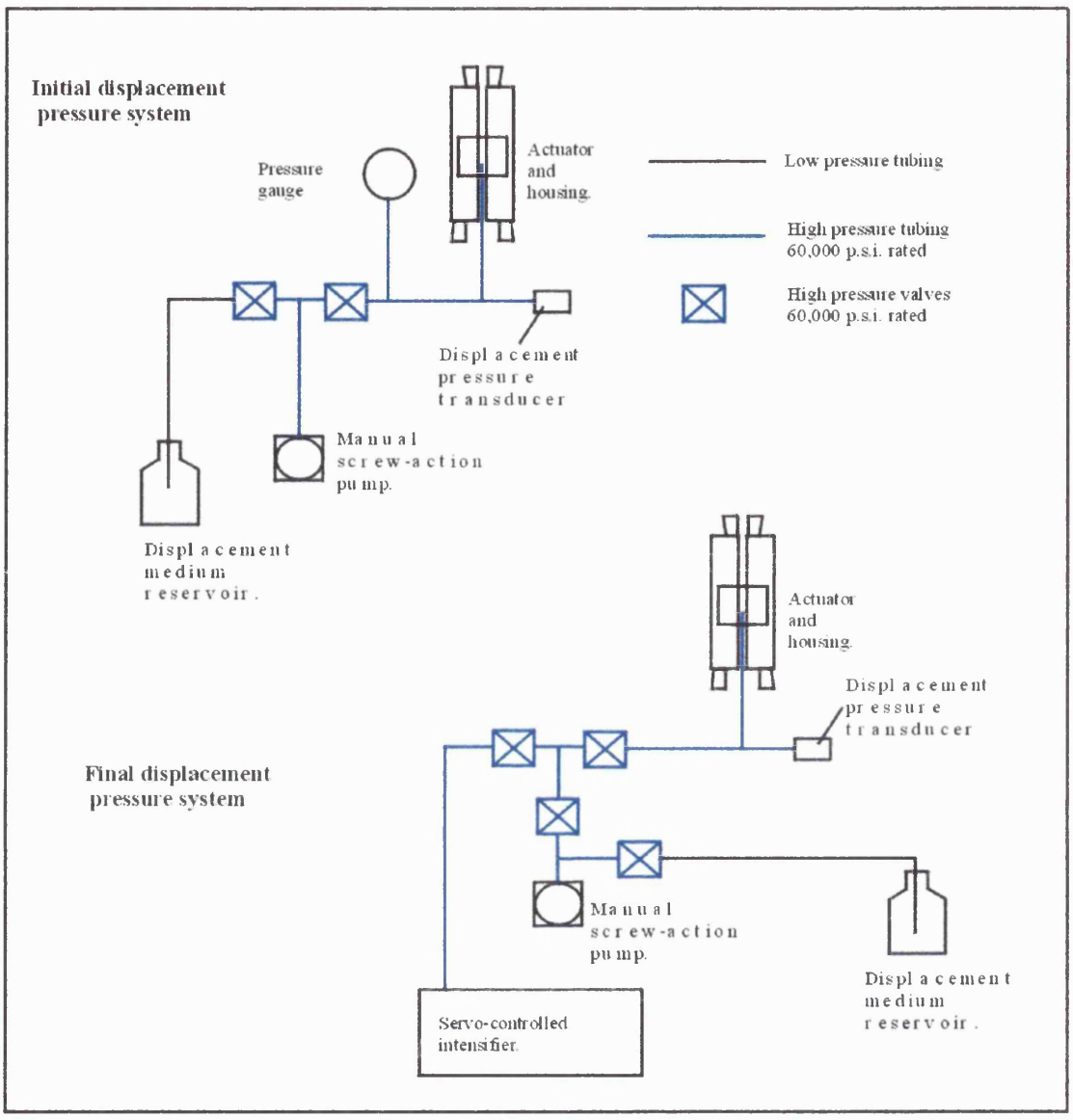

Fig. 6.2 . Original and final displacement pressure systems.

The changes made to the displacement system were instigated for a variety of reasons. The first major change to the system was to replace the water used as actuator fluid to silicon oil. This stopped the actuator fluid from boiling because it was noted that the actuator temperature could get as high as 110°C when the heating element was left on for some time.

The second, more important change to the system was to replace the screw pump with a servo-controlled intensifier as the means for providing the pressure in the actuator. The screw pump is retained in the system to prime the intensifier and to provide displacing pressure at the start of the test below 0.5MPa, the minimum

controllable pressure of the intensifier. The intensifier system is superior to the hand pump for several reasons:

- The pressure can be increased linearly without abrupt changes if the operator changes hands whilst turning the pump handle. At higher pressures (>14MPa) the handle becomes difficult to turn, exacerbating the problem and leading to poor control.
- The new system allows instantaneous reversal of pressure direction at the changeover point
- The new system allows noise free unloading. The hand pump did not unload the sample smoothly, as shown in fig. 6.3, making it difficult to judge the exact position of the unloading line. This is important because knowledge of the gradient of the unloading line is essential for level II tests (ISRM, 1988).
- Load rate can be changed easily by adjusting the ramp voltage of the servo-controller or by using the controlling dial in operator controlled tests. This allows control over the rate of change of the CMOD, an important criterion in the validity of a level II test (ISRM, 1988).

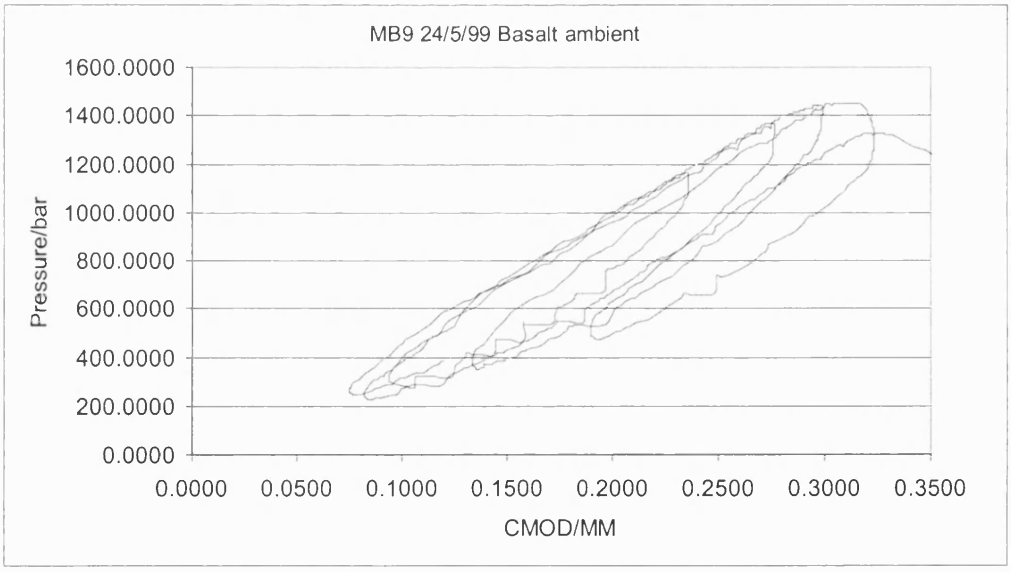

Fig. 6.3. An example of an early level II test carried out using a pre-cracked basalt specimen. The problems of noisy unloading and non-linear loading are clearly evident in this example.

Following the installation of the servo-controlled intensifier, the displacement system went through several incarnations before the final system was selected. In particular, the original priming system was constructed from low-pressure flexible tubing. This was soon found to be inadequate when the tubing failed during priming

(pressures exceeding 2MPa were recorded whilst backing off the piston). A full description of the priming method for the intensifier can be found in section 5.5.2a.

There were also problems finding the correct level of feedback to supply to the controller. Too little feedback and the output pressure had a tendency to drift and responds sluggishly to the control voltage. Too much feedback made the output unstable and difficult to control. These problems could only be solved by trial and error adjustment of the controller open-loop gain whilst using a metal block across the jaws of the actuator to provide a suitable, non-deformable, specimen.

Note: The development of the displacement pressure system proceeded in tandem with that of the force transfer system described below. It should also be noted that fig. 6.3 showing initial tests was performed using the old actuator housing jaws and is, therefore, invalid as a real level II test.

6.4. Force transfer system.

Changes to the force-transfer system (the actuator housing and the actuator itself) became necessary when important flaws were discovered in the original design. The original actuator housings were each made in five pieces. The top and bottom jaws fitted snugly into semicircular plates, which in turn fitted into the main body of the actuator housing. Each element was secured using M3 stainless steel bolts. The initial design is shown in fig. 6.4.

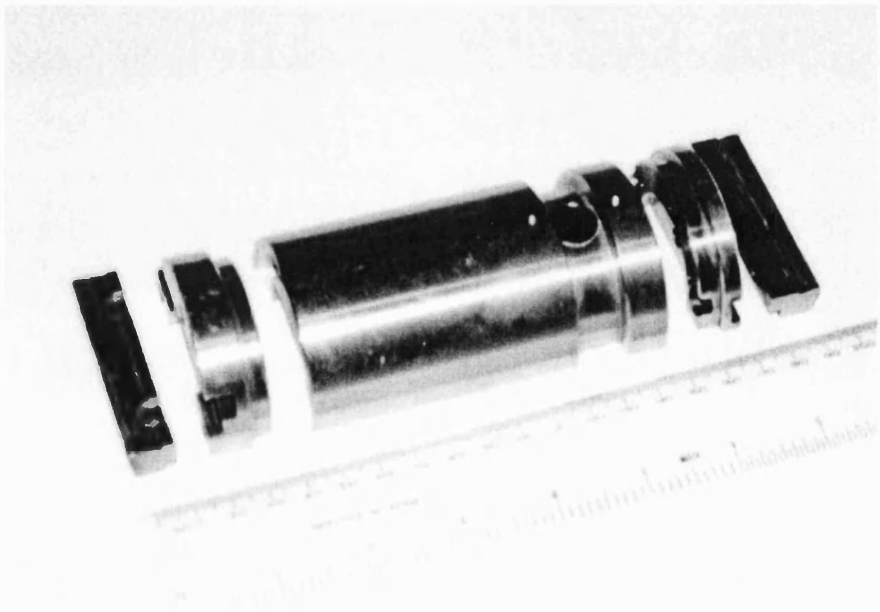

Fig. 6.4. Photograph of initial force transfer system. Half the actuator housing is shown here

6.4.1. Modifications to bottom platten.

The first modification that was made to the system was to put sharper corners into the 'bottom platen', the grooved table against which the bottom jaws react. This was necessary because the knife edge jaws are required to seat in a repeatable position. The initial design had a small radius in the corners, which meant that the jaws tended to raise out of the groove when the displacing force was increased.

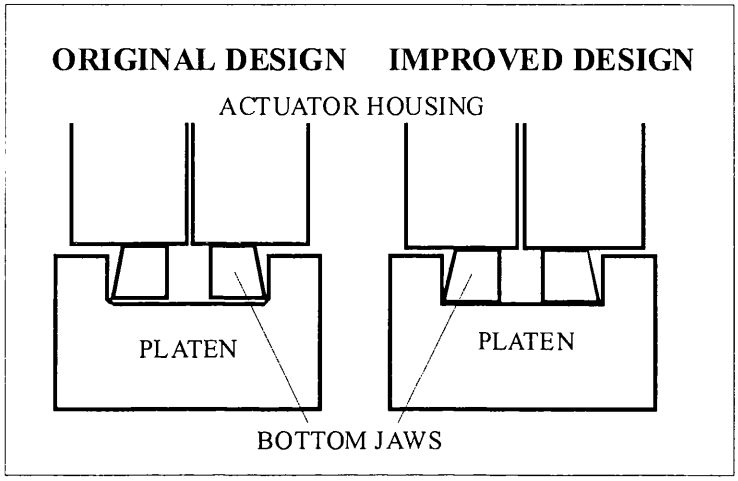

Fig. 6.5. Development of bottom platen showing instability caused by radius corners.

6.4.2. Failings of multi-piece actuator housing.

The initial actuator housing was acceptable for level I tests but it was discovered, after much work, that the housing was simply too compliant too perform level II tests. As discussed in chapter seven, the first measurement required for a level II test is the initial stiffness of the undeformed sample, and the apparatus must therefore be less compliant than the undeformed sample. If it is not, the data extracted from the test will represent the stiffness of the apparatus rather than that of the sample. The worst case is that where the apparatus is much more compliant than the sample even at the point of failure. In this case there will be no change in compliance throughout the test until the sample fails. Described below is the succession of tests that led to the conclusion that the initial actuator housing was more compliant than the samples.

6.4.3. Discovery of flaws in early design.

That the apparatus was too compliant was not immediately obvious during initial testing. The first clue that pointed to this possibility was the failure of experimental tests to match theory. When the fracture introduced into the SR sample reaches the critical point (see ISRM, 1988) the stiffness of the sample falls to half of its

initial value. This is a function of the SR geometry used in level II tests and is not dependent on material or test conditions. This point should also coincide with the point of maximum load and occur well before failure. As can be seen from fog. 6.6, an early test using the original actuator housing shown in fig. 6.4, the compliance changed very little throughout the test.

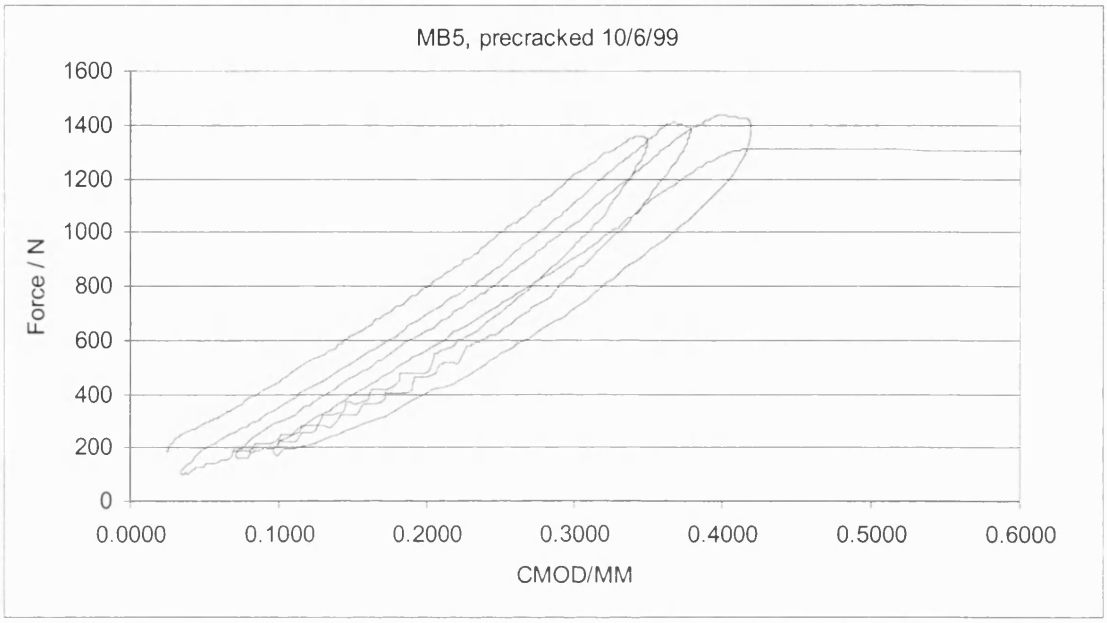

Fig. 6.6. This sample showed no change in compliance over three cycles. Abrupt failure occurred unexpectedly before any change in compliance was observed.

6.4.3a Compliance tests

This result and others like it led to the conclusion that either there was a problem with the apparatus, or that the sample was simply too brittle to change in compliance until failure. To discriminate between these two possibilities, the next set of tests was designed to compare experimental compliances with theoretical ones. The compliance of a pre-cracked basalt sample was measured by monitoring the CMOD and displacement pressure whilst the opening force was increased to approximately 800N. The gradient of this line would represent the stiffness of the sample. Three cycles were made for each data point to ensure repeatability. When the compliance had been measured for a fresh sample, the point of the ligament was cut back using a thin diamond wheel. The depth was then measured using a micrometer and the compliance test repeated. By cutting back the ligament more and more (as shown in fig. 6.7), a plot of compliance against crack advance could be extracted.

The results from the compliance tests showed that there was little change in compliance until large crack depths had developed. Repetition of the tests using an aluminium sample showed a similar and even more pronounced lack of compliance change. Figures 6.8 and 6.9 show the results from the compliance tests. Fig. 6.10 shows normalised results compared with the theoretical and experimental work performed by Bubsey *et al.* (1982).

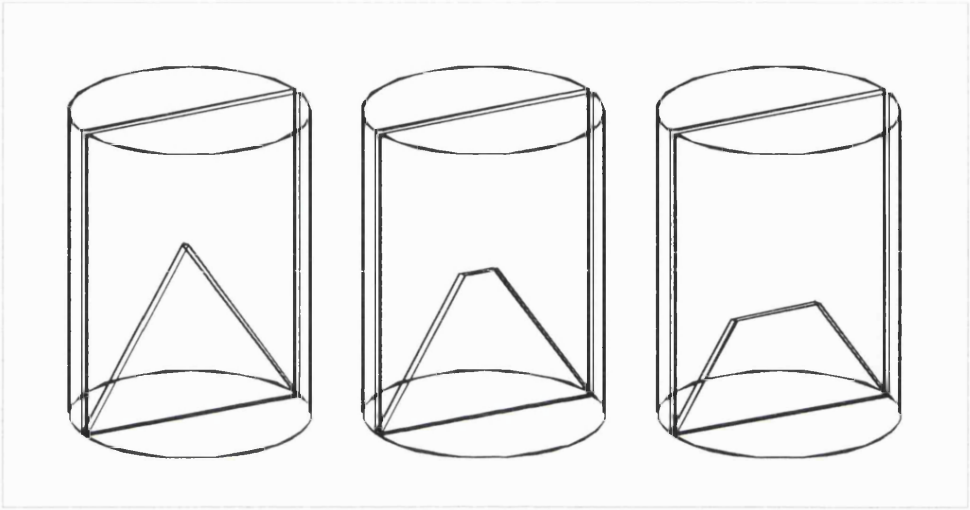

Fig. 6.7. Compliance sample showing how the ligament is cut back for each successive measurement.

According to theory (ISRM, 1988) the point at which the compliance doubles is at a distance 0.34D (where D is the diameter of the specimen) from the apex of the chevron. This is a distance of around 20mm for our samples. If the tip of the notch is 27.1mm from the base of the sample to the crack tip the compliance should double by the time this distance is 47.2mm.

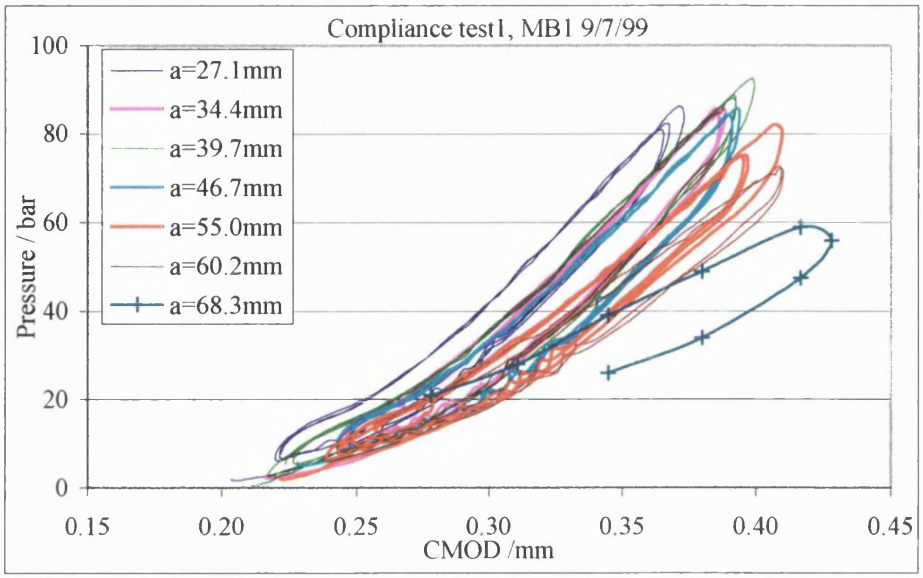

Fig. 6.8. Compliance test results for basalt sample. Compliance is the reciprocal of the gradient of each line. Note that the first four measurements have virtually identical compliances (The low slope at the bottom is due to bedding in). The y axis label is pressure in the displacement actuator.

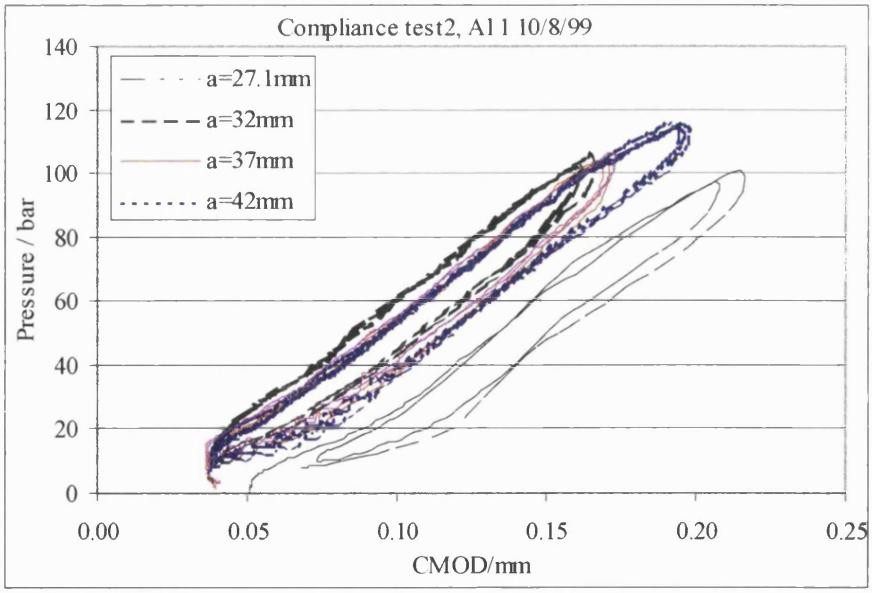

Fig. 6.9. Compliance test results for aluminium sample. Note that all the measurements have similar compliances.

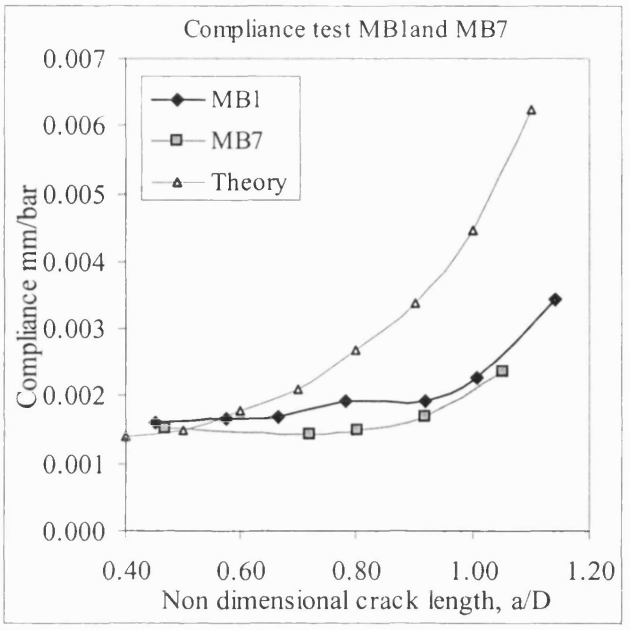

Fig. 6.10. Comparison of basalt compliance test (samples MB1 and MB7) with theoretical curve from Bubsey *et al.* (1992)

6.4.3b Compliance test finite element modelling.

In order to check the theory results of Bubsey *et al.* (1992) and ISRM (1988), the deformation of the sample was modelled using a finite element method. The model represents a typical SR sample made of aluminium. The notched faces that the knife edge jaws sit in were loaded with a 1KN force and the displacement measured for each crack depth. By plotting the ratio of displacement and force against crack depth, a compliance plot similar to fig. 6.10 was achieved. The results of the computer model are shown in fig. 6.11 and the resultant compliance curve is shown in fig. 6.12.

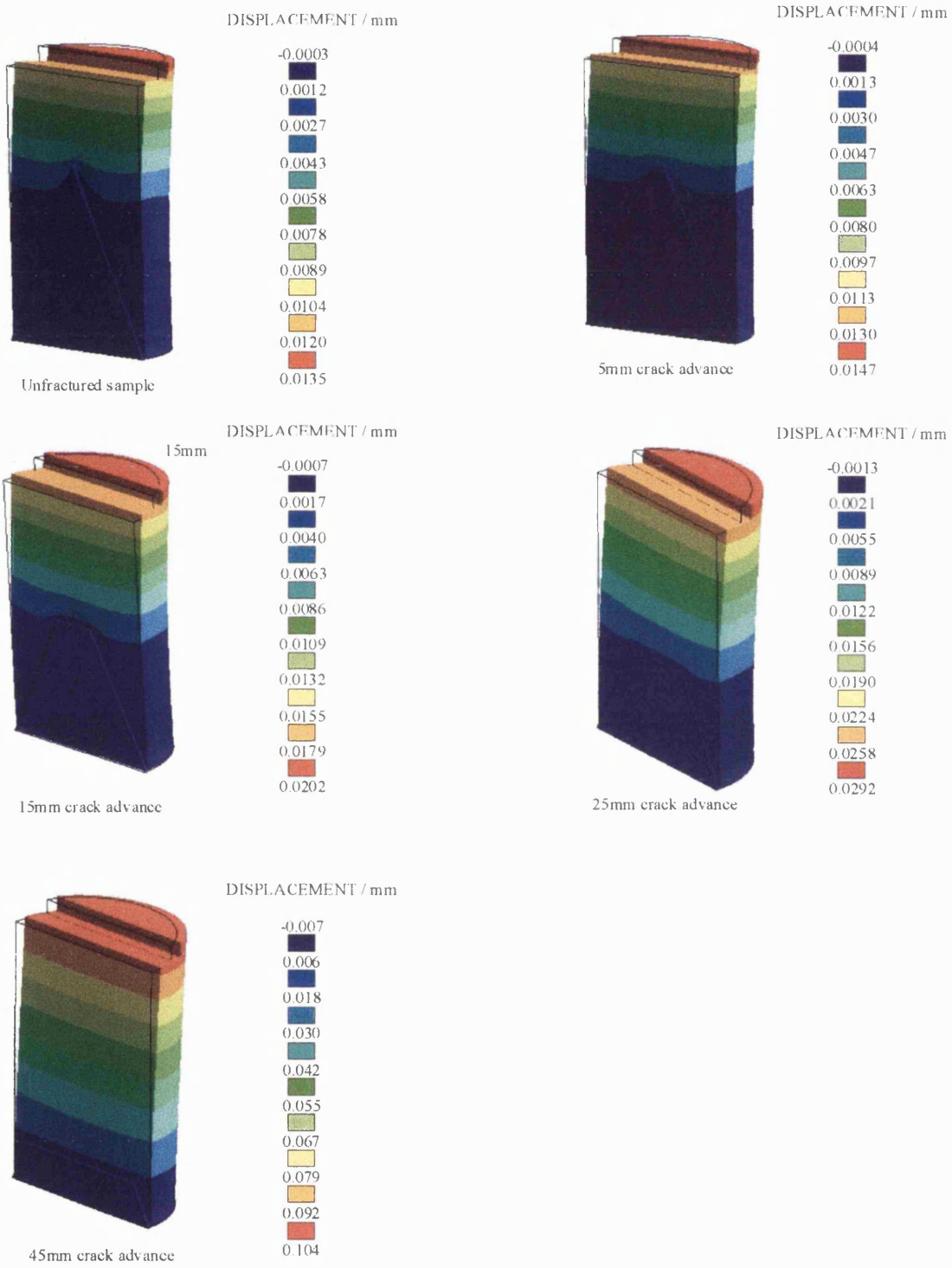

Fig. 6.11. Finite Element plots of deformed aluminium SR sample.

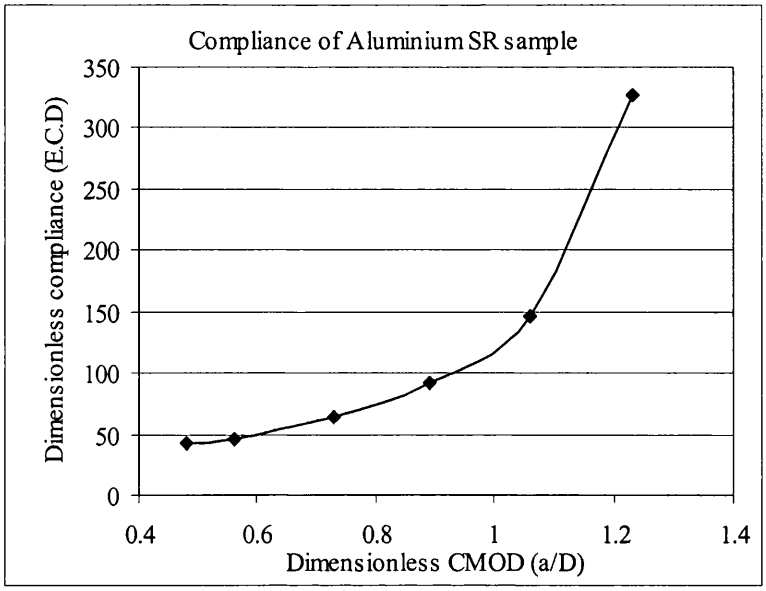

Fig. 6.12. Results from FE analysis. Note that the point at which initial compliance (~45) doubles is at a dimensionless crack extension of 0.86. This agrees well with theory and previous experiments (Bubsey *et al.*, 1982). E is the elasticity modulus, D the sample diameter and C the measured compliance.

The results from this model show that at the critical value of crack extension, a dimensionless value of 0.82 (ISRM, 1988), the stiffness of the sample is halved. This validates the theory of the level II test.

The only explanation for lack of change in compliance for the actual sample is that the actuator jaws must be deforming along with the sample. This would effectively mask any change in the compliance of the sample until it became similar to that of the apparatus. This would also explain the shape of the early level I curves. These were observed to be linear with abrupt failure points whereas theory suggests that the gradient should decrease with a broad peak, failure occurring after maximum load. Fig. 6.13 shows how the compliance of the apparatus would mask the true behaviour of the sample.

The amount of CMOD caused by deformation of the sample is so much less than that caused by deformation of the apparatus that the plot represents the deformation of the apparatus almost entirely. Fig, 6.13 shows that the stiffness of the sample (gradient of the curve) would be masked by that of the apparatus until the two became similar, in this case at around 1500N. It is this deformation of the apparatus that prevented the correct performance of level II tests using the original design for the actuator housing.

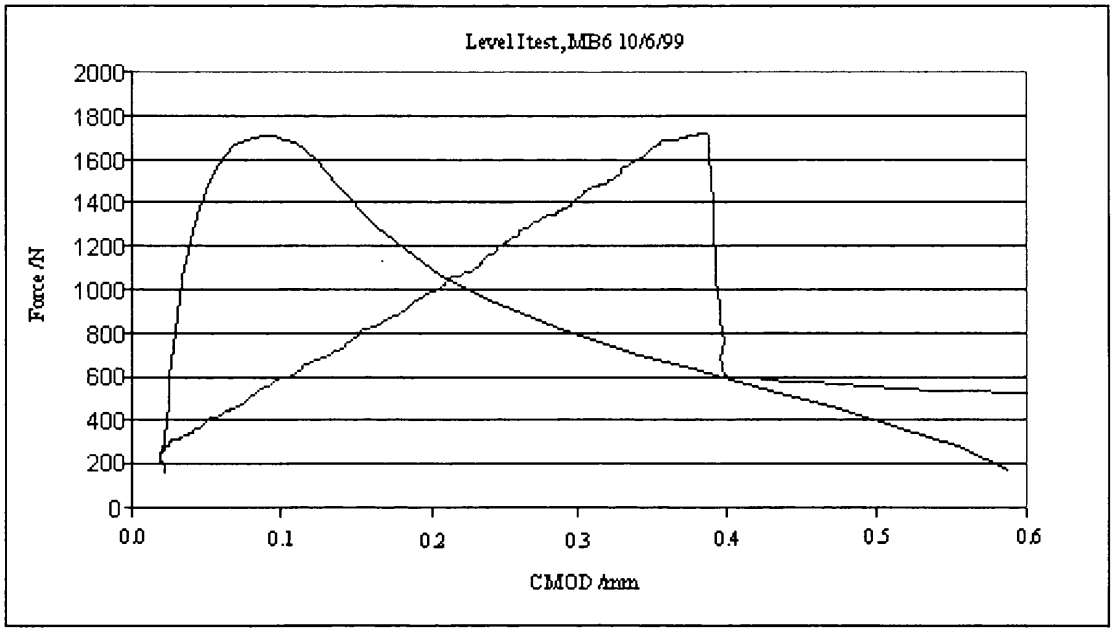

Fig. 6.13. Approximation of expected level I test (black dashed line) and early pre-cracked basalt level I test (solid blue line).

As a final test to confirm this theory, a steel block with a groove machined in it to accommodate the actuator jaws was used in place of a SR sample. The measured 'compliance' of the block would be similar to that of a basalt SR specimen and an aluminium SR specimen if the apparatus was indeed more compliant than each of these specimens. This was found to be the case, as shown in fig. 6.14. Using a similar method to that displayed in fig. 6.11, finite element modelling of the steel block was used to obtain a theoretical compliance. If the apparatus had measured the compliance of the steel block correctly it would have appeared as an almost vertical line in fig. 6.14.

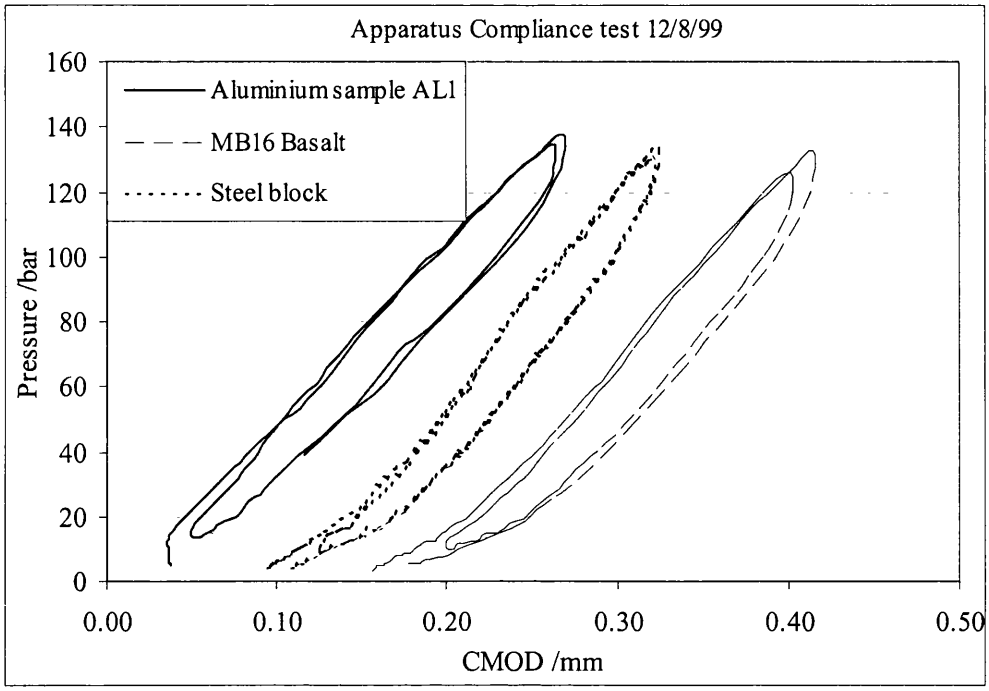

Fig. 6.14. Compliance of apparatus derived from tests using aluminium and basalt SR specimens and a steel block. Compliance of the apparatus is around 2×10^{-7}m/N. Initial compliance for an SR sandstone sample (Matsuki *et al.* 1991a) is approximately 7×10^{-8}m/N. Basalt SR samples would be expected to be even less.

The only possible cause for such high compliance of the actuator housing was the fact that each half was constructed from five separate pieces. Due to the geometry of the jaw design (see fig. 6.4), the M3 bolts holding the jaws to the top and bottom plates were experiencing substantial shear forces. Also, the machining of the pieces left small (of the order of 0.1 mm) spaces between the plates and the jaws. This combination of effects left scope for small deformation of the M3 bolts to occur. This, in turn, meant that the load-line (at the tips of the jaws) deformation was minimal compared to the deformation further down the actuator housing, where the displacement transducer was situated, simply because the tips of the jaws were being held in place by the sample. The effect would occur at the top and bottom of the actuator housing where the jaw was held to the plate. It would also occur on each half of the actuator housing. In summary, a tiny deformation of the jaws caused by undersized bolts and poor machining would be quadrupled by the geometry of design and lead to masking of the true behaviour of the specimen.

6.4.4. Single piece actuator housing.

In order to combat this effect the actuator housing had to be redesigned so that it was made from one piece of metal. The actual design remained identical and the new actuator housing was, again, made from Hastelloy C22 alloy. Before the pieces were made the new design was tested using finite element modelling. In this way, the compliance of the apparatus could be estimated before it was built, allowing any modifications to the design to be made prior to the purchase of these expensive items. The assumptions made for this model were that:

- Both the top and the bottom jaws were constrained immovably.

- The force exerted was at the point at which the actuator piston acts.

- Deformation was measured at the point which the PYC displacement transformer as positioned.

The results from this modelling are shown below in fig. 6.15.

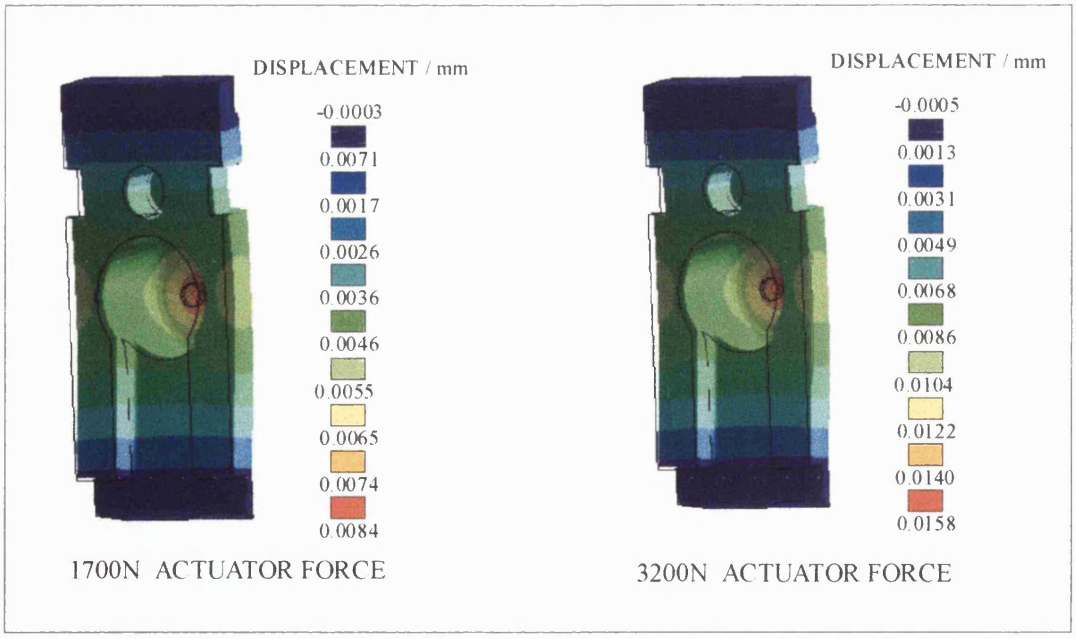

Fig. 6.15. Results from FE modelling of new design for actuator housing.

When the displacement of the PYC transducer position is read from the above plots values for compliance of the measurement line can be obtained. The compliance of the measurement line for this design was 3×10^{-9} m/N. This is nearly two orders of

which was 2×10^{-7} m/N, and is more than an order of magnitude less than the initial sandstone compliance measured by Matsuki *et al.* (1991a). The conclusion of the modelling work was that the design was more than adequate and that the compliance of the apparatus would no longer obscure that of the sample.

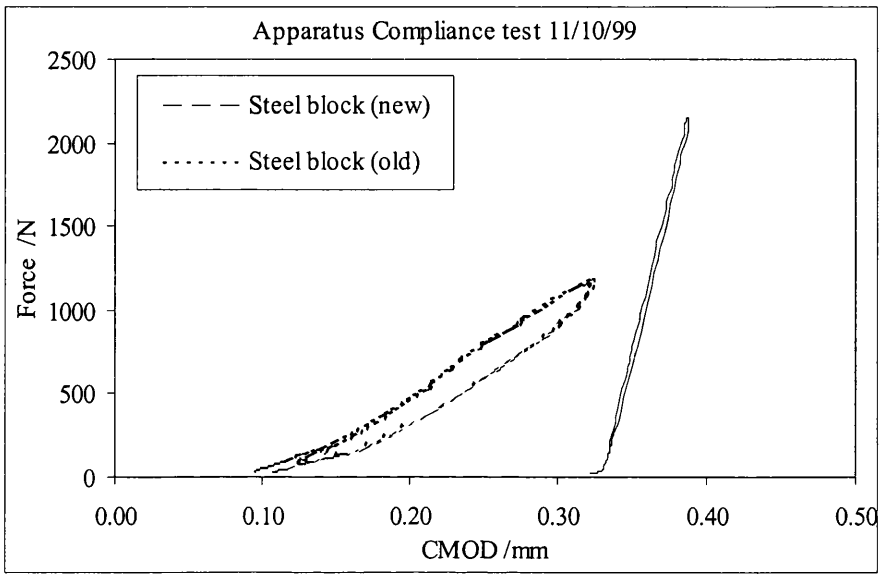

Fig. 6.16. New apparatus compliance showing the vast change in stiffness. This plot justifies the changes made in the design and shows a substantial improvement over the previous actuator housing.

Fig. 6.16 shows compliance plots of new versus old apparatus showing that the design change was, indeed, necessary. The huge increase in gradient between the old and new apparatus plots for the steel block highlights the improvement in apparatus stiffness. The steel block is considered to have stiffness so large that it would appear as a vertical line in fig. 6.16. Thus the gradient of the two plots in fig. 6.16 must represent the compliance of the apparatus, which, for the new apparatus, is about $2.6\text{x}10^{-8}$m/N. Because this is less than the theoretical value, there is still scope for further improvements, but these may require radical design changes and are discussed in chapter 11.

6.5. Displacement transducer.

The original system for measuring the CMOD has remained essentially unchanged. Changes made were minor, but nonetheless important. A minor problem with the initial configuration of the sensor was that the mineral insulated cable had to be bent at a tight angle (not recommended by the manufacturers) and that the cable was so long that it had to be wound around the whole actuator housing before passing

through the feed-through. This meant stress was put on the stiff but fragile cable, which acted like a spring and tended to displace the apparatus.

The main problem encountered with using the IDT was not how it was integrated into the system but how to calibrate it. This problem was made even more intractable by the fact that the output of the IDT varies with temperature. Several methods of calibration using LVDTs or deformation of aluminium samples were attempted unsuccessfully before it was realised that the output of the IDT transducer itself was slightly unstable. This was thought to be due to a poor connection at the back of the sensor caused by continual bending of the mineral insulated cable. The metal target used by the sensor was also found to be far too small (8mm diameter) as it did not cover the face of the sensor (12mm diameter).

When the mineral insulated cable failed completely during disassembly of the apparatus, a new PY106C sensor was purchased together with a shorter cable. This was calibrated by the manufacturers, with the amplifier, at a variety of temperatures using a larger target. The actuator housing was modified to accept the new target and the mineral insulated cable shortened and shaped so that the minimum bend radius was larger and the cable did not displace the actuator housing.

6.6. Heating system.

The design specifications for this project were that the apparatus should be able to heat the specimen to 600°C under 200 bar pressure of CO_2 gas. The initial design of the heating system has remained unchanged, in theory, but the implementation of the design has been completely reworked.

6.6.1a. Original design of heating system: description.

The original heater comprised a single ohmic heating element powered from a standard 13A mains supply via a 60V step-down transformer rated at 300VA. Control for the heater was provided by a thermocouple attached to the heating elements, which in turn was connected to a Eurotherm temperature controller.

The controller output was linked to a logic-controlled diode, which switched power to the coil. The coil was covered in insulating paper and a firebrick was used to reduce the volume inside the vessel. Only one thermocouple was used to monitor the temperature of the sample and it was positioned halfway up the sample. A sketch of this system can be found in fig. 6.17.

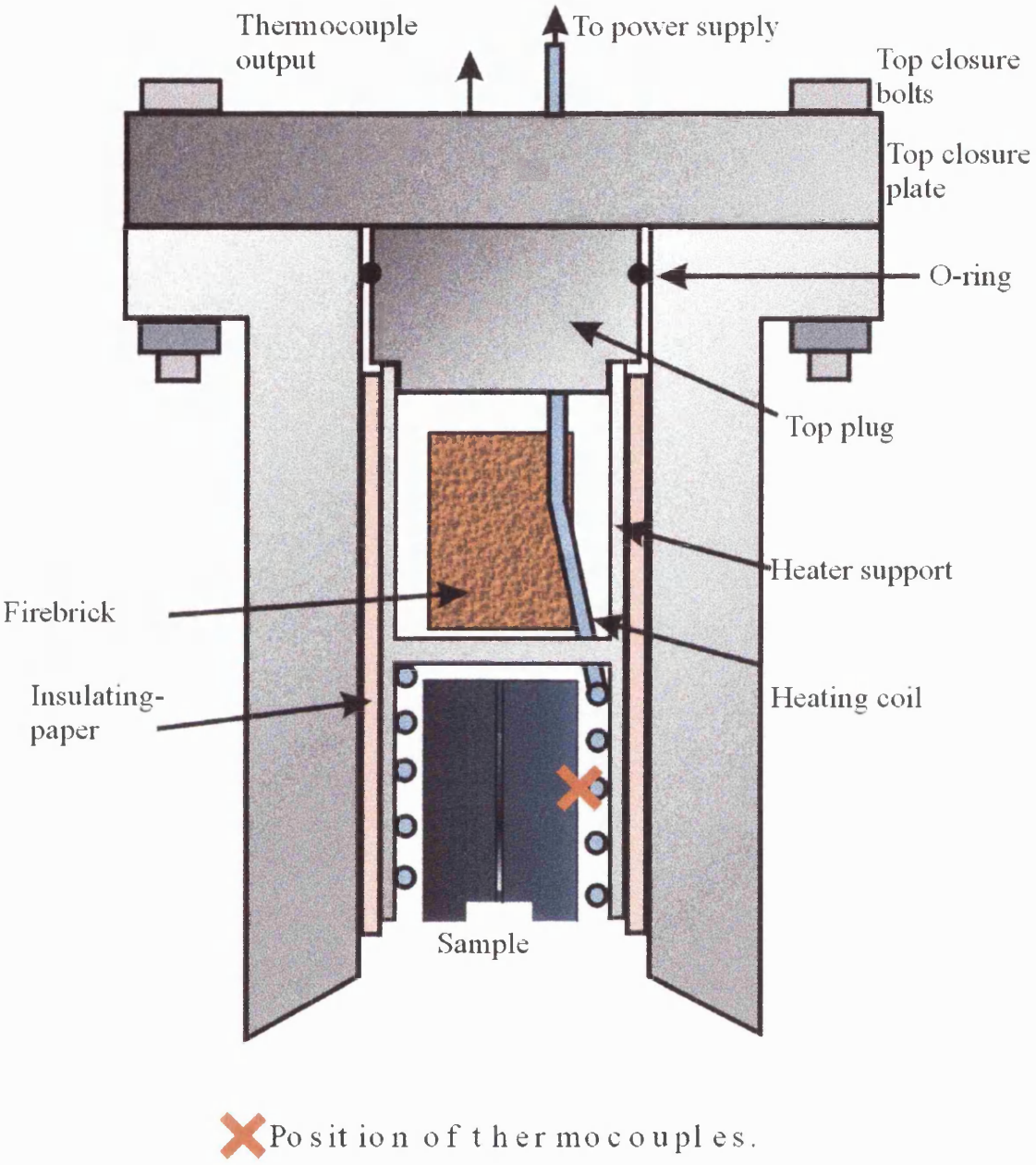

Fig. 6.17. Original heater system showing Hastelloy heater support.

6.6.1b. Original design of heating system: problems.

The original heater coil had a resistance of approximately 6.6Ω, producing around 0.5kW of power when run at 60V. The time required to heat the sample to 500°C was less than 30 minutes for ambient pressures but, when CO_2 or water at 10MPa was used as the confining medium, the sample required several hours of continuous heating to achieve working temperature. Under 20MPa of water, the sample could not achieve a temperature greater than 300°C even after four hours of continuous heating.

In addition to the obvious practical problems associated with such a long warm-up time, the actuator and outer wall of the vessel reached dangerously high temperatures. Overheating of the actuator could ruin the seals, and thermal gradients in the vessel could result in unpredictable stresses in the walls. The addition of another heating coil, run in parallel and inter-coiled with the first reduced the problem slightly by effectively doubling the power supply, but it was not a viable long term option because it involved operating the transformer at much higher levels than recommended for continuous use.

Another problem that became apparent was that the top seals became inefficient after the apparatus had been used at high temperatures. The seals around the top-plug and the thermocouple and heater element feed-throughs were only rated to 150°C, and when the apparatus was dismantled after a test, they were discovered to be hardened and brittle. The top of the vessel had obviously exceeded the working temperature. Therefore Viton seals rated at 250°C were used in place of the original nitrile ones and a thermocouple included in the top plug to monitor the temperature.

Continued testing showed that the vessel-top temperature exceeded 280°C before the sample temperature reached 400°C. Closer inspection of the original heating elements also showed that the cold length (the unheated part of the element) was too short and that the feed-throughs had been welded over an active part of the heater. The heating elements were, in effect, heating the feed-throughs from within. The feed-throughs, in turn, were heating the pressure seals directly. It was impossible, however, to make the weld any nearer the end of the element because the terminations would melt if heated above 150°C during the welding procedure.

The final problem, which became apparent from the use of two thermocouples to monitor the sample temperature was that a substantial thermal gradient existed over the sample. This would mean that, as the fracture progressed into the ligament, the temperature at the crack tip would change, making the test invalid. Convection in the vessel was held to be responsible for this effect and it could only be reduced by minimising the volume of gas in the vessel. Fig. 6.18 indicates all the major problems with the original heater system.

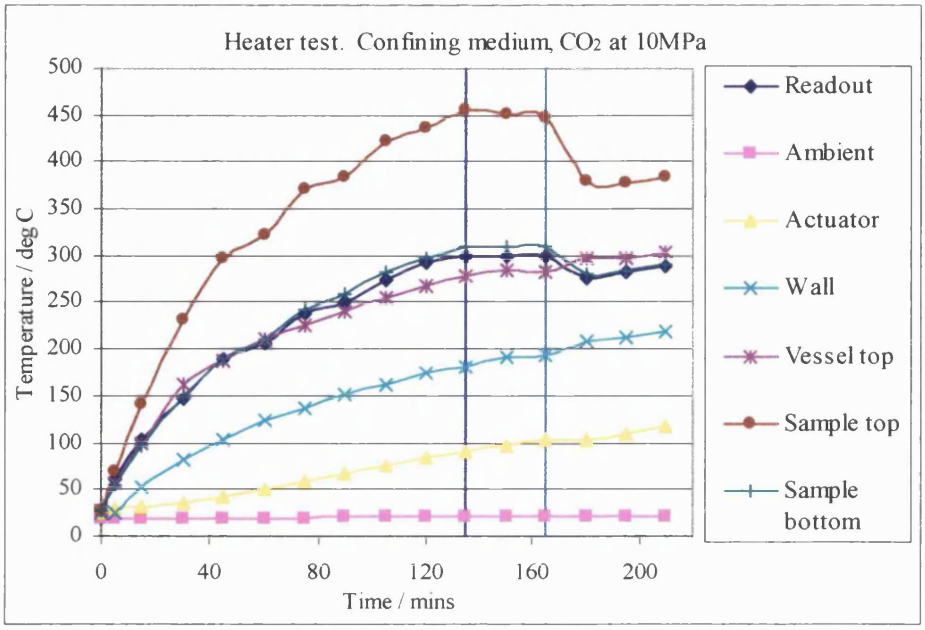

Fig. 6.18. Heater test. This test highlights:- a) long warm up time, b) overheating of vessel top, c) overheating of actuator and vessel outer wall, d) thermal gradient in the sample. At t=135 minutes the controller was set to the same temperature as the readout to measure stability (which was excellent over a 30 minute period) and at t=165 minutes the pressure of CO_2 was increased to 20MPa. The increase in temperature of vessel top when the extra gas is introduced is clear. This is probably due to convection.

6.6.2. Solutions to heater problems.

This initial phase of testing produced the following conclusions:

- Heating elements should be upgraded to produce a higher power output and thus reduce warm-up time.

- Insulation should be improved at the top of the vessel to protect the o-rings. Also, heating elements with longer cold zones should be used.

- Insulation around the coils should be improved to reduce the warm up time and to keep the pressure vessel walls cooler.

- A two zone heating system should be implemented to control the heat input to the top and bottom parts of the sample directly. In this way, the effects of convection in the vessel could be combated. Reduction of the gas volume in the vessel would also reduce this effect.

- The Hastelloy C22 heater support was unnecessary, and in fact acted detrimentally to the heating system because it conducted heat upwards towards the top of the vessel. A support, if used at all, should be outside the insulation and therefore insulated from the heating elements.

6.6.3. First modification to heater system.

Two new heating elements were purchased with longer cold-zones and a completely new control system installed to monitor two channels separately and supply power to two different zones of the heater. An upper insulation block made from ceramic and drilled with holes for feed-throughs replaced the firebrick, and alumina blanket replaced the insulating paper. The metal heater support was abandoned and the furnace held together with heatproof tape around the insulating blanket. However, lacking any mechanical support, it was difficult to ensure the alumina blanket was the same size and shape as the vessel bore and rebuilding the apparatus became a difficult and time consuming task.

New transformers were used in the system so that the coils could each be run at 100V giving a total power output of nearly 4kW. Power for the two-zone heater had to come from a three-phase supply owing to the added demands on current that made standard mains supply inadequate. Additional safety features such as quick-blow fuses and circuit breakers therefore became necessary and were installed as appropriate. A protection monitor and relays were installed to turn off the heating system if the vessel top temperature rose above an operator set threshold. One channel of the control system is shown in fig. 5.8 of the apparatus chapter. The 'sample hi' and 'sample lo' monitoring thermocouples were also used as control thermocouples for the upper and lower zone heaters.

Testing of this new system, shown in fig. 6.18, proved unsuccessful. The initial test-run resulted in one coil failing catastrophically (and violently) due to breakdown of the electrical insulation. The cause of this problem was thought to be that the control (doubling as the sample monitoring thermocouples 'sample hi' and 'sample lo') thermocouples were situated too far from the coils, and could therefore not respond quickly enough to the temperature of the coils.

The controller temperature was only set to 200°C but the actual coils must have reached their maximum operating temperature (1000°C) allowing the insulation in one coil to break down. This problem was probably exacerbated by the tightness of the

coils, which were so close together that mutual heating would have been a powerful effect.

6.6.4 Further developments to heater system.

In order to return the apparatus to working order, the two-zone system was replaced by new coils and the design was modified. A copper sheath and metal supports were included in order to provide strength to the furnace and to facilitate the addition of new elements in the future. The lower support is specifically designed with a 'flared' hole, wider at the bottom than at the top. This guides the sample into the coils and prevents 'snagging' which could deform the coils. In addition the control thermocouples were added separately, and the "sample lo" and "sample hi" thermocouples became dedicated logging sensors. This meant that the coils would never get above the temperatures set at the controller, and the system was thus much safer. In addition the coils were subsequently run at less than 75% power.

The final apparatus, as shown in fig. 5.7, is the result of much development work, but was still not able to hold the apparatus at the required temperatures without thermal gradients when high pressure gas was used as confining medium. Under ambient conditions, the apparatus held the top and bottom zones at 600°C with less than 1°C deviation but the use of high pressure gas gave thermal gradients of up to 200°C.

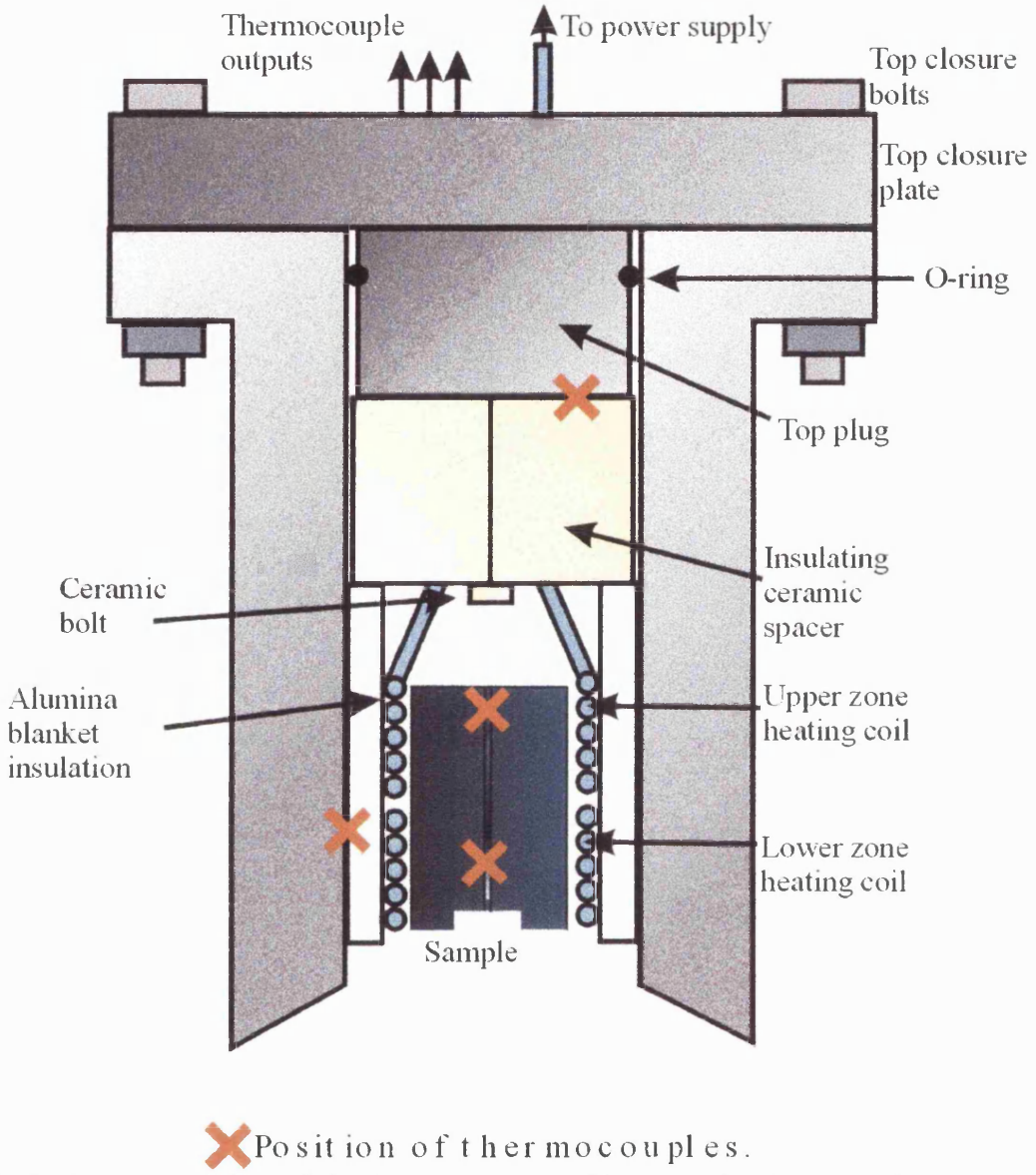

Fig. 6.18. Second revision of the heater system with better insulation and two zone heating.

6.6.5. Modifications to experimental program.

Some early tests utilised a "pre heat" method whereby the samples were heated outside the apparatus and transferred to the cell using tongs and heatproof gloves. This reduced thermal gradients slightly and allowed some measurements to be made using only one coil after the aforementioned coil failure, but it was abandoned as being potentially dangerous.

The realisation that thermal gradients could not be overcome in the timescale of the project meant that a simpler program of tests had to be devised. The test program therefore monitored the variation in fracture toughness with temperature at ambient

pressure and with pressure at ambient temperature. This still allowed investigation into the effects of these variables but meant that a direct measurement at Venusian surface conditions was not made. Further modifications to the apparatus could improve the situation dramatically and make measurements of the effects of changing both variables simultaneously possible.

6.7. Logging system.

After an early change of hardware to upgrade the data-logging card in the computer, the logging system described in chapter five changed little over the course of the project. The initial design used a National Instruments LabPC+ logging card running on a laptop PC. The lack of a cold junction compensator in the card meant that thermocouple inputs would have to be pre-processed prior to entering the logging card. To this end, a three-channel amplifier with cold-junction compensator was constructed. Unfortunately, the output could never be stabilised and the design was abandoned. In addition, the screen resolution and computing power of the laptop were insufficient and the total sampling rate of the logging card was too low to monitor as many channels as were intended for the final design. The solution to all these minor problems was to upgrade the entire hardware system. The new system included an SCB-68 shielded connector block (with in-built cold-junction compensation) and a National Instruments AT-MIO-16XESO logging card, and a 233 MHz PC with 4Mb video-card and high resolution screen. The logging card operated at a total sample rate of 500ksamples/second. The advantage of a computer with excellent screen resolution is that programming in the graphical language, G, used in LabView becomes easier as one can fit the whole 'program' on the screen at once, significant savings in time whenever the logging program had to be modified.

Minor changes were implemented in the logging programs Bridge-logger (BL) and Setup-logger (SL) throughout the project. The major advantage of 'G' is that small parts of the whole VI can be saved as sub-VIs and recreated as needed. The main changes to BL and SL were to add new channels and to incorporate the calibration data (see chapter seven) although BL was also modified to allow the control of the sample rate and buffer size for the logging program in order to conserve disc-space or increase sample rate. This became necessary when it was observed that the changes in the output occurred too rapidly for the original BL program, leading to poor plots of the data.

6.8. Actuator design and seals.

The original actuator had a single acting step seal which was unsuitable for a double acting environment. Because the original apparatus used water as both confining medium and the actuator medium, this went unnoticed and, as long as the pressure was higher in the actuator, the system would still function as required. However, it was soon discovered that if gas was used as the confining medium substantial amounts of gas bled into the actuator piston and even into the intensifier cylinder. This meant that the actuator fluid was very compressible and made control of the level II tests virtually impossible as the apparatus became unacceptably compliant.

Several methods to rectify this problem were tried. The first attempt, a redesigned actuator and piston with double acting seals, was a failure because the friction at the seals was too high. The piston would not move when the pressure in the actuator was raised and, when it eventually did move, the motion was predominantly stick-slip and sample failure occurred prematurely owing to unavoidable overloading.

A second attempt using back-to-back step seals on a longer piston proved more successful, but gas pumping into the gap between the two seals meant some bleeding of gas still occurred. The solution was to make the gap as large as possible and to match the actuator pressure to the confining pressure. This minimised the gas bleed and meant that several tests could be made before the apparatus had to be emptied of actuator fluid, re-primed and the gas bled out to ensure that compliance was minimised.

The modifications to the method can only be a stopgap solution. Further research into better seals that have the following features is necessary:

- Low friction and zero slip/stick behaviour.
- Small size, yet ability to separate gases and liquids.
- Ability to operate up to 50MPa pressure on both sides.

Until a manufacturer of such seals can be found, the apparatus will not be able to perform at optimum level.

6.9. Conclusions.

What started as an uncalibrated, uncommissioned piece of equipment designed specifically for one task is now a useful tool for investigating rock physics under a wide

variety of planetary conditions. This required modification of almost all major aspects of the apparatus in some way.

The work described in this chapter continued over a period of about two years. Although the experimental program had to be re-evaluated and compromises made, the final experimental apparatus and techniques allowed the satisfactory measurement of level II tests at pressures to 20MPa or temperatures up to 600°C. Both gas and liquid confining fluids were also used. In short, the design process was successful, although there are some improvements that can still be made. These are discussed further in chapter 11.

Chapter 7

Experimental techniques used in the measurement of fracture toughness and supplementary data.

7.1. Introduction.

In chapters five and six, the experimental apparatus is described and its evolution summarised. In this chapter the methods and techniques employed whilst using and calibrating the apparatus are described. All aspects of experimental methods are discussed, from calibrating the sensors used in the apparatus to processing the data from the tests. Also detailed are the various supplementary methods used to characterise the rock samples.

7.2. Calibration of sensors.

As described in chapter four, various types of sensor are used in the apparatus, the outputs of which must all be calibrated. The data collection uses a computer with a logging card and so some of the data outputs are *only* displayed on the computer screen and have no physical display on the apparatus. This means that calibration must be accurate and regularly repeatable, as there are few opportunities to validate the data using external gauges. In the final version of the apparatus, only the confining pressure and the control thermocouples have external verification.

7.2.1. Pressure sensors.

The Druck pressure transducers used to measure the confining pressure and actuator pressure were calibrated using a hydraulic dead weight testing machine. The machine is a Budenburg 370 oil operated tester and works on the principle of hydraulic pressure balancing the gravitational force of accurately machined loading weights. The sensor being tested fits into the machine so that it feels the full hydraulic pressure. The weights are incrementally loaded on a piston and the pressure in the piston is adjusted so that the weights are just 'floating'. At this point the output from the transducer is recorded. Care must be taken to ensure that the 'float' point is the same in each case. At least three successive series of measurements were taken for each transducer to

minimise random spurious results. The Budenberg machine itself is independently calibrated to better than 0.05% of the calibration pressure.

The results shown in figures 7.1 and 7.2 are post-amplification. The output of the transducers are on a millivolt scale and so are difficult to measure accurately. The amplifier used for the confining pressure transducer was the RDP Eurocard-based signal conditioning unit, whilst the actuator pressure transducer used the servo-technique servo-controller amplifier.

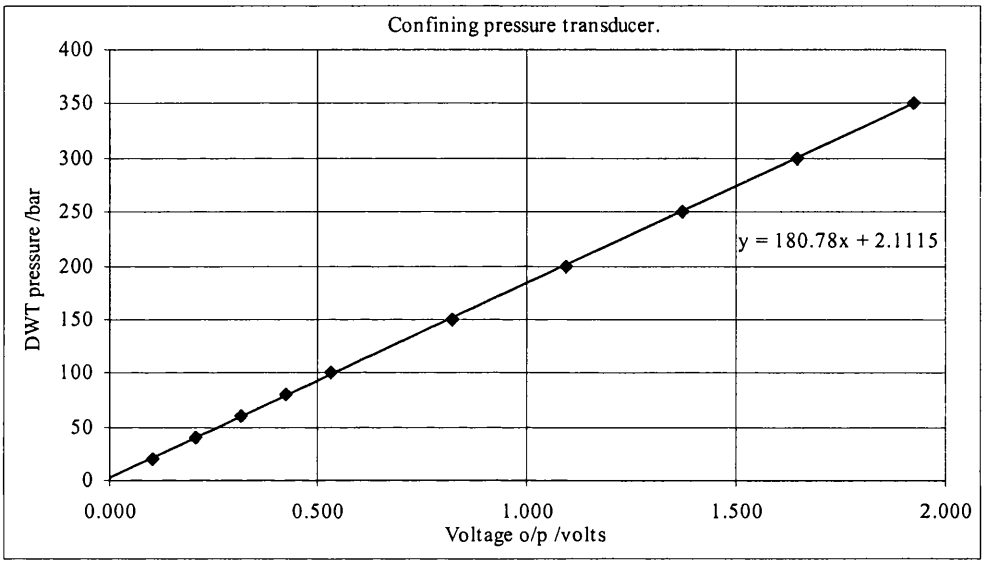

Fig. 7.1. Confining pressure transducer calibration results.

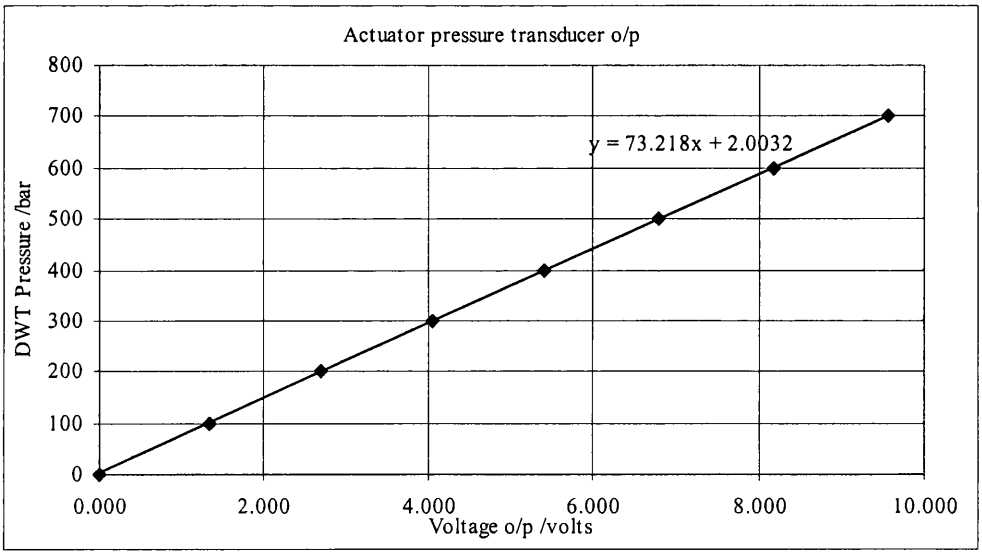

Fig. 7.2 Displacement pressure transducer calibration results.

The result of these two calibrations is a pair of equations linking the voltage output from the transducers to the actual pressure experienced by them. These equations are used by the BL LabView logging VI to display the pressure parameters. Note that

measurement error (from manufacturers data on pressure and standard deviation on voltage o/p) is too small too be visible at this scale.

Confining pressure transducer.

$$\text{Pressure /bar} = 180.78 \times (\text{voltage o/p}) + 2.1115 \qquad (7.1)$$

Actuator pressure transducer.

$$\text{Pressure /bar} = 73.218 \times (\text{voltage o/p}) + 2.0032 \qquad (7.2)$$

The accuracy of these calibrations was confirmed by several repetitions of the calibration procedure through the (approximately) 18-month period of the experimental program. In no case did the results differ by more than 1%. The confining pressure was also measured using a pressure gauge and in all cases this reading agreed with the displayed pressure to within 2%. The actuator pressure was not displayed using the pressure gauge because every effort was made to minimise the volume of actuator fluid in the system to ensure maximum dynamic control.

7.2.2. Inductive Displacement Transducer (IDT).

The method of measuring the displacement used in this apparatus is intrinsically difficult to calibrate. The output of the PYC 106C transducer is non-linear with displacement and varies according to temperature, target size and material and environment.

The initial method of calibration used was to affix two independently calibrated LVDTs to the top of the actuator housing and attempt to match the output of the IDT as the jaws were opened. The LVDTs were held in a jig so that the two transducers sat either side of the jaws, and the outputs were averaged to minimise the effects of twisting.

The results of this calibration were essentially non-repeatable and varied greatly even between successive series of opening and closing of the jaws. The actual LVDT calibration was repeated many times and was found to be repeatable to less than 1%. The discrepancies were therefore due to the IDT or non-reproducible seating position of the jaws. The first attempt to improve the repeatability was to change the shape of the platen into which the lower jaws seat as described in chapter six. This did not greatly

improve the situation and the IDT was therefore removed from the apparatus and calibrated on the bench-top. The target used with the IDT was enlarged and affixed to the (non-rotating) barrel of a micrometer head to move the target away from the IDT whilst monitoring the output. Again, repeatability was poor, leading to the inference that there was damage or a poor connection to the IDT. This was confirmed later confirmed.

Furthermore, the calibrations performed above could only be performed at room temperature. Collaboration with the manufacturers of the IDT (RDP Electronics) revealed that temperature change in the IDT would affect the output to the extent of approximately 0.002 volts per °C. As the IDT was expected to reach 100-200°C this would provide a significant shift in the output. (This is not, in itself, a problem because the method used to determine the Level II fracture toughness only uses ratios of displacement but further results such as Young's modulus can only be extracted if the displacement is known absolutely).

As it was clear that the target material and orientation would affect the results, a slightly larger target was manufactured and polished to produce a completely smooth surface. This was then marked with an orientation mark and sent to RDP electronics for factory calibration with a new PYC106C transducer. The calibration was performed at four different temperatures and 0.15mm spacing with a matched amplifier (S7AC). The settings of the amplifier were tied after calibration to prevent them being changed. The results of the factory calibrations are shown in fig. 7.3.

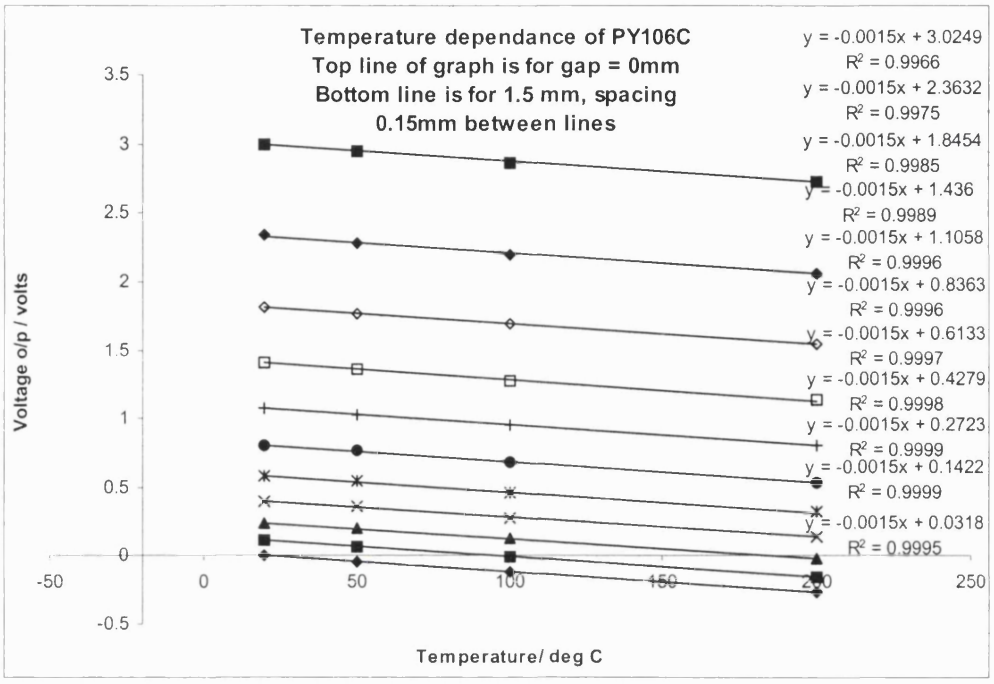

Fig. 7.3. Factory calibration of PYC transducer at various temperatures.

The factory calibration showed that the voltage variation with temperature was constant. Thus by applying a correction factor to the room temperature best fit equation, the displacement as a function of IDT output and temperature can be found.

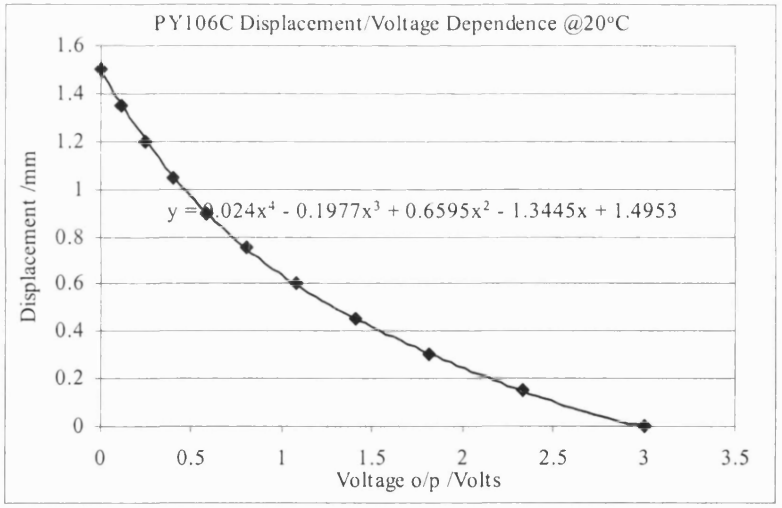

Fig. 7.4. Output from the PYC 106C transducer as a function of displacement.

To obtain the temperature normalised voltage one subtracts 0.0015T volts from the logged voltage, where T = (measured IDT temperature – 20 °C). Then the equation

$$D = 0.024V^4 - 0.1977\,V^3 + 0.6596V^2 - 1.3445V + 1.4953 \qquad (7.3)$$

can be applied where D is the displacement and V the temperature normalised voltage.

Although it is impossible to check the reproducibility of this factory calibration directly, deformation of an elastic aluminium sample proved to be the same over many cycles of loading and unloading.

7.2.3. Thermocouples.

The thermocouples used in this apparatus are all K-type and therefore have well known calibration coefficients. The BL and SL VI both make use of LabView's built-in K-type thermocouple calibration sub-VI which gives the same temperature reading (±1 °C) for all thermocouples as a digital thermometer using that same thermocouple. Thus for the calibration to be incorrect both the sub-VI using the calibration coefficients and the digital thermometer must be flawed and have an identical flaw. This is highly unlikely and thus the temperature readings based on the calibration sub-VI can be held to be reliable with a measurement error of ± 1°C. As the temperatures used in this project are generally of the form "Room-temperature", 150°C, 600°C etc this measurement error is generally small compared to the measured value and is generally ignored in the data and discussion of results.

7.2.4. Force-transfer and CMOD scaling factors.

In order to convert pressure in the actuator to force at the jaws, and displacement at the IDT to CMOD, certain geometrical factors must be applied.

Figure 7.5 shows the dimensions of one half of the actuator housing relevant to these calculations. As the forces act near the line of the pivot at the bottom jaw the effective force at the jaw, F_E can be expressed as $0.504F_A$, where F_A is the applied force at the actuator piston and 0.504 is the ratio of the vertical distances of the acting forces. The ratio of CMOD to displacement at the IDT cannot be assumed to be a simple ratio because the angle the face of the IDT makes to the pivot is too large to assume that $\sin\theta \approx \theta$. In this case a slightly more complicated geometrical approach yields CMOD = 1.83D where D is the measured displacement at the IDT.

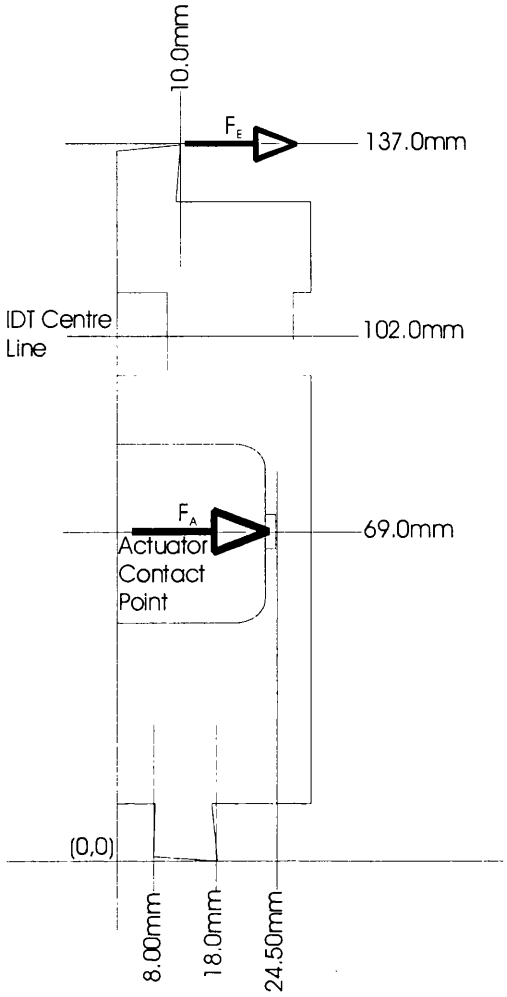

Fig. 7.5. One half of the Actuator Housing showing important dimensions for force and displacement normalisation calculations.

In order to convert the pressure in the actuator into force at the actuator contact point, the area of the piston face must be multiplied by the pressure on the piston. The total area the pressure acts upon is a circle of radius 7.5mm giving a force at the actuator of 17.67P N where P is the actuator pressure in bar. This results in a force at the jaws of 8.90P N. These constants are used when calculating the forces needed to split the samples.

7.3. Sample preparation and treatment.

All the samples used in this study were extracted in large blocks They therefore had to be cored and shaped prior to being used in the tests.

7.3.1. Icelandic basalt samples.

The majority of the samples used in this experimental program are nominally 60mm diameter short-rod fracture-toughness samples of Icelandic basalt (see fig. 7.6). For details of the geological setting of the source and the composition and properties of the samples see chapter eight

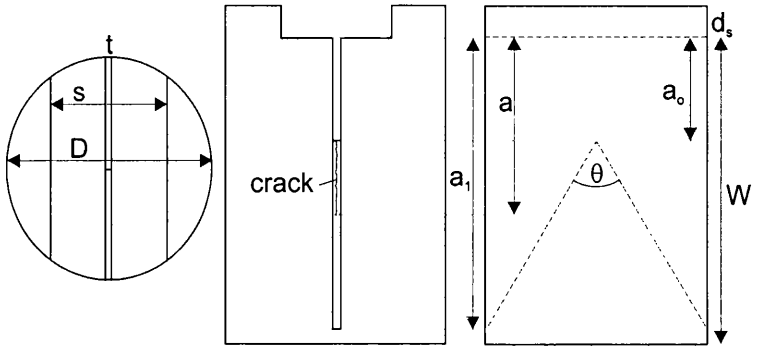

D = Diameter of specimen (59.6mm typically)
w = length of specimen, 1.45.D = 86.4mm
a_0 = tip of chevron position, 0.48.D = 28.6mm
a = crack length
a_1 = chevron flank depth = W (for W=1.45.D)
θ = chevron angle, 54.6°
t = slit width = 2mm
s = slot thickness = 25mm
d_s = slot depth. 7mm<d_s<2mm

Fig. 7.6. Sample dimensions as constrained by ISRM (1988). The use of a 60mm core drill gives cores with a typical diameter of 59.6mm, from which all the other dimensions are derived.

The source material consists of sections of a jointed lava flow which are typically hexagonal in shape with a diameter of approximately 400-500mm and a thickness of 200-400mm. These blocks are normally flat on one side and often need only one saw cut perpendicular to the jointing axis to give a stable base for coring.

7.3.1a. Coring and initial grinding of the samples.

The cores are made using a modified vertical pillar drill with diamond-bond coring bits. The drill is cooled and lubricated with water, which is delivered through the top of the coring bit and constantly flushes sediment from the cutting face. Care was taken to apply a constant pressure to the drill to ensure that the cores were constant in diameter with a smooth surface. Where possible a long (250mm) core-drill was used to maximise the length of the cores. Each sample must be 100mm in length prior to the next step in the preparation and so two samples can be taken from each core.

Alternatively, if a fracture exists in the horizontal plane of the block, this technique maximises the chance of being able to extract one sample.

The next step in preparation is to cut the cores into lengths between 90 and 98mm using a high-speed diamond rock-saw. These cores are then shortened to between 89 and 95mm using a surface-grinding machine. Whilst grinding, the cores are held in a jig attached to a magnetic base which has been clocked-up to ensure the sides of the cores are vertical. This means that, after grinding, the sample ends are perpendicular to the sides. Each sample is then given a code, which is marked upon one end and on one side with a permanent paint-pen. The next stage is to measure a number of key physical properties (see chapter eight) before thermally cracking the samples in an oven.

7.3.1b. Heat Treatment and final grinding.

Thermal cracking is performed to remove the effect of thermal cracking from the experiments. If the samples were not thermally cracked then it would be impossible to distinguish changes in toughness due to temperature from those caused by thermal cracking during heating. The thermal cracking is done prior to notching and slitting to ensure that any cracks formed are not constrained or initiated by the slit or notch.

The thermal cracking method is straightforward. The samples are placed in a thermally controlled oven at room temperature. The ramp rate of the oven is set at 2°C per minute for both heating and cooling whilst the hold temperature is set to be 600°C for 2 hours. Thus the samples are allowed to heat and cool at the same rate, the whole process taking approximately 12 hours.

After heat treatment, the samples are notched to an exact depth using a linear, vertical, diamond-grinding wheel. This step departs slightly from the standard ISRM (1988) method, which suggests the use of end plates affixed to the sample. The use of a notch means that the sample itself forms the face on which the jaws load. For hard rocks this gives more accurate seating and is more efficient with regard to sample preparation than the standard ISRM methods. Again, the samples are held in a jig to ensure the cut is exactly perpendicular to the sides of the sample. Each notch was cut such that the distance w was 86.4mm ±1mm, the notch depth itself being unimportant provided that it is greater than 2mm and less than 7mm.

7.3.1c. Chevron ligament cutting.

The slit that makes up the chevron ligament is cut with a 2mm diamond wheel on the same linear grinding machine that is used to make the notch. The sample is held in a specially made jig (see fig. 7.7) which is clocked up against the grinding wheel to ensure the slit is perpendicular to the sides of the sample. The slit is made in two sections taking many small cuts prior to turning the sample over to cut the other side of the ligament.

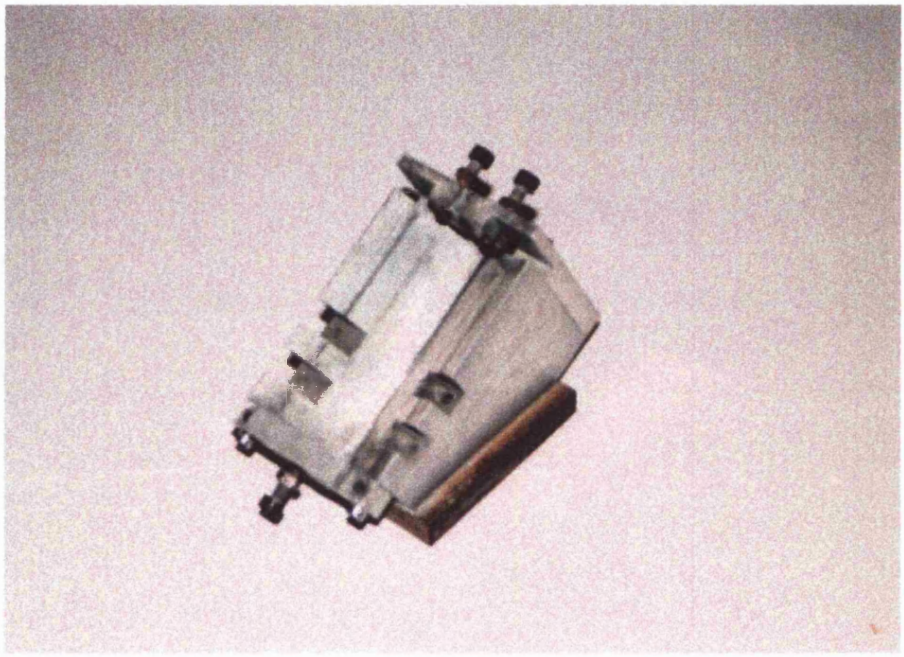

Fig. 7.7. The aluminium jig used to ensure that a correctly angled slot is cut in each sample.

At each stage of the cutting process the jig is held in place using a magnetic base and positioned so that many samples can be produced without having to readjust the jig. This 'batch' method is the most efficient means of production and the use of vernier callipers to measure samples ensures that they fall within specified tolerances at each stage of production. Nevertheless, each sample took an average of 2 hours to make and the production of the 60 or so samples used formed a significant portion of the total experimental time.

7.3.2. Tanzanian natrocarbonatite.

Natrocarbonatite was intended as a secondary part of the experimental program, a fact that complicated the sample preparation procedure significantly. Only 40kg (in two blocks) of material were collected owing to the remote location of the source (see

chapter eight), and therefore smaller, 38mm diameter cores were used to maximise the number of samples. Unfortunately the blocks of material collected contained pre-existing fractures that made even the use of even small cores impossible. This was discovered after coring had been done on the blocks and no usable cores were extracted. The following is a description of the method used prior to this discovery.

An important consideration that complicated the method was the fact that natrocarbonatite reacts with water. The blocks of natrocarbonatite were extracted from a fresh lava flow that was still at approximately 100°C. They were immediately packed in plastic with silica gel desiccant and stored in an oven (again with desiccant) when they were returned to the laboratory. The rock was therefore assumed to be in its original state with little modification due to atmospheric water. All stages of the sample preparation procedure, however, require water as coolant and lubricant. This would soak the samples in water and no amount of rapid drying could remove the water before substantial modification had occurred.

The solution to this problem was to use kerosene as the lubricating/cooling fluid. Kerosene typically contains 5-10% water, however, and so it had to be dried using anhydrous calcium sulphate. 500g of desiccant were used per 25 litres of kerosene.

The initial stage of sample preparation was to cut a flat face on both blocks using a large, diamond cutting wheel. The water in the reservoir was replaced with kerosene. Care was taken to ensure that there was good ventilation in the working area to prevent dangerous build-up of fumes. Kerosene fumes are not harmful, but can lead to dizziness and nausea if allowed to become highly concentrated. Gas and particulate filter breathing masks were used as a further precaution.

Having cut a flat face in the blocks, the smaller block was immersed in a bath of kerosene and cored using a 1½" (38mm) core drill. This method however, proved to be unsatisfactory owing to build up of material at the cutting face. It also meant that no cores were extracted from the smaller block

Having only one block of material meant that the extraction of every possible core became vital. Detailed drawings of the block ensured the coring angles least likely to intersect fractures could be identified. Unfortunately, even these precautions were insufficient to obtain any homogeneous samples. All the cores contained macroscopic flaws that made fracture toughness testing impossible. Further work using this material could involve re-melting the fragments and casting them into suitably sized cores but in the timescale of this PhD this could not be attempted.

7.4. Pre-testing measurements made on the samples.

In order to characterise the samples, certain other measurements were made. These included P-wave velocity measurements before and after heat treatment, some S-wave velocity measurements, density measurements before and after heat treatment, and bulk composition (both elemental and mineralogical). The methods used for these measurements are described below.

7.4.1. Density and P and S wave velocity measurements.

The P and S-wave velocity measurements made use of the same apparatus, only the transducers themselves being changed for the two types of wave.

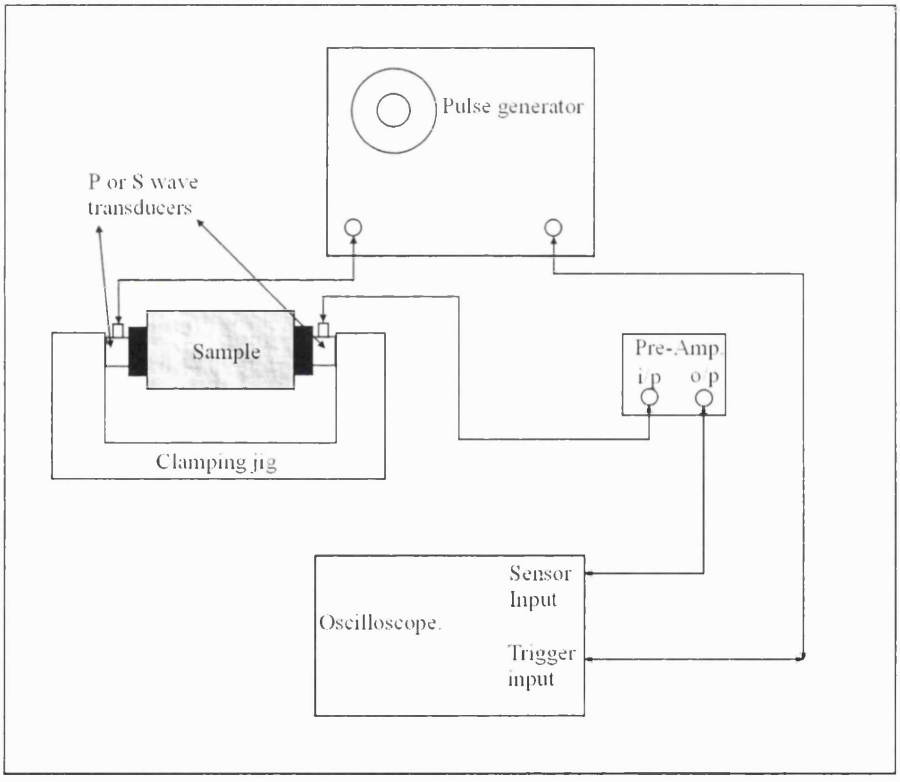

Fig. 7.8. Wave velocity measurement apparatus.

The measurements of the P-wave velocities were made before and after heat treatment for nearly all the samples. Density before and after heat treatment was also recorded by measuring the mass (using a Sartorius electronic top-pan balance) and the volume (using accurate measurements of length and diameter) of the samples. The samples were dried for 48 hours at 60-70°C prior to any of these measurements.

S-wave velocity measurements were made after heat treatment and K_c testing on half of the split core for only 1 sample each for any given test condition. Several S-wave velocity measurements were also made on dry, non-treated material.

7.4.2. Bulk mineralogical and chemical composition.

For comparative purposes, the bulk composition of the Icelandic basalt samples was determined using a variety of experimental techniques. X-ray fluorescence spectroscopy was used to measure elemental composition by compressing 0.5g of powdered material into a pellet which was scanned by the spectrometer. By using a large beam size with respect to the mineral size a mean elemental composition could be built up. The measurement was repeated 10 times over the surface of the pellet and the mean elemental abundance calculated. This gave a precise measurement of the abundance of each element and enabled an estimate of the error on the reading to be made.

X-ray diffraction was used to measure the bulk mineralogy of the basalt. By scanning a thin section of the sample, several distinct minerals could be identified and their chemistry investigated in detail. Superimposing a map of the different minerals onto an image of the specimen and estimating the surface area occupied by each type of mineral allowed a measurement of the bulk mineralogical composition to be made. Several different samples were measured in this way to give an error estimate. The results are presented in chapter eight.

7.5. Fracture toughness testing methodology.

7.5.1. Sample pre-treatment.

The samples were stored at room temperature in a dry laboratory but still had to be dried thoroughly prior to testing. The same drying method was used for every sample to ensure experimental consistency. Each sample was placed in an oven at 60-70°C several days before testing. The drying time allowed was 60-70 hours per sample, the tolerance being necessary to fit in with a sensible working day. When the samples were removed from the oven they were transferred to an airtight box containing silica gel to cool (if the required sample temperature was lower than oven temperature) or transferred to the pre-heating oven or directly to the apparatus if they were to be tested at high temperatures. The samples were considered 'spoiled' if not used within several

hours of drying and were returned to storage to be re-dried for another test. Note that the drying was not rigorous. However, the strain rate was so high in the experiments that a small amount of water, of the order of tenths of a percent by mass, would not affect the results. Dynamic fracture dominated over stress corrosion.

7.5.2. Experimental method.

The experimental procedure was split up into several processes. Firstly, the cell was pressurised (if appropriate) with the confining medium. Secondly, if required, the sample had to be heated to the appropriate temperature. Next, the sample was loaded/unloaded as many times as appropriate for the level II test. Finally, the pressure was released and the apparatus allowed to cool safely. The sample was then removed, held together using tape and stored prior to observation under the SEM (see section 7.6). The apparatus was then cleaned using an airline to remove rock fragments, allowed to cool and reset for the next test.

7.5.2a. Intensifier priming.

Prior to any tests, the intensifier had to be primed. This involved filling the intensifier with the displacement fluid (water) and bleeding out the air in the system.

This was accomplished by pumping the fluid from the reservoir into the intensifier and using a series of valves to isolate it, whilst drawing more fluid into the hand pump. To complete the process, the piston was removed from the actuator and fluid flushed through the system until no air bubbles were seen to escape from the actuator. The apparatus was then re-assembled and the hand pump isolated.

7.5.2b. Confining pressure.

As described in chapter five, confining pressure was supplied by either the gas booster or the liquid pressure pumps. Both were powered by the laboratory airline operating at 100-150psi (7-10bar) and could be adjusted by their individual regulators. See fig. 5.5 for details of the confining pressure system.

The gas booster was operated by allowing the cell to reach bottle pressure (50-60bar in the case of CO_2) before the booster takes over. The rate of pressure increase is initially slow owing to the compressibility of the gas. Once the pressure had reached 70-80bar, however, the rate of pressure increase became faster allowing the whole cell to be charged to 300 bar in around 30 minutes. The cell had to be pressurised to around

10% higher than the operating pressure because the gas was heated slightly during pumping and so lost pressure as it cooled. The exact pressure could be set using the pressure relief valve. After the test the gas was vented to the atmosphere, again using the pressure relief valve. Care was taken to vent the gas slowly because the nearly adiabatic decompression of the gas caused a large temperature drop. Rapid venting can therefore lead to the formation of dry-ice which can cause a blockage in the plastic waste line.

The liquid pump was far simpler to operate because the medium is incompressible. Thus pumping time is much shorter (of the order of several minutes) whilst the pressure can be released quickly without fear of decompression temperature changes. The only modification to the methodology was the addition of a high-pressure tap at the top of the vessel, which was opened during discharge of the waste liquid. This allowed air to be expelled from the vessel as the liquid was pumped in and also allowed the liquid to be drained quickly when the pressure was released.

As the confining pressure was increased, the actuator pressure was also increased to prevent bleed through of the confining medium into the actuator. The actuator pressure was generally allowed to lag behind the confining pressure by around 0.5-1 bar.

7.5.2c. Heating of samples.

A large percentage of the experiments performed were at temperatures above ambient. The twin coil heater system provided adequate power to heat the samples to over 600°C and the power levels of the controllers were both set to about 60%. The heating process is simple: once the pressure vessel is in place, the two heaters are set to the required temperature and the controllers vary the power to keep the temperature of the control thermocouples within ± 1^0C of the set point. The auto-tuning function of the controllers removes overshoot problems and was performed only once, at the outset of the experimental program.

The heating system worked exceptionally well at ambient pressure. However, the problem of how to keep the sample at high temperatures whilst minimising thermal gradients is exacerbated by the addition of a high pressure confining medium. Convection of high-pressure gas is particularly efficient at removing heat from the lower part of the sample to the top of the vessel. Despite the use of a two-zone heater, thermal gradients up to 200°C still occurred over the specimen when using a gaseous

confining medium at pressure. In the end, it was decided that such large thermal gradients would invalidate the results and so the tests that required elevated temperatures were all carried out at ambient pressure. This allowed excellent control of thermal gradients, which were less than 10°C.

It should be noted that the tests carried out at 450°C were all performed early in the experimental program before the apparatus had been fully developed. Only one heating coil was used at this time and thermal gradients for early tests were significant even at ambient pressure. To combat this, the samples were first heated in an oven to approximately 500°C and then transferred to the apparatus using furnace tongs. The vessel was then lowered over the sample and the heater set to the appropriate level for the test. This use of this method reduced the thermal gradients to less than 30°C across the sample.

7.5.2d. Sample deformation method.

The application of force to the sample will lead to displacement of the load line. According to the ISRM (1988) the displacement rate at the load line must exceed the following limit:

$$\dot{CMOD} > \frac{0.017 K_{sr}}{E\sqrt{D}} \tag{7.4}$$

where K_{sr} is the expected level I fracture toughness, E is the approximate Young's modulus and D is the diameter of the sample. For typical values of $K_{sr} = 2.5 MPa.m^{1/2}$, E $\approx$ 50 GPa and D = 60mm, which means that the rate of change must be greater than 0.01mm/s. This is easily exceeded using the servo-controller, or even the hand-pump, to govern the pressure in the actuator piston.

The best way to obtain good data is to increase the force to about 5-10% of the expected failure force and cycle the load up and down a few times in this region before the actual test. This serves two purposes. Firstly, if there are flaws in the sample, this action will probably cause it to fail and the sample can then be replaced and the test begun again. If the load is increased too much and premature failure occurs, the sample can, in the worst case, shatter, causing damage to the apparatus. Secondly, and more importantly, this low-level loading allows the sample to bed-in so that when the load is increased further, a more linear initial compliance reading is obtained.

When the actual test is run, the BL VI must be restarted and the load increased until a small change in slope occurs. The load should then be instantaneously released

and the actuator force allowed to drop to around 30% of the reversal load. The load is again increased until, when a change in compliance is again observed, the reversal process is repeated. Initial studies showed that the basalt samples were very unlikely to fail before 1.0kN force. In general, 5 or 6 loading/unloading cycles were made before this point. When the compliance began to change quickly, i.e. near the maximum force, some skill was required on the part of the operator to reverse the load quickly. Initially, the criterion set for reversal of load after this maximum point was that the load should only be reversed if a decrease in force with an increase in CMOD was observed. Initial tests showed that this was rarely observed and often led to failure directly after the maximum load without further cycles. Thus the reversal criterion was slackened somewhat and the load was generally removed as soon as, or even slightly before, the force-CMOD curve began to flatten. This enabled further cycles to be made after the measurement point as required by the ISRM (1988) method. The apparatus was then depressurised (if necessary) and allowed to cool before being cleaned and prepared for the next run.

7.5.3. Data analysis.

The data extracted from these tests can be subjected to a variety of analytical methods. The simplest result that can be obtained is the level I fracture toughness, which requires only knowledge of the maximum load in the test, F_{max}. Level II testing requires more data analysis, but is a more accurate description of the material properties because it takes into account anelastic behaviour and non-recoverable strain in the sample as well as hysteresis in the apparatus. Also, the K-resistance curve for the sample can be generated using the method of Matsuki (1991), which gives some idea of the size dependence of the sample. If a flat K-resistance curve is generated the specimen size is taken to be sufficiently large to avoid affecting the measurement. A full description of the methods used can be found in ISRM (1988) and Matsuki (1991).

7.5.3a. Level I and II fracture toughness measurements.

The data were saved on hard disk as raw voltage data. The two critical parameters were the IDT voltage and the displacement pressure transducer output voltage. These data were converted to their respective physical properties using the calibration equations above. The results were then plotted on A3 paper for analysis. The method used to find K and K_c was that of ISRM (1988). Figure 7.9 shows the

construction lines used when making these measurements. For each cycle, an unloading line was constructed which starts at the point at which CMOD began to decrease, passed through the point at which the next reloading cycle has half the load of the previous unloading point, and extended to the x-axis. The hysteresis in the unloading cycle was then accounted for by dropping a line from the halfway point of the unloading line to the reloading curve. The unloading line was then moved down by half this distance (Fig. 7.9a) to form a corrected unloading line.

An unloading line of this kind could be constructed for each cycle. The two unloading lines with slopes that most closely spanned the value of half the initial slope were used to calculate p, the degree of non-linearity, which is given by X_u/X_l. The level I fracture toughness was then given by

$$K = {24.0F_{max}}/{D^{1.5}} \tag{7.5}$$

where F_{max} is the maximum force, D is the diameter of the sample and the level II fracture toughness was given by

$$K_c = \sqrt{\frac{(1+p)}{(1-p)}} K_{SR} \tag{7.6}$$

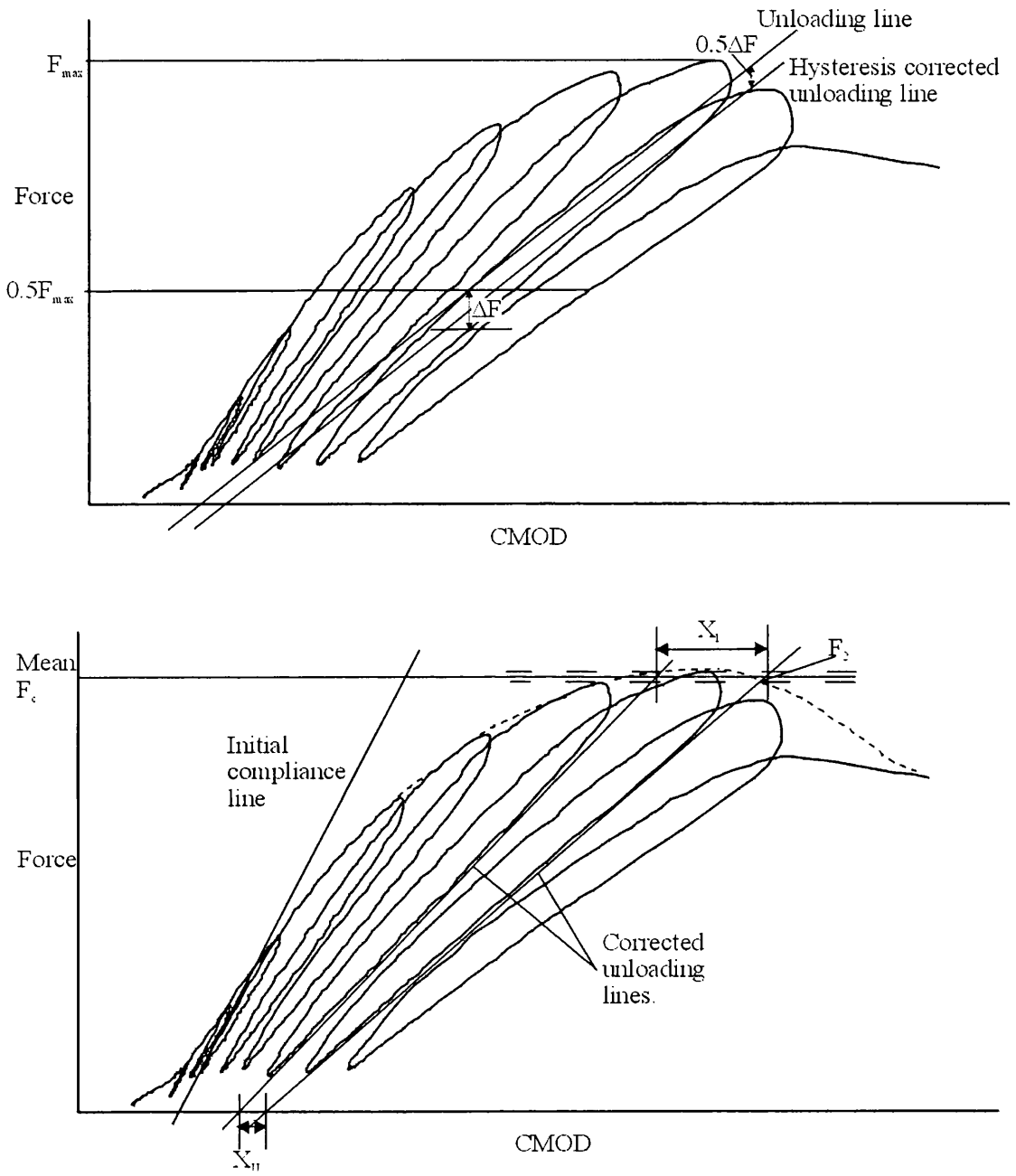

Fig. 7.9. Construction lines used when performing level II data analysis. In fig. a) (top) the construction of a corrected unloading line is shown. In fig. b) the degree of non-linearity can be calculated from a pair of unloading lines. The initial slope is S_I, ΔF is the amount of hysteresis, X_u and X_l are used to calculate the degree of non-linearity. F_{max} is the maximum force and F_c is the mean force between where two adjacent unloading lines meet the smoothed force/CMOD line (dotted).

If the unloading lines with slopes nearest to $0.5S_i$ did not span the maximum point, then a modification to the method had to be made. First, a line was constructed which started at the point at which the shallower unloading line crosses the smoothed track of the unloading cycles (F2 on fig. 7.9b) and ended at a point on the steeper

unloading line. The point on this line was such that the x-axis distance from this point to the base of the steeper line was the same as the distance from F_2 to the base of the shallower line. This distance was recorded as 'x_2'. Secondly, a point on this line with force equal to $0.5S_i.x_2$ was marked. A line was then constructed that met the x-axis a distance x_2 from this point. This line had a slope of $0.5S_i$ by definition. Finally, the point at which this line met the smoothed track of the unloading cycles was noted and the force at this point recorded as F_c. The level II fracture toughness was then given by

$$K_c = \sqrt{\frac{(1+p)}{(1-p)}}\frac{F_c}{F_{\max}}K_{SR} \tag{7.7}$$

These results are for perfect specimens that do not deviate from the standard measurements shown in fig. 6.6. For deviations in w, D and θ a linear correction factor C_k in K and K_c had to be introduced where

$$C_k = (1 - \frac{0.6\Delta w}{D} + \frac{1.4\Delta a_o}{D} - 0.01\Delta\theta) \tag{7.8}$$

and Δw, Δa_o and $\Delta\theta$ are the deviations from the standard measurements for each individual sample. This factor, when due care is taken in preparing the samples, was generally between 0.99 and 1.01 and could therefore be ignored.

7.5.3b. K-resistance curve or 'Matsuki' method.

The K-resistance curve is the equivalent to the variation of corrected fracture toughness with crack extension (Matsuki *et al.*, 1991). By considering all the unloading cycles in a level II data set, the average degree of non linearity, p, for a given cycle can be found by constructing the unloading lines for itself and the two adjacent cycles. The mean value of p for a cycle is then found from these adjacent cycles. The load at the unloading point of the i'th cycle is then F_I and the fracture toughness for cycle i is given by

$$K_c = \sqrt{\frac{(1+p)}{(1-p)}}Y_i'F_i \Big/ D^{1.5} \tag{7.9}$$

where Y_i' is the non-dimensional stress intensity factor for cycle I given by

$$Y' = 0.5\left[\frac{dg}{d\alpha}\Big/\left\{(\alpha-\alpha_0)\tan\frac{\theta}{2}\right\}\right]^{0.5} \tag{7.10}$$

Where α = a/D and g is the compliance based solely on the geometry of the sample and is of the form $g = g_i.f(\alpha)$. From the work of Shannon *et al.* (1982) the shape of the compliance curve is given by

$$f(\alpha) = 4.08 - 19.26\alpha + 41.98\alpha^2 - 39.15\alpha^3 + 15.52\alpha^4 \qquad (7.10)$$

The data allow the ratio of g_i/g to be calculated from the printouts. The value of α can then be extracted by solving (7.10) or by approximation methods. The value of Y' can therefore be extracted using knowledge of g, g_i and differentiating (7.10).

The resulting values of K_c will then be dependent on α and therefore a, the crack extension. The results of this method are plotted as a graph of K_c against a and will generally flatten of to a plateau value for K_c as a increases.

7.6. Post testing measurements.

The final measurement made on the samples was observation of the fractured surfaces using a scanning electron microscope. SEM observations were made to investigate whether the cracks are intra or inter-granular and to look for signs of non-brittle behaviour.

After testing, the two halves of the sample were taped together and stored away from dust and humidity. On completion of the experimental measurements, one half of one sample representing a each set of conditions was taken and the point of the fracture cut out of the half-cores using a diamond cutting wheel to produce small cubes of material with one face being the point of the fracture. After drying at 60-70°C for 48 hours these cubes were mounted on metal stubs using epoxy resin with the fractured face upwards and cleaned using an airbrush. The cubes were then coated with a gold layer using an ionising sputter coating machine prior and examined with a Zeiss 940 digital scanning electron microscope. When making the observations, care was taken to ensure that no pores were imaged and that the area in the image was typical of the fracture surface. Two images were taken for each sample at 2000 and 5000X magnification. The results are shown in chapter nine.

7.7. Conclusion

The methods and techniques described in this chapter were modified over the course of the project. The development of both apparatus and techniques are discussed in chapter six. The apparatus was new and untested, and therefore the calibration and

testing of the apparatus took more time than was expected. The development of the techniques continued throughout the project and led to the methods described in this chapter.

The increased development time of the apparatus and techniques led to a decrease in the number of experimental measurements that could be made. Future projects using this apparatus will have the advantage of calibrated, working apparatus and well-defined procedures for testing. The methodology allows efficient processing of samples and, with a good supply of specimens, many measurements can be made each day unless very high temperature tests are required.

Chapter 8

Terrestrial analogues for rocks forming the Venusian plains.

8.1. Introduction.

Chapter two described the Venusian plains and the conclusion of the chapter was that the primary experimental candidate rock should be fine grained, low porosity basalt which had been subjected to little weathering. A secondary sample type, natrocarbonatite was selected on the basis of the morphology of the canali and possible surface-atmosphere interactions. In this chapter I describe the sample collection fieldtrips made during this project and present the results of measurements made to characterise the samples and to show their suitability as Venusian analogues. Field logs for the Iceland and Tanzanian work can be found in Appendix II.

8.2. Sample collection for experiments.

The localities chosen as sources for the end-member rock types were Oldoinyo Lengai in Tanzania and southern Italy for carbonatites and Iceland for basalt. The carbonatites of southern Italy are calciocarbonatites (high proportion of calcium carbonate) whereas the carbonatites of Tanzania are natrocarbonatite (potassium and sodium carbonate rich). The natrocarbonatite from Lengai is freshly emplaced and this is the only place in the world with active carbonate volcanism. The calciocarbonatites from Italy are much older.

8.2.1. Mt. Vulture, Southern Italy.

The trip to Vulture in the spring of 1998 was exploratory work to assess the suitability of the rock types found in the region. Figures 8.1 and 8.2 show the location and geography of the region. The volcanic activity at Vulture terminated at ~0.13Ma (Rosatelli *et al.*, 2000) and the latest stages comprise melilite-carbonatite tuff deposits.

Although Venusian material unlikely to be pyroclastic, it was hoped that the Vulture rocks would be sufficiently fine grained and welded to give a strong, heterogeneous rock that might be a suitable analogue. Several large blocks of material were found that were initially thought suitable but the extreme weathering of all the

samples meant that the rocks were friable and extremely weak. For these reasons, these rocks were deemed unsuitable for laboratory testing.

Fig. 8.1. Map of Italy showing location of Mt Vulture (red cross).

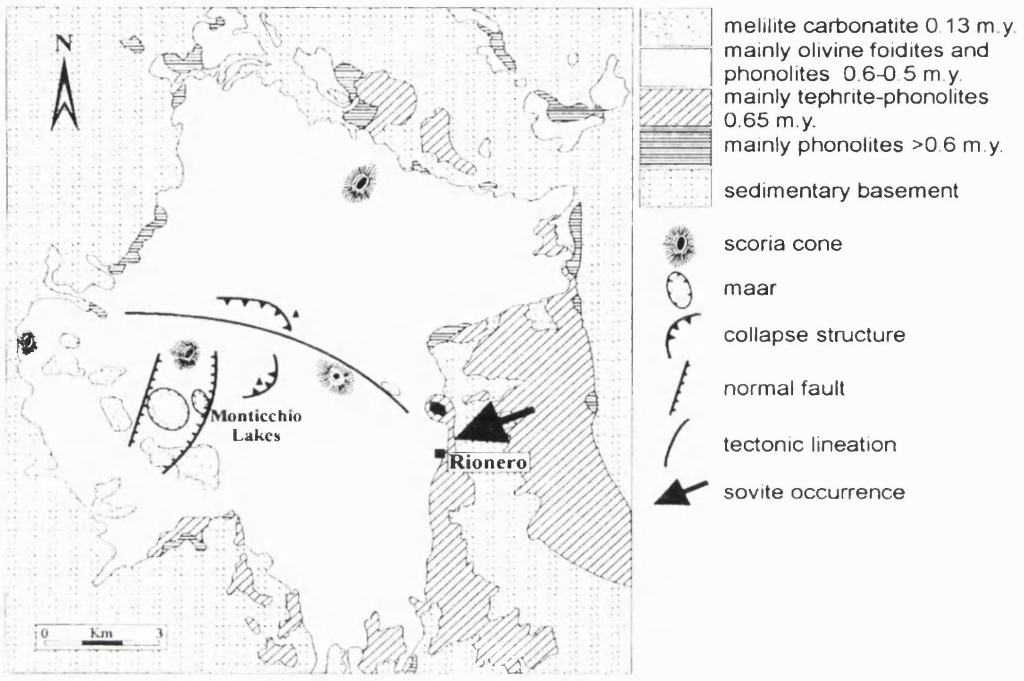

Fig. 8.2. Sketch map of Vulture showing crater lakes and Monticchio carbonate tuff formation (after Rosatelli *et al.*, 2000). Noted with an arrow is the only known example of Italian intrusive calcite-carbonatite.

8.2.2. Oldoinyo Lengai, Tanzania.

8.2.2a. Oldoinyo Lengai: introduction.

Natrocarbonatite lava is low in viscosity and has been observed to form channels, tubes, braided features and other flow patterns similar to those observed (albeit at scale a scale three or more orders of magnitude larger) as canali on Venus. Natrocarbonatite lava reacts quickly with water, and weathering from pristine solid rock to much softer, hydrous minerals can take a few hours (in wet weather) to several weeks. In order to use natrocarbonatite lava as a Venusian analogue, pristine material would have to be collected because there would be no hydrous alteration on Venus.

Lengai is one of several large volcanoes found on the floor of the East African rift valley and is situated some 65km south of the Tanzania-Kenya border. Run off from its exceptionally symmetrical cone-shaped flanks drains into Lake Natron, a highly alkali body of water with an area of some 800km^2. The location and a sketch of the surrounding area is shown in figure 8.3.

The volcano has been quietly active since the last large plinian eruption in 1966-1967, with only sporadic eruptions of lava onto the crater floor and the occasional minor eruption of ashes and lava. Since the late 1960s, the crater has been slowly filling up

with lava erupted from hornitos and vents on the crater floor. In 1997, the lava began to locally over spill the crater rim forming flows that continued down the flanks. At the time of fieldwork, Spring 1999, the volcano had just begun to overflow the crater and there were sporadic eruptions onto the crater floor.

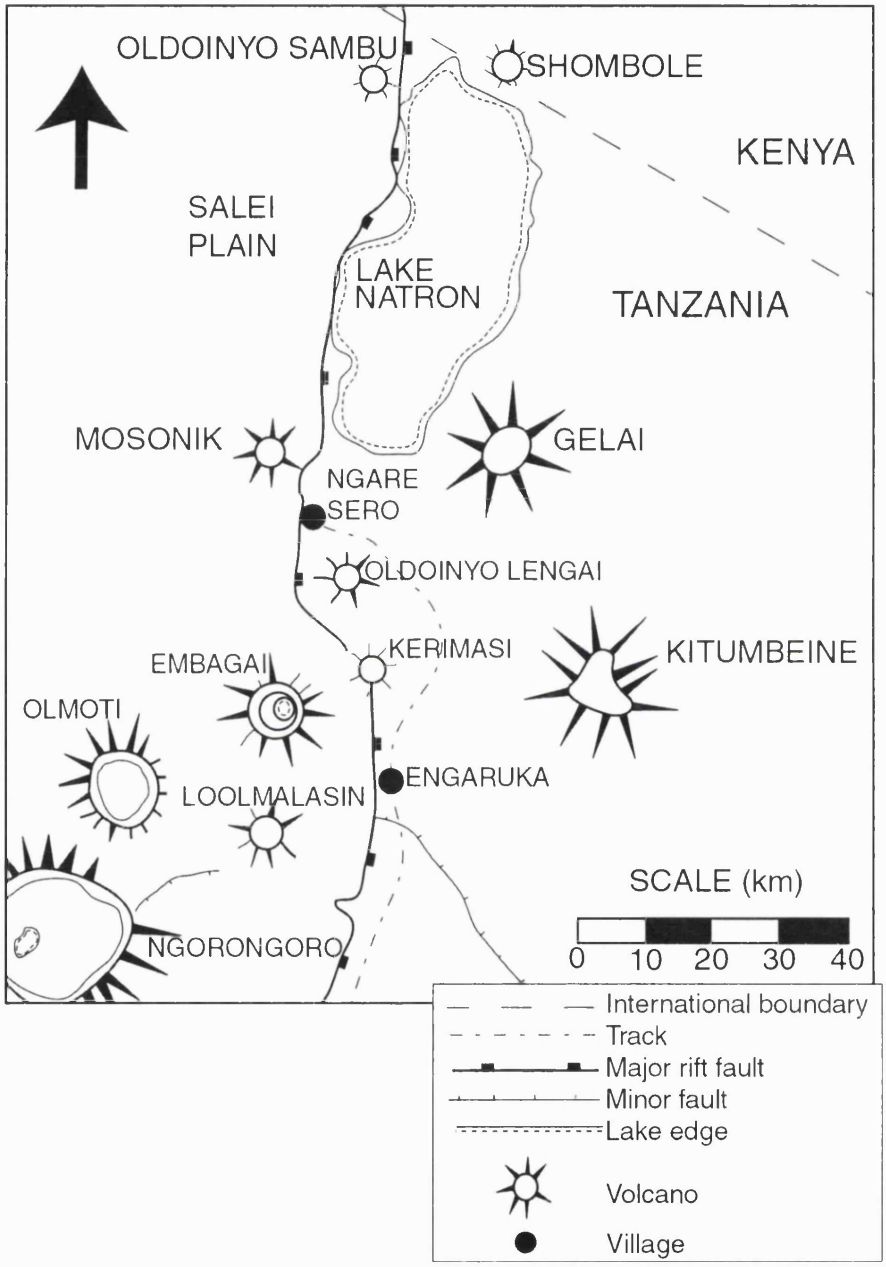

Fig. 8.3. Sketch map of area surrounding Oldoinyo Lengai. Base camp for the fieldwork was at Ngare Sero (after Church, 1995).

8.2.2b. Oldoinyo Lengai: sample collection field work 1999.

The sample collection fieldtrip was carried out as part of a larger trip to the East Africa rift valley in the spring of 1999. Three researchers took part and preliminary results of the work carried out can be found in Genge *et al.* (2000). The sample collection carried out in Tanzania was prepared in the knowledge of the recent activity at Lengai and it was hoped that a fresh flow could be sampled and several tens of kilograms of material returned for physical testing.

The fieldwork lasted just over 10 days, three of which were spent travelling between Nairobi and the base camp at Ngare Sero. The ascent of the Volcano took nearly 6 hours owing to its extremely steep flanks. Two days and one night were spent at the summit of the volcano and extra days were allowed in the schedule to give the best chance of sampling a recent flow.

On reaching the summit a recent flow was discovered and its surface temperatures found to be 100-150°C. This flow started at a dome-shaped hornito around 15m in diameter and 6-8 metres high and was characterised by braided channelised/lava tube morphology. The flow extended for around 120m and terminated in a pond of lava with a fractured and ropy surface. The flow thickness was about 10-30cm and the width of the flow varied from 2 to 5m. Morphological features of interest included numerous over-bank spills and break-outs and clearly defined levees. Downstream, the textures became more disturbed and ropy flow lines could be seen on the surface of the lava, indicating that a crust had formed, which was deformed by the moving lava underneath.

Two blocks of material were obtained from this flow. They were cut out of a filled channel about 10m from the start of the flow. In order to extract the blocks a Partner K700 rock saw was used. This saw is air-cooled and portable and was therefore ideal for this fieldwork. Vertical cuts were made in the flow followed by diagonal cuts into the sides of the channel. The blocks were then prised out with a large hammer, left to cool for several hours and then wrapped up in sturdy plastic with silica gel desiccant.

Two of us stayed overnight at the summit to map the crater the next day. Unfortunately the mist was too thick to make this possible. The fieldwork allowed us to collect nearly 45kgs of material in two large blocks. This material was returned to London and kept in a dry oven at 85°C to prevent water degradation of the sample.

Fig. 8.4. Inside the crater of Oldoinyo Lengai. The infilled lava tube and sample extracted from it are shown.

Fig. 8.5. Source of lava flow from which sample was extracted. Note how lava older than a few weeks appears brown, fresh lava appears dark grey and fresh lava modified by meteoric water appears snowy-white.

8.2.3. Seljadalur, Iceland.

The majority of the tests in this study were intended to be on basalt. A large stock of Icelandic basalt, collected in 1995, was held in the Department of Geological Sciences at UCL at the start of the project and this was replenished in the autumn of 1999 with another sample collection trip to the same source.

Iceland is a volcanic island that sits at the top of the Mid-Atlantic ridge above a stationary hotspot. Thus the volcanism on Iceland is fed by diapiric activity as well as by rift-associated melts. The rift volcanoes produce a range of rock types from tholeiites, through mid-ocean ridge basalt (MORB) to rhyolites and dacites.

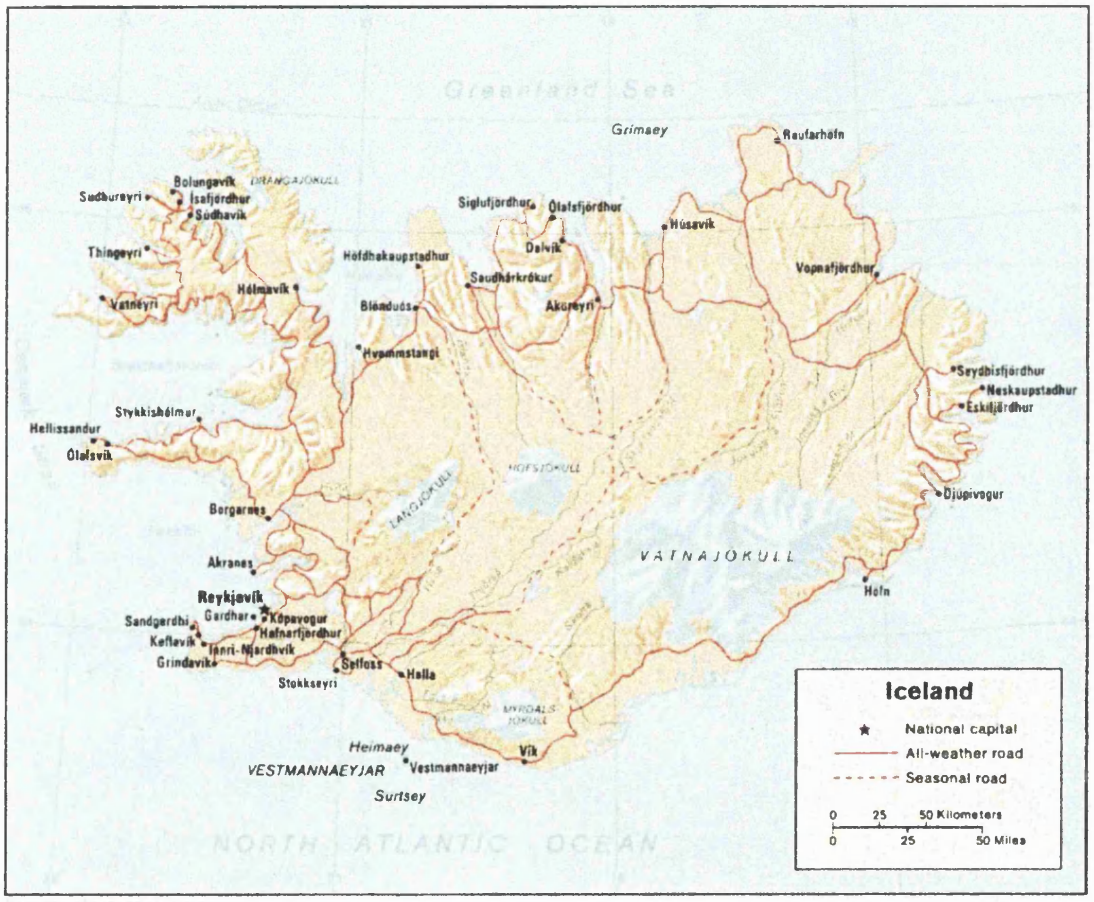

Fig. 8.5. Sketch map of Iceland. Seljadalur is in the south-west of the island about 25km east of Reykjavik.

Fig. 8.6. Columnar basalt at Seljadalur quarry. The columns in this photograph are about 30cm in diameter.

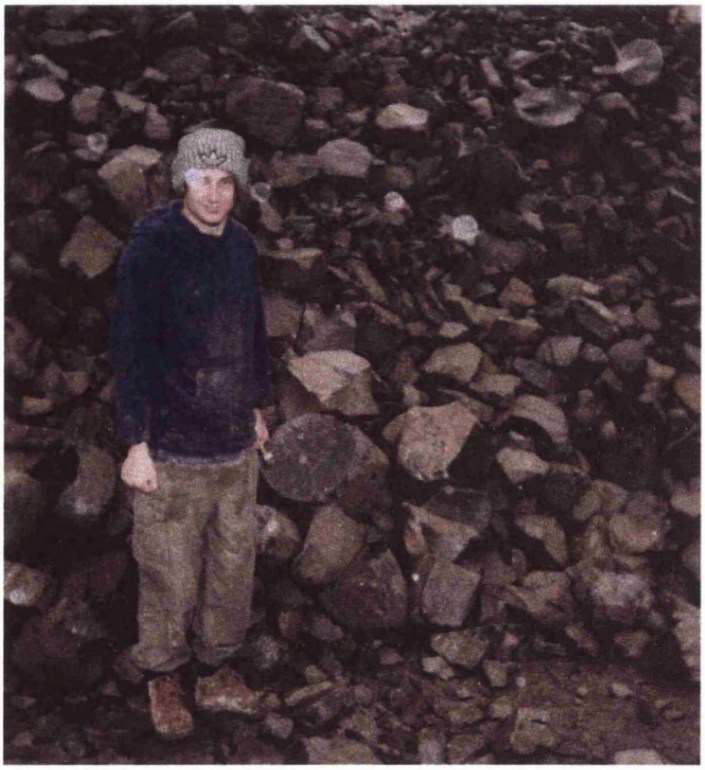

Fig. 8.7. Columnar rubble. Fallen blocks form rubble at the base of the columns and are ideal sample material for tests.

The rocks used in this study were from an area called Seljadalur, a large quarry 20-30 km East of Reykjavik. The location of this quarry is shown in figure 8.5. The local area is made up of large fields of columnar lava flows which have been identified as relatively young (<0.7Ma, Saemundsson and Einarsson, 1980) and unweathered. The

columns are exposed where the quarry workings, which provide material for road building, form small cliffs about 5-10m high (fig. 8.6). The columns tend to fall from the cliffs, forming a rubble of polygonal blocks around 30-50cm in width and 20-30cm in height (fig. 8.7).

Sample collection in August 1999 was facilitated by access to a 4WD vehicle belonging to a team of geologists from UCL working in Iceland as I was able to collect over 650kgs of samples in 21 large blocks. The rock was first checked to ensure it was a similar grain size and coloration to the 1995 material. The material was extracted from the same flow as that of the 1995 expedition so that there was no discernible change between the two types of sample. The blocks were chosen to minimise fracturing within the blocks was minimised and so that the depth of each block was greater than 25cm to allow two samples to be extracted from each core.

The rocks from this flow are ideal candidates for Venus analogue material because they are very fine grained, have low vesicularity. As they show no anisotropy and, as shown below, posses similar composition to those measured at the sites of the Russian Venus probes, they are thus ideal laboratory specimens.

8.3. Suitability of collected laboratory analogue material: results from characterisation measurements.

The mineralogy and elemental composition of the basalt samples were measured using an electron probe as described in section 7.4.2. The method used to determine the mineralogy also provides a simple method of estimating porosity and grain size and showed that the samples were of low porosity, high density and very small grain size.

8.3.1. Mineralogy and grain size.

The mineralogy of the samples is quite simple and is restricted to only four main minerals: plagioclase feldspar, clinopyroxene, olivine and magnetite. There was no change in mineralogy after heat treatment, although some samples showed a very slight change in density. The percentage volume proportions are shown in table 8.1.

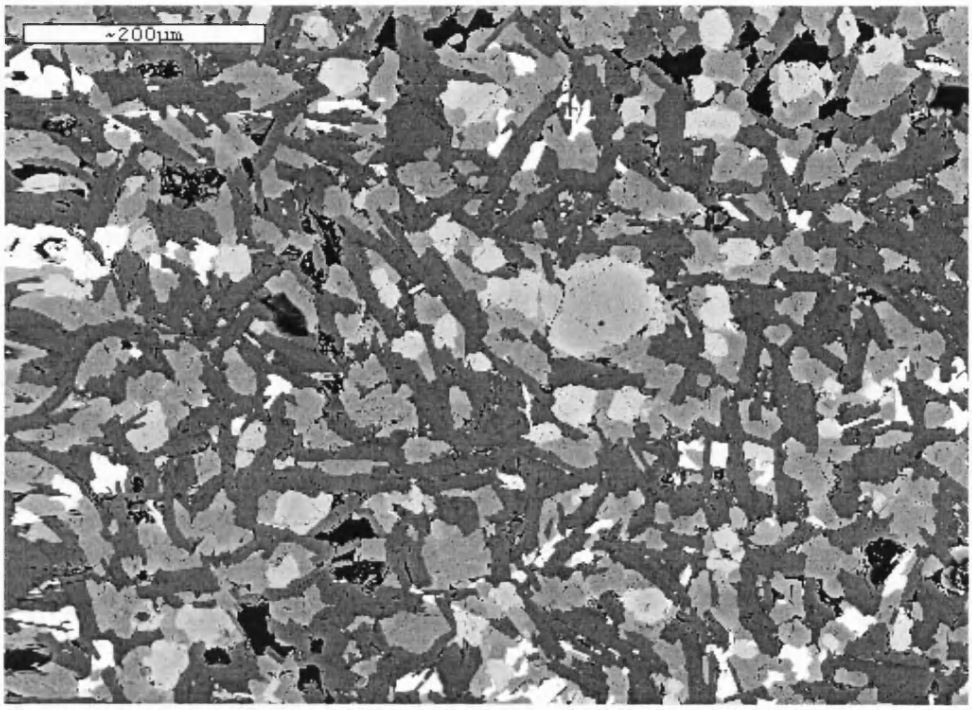

Fig. 8.1. Example of an electron backscatter image of a sample of Iceland basalt. Darkest grey represents feldspar, mid-grey represents pyroxene, zoned mid to light grey represents olivine and white is magnetite. Black areas are voids.

Mineral	% volume.
Magnetite	3-4
Olivine	6-8
Clinopyroxene	26-30
Plagioclase feldspar	59-61
Voids (porosity)	0-2

Table 7.1. Mineralogy of Icelandic basalt. The percentage volume column gives the range of measured values for five samples.

The individual minerals have fairly typical elemental compositions, except there is a relatively high iron content which implies that the entire suite must have crystallised from a fairly iron rich melt. The olivine, in particular, is high in iron oxide, especially near the margins of the grains. Also readily apparent is the fact that the samples are essentially very fine grained, most of the grains being <100μm in diameter.

8.3.2. Elemental abundance.

The elemental composition of the rocks was measured with the electron probe apparatus by using a large sampling beam and integrating the results over 10 different

areas of the slide to give elemental abundance. The results are shown in tables 8.2 and 8.3.

Oxide	1	2	3	4	5	6	7	8	9	10	Mean	StDev.
SiO_2	46.76	46.24	46.10	47.54	45.98	45.67	46.59	46.77	46.21	48.01	46.59	0.72
TiO_2	2.15	2.35	2.31	1.95	2.11	2.54	2.30	2.58	2.43	2.38	2.31	0.20
Al_2O_3	17.15	15.96	17.38	15.90	16.38	16.56	17.27	17.31	17.11	17.27	16.83	0.58
FeO	13.13	13.36	13.91	13.26	14.58	14.25	13.37	13.21	13.39	11.77	13.42	0.76
Na_2O	2.65	2.48	2.67	2.65	2.76	2.59	2.75	2.68	2.69	2.69	2.66	0.08
MnO	0.31	0.24	-0.09	0.17	0.25	0.17	0.39	0.24	0.24	0.26	0.22	0.13
MgO	3.90	4.57	3.84	4.83	4.99	4.21	4.04	3.93	3.92	4.45	4.27	0.42
CaO	13.61	14.51	13.70	13.42	12.65	13.58	12.99	12.93	13.85	12.89	13.41	0.56
K_2O	0.33	0.26	0.29	0.19	0.25	0.26	0.31	0.29	0.18	0.23	0.26	0.05
Total	100.0	100.0	100.1	99.9	100.0	99.8	100.0	99.9	100.0	99.9	100.0	

Table 8.2. Elemental abundance of Icelandic basalt used in rock mechanics tests.

Oxide	Venera 13	Venera 14	Vega2	Iceland basalt mean
SiO_2	45.1 ± 3.0	48.7 ± 3.6	45.6 ± 3.2	46.59 ± 0.72
TiO_2	1.59 ± 0.45	1.27 ± 0.41	0.2 ± 0.1	2.31 ± 0.20
Al_2O_3	15.8 ± 3.0	17.9 ± 2.6	16.0 ± 1.8	16.83 ± 0.58
FeO	9.3 ± 2.2	8.8 ± 1.8	7.74 ± 1.1	13.42 ± 0.76
Na_2O	-	-	-	2.66 ± 0.08
MnO	0.2 ± 0.1	0.16 ± 0.08	0.14 ± 0.12	0.22 ± 0.13
MgO	11.4 ± 6.2	8.1 ± 3.3	11.5 ± 3.7	4.27 ± 0.42
CaO	7.1 ± 0.96	10.3 ± 1.2	7.5 ± 0.7	13.41 ± 0.56
K_2O	4.0 ± 0.63	0.2 ± 0.07	0.1 ± 0.08	0.26 ± 0.05

Table 8.3. Compiled results from Venusian lander XRF data compared to laboratory samples used in tests.

The results indicate that, although the laboratory samples chosen are higher in iron content than the rocks sampled by the Russian probes, the general mineralogy and appearance is similar to that we might expect on Venus. The silicate abundance is very similar to the laboratory analogue material. The grain size is very small and porosity low, as might be expected for Venusian rocks. No details are given here of the Tanzanian carbonatite because it was not used in any fracture toughness tests, as explained in sections 1.5 and 7.3.2.

8.3.3. Density.

Density measurements from the samples were made by simply measuring the mass and volume of the samples before and after heat treatment. All samples were dried at 90°C for at least 72 hours before these measurements were made.

Mean density before HT (>30 samples)	2.95 ± 0.02 gcm^{-3}
Mean density after HT (>30 samples)	2.93 ± 0.0 4gcm^{-3}

The results show that this basalt is very dense (owing to its low porosity and high iron content) and shows little variation between samples. The density slightly decreased with heat treatment as would be expected owing to the slight volume increase induced by additional thermal cracking.

8.4. Conclusions.

The sample collection fieldwork performed during this project was successful in returning suitable samples but the natrocarbonatite was found to be pervaded with fractures making it unusable in fracture mechanics tests. Further work with this material may be able to melt and recast the samples to form homogeneous test specimens, but this is outside the scope of the present project.

The Venus analogue material used in all the fracture toughness tests is basalt from Iceland. The material is an excellent Venus analogue and conforms to all the criteria set out for such test specimens. It also shows a similar composition to that measured by the Venera and Vega probes that landed on Venus.

Chapter 9

Experimental results.

9.1 Introduction.

The aim of the experimental work was to characterise the fracture toughness of basalt as a function of temperature, pressure and confining medium. The experiments were designed to ensure that the pressures and temperatures spanned those currently existing on the surface of Venus.

Chapters five, six and seven dealt exclusively with how the apparatus used in this study was designed, constructed, calibrated and put to use. Presented in this chapter are the data obtained from over 30 short-rod (SR) fracture toughness tests, together with a summary of these data corrected for non-linearity (level II). Throughout this chapter, the SR fracture toughness will be referred to as 'K' whilst the corrected SR fracture toughness will be designated as 'K_c'. The subscript SR is dropped from the usual nomenclature because all the tests described use the short-rod geometry.

9.2.1. Raw data obtained from fracture toughness measurements.

Table 9.1 shows a list of the samples used in this study from which data were included in the final results section. All the samples used from four blocks of basalt collected in 1999 are shown whereas only those samples collected in 1996 from which data are taken for this chapter are included.

The table clearly shows the difficulties involved in this sort of study. 40% of the 1999 samples failed prematurely, yielding no usable data, because of flaws in the sample (mb99_29) or apparatus failure (mb99_5). Also, some of the tests were run under less than ideal conditions. For example, some of the tests are marked "poor TG" indicating where failure of one heating element resulted in thermal gradients across the samples. Pristine data are unlikely to be collected in this kind of study because the apparatus is so new. This was the first study to use the equipment to measure level II fracture toughness, and level II fracture toughness measurements at temperature and pressure were found to be very difficult to perform. Further modifications to the design of the apparatus that would improve the quality of data are described in chapter 11.

I.D	Date	Block	Heat Treated?	dry time /hours	Pressure /Bar	Medium	Temp. °C	Comments
mb99 1	1999	1	yes	>72	100	CO2	AMB	Good test.
mb99 2	1999	1	yes	>72	100	CO2	AMB	Good test.
mb99 3	1999	1	yes	>72	100	CO2	150	Good test. (poor TG)
mb99 4	1999	1	yes	>72	42	CO2	AMB	Good test. (poor TO)
mb99 5	1999	1	yes	>72	100	CO2	450	Failed due to servo-controler failure
mb99 6	1999	1	yes	>72	100	CO2	AMB	Good test.
mb99 7	1999	1	yes	>72	1	AIR	150	Possibly ok, late TF
mb99 8	1999	1	yes	>72	200	AIR	AMB	Good test.
mb99 9	1999	2	yes	>72	1	AIR	300	Good test.
mb99 10	1999	2	yes	>72	1	AIR	300	Good test.
mb99 11	1999	2	yes	>72	50	CO2	AMB	Good test.
mb99 12	1999	2	yes	>72	150	CO2	AMB	TF,
mb99 13	1999	2	yes	>72	50	CO2	AMB	Good test.
mb99 14	1999	2	yes	>72	150	CO2	AMB	Good test.
mb99 15	1999	2	yes	>72	200	CO2	AMB	Good test.
mb99 16	1999	2	yes	>72	1	AIR	600	TF,
mb99 17	1999	2	yes	>72	1	AIR	600	Possibly ok. Late TF
mb99 18	1999	2	yes	>72	1	AIR	300	Good test.
mb99 19	1999	2	yes	>72	1	AIR	600	TF,
mb99 20	1999	3	yes	>72	1	AIR	600	Early double TF
mb99 21	1999	3	yes	>72	1	AIR	600	double TF
mb99 22	1999	3	yes	>72	100	WATER	AMB	Good test
mb99 23	1999	3	no	x	x	x	x	EXPLODED IN HEAT TREATMENT
mb99 24	1999	3	no	x	x	x	x	EXPLODED IN HEAT TREATMENT
mb99 25	1999	3	yes	>72	1	AIR	150	Good test (poor TO)
mb99 26	1999	3	yes	>72	100	CO2	AMB	TF,
mb99 27	1999	3	yes	>72	100	CO2	100	Good test (Irregular o/p)
mb99 28	1999	3	yes	>72	1	AIR	450	TF,
mb99 29	1999	3	yes	>72	1	AIR	150	TF, flawed sample
mb99 30	1999	3	yes	>72	1	AIR	300	TF
mb99 31	1999	4	yes	>72	1	AIR	600	Early TF
mb99 32	1999	4	yes	>72	200	CO2	AMB	Good test
mb99 33	1999	4	yes	>72	150	CO2	AMB	Good test
mb99 34	1999	4	yes	>72	100	WATER	AMB	Good test
mb99 35	1999	4	yes	>72	1	WATER	AMB	Good test
mb 22	1996	-	yes	>72	1	AIR	AMB	Good test
mb 23	1996	-	yes	>72	1	AIR	450	Good test (Very Poor TG)
mb 31	1996	-	yes	>72	1	AIR	AMB	Good test
mb 32	1996	-	yes	>72	1	AIR	450	Good test (Very Poor TG)
mb 33	1996	-	yes	>72	1	AIR	AMB	Good test
mb 34	1996	-	yes	>72	1	AIR	AMB	Good test
mb 36	1996	-	yes	>72	1	AIR	450	Good test (Very Poor TG)

Table 9.4. Sample identification and summary of experiments carried out in this study. Initial apparatus testing specimens were also used but are not included in this table. TF = transverse failure of specimen. TO = "turn over". E.g. Poor TO implies the specimen failed with little change in compliance. Poor/very poor TG = poor/very poor thermal gradients. "Poor" implies a difference between top and bottom sample of 50°C and "very poor" implies a difference up to 100°C. The total premature failure rate of the samples was about 40%.

In total, four successful experiments were performed at ambient conditions; three at each elevated temperature (150°, 300°, 450°, 600°) and ambient pressure and three at each elevated CO_2 pressure (50bar, 100bar 150bar, 200bar) but ambient temperature. The exceptions were that only two successful experiments were performed at 50bar, 150bar and 600°C owing to multiple sample failure. Three extra experiments were carried out using water as the confining medium: one at ambient pressure and two at 100 bar pressure. Two tests were completed at moderate temperatures (100-150°C) under 100 bar CO_2. Three tests using sandstone were also performed during the

development of the apparatus but these can only be considered valid as level I tests because they did not use the single piece actuator housing (see chapter six).

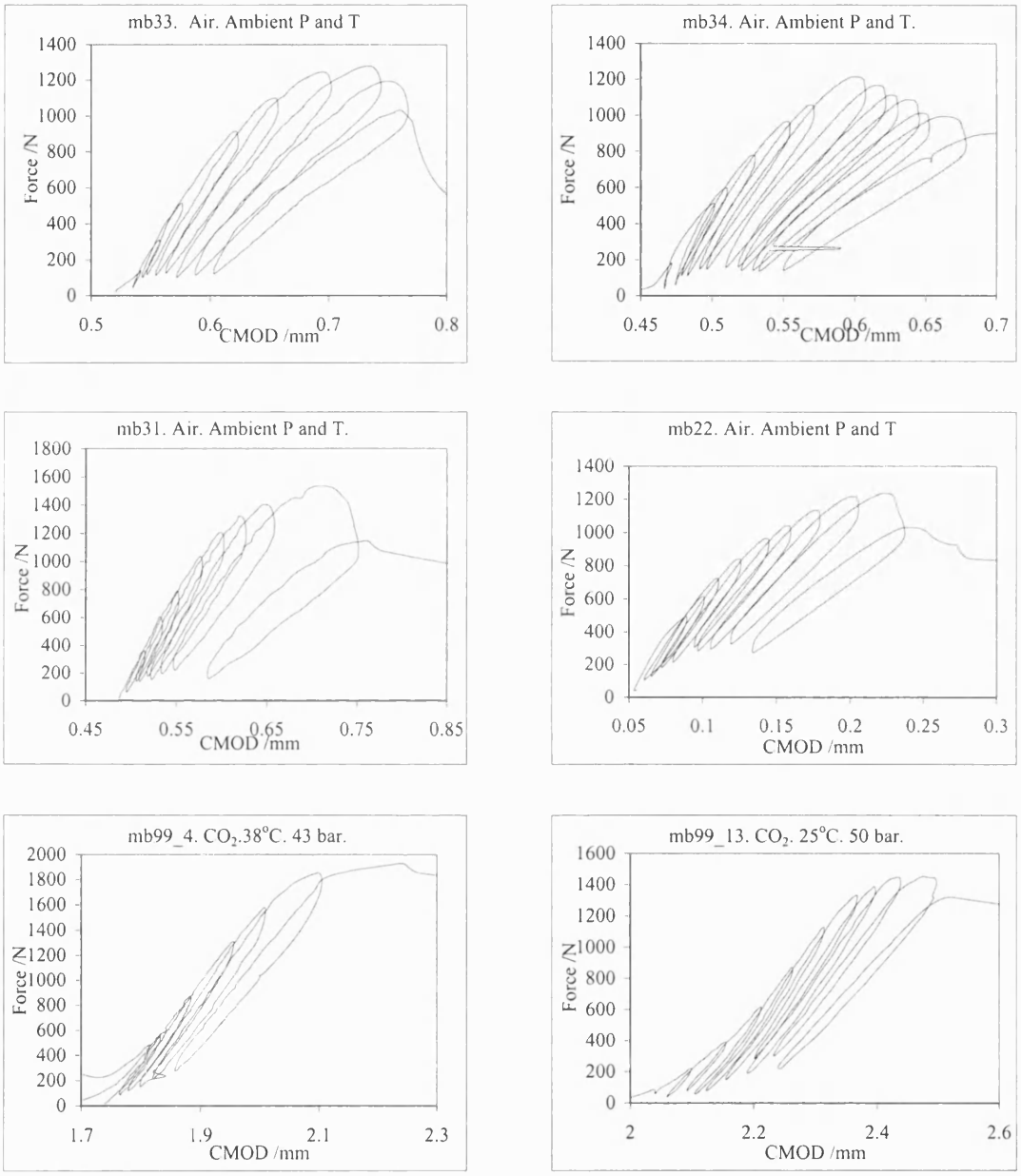

Fig. 9.1 Plots of crack mouth opening displacement (CMOD) against opening force for (approximately) constant ambient temperature (20-45°C) and varying pressure (1-50 bar) with CO_2 or air as confining medium.

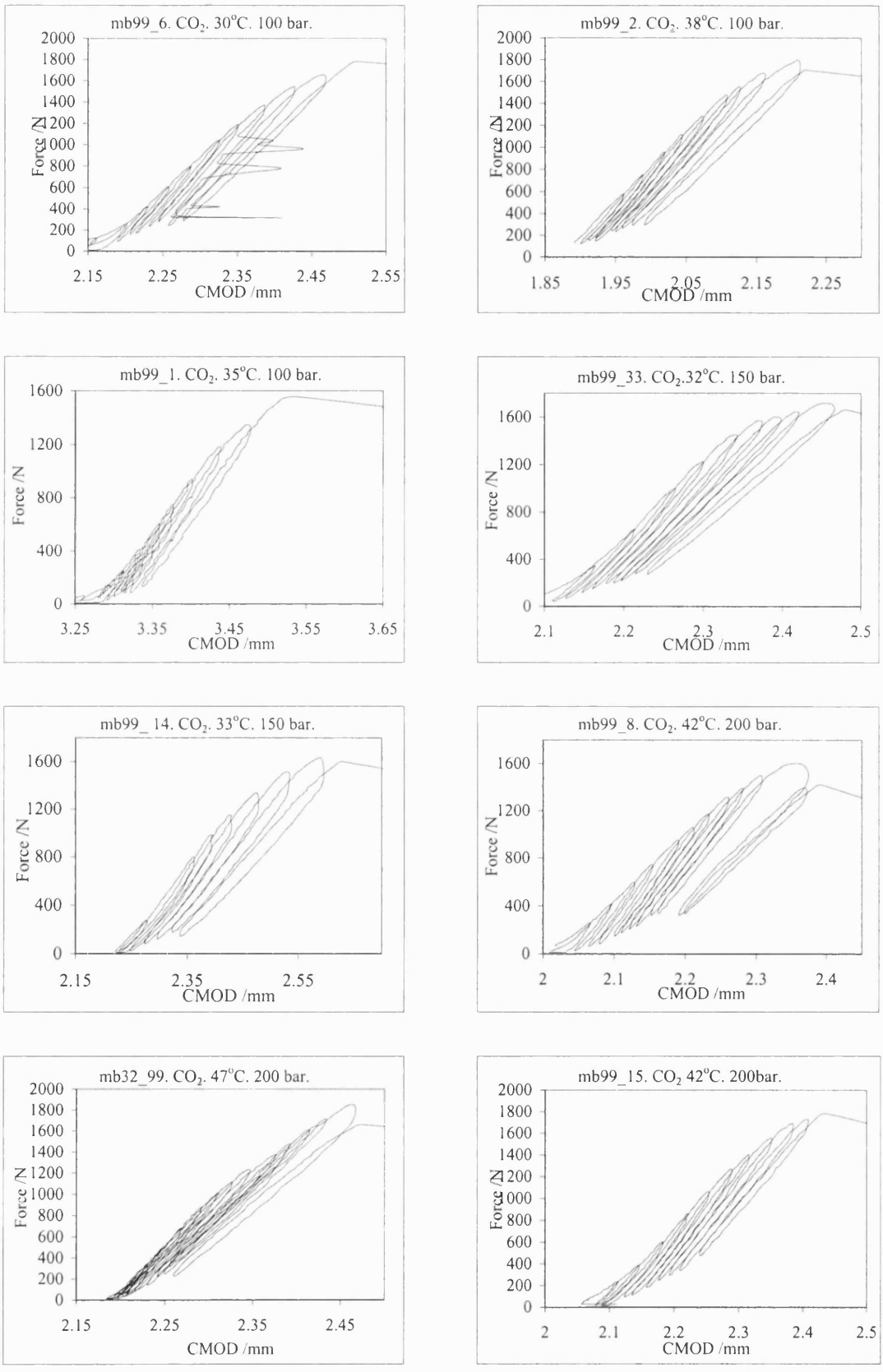

Fig. 9.2. Plots of CMOD against opening force at ambient temperature and varying pressure (100-200 bar) with CO_2 as confining medium. Note spikes in first plot caused (almost certainly) by faulty connection in the voltage amplifier.

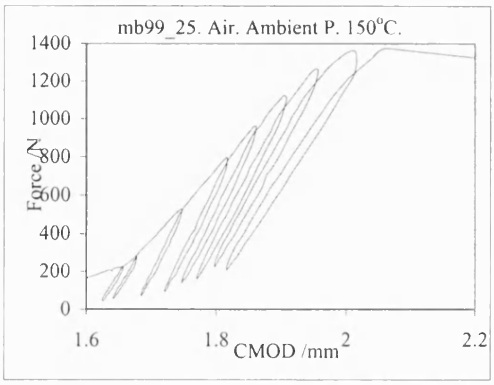

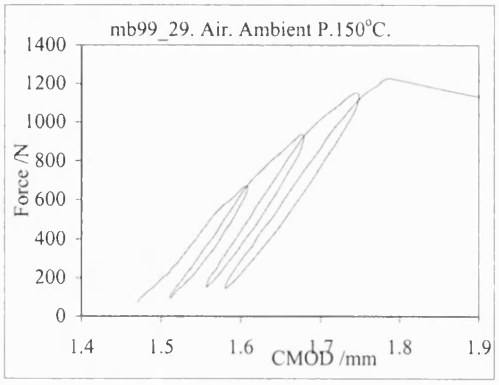

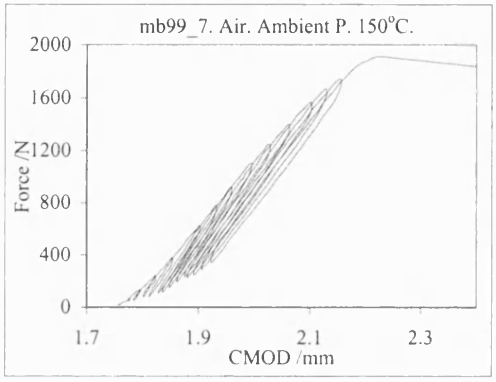

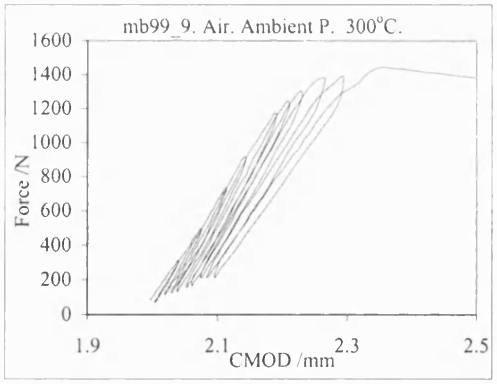

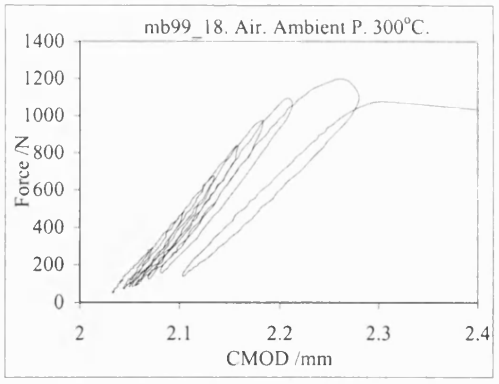

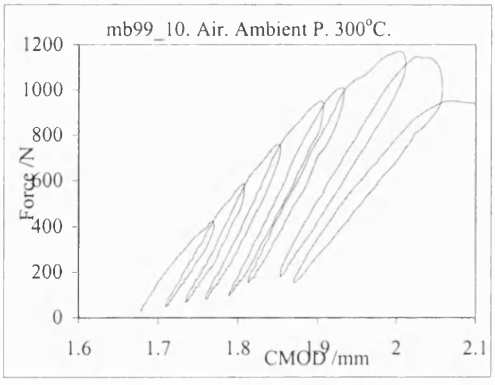

Fig. 9.3. Plots of CMOD against opening force at ambient pressure and varying temperatures (150-300°C) with air as confining medium. Note peculiar shape of first plot

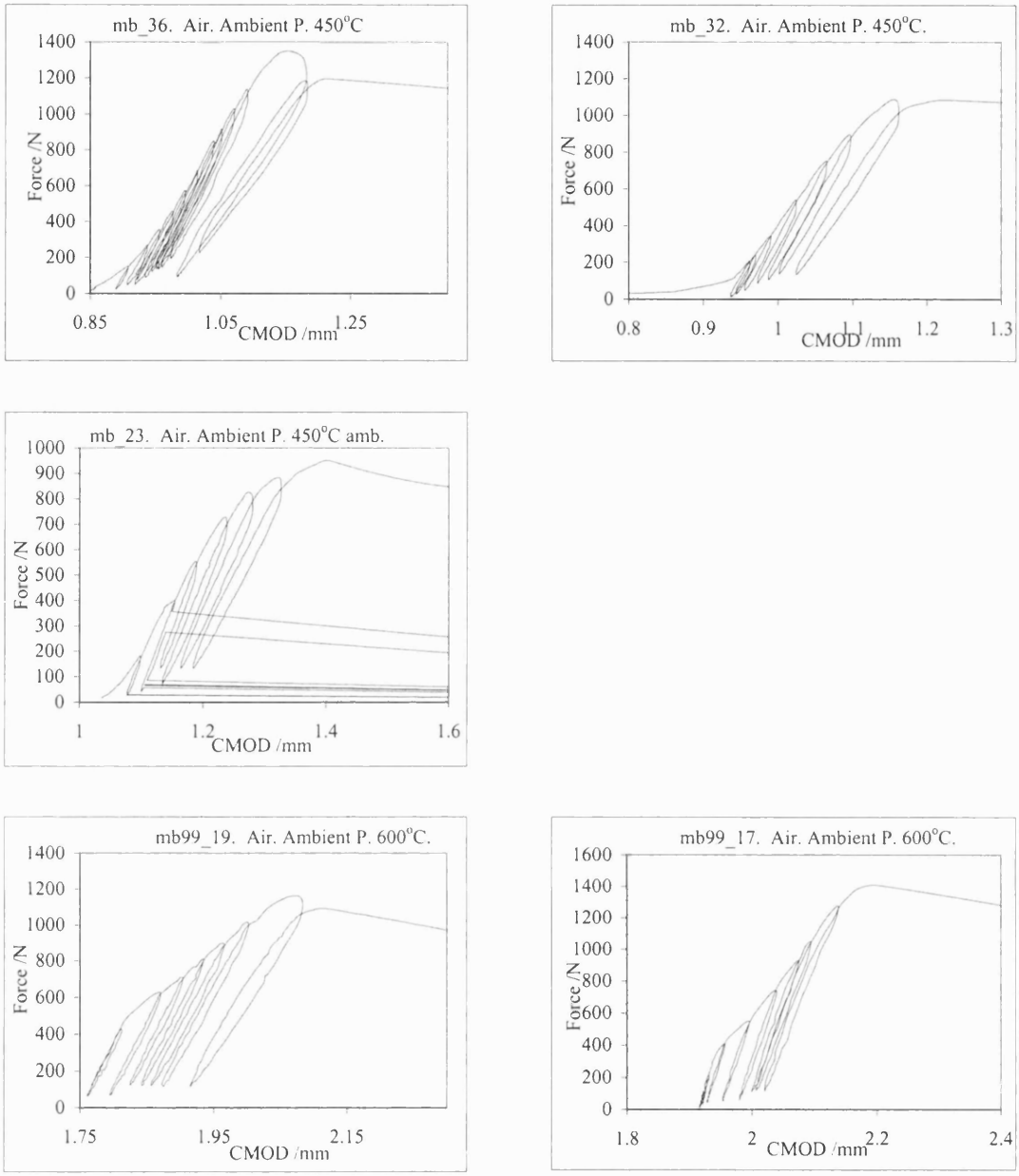

Fig. 9.4. Plots of CMOD against opening force at ambient pressure and varying temperatures (450-600°C) with air as confining medium. Note peculiar shape of plots (the unloading lines appear to be displaced but are still parallel) at 600°C and spikes in 3rd plot.

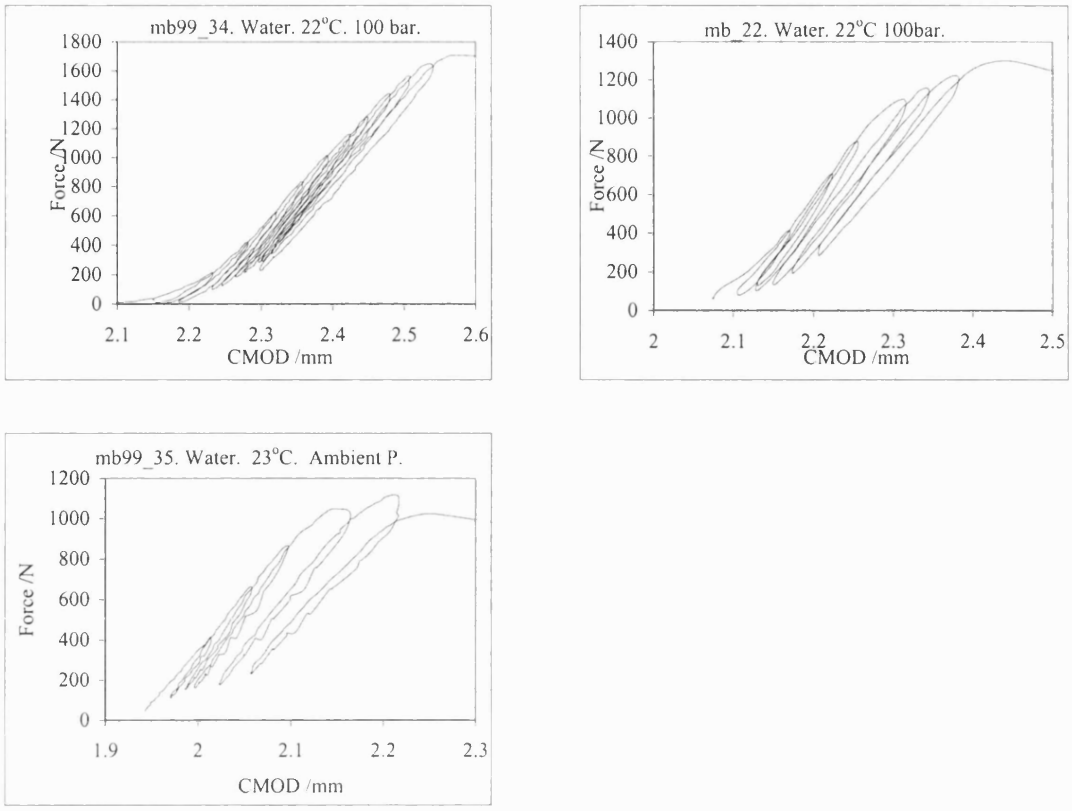

Fig. 9.5. Plots of CMOD against opening force at ambient and 100 bar pressure and at ambient temperature. Water is used as the confining medium. Note that only these few tests were carried out to show the effects of water saturation on the samples.

9.2.2. Comments on raw data plots.

As can be seen from the plots above, the logged data often deviates substantially from the ideal shape one would expect from a level II test. The causes of the deviations can be categorised as follows:

- Poor turnover. The sample fails without substantial change in compliance (gradient of unloading line). e.g. Mb99_34 or mb99_7
- Slip. The unloading/reloading cycles move along the CMOD axis without a change in compliance. e.g. mb99_17 and mb99_19.
- Unstable failure. Lack of unloading/loading cycles after the maximum force. Many samples show this problem.

Also seen are 'spikes' caused, most probably, by poor connections in the amplifier. These are insignificant, however, because they do not obscure the shape of the curve in any way, even when they are severe and frequent (e.g. mb99_6).

The biggest problem with the apparatus is the use of a hydraulic piston to provide the splitting force. Although a novel piece of engineering that allows the

apparatus to be used at high pressure, it has disadvantages over the traditional, load frame method. Firstly, there is some degree of elasticity in both the actuator housing and in the hydraulic fluid itself. This leads to energy storage in the apparatus at higher forces and is probably responsible for the poor turnover and unstable failure of some samples after the peak stress. Stick-slip and bleed-through effects in the piston may also be responsible for the slip effects seen at higher temperatures. Future modifications to the apparatus must address these issues as discussed in chapter 11. Despite these problems, the results still enable level II fracture toughness measurements to be made using the ISRM (1988) standard methods, which describe how to deal with the problems of premature failure and poor turnover. The slip problem does not affect the results as it has little bearing on the method used to find level II fracture toughness, although application of the Matsuki *et al.* (1991a) method becomes inappropriate in these cases.

9.3. Summary of results using ISRM methods to calculate K and K_c

The raw data shown in figs. 9.2-9.6 were processed using the methods described in ISRM (1988) and outlined in chapter 5. The results, both uncorrected and corrected for non-linearity, are shown below. The values of K and K_c are obtained from the equations

$$K = 24.0F_{max} / D^{1.5} \tag{9.1}$$

and

$$K_c = \sqrt{\frac{(1+p)}{(1-p)}} F_c / F_{max} K \tag{9.2}$$

where p is the degree of non-linearity, F_{max} the maximum load, F_c the corrected load (see ISRM, 1988 and chapter five), K the uncorrected fracture toughness and K_c the corrected fracture toughness.

Sample I.D.	Nominal temp /°C	Nominal press. /bar	K MPam$^{1/2}$	K_c MPam$^{1/2}$
mb33	30	1	2.12	2.24
mb22	30	1	2.04	2.30
mb34	30	1	2.00	2.34
mb31	30	1	2.54	2.59
mb99_29	150	1	2.02	3.96
mb99_7	150	1	3.15	4.48
mb99_25	150	1	2.27	2.90
mb99_10	300	1	1.93	1.66
mb99_9	300	1	2.38	2.77
mb99_18	300	1	1.97	2.06
mb36	450	1	2.22	2.16
mb32	450	1	1.77	2.35
mb23	450	1	1.57	2.10
mb99_17	600	1	2.32	2.56
mb99_19	600	1	1.92	2.55
mb99_11	30	50	2.38	2.94
mb99_13	30	50	2.40	2.97
mb99_4	30	50	3.18	3.52
mb99_6	30	100	2.93	3.38
mb99_2	30	100	2.97	2.99
mb99_1	30	100	2.56	2.87
mb99_14	30	150	2.68	2.62
mb99_33	30	150	2.94	4.42
mb99_32	30	200	3.05	4.56
mb99_15	30	200	2.83	2.74
mb99_8	30	200	2.65	2.77
mb99_3	150	100	2.70	2.86
mb99_27	100	100	2.84	3.78

Table 9.2. Results from main series of tests showing level I and II fracture toughness measurements for sample tested using air or CO_2 only.

These results are summarised in fig. 9.6. The results at given temperatures or pressures can be averaged either by the method of weighted mean for K_c, which has indication of possible errors on each measurement, or by a simple mean for K. These results are shown in fig. 9. 7. See section 9.4 for summary of error analysis.

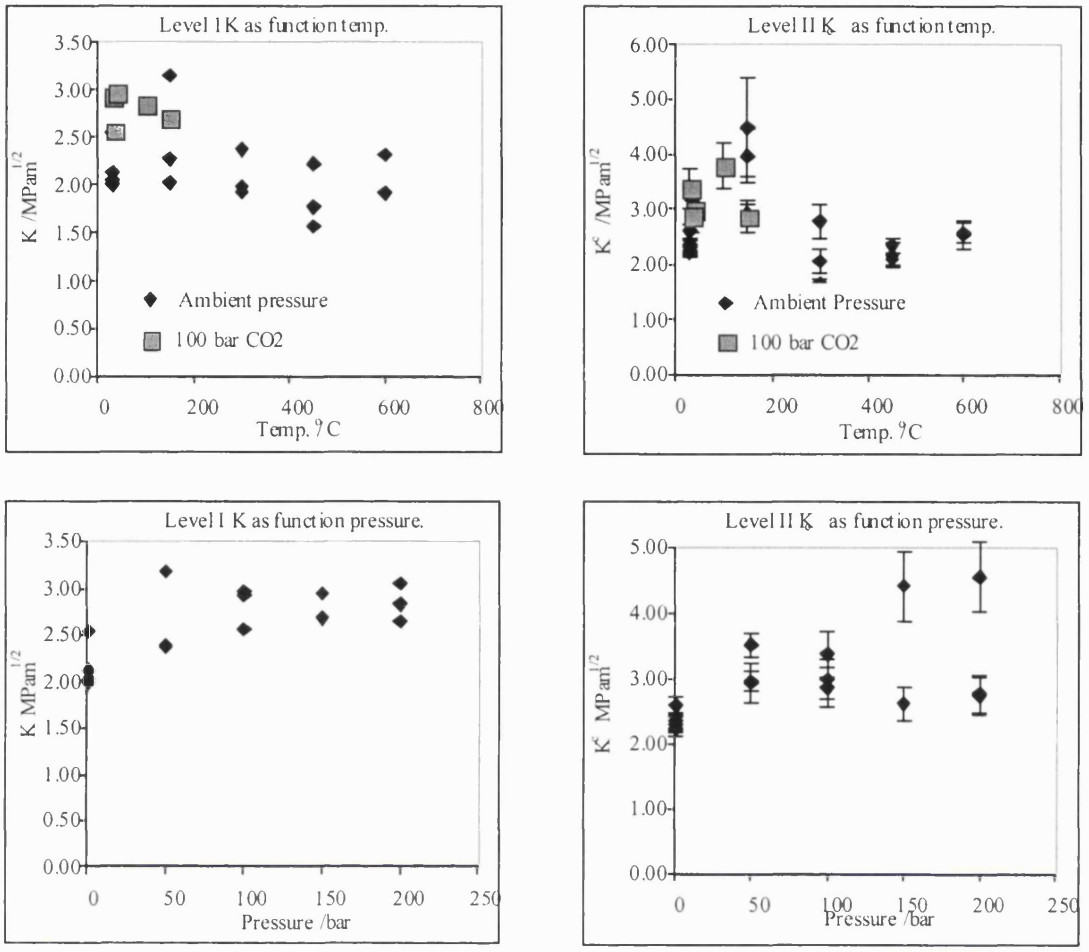

Fig. 9.6. Plots of K and K_c as a function of temperature and pressure. Measurement errors are small for K because the only sources of error are F_{max} and D, both of which have small percentage errors. Measurement error in K_c is based upon error in p and F_c, both of which are significant. See 9.4 for error analysis.

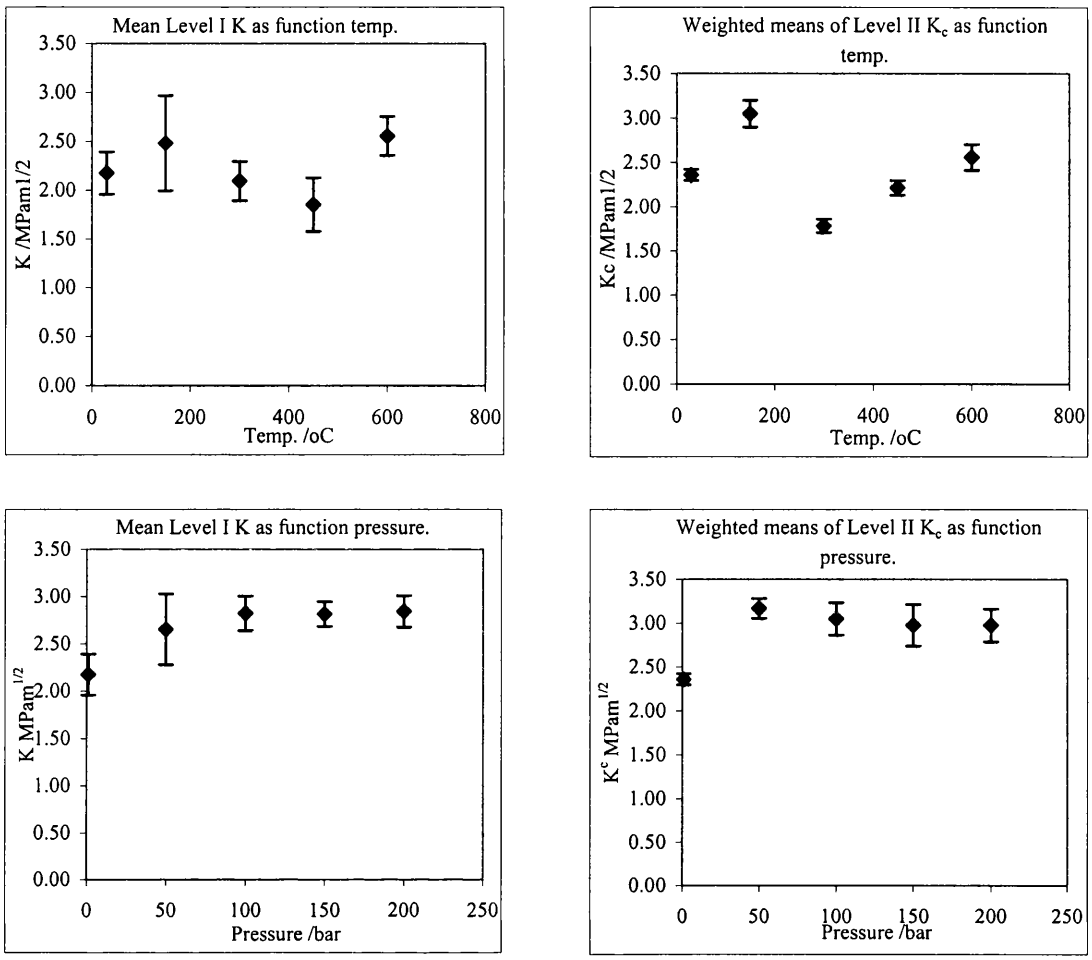

Fig. 9.7. Mean results for K as a function of temperature and pressure and weighted mean results for K_c, again as a function of temperature and pressure. Errors on K are from standard deviation of the measurements. Errors on K_c are from error on a weighted mean.

These results show a marked increase in fracture toughness with pressure. The value for K_c jumps from about 2.4MPam$^{1/2}$ to just over 3.0MPam$^{1/2}$ for even a modest increase in pressure. The fracture toughness also increases with temperature at around 150-200°C but then drops back to near its starting value at higher temperatures. Note that all the samples are heat treated to induce thermal cracking before they are tested. Thus the behaviour should be independent of thermal cracking effects. These results will be discussed further in chapter 11.

9.4. Error analysis.

The measurement of the physical quantities used in calculating the fracture toughness must include random error. The calibration of the displacement transducer, the pressure transducers and the amplification hardware can all introduce non-linearity into the measurements. This cannot be quantified and all care has been taken to ensure

that the calibration of this hardware is accurate and repeatable. There are no x-axis error-bars on the plots of figs. 9.6 and 9.7 because these results are fixed variables and will be the same for one sample as for another, whether or not some systematic error is present. The calibration procedures were all carried out several times over the course of the project so that errors between samples were eliminated. Furthermore any random measurement error will be small with respect to the size of the variable because both the temperature and pressure were actively controlled.

Random measurement error on K is also considered to be small because the value of K relies solely upon the value of F_{max}. The only random error introduced in to the process will be when measuring the height of this peak from the data plot. Again, assuming the pressure transducer calibration has negligible random error, this can be assumed to be small compared to the value of F_{max} itself and can therefore be ignored.

When evaluating K_c, however, one has to measure the value of X_u and X_l in order to find p, the degree of non-linearity. Even when the raw data are printed at the largest scale possible, a random measurement error is present in the values X_u and X_l. This leads to error in p and therefore K_c owing to the inherent difficulty in using the level II method and the need for construction lines and points (see chapter seven).
Recalling the equation for K_c we can separate it into two parts:

$$K_c = \sqrt{\frac{(1+p)}{(1-p)}} F_c / F_{\max} K = Z\left[F_c / F_{\max} K\right] \tag{9.3}$$

We can define the random error in Z due only to error in p simply as

$$\Delta Z = \left(\frac{dK_c}{dp}\right)\Delta p \tag{9.4}$$

where

$$\Delta p^2 = \left(\frac{X_u + X_l}{2}\right)^2 \left[\left(\frac{\Delta X_u}{X_u}\right)^2 + \left(\frac{\Delta X_l}{X_l}\right)^2\right] \tag{9.5}$$

thus giving

$$\Delta Z = (1+p)^{-1/2}(1+p)^{-3/2}\Delta\overline{p} \tag{9.6}$$

But, as in (9.2), the methodology of ISRM (1988) uses the value F_c which, in many of the results plots, is difficult to ascertain. Thus this value is also ascribed a random measurement error. This value is 5% for most plots although, where F_c is very difficult to estimate, it is given a 10% error. The fractional error in Z due to Δp alone can then be simply combined with the 5 or 10 % error in F_c to give

$$\Delta K_c = K_c \sqrt{\left(\frac{\Delta Z}{Z}\right)^2 + \left(\frac{\Delta F_c}{F_c}\right)^2} \tag{9.7}$$

where $\Delta F_c/F_c$ is 0.05 or 0.1 as estimated from the individual data plot.

Assuming the absolute values for the measurement errors in X_u and X_l are 0.5mm we can calculate an estimate of absolute error on K_c. These results are used as the values for the error bars in Fig. 9.6.

9.5. Application of Matsuki et al. (1991a) method to results.

As described in chapter seven, the Matsuki method uses the crack resistance curve (i.e. the fracture toughness variation with crack extension) to determine a stable point beyond which fracture toughness can be measured confidently. Crack resistance curves have been plotted for all the above data, although some have only 1 or 2 points owing to a lack of loading/unloading cycles. The equation used to generate the results of figs. 9.8 and 9.10 is

$$K_c = \sqrt{\frac{(1+p)}{(1-p)}} Y' F_i / D^{1.5} \tag{9.8}$$

where p is the average degree of non-linearity (for a given cycle) derived from the plot of CMOD against load (such as those in figs. 9.1-9.5), Y' is the non-dimensional stress intensity factor, F_i the force at which the linearised unloading line meets the envelope of the CMOD/load plot, and D the specimen diameter.

The error bars are constructed using the method described in section 9.4. Again, the error in Y' and D is assumed to be insignificant. The results for all the Matsuki method analyses are shown in figs. 9.8-9.10.

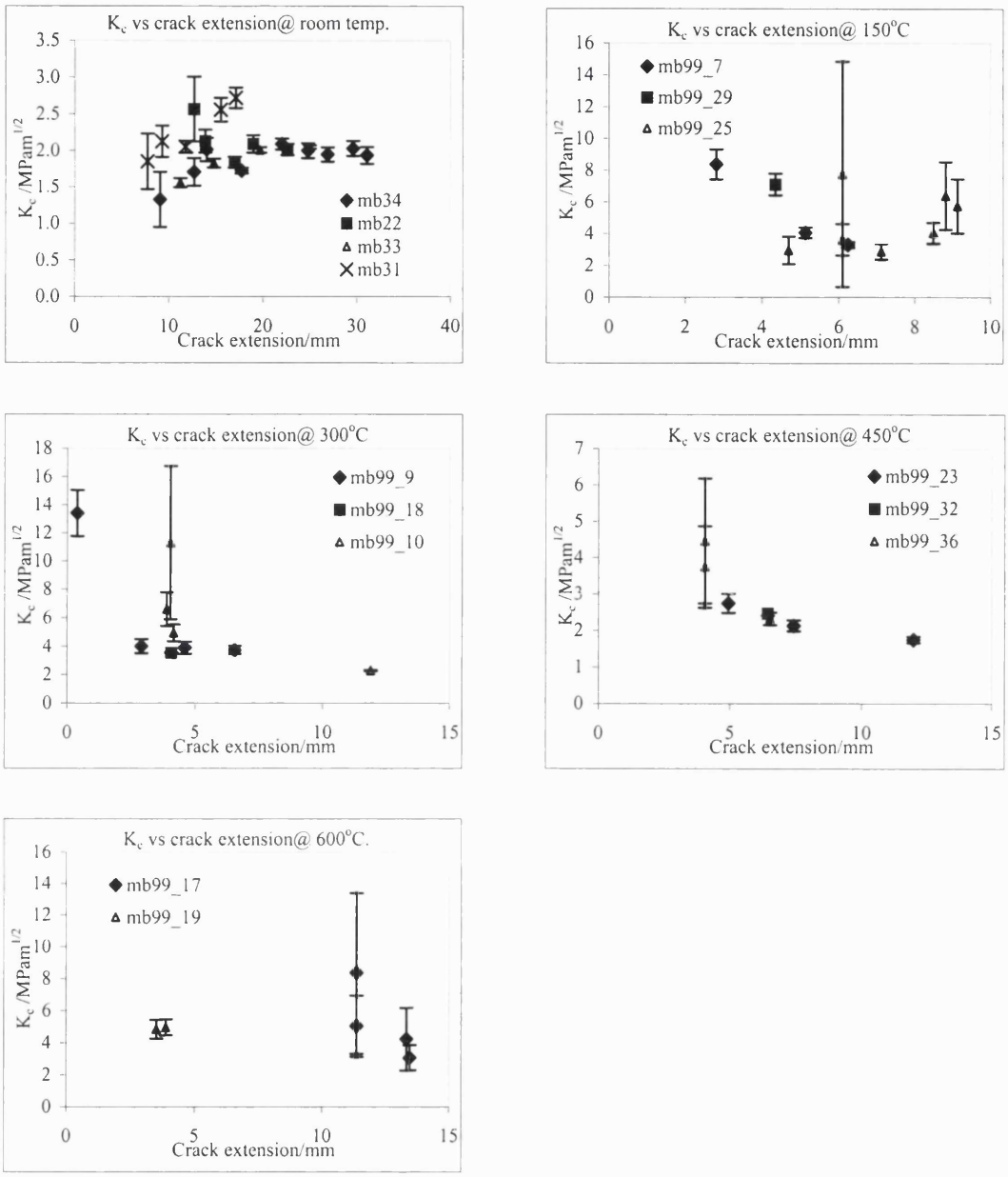

Fig. 9.8. Matsuki method plots of fracture toughness against crack extension for varying temperature at ambient pressure. Error bars as described in text.

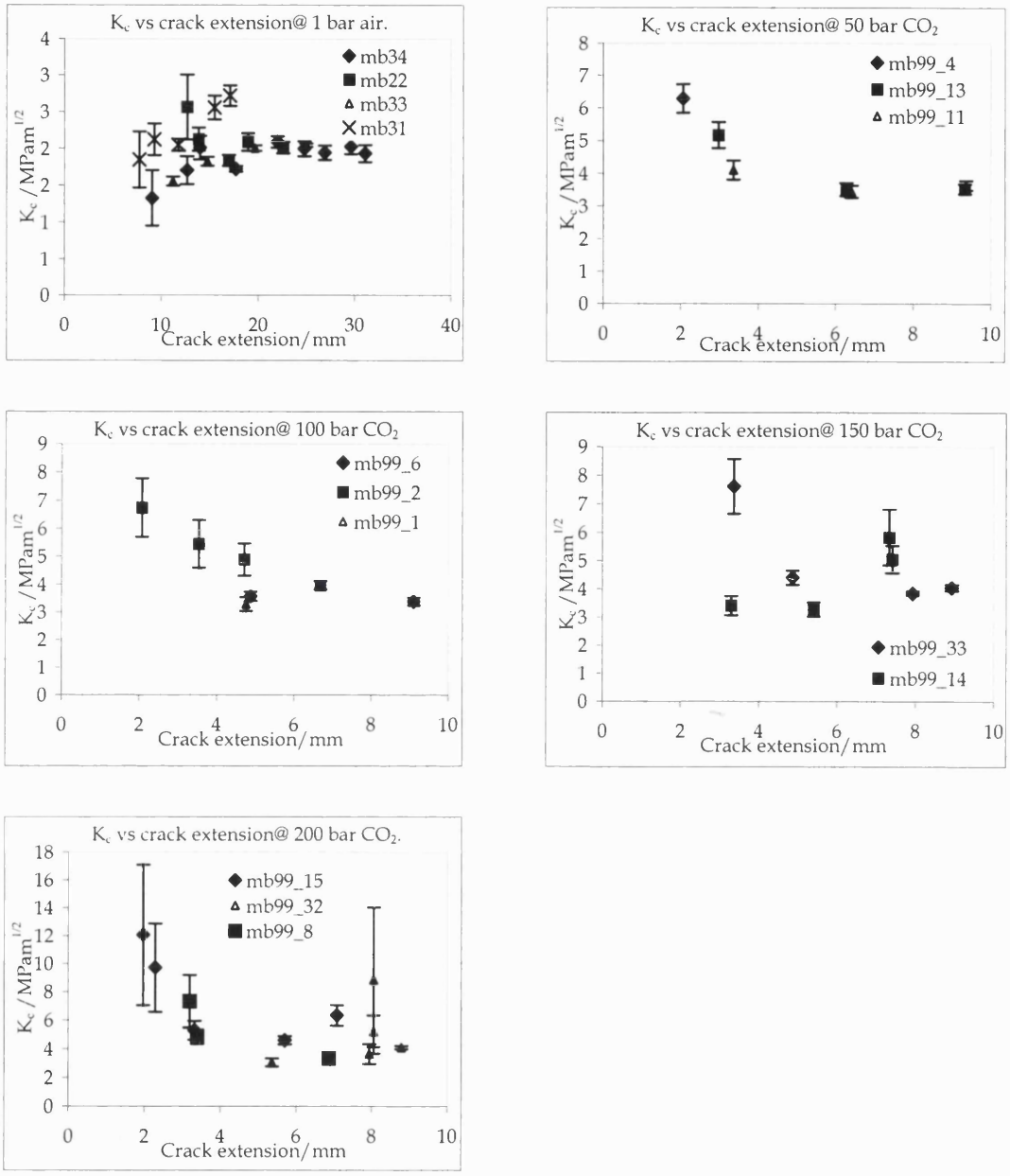

Fig. 9.9. Matsuki method plots of fracture toughness against crack extension for varying pressure at ambient temperature. Error bars as described in text.

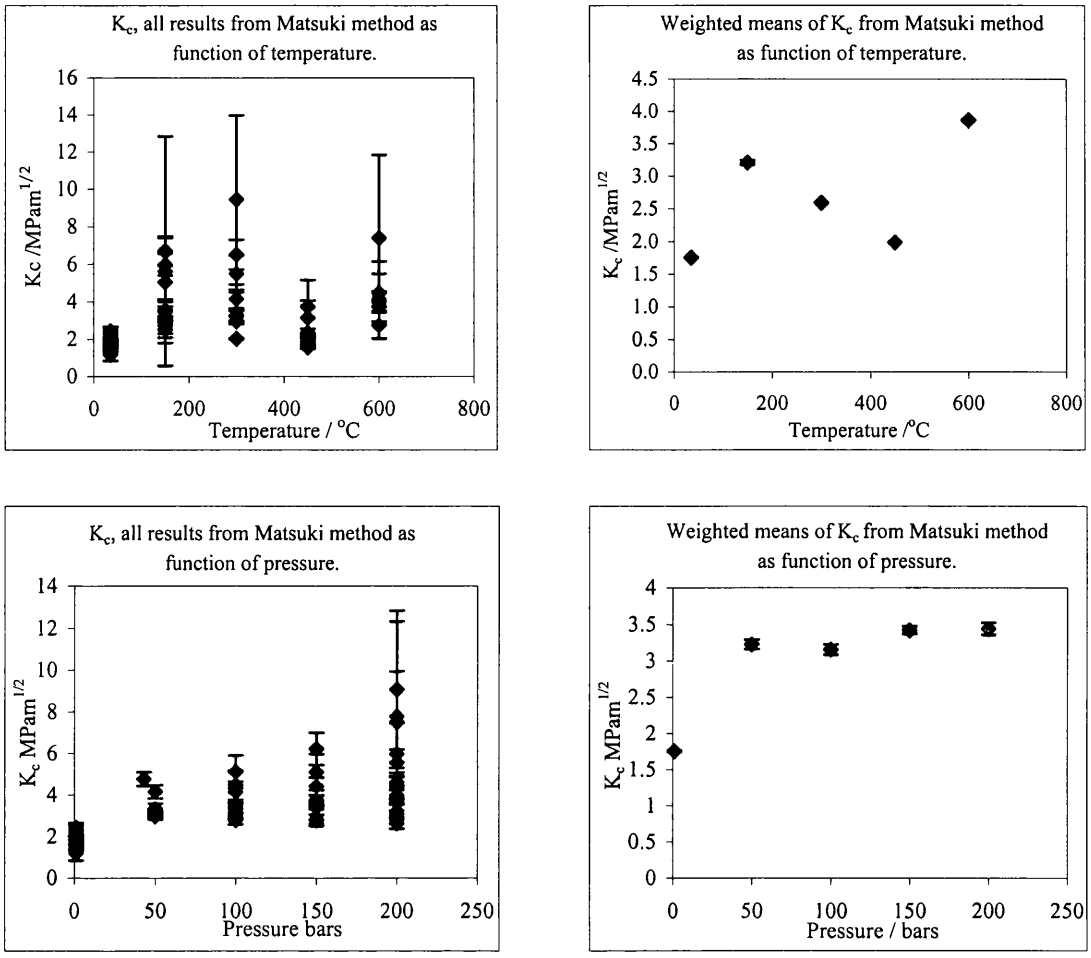

Fig. 9.10. Matsuki method results for K_c as function of temperature and pressure. In these plots all values of the K resistance curve have been assumed to be valid representations of K_c.

The results of figs. 9.8 and 9.9 show little agreement with the expected shape of K-resistance curve as seen in Matsuki *et al.* (1991a). Almost all the plots show a pronounced decrease in K-resistance with extension rather than an increase. The results at ambient temperatures and pressure, however, are as expected and show a plateau in K_c values. The simple analysis of experimental error shows how critical the value of p, the degree of non-linearity, is to the result of the K-resistance calculation. Those plots with very small values of X_1 show larger experimental errors because the fractional error in measurement is so much greater. The same applies to the actual measurement of p. High values of p lead to high values of K_c. Thus those graphs with poor turnover (little change in compliance) will tend to have high values of p and therefore K_c.

The results from fig. 9.10 are similar to those of fig. 9.7, although the values of K_c are slightly higher. Also, the higher temperature measurements of K_c are much higher using the Matsuki method than the ISRM method. Of course, the Matsuki method results in fig. 9.10 include results taken at small values of crack extension which

biases the results. The fact that these data give higher values of K_c than the ISRM method is unexpected. Moreover, the K-resistance curve increases to a plateau in few of the data. The implications of these measurements are discussed in chapter 11.

9.6. Fracture toughness as a function of characterisation measurements.

By plotting the fracture toughness results from all the samples as a function of the density or p-wave velocity, we can assess whether the results show a trend with pressure or temperature or depend upon other variables.

The statistical quantity used to discriminate between a trend and a random population of points appearing to have a trend is the correlation coefficient, r. This quantity can be easily calculated from pairs of points using the formula

$$r = \frac{\sum (x - \bar{x})(y - \bar{y})}{\sqrt{\sum (x - \bar{x})^2 (y - \bar{y})^2}} \tag{9.9}$$

where x and y are pairs of co-ordinates and barred quantities represent mean values.

The modulus of r represents the degree of correlation. A value of 1 indicates that all the data follow a straight line and are geometrically linked. A value of 0 indicates that there is no dependence of one variable on the other. A negative value of r implies an inverse relationship. The r-value can also then be compared with tables of significance to assess the likelihood that the trend is "real" rather than random. The larger the number of data points, the lower the r-value need be for significant dependence. For a trend to be significant at a confidence level, the r-value of the data should be greater than the percentage confidence r-factor for a given sample population. The 90% and 99% probability factors are quoted here from standard tables (Bailey, 1959). Significance of trends can therefore be described as high if the r-value is higher than the 99% confidence value or medium if higher than the 90% value. Trends with an r-value below the 90% level are not significant.

The results from these characterisation measurements are summarised in table 9.3.

Sample I.D.	Density /gcm^{-3}	Nominal temp /°C	Nominal press. /bar	Non-linearity, p	V_p /kms^{-1}	V_s /kms^{-1}	K_c MPam$^{1/2}$	Damage param.	P-wave Mod. /GPa
mb33	-	30.00	1.00	0.05	-	-	2.24	-	
mb22	-	30.00	1.00	0.12	-	2.39	2.30	1.16	
mb34	-	30.00	1.00	0.16	-	-	2.34	-	
mb31	-	30.00	1.00	0.06	-	-	2.59	-	
mb99_29	2.90	150.00	1.00	0.70	4.82	-	3.96	0.82	67.37
mb99_7	2.95	150.00	1.00	0.40	4.62	2.41	4.48	0.66	62.97
mb99_25	2.91	150.00	1.00	0.26	4.80	-	2.90	0.94	67.05
mb99_10	2.96	300.00	1.00	0.04	5.05	-	1.66	1.28	75.49
mb99_9	2.96	300.00	1.00	0.19	4.97	-	2.77	3.21	73.11
mb99_18	2.95	300.00	1.00	0.17	4.93	2.50	2.06	1.79	71.70
mb36	-	450.00	1.00	0.10	-	-	2.16	-	
mb32	-	450.00	1.00	0.28	-	-	2.35	-	
mb23	-	450.00	1.00	0.30	-	2.34	2.10	1.38	
mb99_17	2.99	600.00	1.00	0.10	5.06	2.32	2.56	3.53	76.55
mb99_19	2.99	600.00	1.00	0.37	4.99	-	2.55	1.20	74.45
mb99_11	2.96	30.00	50.00	0.28	5.05	-	2.94	0.99	75.49
mb99_13	2.96	30.00	50.00	0.33	5.09	2.47	2.97	0.90	76.69
mb99_4	2.96	30.00	50.00	0.11	4.81	-	3.52	0.90	68.48
mb99_6	2.96	30.00	100.00	0.18	4.80	-	3.38	0.90	68.20
mb99_2	2.93	30.00	100.00	0.13	4.71	-	2.99	0.77	65.00
mb99_1	2.95	30.00	100.00	0.15	4.59	2.56	2.87	0.33	62.15
mb99_14	2.97	30.00	150.00	0.04	4.68	-	2.62	0.52	65.05
mb99_33	2.93	30.00	150.00	0.53	4.67	2.40	4.42	0.80	63.90
mb99_32	2.88	30.00	200.00	0.53	4.85	2.40	4.56	0.82	67.74
mb99_15	2.93	30.00	200.00	0.07	4.67	-	2.74	0.76	63.90
mb99_8	2.93	30.00	200.00	0.24	4.52	-	2.77	0.70	59.86
mb99_3	2.93	150.00	100.00	0.21	4.59	2.31	2.86	0.88	61.73
mb99_27	2.91	100.00	99.50	0.30	4.98	-	3.78	0.96	72.17

Table 9.3. Characterisation measurements.

The associated random error on each of these values depends largely on the method by which they were measured. Summarised below are the experimental errors estimated using standard techniques.

Measured or calculated quantity	Typical value	Estimated error	% error
S wave arrival time	30us	0.5us	1.7
P wave arrival time	18us	0.1us	0.6
Sample length	80mm	0.2mm	0.3
Sample diameter	60mm	0.2mm	0.3
V_s	5.0 km/s	-	1.7
V_p	2.4 km/s	-	0.7
Sample mass	-	0	0
Sample volume	-	-	0.5
Sample density	2.94 gcm^{-3}	-	0.5
Initial K_c stiffness	-	5%	5
P wave modulus	-	-	1.1
Poisson ratio v	0.32	-	3.7
Poisson ratio v_o	0.18	-	3.7
Damage paramater	-	-	10.4
Wave-vel. E modulus	-	-	5
Frac.-mech. E mod.	-	-	5

Table 9.4. Summary of experimental error estimates and calculations.

9.6.1. Density.

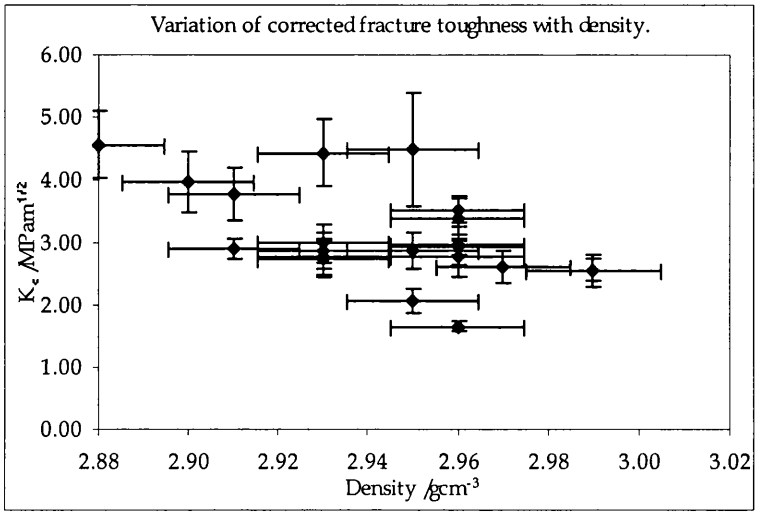

Fig. 9.11. Non-linearity corrected fracture toughness results from all experiments plotted as function of density. r-value = -0.54. 90% confidence r-value = 0.4. 99% confidence r-factor = 0.59.

Fig. 9.11 shows a large spread in the distribution of points and, although a slight inverse relationship exists, there is no clear trend between the variables. This is as expected because the percentage variation in density between the samples is very small (about 1%). Unless density was the controlling factor, we would therefore be unlikely to see a clear trend. Some authors (Brown and Reddish, 1997, Rist *et al.*, 1999) have found a correlation between density and fracture toughness, although this is between different rock types and over a density variation of about 30% in Brown and Reddish (1997) and for ice in Rist *et al.* (1999). The experiments performed by Brown and Reddish (1997) were only level I tests and used chevron bend (CB) specimens as opposed to short-rod samples. It should be noted that the ambient conditions results from this study agree well with the empirical result from Brown and Reddish (1997), which is described by

$$K = 3.21\rho - 6.95 \qquad (9.10)$$

The results of the present study at ambient temperatures give a fracture toughness of 2.40 $\pm$0.05 MPa.m$^{1/2}$ compared to 2.45 MPam$^{1/2}$ from (9.10). It should be noted that Brown and Reddish (1997) used only uncorrected CB specimens, which will tend to increase the value of K slightly (Matsuki *et al.*, 1991b). They do not state whether they use the corrected stress intensity factors for CB specimens of Matsuki *et al.* (1991b) which would tend to reduce the fracture toughness values by 10%. The results from our study are therefore approximately consistent with the work of Brown and Reddish (1997).

9.6.2. P-wave velocity and P-wave modulus

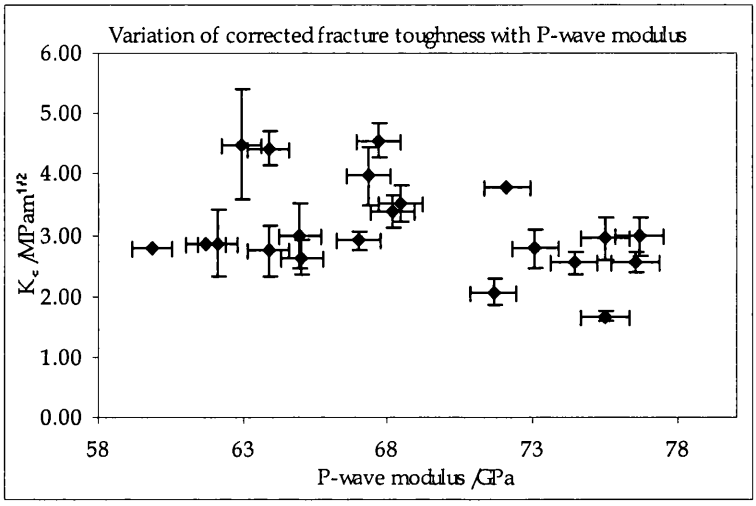

Fig. 9.12. Non-linearity corrected fracture toughness results from all experiments plotted as function of P-wave modulus as measured prior to testing but after heat treatment. r-value = 0.34. 90% confidence r-value = 0.37, 99% confidence r-value = 0.55

The P-wave velocity depends upon the density, bulk modulus and shear modulus of the sample. P-wave velocity itself is not a good characterising measurement but by normalising the results with density we can plot the P-wave, or 'axial', modulus instead.

$$V_p = \sqrt{\frac{\chi}{\rho}} = \sqrt{\left(K + \frac{4}{3}\mu\right)/\rho} \qquad (9.11)$$

where V_p is the P-wave velocity, K is the bulk modulus, μ is the shear modulus, ρ is the density and χ the P-wave modulus. P-wave modulus is a representational elastic modulus in the direction of propagation of the wave. As shown in figure 9.11, there is no significant trend in these data between P-wave modulus and fracture toughness.

9.6.3. Thermal cracking damage parameter.

The measurements of density and P and S-wave velocities before, and after, heat treatment allow an estimate of the amount of cracking damage introduced into the sample to be made. If the cracking damage was different for each sample then this, rather than the temperature or pressure could be the controlling factor for variations in fracture toughness,. S-wave velocity measurements were made for one sample at each set of experimental conditions, and five S-wave velocity measurements from undamaged basalt were averaged to give a 'before heat treatment' figure. P wave velocity measurements were made for each sample, before and after heat treatment.

The crack density parameter can be related to Poisson's ratio in a variety of ways, but a simple method is that of Ayling *et al.* (1993) who use

$$\varepsilon = \frac{(45/16)[(\nu_o - \nu)(2-\nu)]}{(1-\nu^2)(10\nu_o - 3\nu\nu_o - \nu)} \tag{9.12}$$

where ν_0 is the Poisson's ration of the uncracked sample, ν is the Poisson's ratio of the damaged sample and ε is the damage parameter. In theory, ν_0 is measured for a perfectly undamaged body but the measurements taken in this study, prior to heat treatment, will be influenced by previously existing microcracks. Thus, the damage parameter is normalised to the 'before heat treatment' state for each sample. The data still provide an internally consistent means of estimating which sample has been damaged most. The Poisson's ratio for each sample is calculated from Gueguen and Palciauskas (1994)

$$\nu = \frac{1}{2}\left[\frac{(V_p/V_s)^2 - 2}{(V_p/V_s)^2 - 1}\right] \tag{9.13}$$

where V_p and V_s are the P and S-wave velocities. The results of figure 9.12 show that there is no significant dependence of fracture toughness on the crack damage parameter.

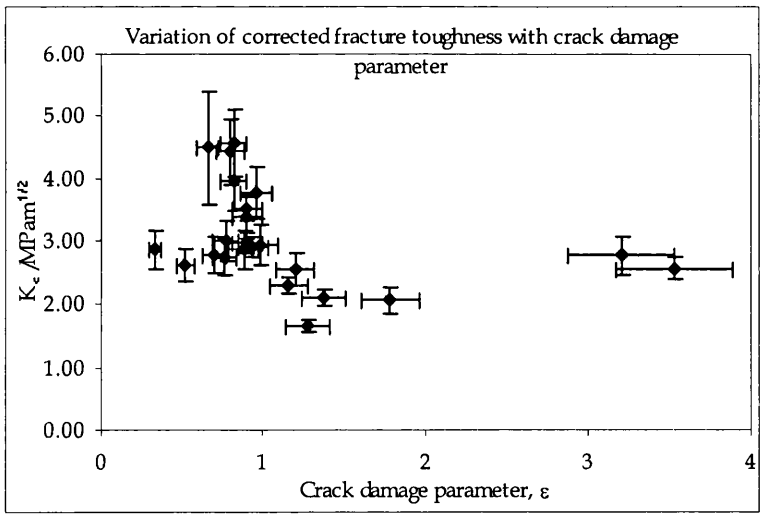

Fig. 9.13. Non-linearity corrected fracture toughness results from all experiments plotted as function of the damage parameter, which was calculated from P and S-wave velocity measurements before and after heat treatment. r-value = 0.33, 90% confidence r-value = 0.36, 99% confidence r-value = 0.54.

9.7. Non-linearity correction factor, p.

The anelastic, or non-linearity, correction factor, p, is found graphically from a pair of linearised unloading lines. The value of p can have a great bearing on the value of K_c: large values of p increase the value of K_c dramatically. A p-value of 0.1 increases the factor multiplying the fracture toughness by up to 10%, whilst a p-value of 0.3

increases it by up to 36%. The p-value is thus the controlling factor for test specimens which show a similar level I fracture toughness but have a different value for level II fracture toughness. As p is an indicator of non-linearity in the samples, we can plot p as a function of pressure and temperature to provide information about the level of anelastic deformation. The results show that neither temperature nor pressure has a strong dependence on p, although both show a slight positive trend. The r-values for each variable are below the level of significance.

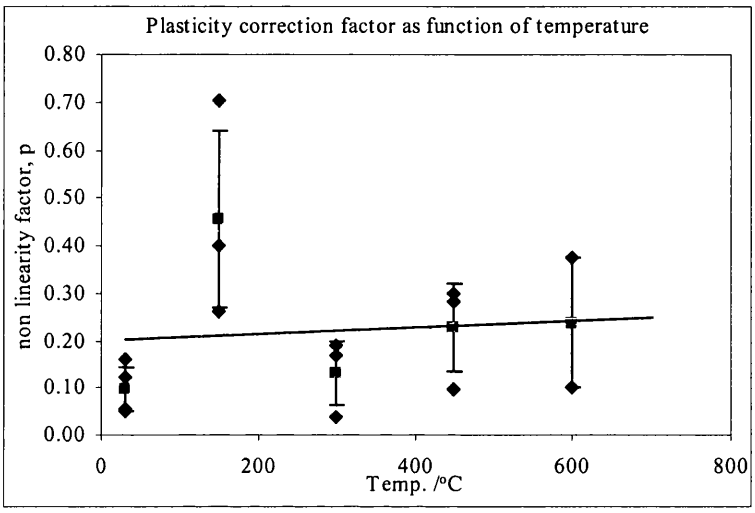

Fig. 9.14. Non-linearity factor, p, as a function of temperature. Pink squares with error bars represent the mean values with associated standard deviations. r-value = 0.08. 90% confidence r-value = 0.44, 99% confidence r-value = 0.64

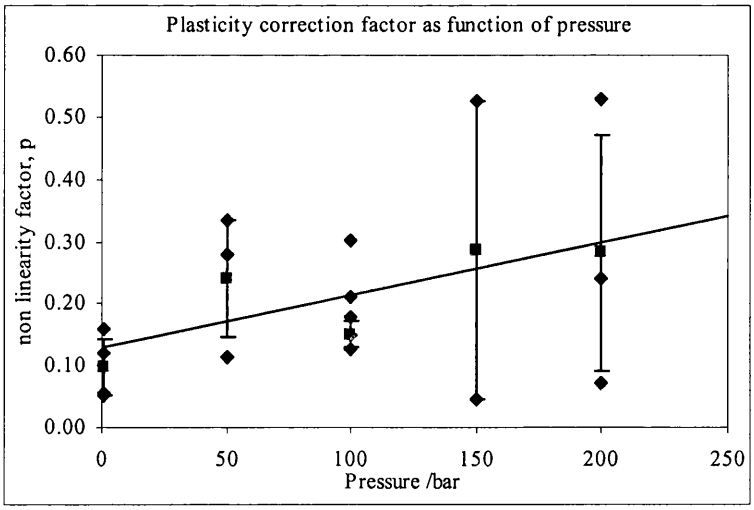

Fig. 9.15. Non-linearity factor, p, as a function of confining pressure. Pink squares with error bars represent the mean values with associated standard deviations. r-value = 0.40. 90% confidence r-value = 0.44, 99% confidence r-value = 0.64

The Level I and II fracture toughness can be displayed together as a function of p. Fig. 9.15 shows that the level I fracture toughness is independent of p whereas the corrected value shows a distinct positive trend. This is because, as noted above, the p

value tends to increase the fracture toughness. But it is interesting to note that there is no dependence of level I toughness on p. It would seem sensible to assume that the load at failure, the controlling factor for level I tests, would increase for those samples that showed high p values. This is not the case and, although the results from fig. 9.6 and 9.7 show a dependence of level I toughness with temperature and pressure, there is no indication that this is linked to increased non-linear behaviour.

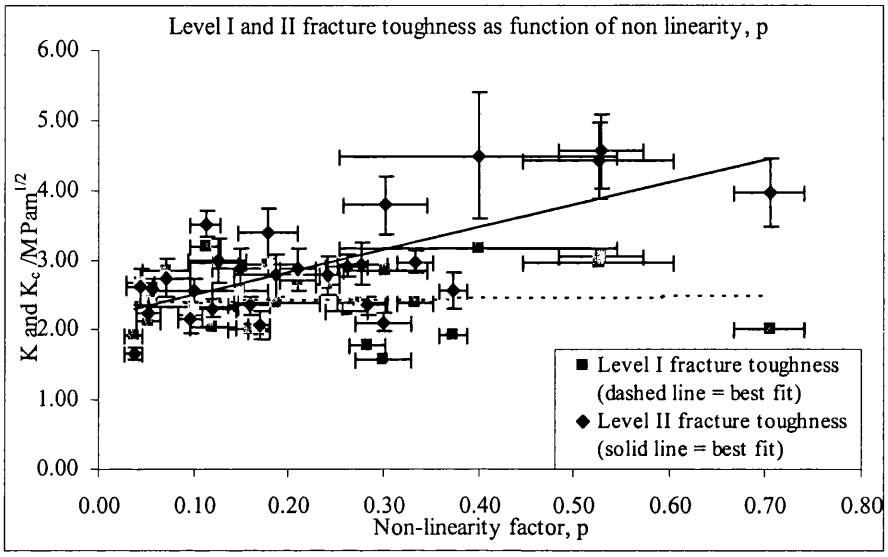

Fig. 9.16. Variation of K and K_c with non-linearity factor, p. r- value for Kc = 0.70, r-value for K = -0.21. 90% probability r-value = 0.31, 99% probability r-value = 0.48.

There is an increased spread of p-values at higher temperatures and pressure. This almost certainly represents an apparatus effect and is particularly obvious when the ambient conditions results are removed from Fig. 9.13 and 9.14. Only those results at ambient temperatures and pressures show consistently low p-values. This seems to suggest that the higher measurements of fracture toughness are not due to increased anelastic behaviour in the sample because there is no positive correlation between the p-factor and temperature and pressure.

The exception to this comment is that both Level I and II fracture toughness and p-factor all show an increase at 150°C. This is in agreement with the work of Meredith and Atkinson (1985), who have found a slight toughening with temperature up to 200°C followed by a decrease at higher temperatures for gabbro and granite. This is discussed in chapter 11.

9.8. Young's modulus measurements from Level II fracture toughness tests and P and S-wave velocity measurements.

The Young's modulus for the samples can be calculated both from the initial slope of Level II fracture toughness tests and from measurements of P and S-wave velocities. The appropriate equations for each of the two methods are:

$$E = \frac{84.5 S_i}{D} \tag{9.14}$$

$$E = \left(\frac{3\left(\frac{V_p}{V_s}\right)^2 - 4}{\left(\frac{V_p}{V_s}\right)^2 - 1} \right) \rho V_s^2 \tag{9.15}$$

where S_i is the initial stiffness of the loading line for a level II test (in $KNmm^{-1}$) and D is specimen diameter (in mm). V_p and V_s are the P and S-wave velocities and ρ is the sample density. These results are summarised in table 9.8.

Sample I.D.	Nominal temp /°C	Nominal press. /bar	K_c $MPam^{1/2}$	E /GPa (wave vel.)	E /GPa (Frac. Mech)
mb33	30.00	1.00	2.24	-	11.18
mb22	30.00	1.00	2.30	45.07	12.96
mb34	30.00	1.00	2.34	-	12.54
mb31	30.00	1.00	2.59	-	10.33
mb99_29	150.00	1.00	3.96	44.95	9.41
mb99_7	150.00	1.00	4.48	44.96	10.35
mb99_25	150.00	1.00	2.90	45.02	10.60
mb99_10	300.00	1.00	1.66	46.53	10.75
mb99_9	300.00	1.00	2.77	46.31	10.80
mb99_18	300.00	1.00	2.06	48.90	10.95
mb36	450.00	1.00	2.16	-	11.88
mb32	450.00	1.00	2.35	-	10.20
mb23	450.00	1.00	2.10	43.68	9.92
mb99_17	600.00	1.00	2.56	44.01	20.71
mb99_19	600.00	1.00	2.55	46.83	10.61
mb99_11	30.00	50.00	2.94	46.57	9.49
mb99_13	30.00	50.00	2.97	48.64	9.84
mb99_4	30.00	50.00	3.52	45.86	14.24
mb99_6	30.00	100.00	3.38	45.78	13.43
mb99_2	30.00	100.00	2.99	44.96	12.35
mb99_1	30.00	100.00	2.87	49.20	14.52
mb99_14	30.00	150.00	2.62	45.57	10.52
mb99_33	30.00	150.00	4.42	44.45	12.02
mb99_32	30.00	200.00	4.56	44.39	15.32
mb99_15	30.00	200.00	2.74	44.94	12.51
mb99_8	30.00	200.00	2.77	44.25	12.39
mb99_3	150.00	100.00	2.86	41.59	-
mb99_27	100.00	99.50	3.78	45.52	-

Table 9.5. Young's modulus measurements using the wave velocity and fracture mechanics methods.

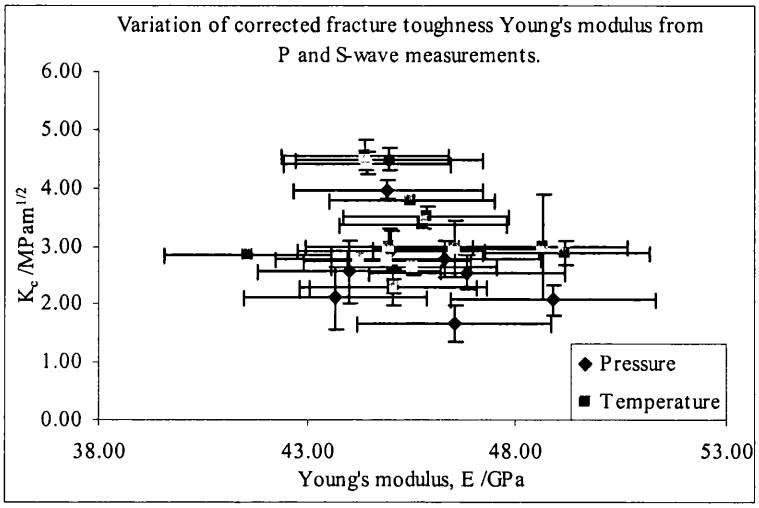

Fig. 9.17. P and S-wave velocity measurement evaluation of E. Note scale of x-axis.

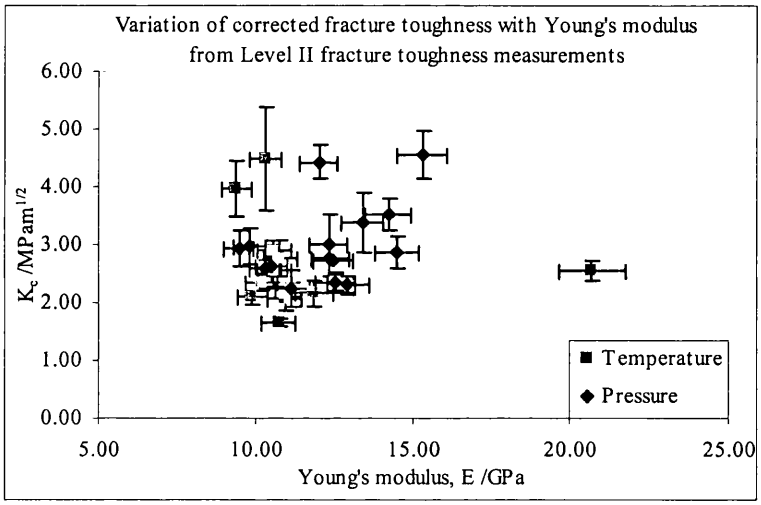

Fig. 9.18. Level II fracture toughness measurement evaluation of E. Note scale of x-axis.

Note that in figs. 9.16 and 9.17 there is no dependence of fracture toughness of the total data set on Young' modulus, the r-values for both being less than 0.25 and thus much lower than the 90% confidence value of 0.36. The values of E obtained from the fracture toughness measurements are about a factor of four lower than those from wave velocity measurements. Moreover, the values of E obtained from the fracture toughness measurements show a split between the measurements taken at pressure >5MPa and the measurements taken at temperature but at ambient pressure, the aforementioned generally being 20-30% higher. Also, as shown in fig. 9.18, there is no correlation between samples with high Young's modulus calculated using one method and those with high Young's modulus calculated using the other. The correlation coefficient for this comparison is 0.22, again less than the 90% confidence value of 0.36. These

comments are discussed fully in chapter 11.

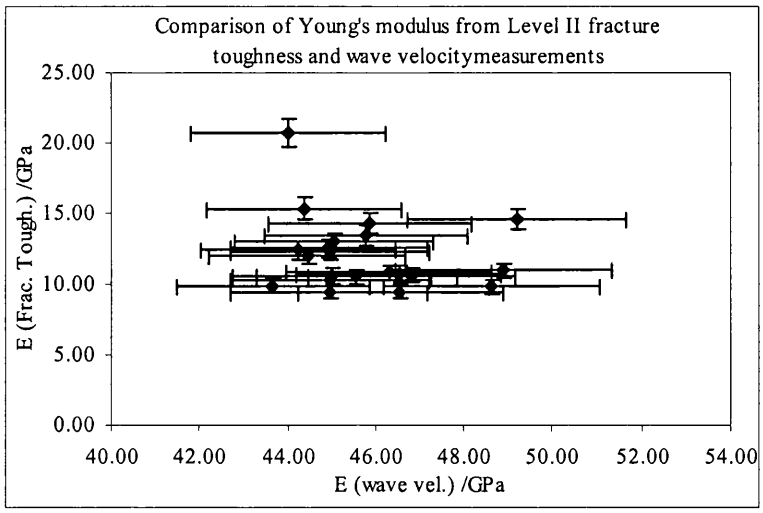

Fig. 9.19. Correlation between Young's modulus calculated using the two methods.

9.9. Other fracture toughness measurements.

In addition to the main experimental program, several other fracture toughness measurements were made. Some tests were performed on basalt using water as confining medium to investigate the effects a liquid, rather than gaseous, medium had on the results. Three samples were tested, one at 1.0 bar and two at 100 bar confining pressure. The results are shown in table 9.9 and are compared with the mean values of the results obtained using dry gas (air or CO_2) in the main part of the project.

A small number of tests using Darley Dale sandstone samples were also performed in an attempt to extract a reliable level II test from the old actuator housing (see chapter six).Three sandstone samples were tested, of which one failed and the other two yielded only usable level I measurements owing to zero turnover in the level II plots. One sample was dried for >72 hours before testing, the other was saturated with water. Both were tested at ambient temperature and pressure. The level I fracture toughness of the wet specimen was 0.42MPa.m$^{1/2}$ whereas that of the dry specimen was 0.85MPa.m$^{1/2}$. Experimental error on both these measurements was estimated as 5%.

Sample	Pressure	Medium	K /MPam$^{1/2}$	K_c /MPam$^{1/2}$	Err. K_c
mb99_35	1	water	2.01	2.31	0.16
Mean*	1	air	2.17	2.37	0.12
mb99_34	100	water	2.8	2.9	0.2
mb21	100	water	2.14	2.97	0.14
Mean*	100	CO_2	2.77	3.05	0.2

Table 9.6. Results from tests using water as confining medium. Mean* notes the mean results from the main set of experimental data (see table 9.2).

The results from table 9.6, unlike those obtained early in the project from sandstone samples, show water to have little effect on the fracture toughness of the material. All of the values obtained for the basalt are slightly lower than those obtained from the dry tests but they are the same within experimental error and so no importance can be attached to this trend. The basalt may have been affected less by water than sandstone because it has much lower porosity.

9.10. Analysis of crack faces by SEM and microscopy.

The mode of failure (transgranular, intergranular, plastic) of the samples was difficult to observe during testing. Accordingly a selection of crack surfaces were inspected under the SEM. The samples were scanned for examples of transgranular and intergranular failure and for non-brittle processes. Lower resolution optical microscopy of the crack surface was also used for one sample tested at 600°C, one sample tested under 200 bar CO_2, and one sample at ambient pressure and temperature to investigate any macroscopic difference in mode of failure.

9.10.1. SEM results.

None of the examples shown in figures 9.19 show evidence of anything other than brittle deformation except, possibly, for fig. 9.20.b, which shows sub parallel ridges disturbed by a transverse feature which may be a region that failed by limited flow. There are examples of both inter and transgranular cracking in the samples. Hackle marks on grain faces (e.g. bottom of fig. 9.19.e) and grain boundary debris suggest intergranular failure whereas clearly defined intra-granular failure is also clearly visible (e.g. fig. 9.19.b). Scalloped edges and curved stepped edges of grains are commonly observed (e.g. figs. 9.19d, 9.20.d and 9.22b) suggesting that brittle fracture of the grains is the dominant failure mode. There is no obvious variation in behaviour over the range of temperature and pressures at which the samples were tested and the assumption that brittle processes would control failure at all conditions is therefore supported.

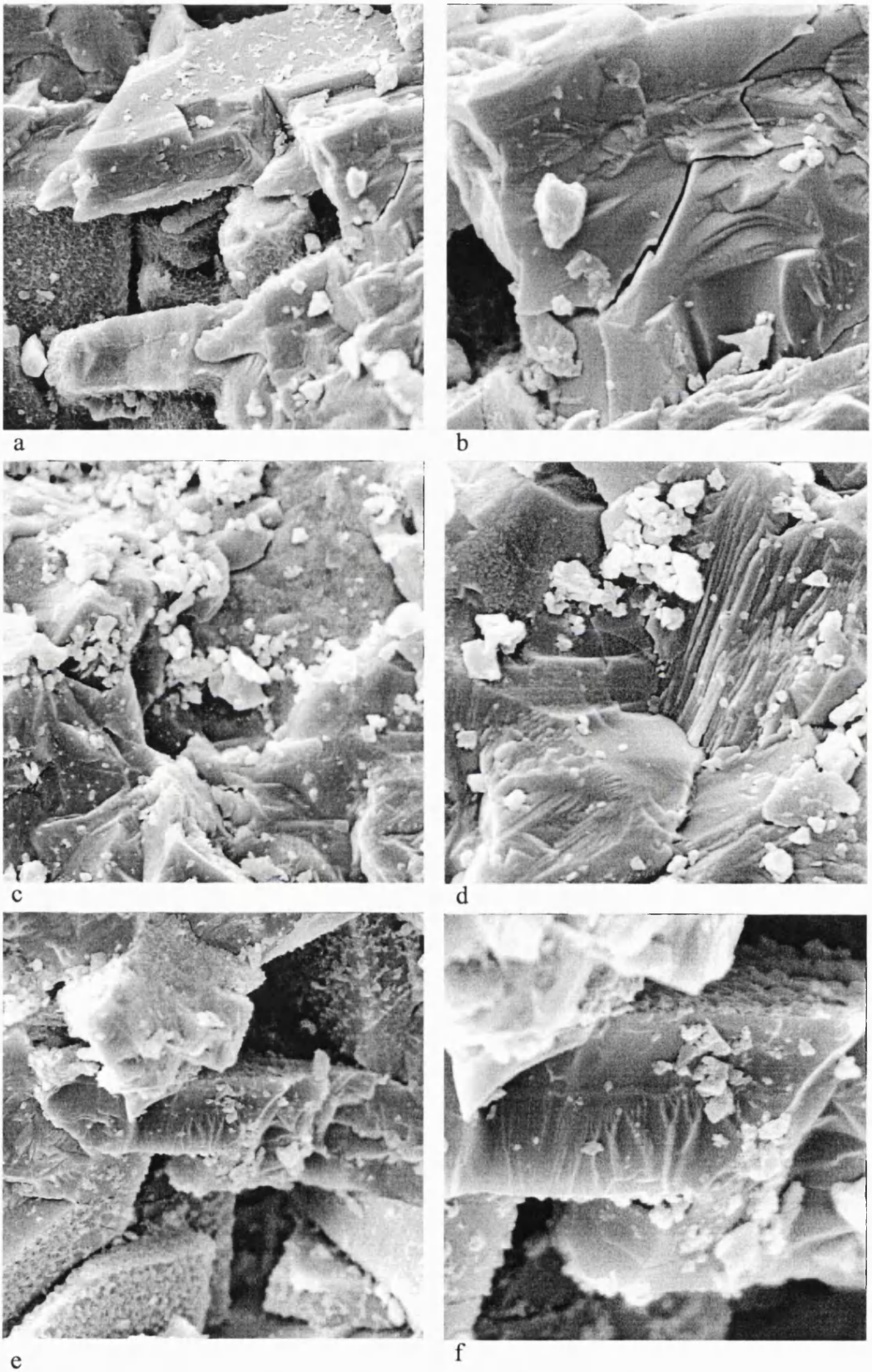

Fig. 9.20. SEM micrographs of crack surfaces. Left hand column are all x2000 with a field of view of 50μm. Right hand column are all x5000 with a field of view of 20μm. All samples pictured above were tested at ambient temperature. a and b were tested under 1 bar of air; c and d were tested under 50 bar CO_2; e and f were tested under 100 bar CO_2.

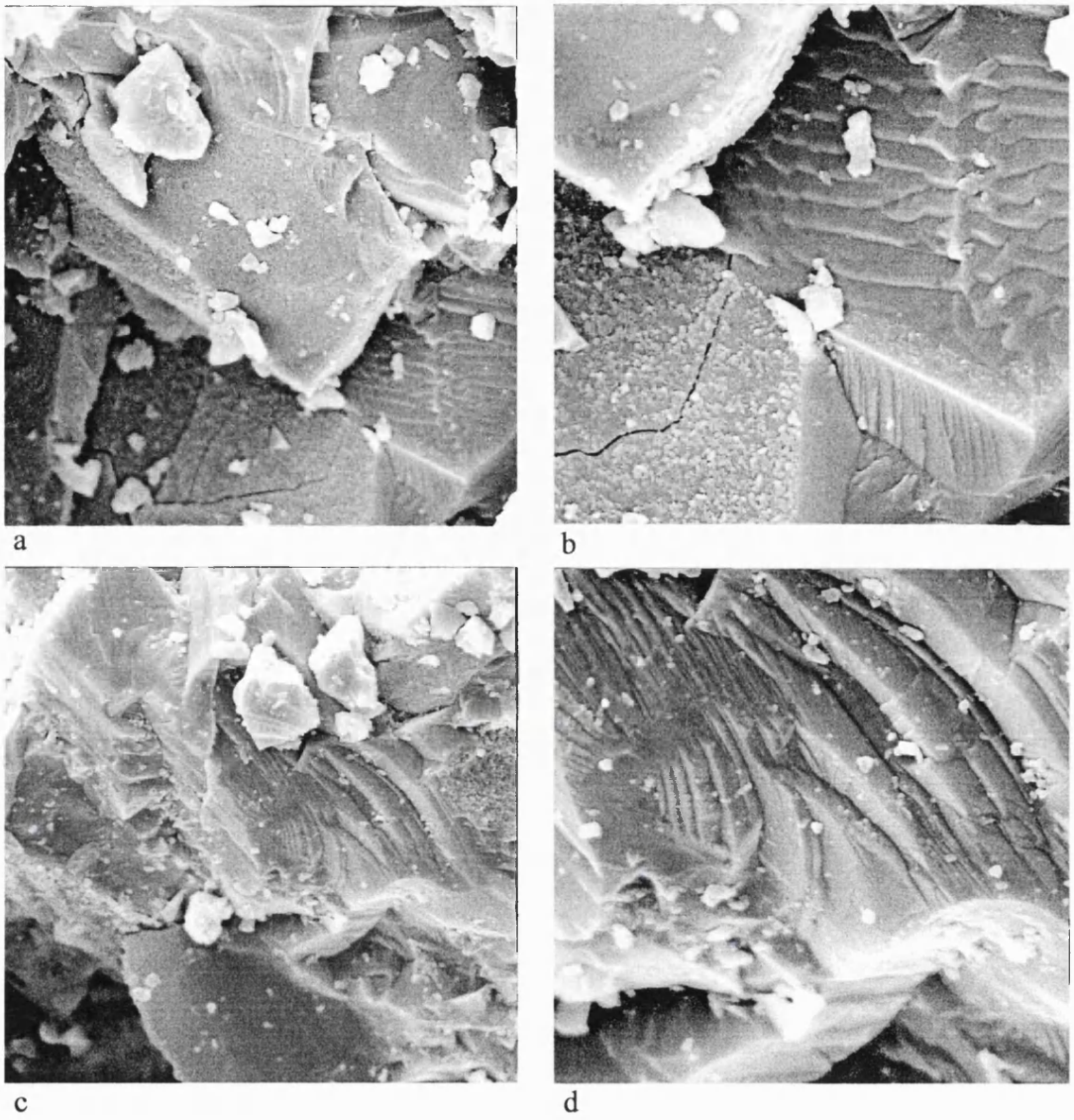

Fig. 9.21. SEM micrographs of crack surfaces. Left hand column are both x2000 with a field of view of 50μm. Right hand column are both x5000 with a field of view of 20μm. Both samples pictured above were tested at ambient temperature. a and b were tested under 150 bar CO_2 and c and d were tested under 200 bar CO_2.

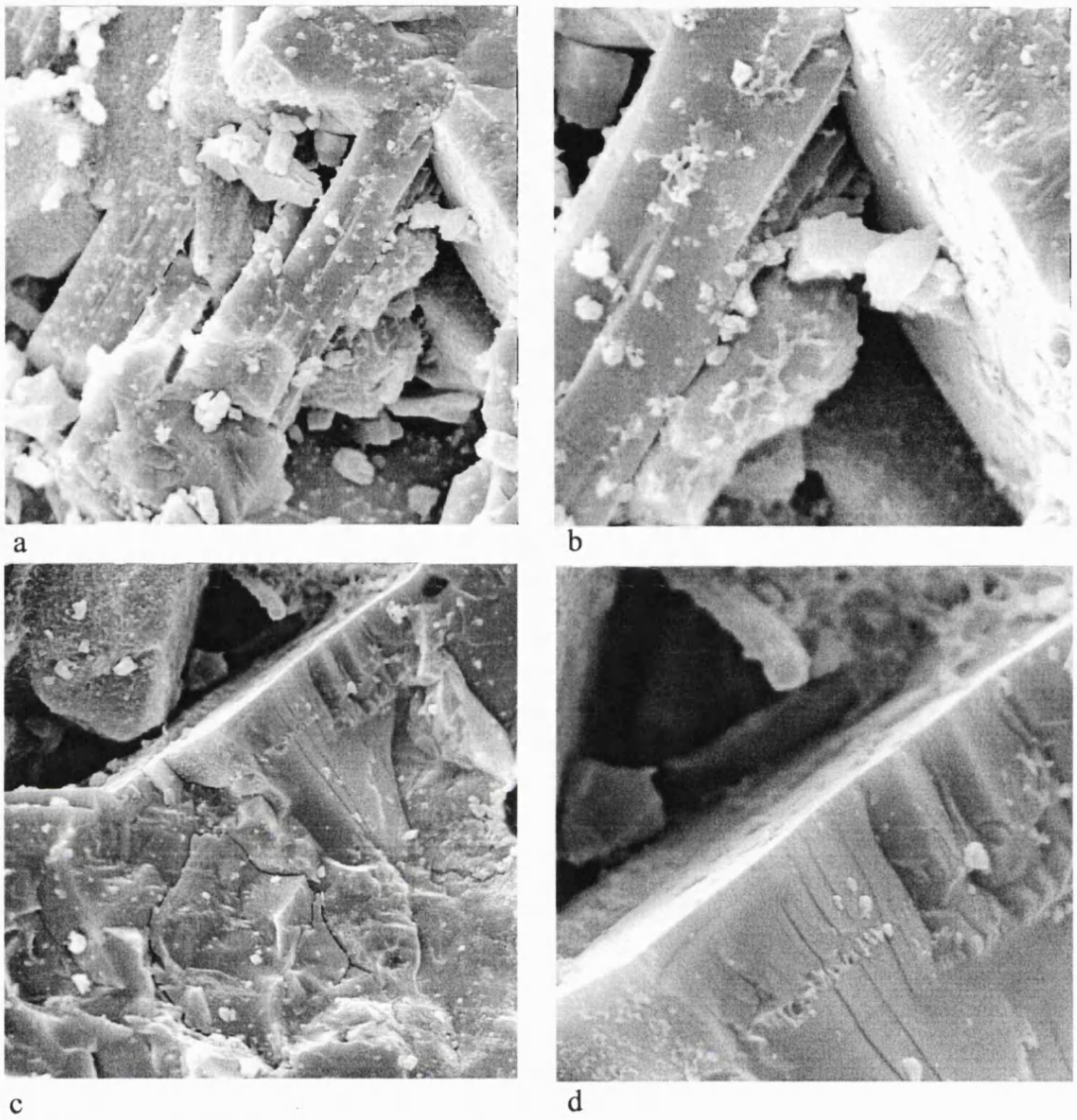

Fig. 9.22. SEM micrographs of crack surfaces. Left hand column are both x2000 with a field of view of 50μm. Right hand column are both x5000 with a field of view of 20μm. Both samples pictured above were tested at ambient pressure. a and b were tested at 150°C and c and d were tested at 300°C.

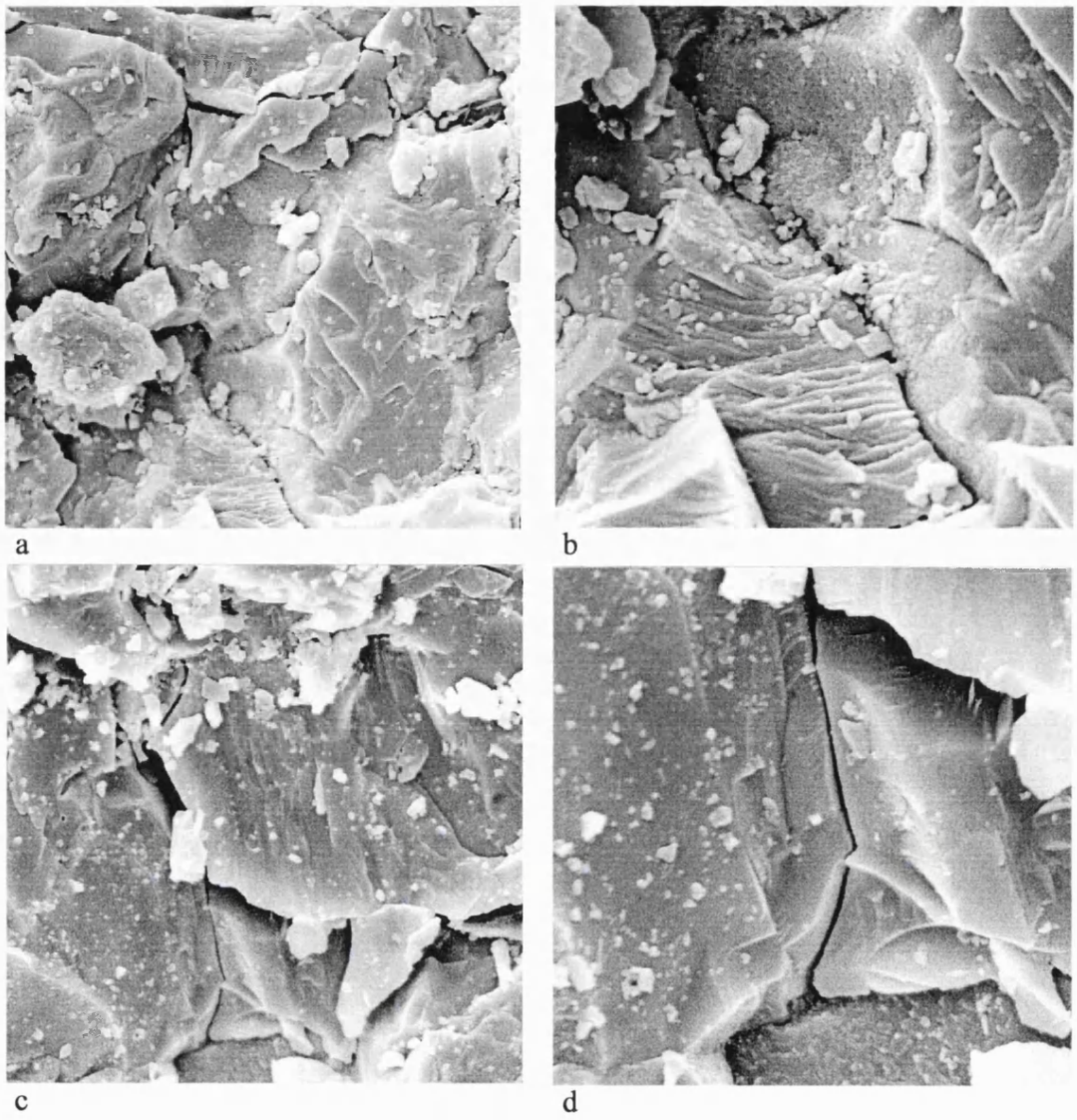

Fig. 9.23. SEM micrographs of crack surfaces. Left hand column are both x2000 with a field of view of 50μm. Right hand column are both x5000 with a field of view of 20μm. Both samples pictured above were tested at ambient pressure. a and b were tested at 450°C and c and d were tested at 600°C.

9.10.2. Optical microscopy of crack faces.

A binocular microscope was used to examine the opposite crack surfaces to those that had been sampled for observation using the SEM. There was a slight difference in the roughness of the three samples observed. The sample tested under ambient conditions was slightly rougher whereas the two samples tested at extremes of pressure and temperature had crack faces that were smoother. This may be because more stable cyclical crack growth occurred for the ambient sample. The poor turnover in the level II plots of the samples tested at extreme conditions tends to reinforce this idea (fig. 9.1).

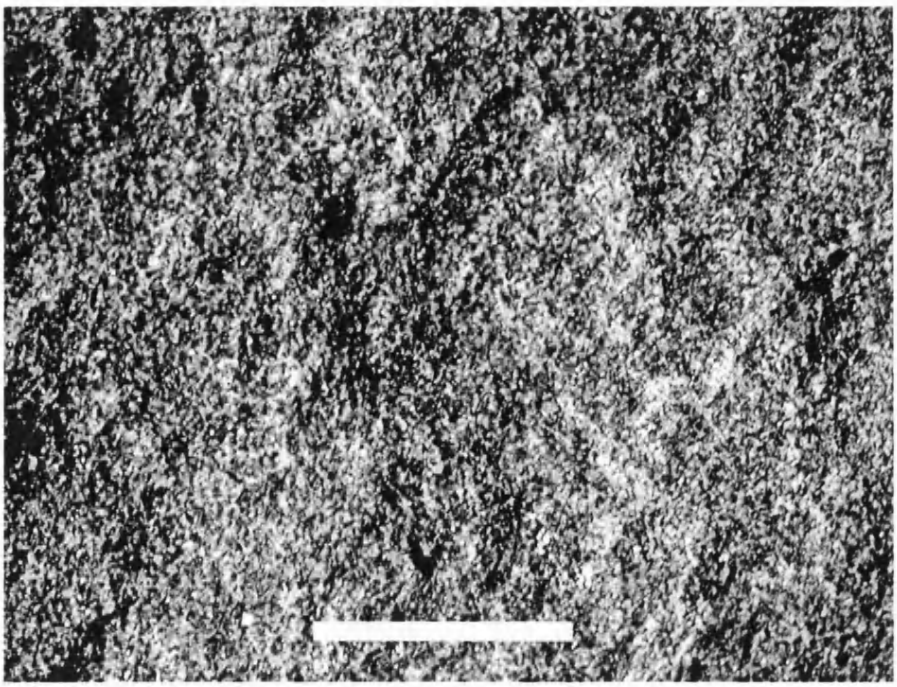

Fig. 9.24. Optical image of crack surface. Sample tested at ambient conditions. Scale bar is 3.5mm.

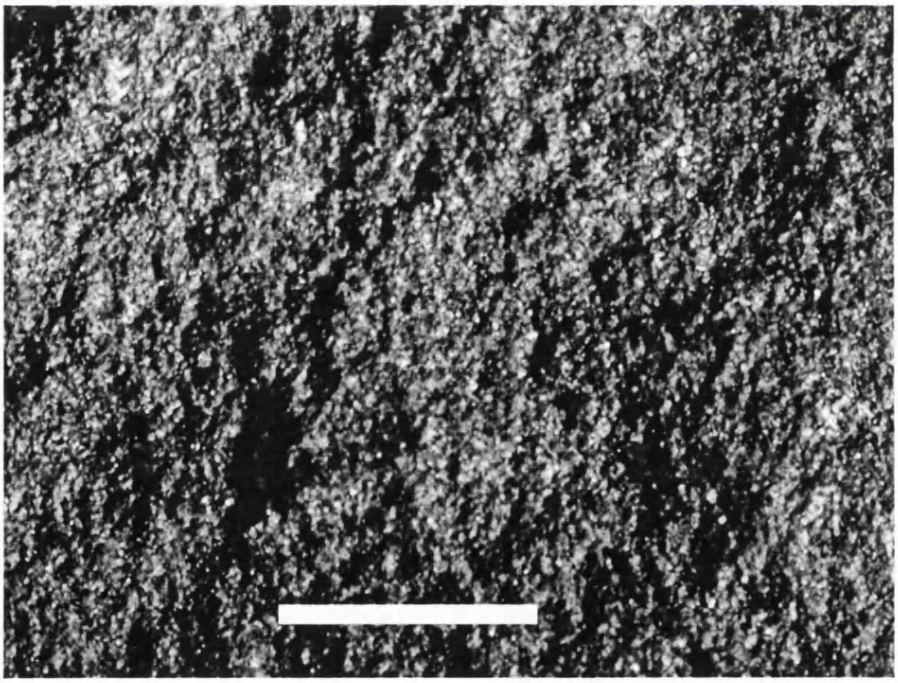

Fig. 9.25. Optical image of crack surface. Sample tested at ambient pressure and 600°C. Scale bar is 3.5mm.

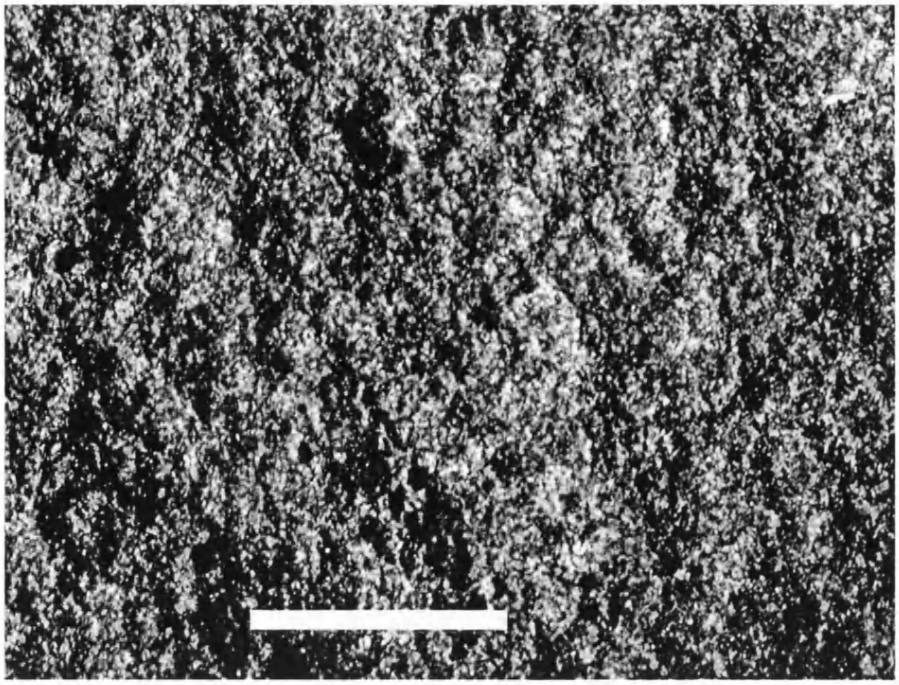

Fig. 9.26. Optical image of crack surfaces. Sample tested at ambient temperature under 200 bar CO_2. Scale bar is 3.5mm.

These images show little difference between the crack faces of end-member samples tested at extreme conditions. There is a slight difference in small-scale homogeneity for the extreme conditions samples, which appear to be rougher on the sub-millimetre scale but smoother on the millimetre scale. This may be because there were fewer cycles of loading and unloading that caused crack propagation in these samples. The sample tested at ambient conditions had more episodes of crack growth, resulting in a less flat failure plane.

9.11. Conclusions.

The data obtained show a distinct difference between the action of temperature and pressure on the value of fracture toughness. A confining pressure of as little as 50bars (5MPa) increases the corrected fracture toughness of basalt from the ambient pressure and temperature value of around 2.4 $MPam^{1/2}$ to approximately 3.0 $MPam^{1/2}$. Further increases in pressure to 200 bars were found not to increase the fracture toughness any further. The use of water as confining medium did not weaken the samples appreciably (unlike earlier tests on Darley Dale sandstone). Water at 100 bar toughened the samples to around 3.0$MPam^{1/2}$ in the same way as the use of high-pressure gas. Level I data showed similar trends to the corrected measurements, implying that the anelasticity factor did not have a controlling influence on these data.

Fracture toughness at 150°C was around 3.0MPam$^{1/2}$ but dropped to the level recorded for ambient tests at temperatures up to 600°C. These results should be independent of thermally induced crack growth owing to pre-cracking. The results are in agreement, however, with other studies, such as Meredith and Atkinson (1985), which did not thermally pre-crack the specimens. Possible explanations for this effect are discussed in chapter 11. Level I data followed the trends described for the level II tests but also showed an increase in fracture toughness at 600°C. The anelasticity factor, p, was highest for the 150°C measurements, which may be due to increased plastic behaviour at this temperature.

That the trends in fracture toughness were due to temperature and pressure, and not some other factor, was shown to be true by comparing the fracture toughness data with P-wave modulus, density and the thermal cracking parameter. None of these variables had a controlling influence on the value of fracture toughness measured. Variations in the anelasticity factor, p, could not be linked to level I fracture toughness but had a strong effect on level II toughness.

The K-resistance curve or Matsuki (1991a) method was applied to all the samples. Only those samples tested at ambient temperatures and pressures showed a typical K-resistance curve with a plateau. This is almost certainly due to apparatus effects as discussed in chapter 11. The Matsuki method results at ambient pressures and temperatures showed that the sample size of the specimens was sufficiently large that the data was valid because the plateau region was reached before the critical crack length.

Measurements of Young's modulus from the level II plots were very low compared with expected values (approximately 10GPa compared to an expected value of around 50GPa) even allowing for the thermal cracking damage introduced into the samples. There was a disparity between Young's modulus measured using this method and that measured using wave velocity measurements, which were a factor of three to four higher and closer to expected values. Also, the level II test results for Young's modulus were split into two populations: those performed at pressure and those performed at temperature. The pressure population had a measured Young's modulus about 50% higher than the temperature population. These results are discussed in chapter 11.

SEM and microscopy studies of the crack faces after testing revealed that the dominant failure mode is brittle intra and inter-granular cracking. There is no

observable change in failure mode with increases in temperature or pressure.

The actual value of fracture toughness of the Venusian crust is, obviously, impossible to measure at present, but this study constrains how it will vary with temperature and pressure and proposes an acceptable estimate. The present Venusian surface value of fracture toughness of basalt as measured from this study is proposed to be $3.0MPam^{1/2}$. This will change little with increases or decreases in temperature or with an increase in pressure up to 200 bars. The equivalent depth of overburden pressure associated with the highest pressure (200bar) at which fracture toughness was measured in this study is 0.77km. Thus, a value for fracture toughness of $3.0MPam^{1/2}$ is consistent with all proposed surface temperatures in the last 0.7Ma of Venusian history (Anderson and Smrekar, 1999) and for all depths up to approximately 800m and probably deeper.

Chapter 10

Application of fracture mechanics to experimental data and results from imagery.

10.1. Introduction.

Up to this point, I have discussed the results of experiments performed on laboratory scale samples of the order of a few centimetres and examined imagery from the surface of Venus showing structures with spacings of the order of kilometres. This chapter brings the two themes together and explains how the laboratory measurements are relevant to planetary issues.

To summarise, the results of the experimental work show that Venusian temperatures do not greatly affect the fracture toughness of basalt, whereas Venusian surface and shallow crustal pressures increase the fracture toughness of basalt by about 20%. The fracture toughness of basalt under Venusian conditions is ascribed a value of $3.0MPam^{1/2}$. The imagery work showed that the fractures were commonly concentric, with spacing slightly decreasing with distance from the centre of deformation. Typical spacings were 0.8-1.2km in the regions studied. Also, the widths of the fractures are less than 1 pixel in FMAP Magellan imagery, implying that the fracture widths are less than 75m, the size of one pixel.

A realistic theoretical model to describe these features must be capable of explaining the spacing and patterns observed in the imagery, using material values compatible with those obtained from the experiments. As described in section 3.7, previous models (Anderson and Smrekar, 1999; Banerdt and Sammis, 1992) of formation do not explain the spacing or distribution of CSPF adequately. This chapter presents the results from a new model using fracture mechanics data from experiments.

10.2.1. A new model for CSPF.

Consider a large rock mass with some pre-existing fracturing deformed by a remote tensile stress. In fracture mechanics theory (chapter four), mode I failure is assumed to initiate at the pre-existing flaw that is most deleterious for the given tensile stress field, and advances in a sense perpendicular to the principle tensile stress. Assuming, as we have, that the Venusian plains are composed of basaltic flood lavas, we should expect a large amount of jointing in the rock mass due to cooling. This is

reinforced by observations of joints forming in terrestrial lava-lakes at temperatures much higher than those on Venus (Johnson and Sandwell, 1992), and by surface observations of Venus which show blocky and fractured bedrock with spacings of the orders of a few decimetres (Garvin *et al.*, 1984). Thus, a large rock mass with pre-existing fractures is a suitable approximation to the plains of Venus prior to deformation by CSPF.

If we assume that the rock mass can be described as an elastic body, and that a tensile stress causes the largest and most appropriately aligned fracture to extend, we can calculate how deeply the fracture will propagate, infer the state of stress around it and calculate the effect this has on the initiation of new flaws. This is the basic method used in the model described here, which can be termed a fracture mechanics extension of the stress shadow model.

10.2.2. The edge crack

With reference to chapter four, we can interpret CSPF in the Venusian plains as being edge cracks in an elastic, semi-infinite plate and use stress intensity factors to describe their behaviour. Modelling the cracks as edge cracks in a plane is a valid assumption because the mean length of the fractures, as shown in chapter three, is approximately 20km and there is no break in slope for greater lengths. This is in contrast to the features with normal fault morphology described in Bowman and Sammis (1995) which were found to intersect CSPF in some parts of the study area, and it implies either that there is no mechanical boundary at depths up to 40 km (if the cracks are semi-circular) or that the fractures penetrate only to shallow depths. The depth to the brittle-ductile transition is likely to be much less than 40km (Solomon *et al.*, 1992) which implies that the latter holds. As the spacings are small, it is unlikely that the cracks would be semi-circular or deep semi-elliptical because they would leave thin slivers of material inclined to block rotation and down dropping. The stress shadow principle also forbids this. I therefore conclude that the length of each crack is much greater than its depth, and that we can treat the problem as 2-dimensional and model the fractures as edge cracks in a plate.

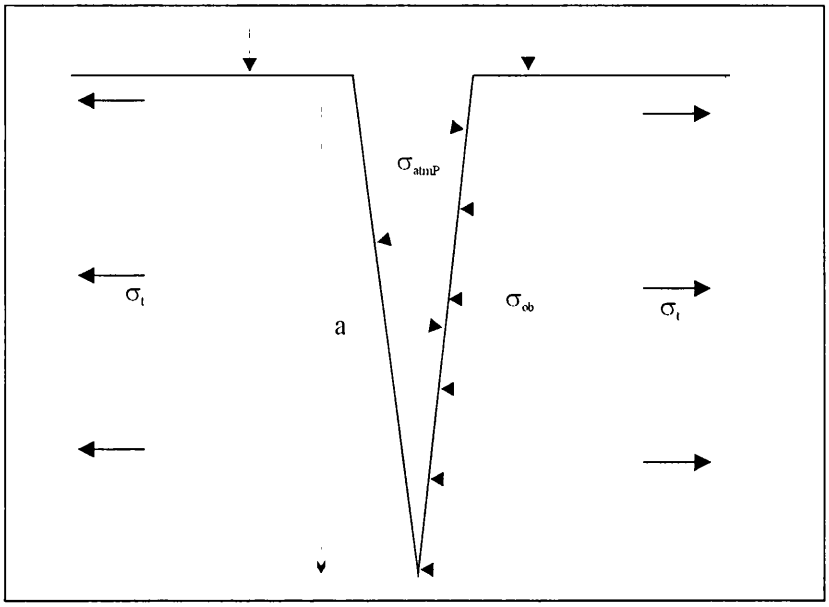

Fig. 10.1. Stresses acting upon a crack in an elastic, infinite half-plane (horizontal scale much exaggerated).

Fig. 10.1 shows a crack in a half-plane subjected to a tensile stress σ_t in the horizontal direction. A horizontal stress, σ_{ob} due to the overburden pressure, acts to oppose this tension and increases linearly (assuming constant density of material) with depth. The effects of a dense atmosphere, such as that of Venus, are shown as a stress acting perpendicular to any free surface, σ_{atmP}. Intuitively it would seem from the above diagram that the atmospheric pressure would tend to add to the tensile stress that is opening the fracture. However, the lithostatic overburden pressure must also include the extra vertical pressure associated with the atmosphere. As this stress acts in all directions, the atmospheric component cancels that acting on the faces of the crack. Therefore the problem reduces to that of the case with no atmosphere. This is valid because the length of time required for extensional stress to build up in the lithosphere is greater than the relaxation time required for lithostatic pressure to become isotropic. It should also be noted that the density of the atmosphere is still much less than that of the rocks ($60 kgm^{-3}$ as opposed to $3000 kgm^{-3}$) and thus the difference between the lithostatic pressure and the atmospheric pressure can also be ignored. For an isolated edge crack, the stress intensity factor for a tensile load is given by

$$K = 1.12\sigma_t\sqrt{\pi a} \qquad (10.1)$$

where a is the depth of the crack and σ_t the applied load (Lawn, 1993). The stress intensity factor for an edge crack loaded by a linearly varying stress at its margins, however, is given by

$$K = 0.683\sigma_d\sqrt{\pi a} \tag{10.2}$$

where σ_d is the linearly varying stress (Hartranft and Sih, 1973). In this case, σ_d is the overburden pressure and can be written as

$$\sigma_d = \rho g z \tag{10.3}$$

where ρ is the density of the rock, g is the gravitational force and z the depth. These two stress intensity factors can be summed to give the total stress intensity factor for the system where a is now replaced by z, the depth of the crack

$$K = 1.12\sigma_t\sqrt{\pi z} - 0.683\sqrt{\pi}\rho g z^{3/2} \tag{10.4}$$

Note that the overburden pressure stress intensity factor is negative because it opposes the opening action of the tensile stress. A negative stress intensity factor indicates a closing regime. Wherever this stress intensity factor exceeds the fracture toughness of the material, a crack will grow perpendicular to the most tensile force. When it is equal to or less than the fracture toughness of the material, the crack will not propagate further. Hence for crack extension $K>K_c$. This result is shown graphically in figure 10.2 for various values of σ_t. This method has also been used to interpret crevasses in ice (Rist *et al.*, 1996).

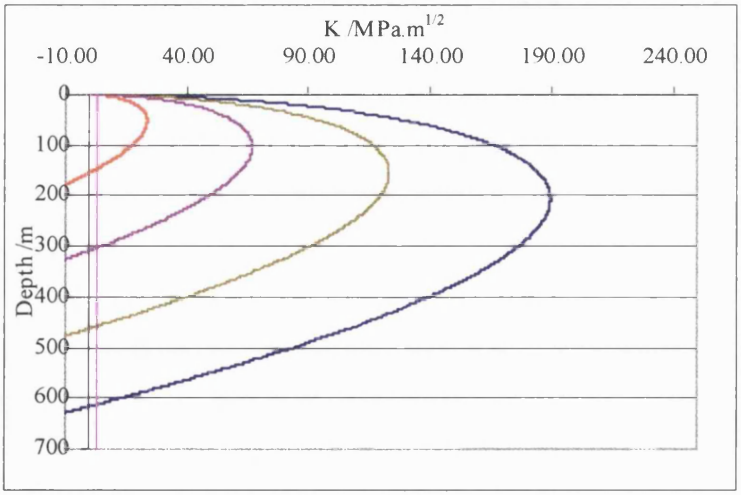

Fig. 10.2. Penetration depths of a single crack. Pink line represents experimental fracture toughness results, K_c where K_c = 3.0 MPam$^{1/2}$ from experiments (chapter nine) and is shown by the vertical pink line. The plots are: red, σ_t = 2.5MPa; purple, σ_t = 5.0MPa; green, σ_t = 7.5MPa and blue, σ_t = 10.0MPa.

In figure 10.2, the crack will be unstable to the right of the fracture toughness line and stable to the left. Realistic variations in fracture toughness make very little difference to the depth of propagation. However, the depth of a starter crack required

before the system becomes unstable depends greatly upon the value of K_c. The part of the graph near the origin is almost exactly the same as a plot of the stress intensity factor of an edge crack solely loaded by σ_t (the effects of overburden being insignificant at these depths). Thus the plot serves as a crack initiation criterion indicating the maximum crack length stable for a given tensile load. A close-up of this part of the graph is shown in figure 10.3. The dependence on the size of the starter crack required (i.e. the depth at which a given tensile load will begin to propagate the crack) is clearly shown. The experimental values for fracture toughness measured under 10MPa of pressure have a mean of 3.0MPam.$^{1/2}$ and are as reliable a measure of the resistance to fracture of Venusian rocks as can be made at this time.

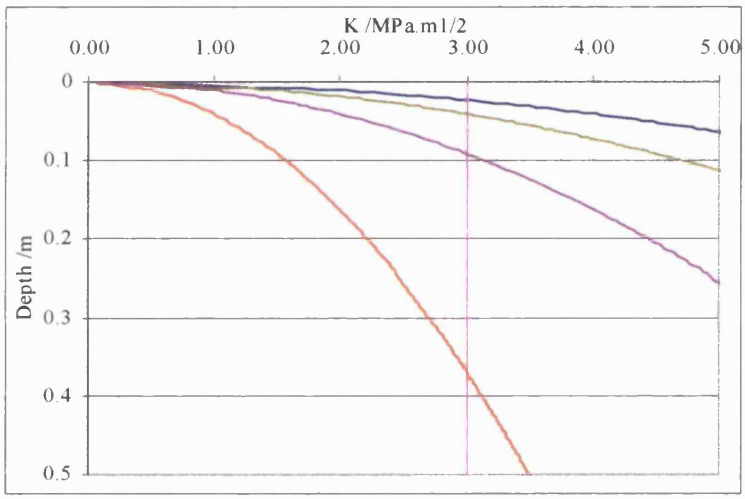

Fig. 10.3. Required length for instability of an edge crack. Plots as for figure 10.3: red, σ_t = 2.5MPa, purple, σ_t = 5.0MPa, green, σ_t = 7.5MPa and blue, σ_t = 10.0MPa. Experimental results approximated by K_c = 3.00 (pink line).

Fig. 10.3 shows how the value of K_c controls the scale of starter crack required. A tensile stress of 10MPa will initiate crack growth in appropriately aligned cracks as small as 10cm, whereas a 2.5MPa remote stress requires a much larger crack, 60cm in depth, before propagation occurs. Table 10.1 shows the size required for a variety of stresses. The coupling between the fracture toughness and crack size population and the influence it exerts on crack spacing will be explored further in sections 10.5 and 10.6.

Remote stress /MPa	Smallest crack size for propagation /metres.
1.0	2.28
1.5	1.01
2.5	0.36
5.0	0.09
7.5	0.04
10.0	0.02
20.0	0.01
15.0	0.01
>15	< 0.01

Table 10.1. Smallest crack which will propagate in a given remote tensile stress field. Any crack larger than this value will extend until stopped by the arresting effects of overburden.

10.3. Multiple edge cracks.

The single edge crack, although useful in highlighting the effects of changes in the controlling variable, is not an accurate representation of the problem. We need to consider multiple cracks in order to model CSPF. The first step is to qualitatively explain how CSPF may have formed.

Let us consider a homogenous plain of basaltic rock, containing a large number of small joints caused by thermal stresses as it cooled. Owing to a remote, regional tectonic force, the portion of the lithosphere of which this large basaltic province is a part begins to be subjected to a horizontal tensile stress. If the local tensile stress becomes large enough, crack extension at the most deleterious defect will occur. As the tensile stress increases with time, the crack propagates deeper whilst other, smaller or less appropriately aligned cracks also begin to extend. However, cracks in the vicinity of the deeper flaws are shielded from the tensile stress by the mechanism of stress shadowing (fig. 3.25). Thus only the deeper cracks propagate. As the tensile stress increases to its maximum, these flaws grow, their stress shadows excludes an increasing number of other cracks from propagating until a saturation point occurs. At this point no new cracks can open at the surface owing to the shielding effects of the deeper cracks.

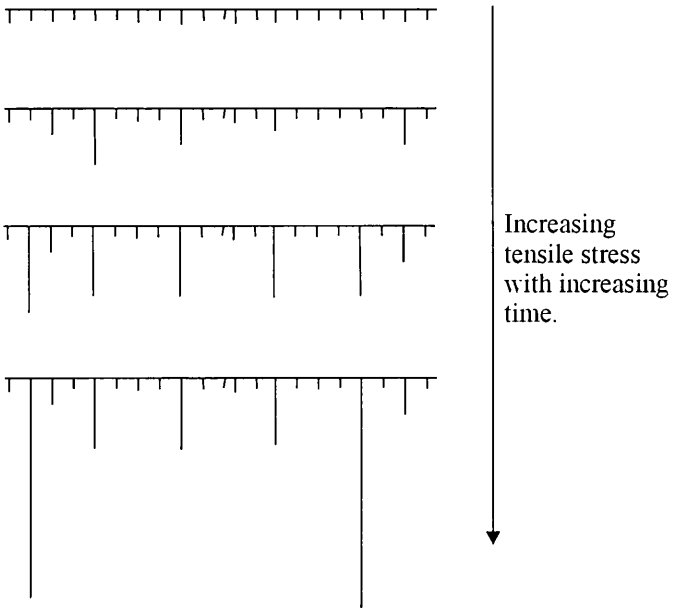

Fig. 10.4. Two-dimensional side-view of propagating cracks starting from cooling joints. As the stress increases certain cracks will grow until they shield all other defects from the tensile stress. This model has been proposed by Nur (1981) for fractures in rocks and a similar model tested by Geyer and Nemat-Nasser (1982) using hot glass plates suddenly cooled to generate a tensile stress.

From a three dimensional perspective, the cracks would also be seen to propagate laterally, their terminations occurring where the tensile stress becomes too low, at stress shadow regimes caused by other cracks, or at mechanical boundaries such as large faults. The first crack formed would probably extend the furthest, with other cracks taking the "available stress" where they could. In this way a fully developed field of fractures would consist of long, shallow fractures whose spacing depended upon their depth and available tensile stress. The available tensile stress would depend upon the depth and proximity of neighbouring cracks. Thus the problem of saturation spacing becomes a balance between the depth a set of fractures can be driven by a tensile stress and the closest spacing that such cracks can take whilst barely excluding propagation of new cracks at the surface.

10.4. Application of fracture mechanics to multiple crack problem.

If we consider a part of a large field of equally spaced, parallel fractures we can approximate them as a set of repeated edge cracks as shown in fig. 10.5.

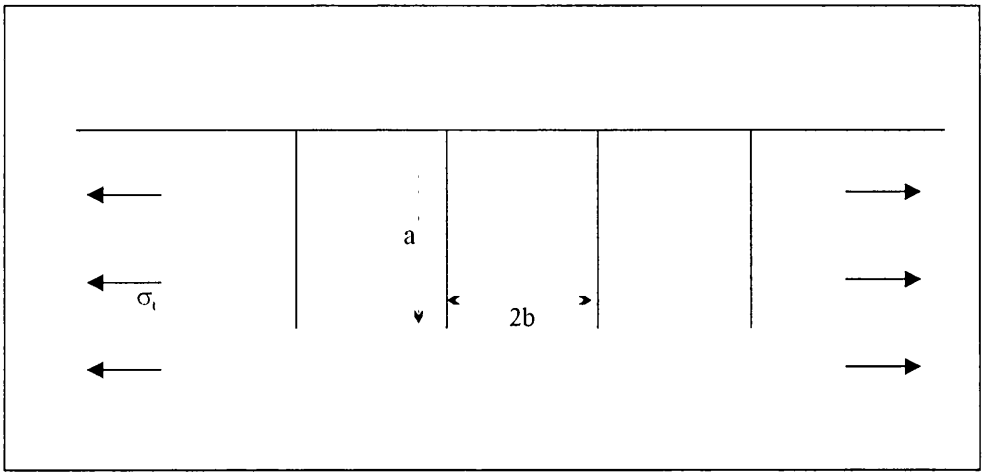

Fig. 10.5. Multiple crack problem (only three are shown here for clarity but the solution is only relevant to large numbers (greater than about 10) of parallel edge-cracks). All cracks are considered to have a depth a and are a distance 2b apart. The tensile force is denoted σ_t.

Not only do multiple cracks affect the local stress, they also have the effect of reducing the stress intensity factor at the crack tips. This problem has been addressed by several authors, using a variety of methods (Bentham and Koiter, 1973; Nied, 1987; Sassolas *et al.*, 1996) although the results are all very similar. Bentham and Koiter (1973) gave the following formula for the mode I stress intensity factor for exactly the type of problem shown in fig. 10.5.

$$K_{MC} = F\left\{\frac{b}{s}\right\}\sqrt{\frac{b}{s}}\sigma_t\sqrt{\pi a} \tag{10.5}$$

where a, b and σ_t are as for figure 10.5 and s = b + a. The subscript MC refers to multiple cracks. F{b/s}is a function that describes the geometry of the problem, similar to the factor 1.12 π in equation (10.1) and is shown in fig. 10.6 and given by

$$F\left\{\frac{b}{S}\right\} = \frac{1}{\sqrt{\pi}}\left[1+\frac{1}{2}\left(\frac{b}{S}\right)+\frac{3}{8}\left(\frac{b}{S}\right)^2+\frac{5}{16}\left(\frac{b}{S}\right)^3+\frac{35}{128}\left(\frac{b}{S}\right)^4+\frac{63}{256}\left(\frac{b}{S}\right)^5+\frac{231}{1024}\left(\frac{b}{S}\right)^6\right]$$

$$+22.501\left(\frac{b}{S}\right)^7+-63.502\left(\frac{b}{S}\right)^8+58.045\left(\frac{b}{S}\right)^9-17.577\left(\frac{b}{S}\right)^{10} \tag{10.6}$$

Thus (10.5) gives the stress intensity factor for a series of parallel edge cracks which tends towards the value of the single crack as 2b tends to ∞ as shown in fig. 10.6.

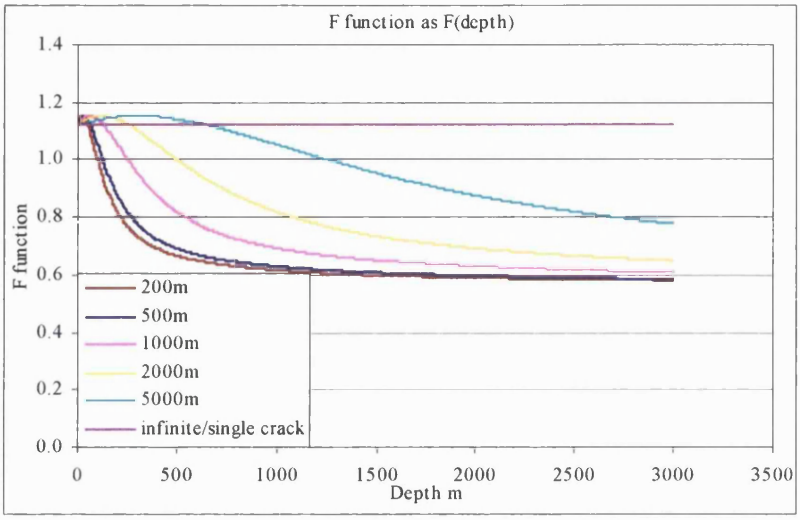

Fig. 10.6. 'F-function' as a function of depth for various values of 2b (crack spacing) as shown in the legend.

The linearly increasing overburden pressure also has an associated stress intensity factor, which is (modified from the result of Hartranft and Sih, 1973)

$$K_{OB} = 0.693\rho g a^{3/2}\sqrt{\pi} \tag{10.7}$$

where ρ is the density of the rock, g the acceleration due to gravity and a the depth of the crack. The signs of these stress intensity factors, K_{MC} and K_{OB}, are obviously opposite because the overburden tends to close the crack whilst the tensile stress works to extend it. Hence the overall stress intensity factor for the system is given by

$$K = K_{MC} - K_{OB} \tag{10.8}$$

which in full is

$$K = \sqrt{\pi}.\left[F\left\{\frac{b}{s}\right\}\sqrt{\frac{b}{s}}.\sigma_t\sqrt{a} - 0.693\rho g a^{3/2} \right] \tag{10.9}$$

When this stress intensity factor is greater than the fracture toughness of the rock, the crack will be unstable and grow. If (10.9) is less than the fracture toughness, however, the crack will be stable. By plotting (10.9) against depth as in section 10.2.2, we can find the depth of stability for a given tensile stress. These data are shown in figure 10.7. It is clear that for increasing tensile stress the material properties of the rock become less and less significant. Hence the fracture toughness envelope is omitted in the latter plots in fig. 10.7 due to it being virtually identical to the y-axis. The results from figure 10.7 allow us to plot spacing of fractures against depth of penetration for a variety of different applied stresses (fig. 10.8). This plot shows a family of curves, each internally consistent in that the depth to which they penetrate is controlled by the stress and the spacing.

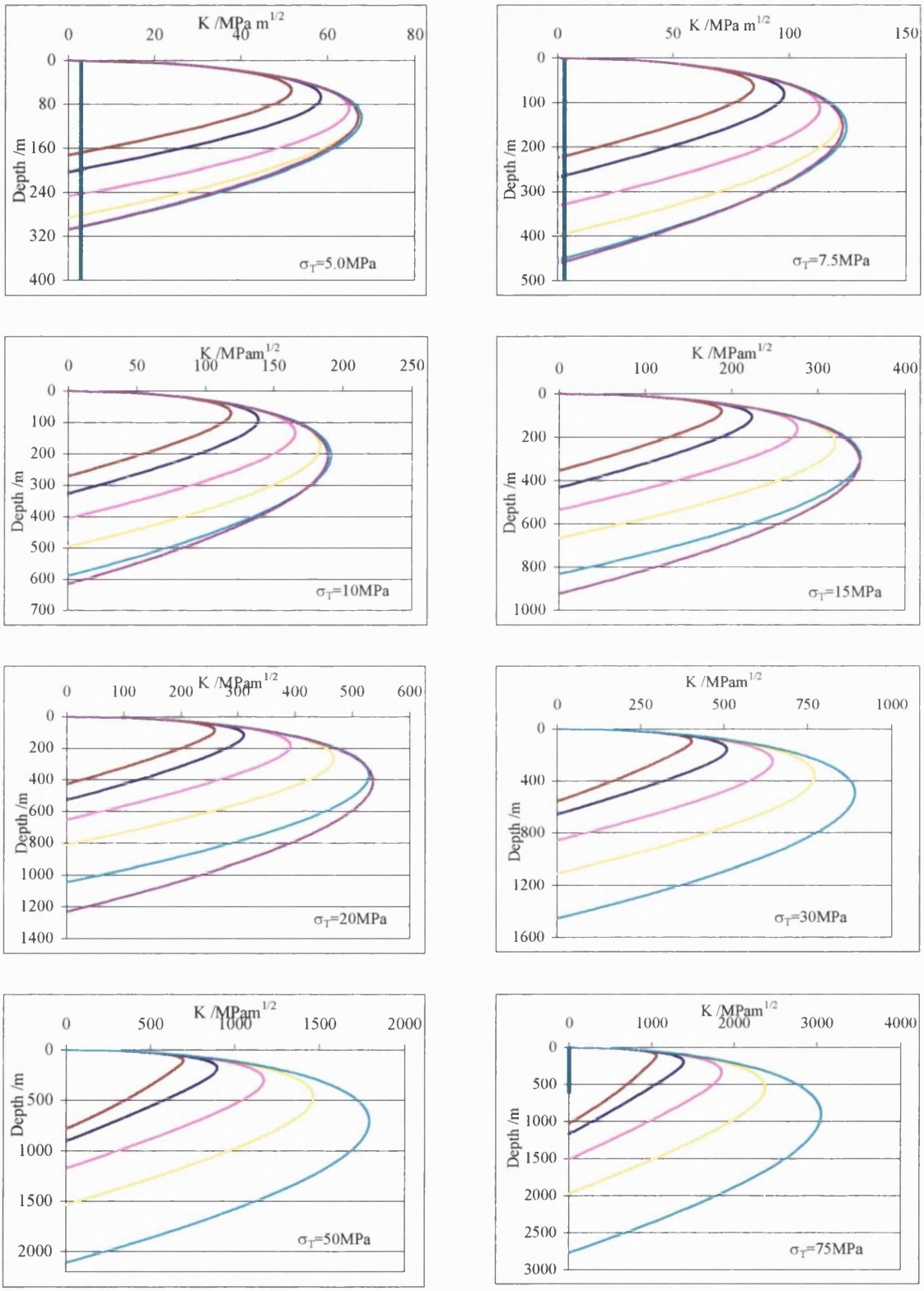

Fig. 10.7. Stress intensity factors of multiple crack system for a variety of crack spacings. Brown =200m spacing, dark blue =500m spacing, pink =1000m spacing, yellow =2000m spacing, pale blue =5000m spacing, purple =infinite spacing (single crack). The green line (or the y-axis for larger stresses) represents the experimental fracture toughness. Crack propagation occurs to the right of this line, stability occurs to the left. Note single crack result is omitted from plots with higher stresses.

The initiation criteria would be similar to those shown in fig. 10.3 but controlled by the stress shadowing mechanism referred to in section 10.2. In almost all cases shown in fig. 10.7, the depth of crack penetration is essentially independent of the fracture toughness of the material because the experimentally measured fracture toughness is much smaller than stress intensity factor.

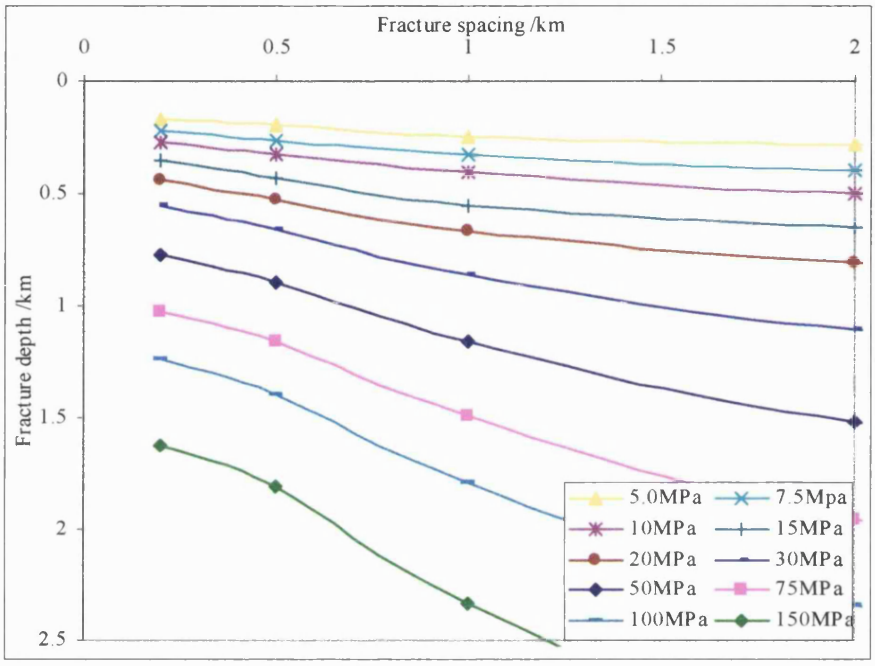

Fig. 10.8. Effects of crack spacing on penetration of cracks. The plot clearly shows that, for a given applied stress, the closer the cracks are spaced, the shallower their penetration.

Fig. 10.8 shows that a continuum of different stresses and depths are consistent with a given crack spacing. Obviously, this plot describes only fully-grown fractures and does not take into account initiation of cracks. By applying the stress shadow principle, we can now analyse how the spacing of fractures may affect initiation of new fractures and bring this result to bear on the results from fig. 10.8.

10.5. Stress shadow for vertical edge crack.

There is no exact solution for the horizontal stress relief at the surface of a semi-infinite half-plane, loaded in remote tension and close to an edge crack (Paris, P. C., personal communication, 2000). The solution for a Griffith flaw of length 2a does have a solution and is estimated to describe the case of an edge crack of length a, with an error of less than 10% (Paris, 2000). The edge crack can also be approximated by a

linear increase in stress from the edge of the crack with a gradient of $1/\pi$ (Bazant, and Cedolin, 1991). The Griffith flaw and Bazant approximations are shown in fig. 10.9.

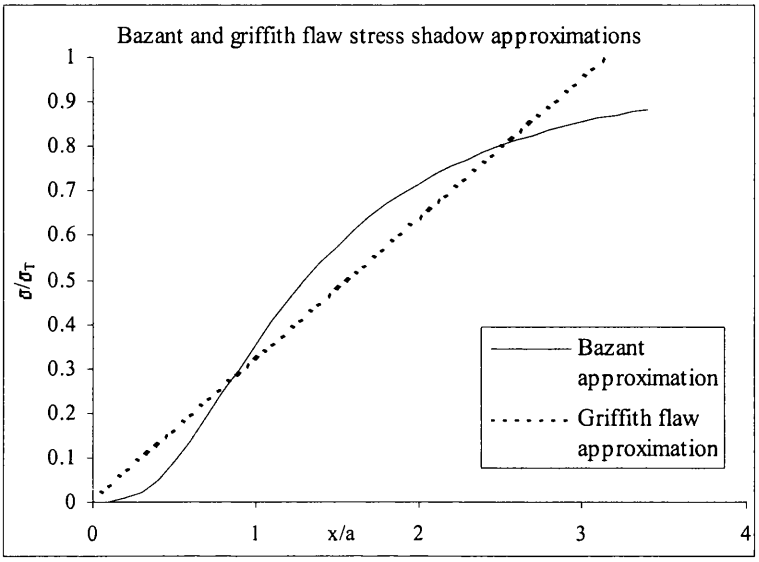

Fig. 10.9. Bazant and Griffith flaw approximations for the stress shadow near an edge crack of length a. σ/σ_T is the fraction of the remote stress felt at the surface at a distance x/a from the edge of the crack. x is the horizontal distance from the crack.

The Bazant approximation assumes that the horizontal surface stress close to the crack returns to the level of the remote stress at a distance of πa from the crack. In the case of multiple fractures, the spacing at which the stress reaches the value of the remote tensile stress midway between two fractures is $2\pi a$, assuming that only the stress shadows from adjacent cracks modify the surface stress. The stress does not have to return to the level of the remote stress to initiate a new fracture, however, because the pre-existing flaws may extend at stresses less than this. We can approximate these pre-existing flaws as small edge cracks that can be found at all points throughout the semi-infinite plane and calculate the stress required for crack initiation from (10.1). We can then equate this stress to the stress close to an edge crack given by the Bazant approximation as

$$\sigma = \frac{\sigma_t x}{\pi a} \qquad \text{as long as } \frac{2b}{a} \le \pi \qquad (10.10)$$

where x is the distance from the edge of the crack. The critical spacing at which this stress is just enough to initiate fracture will then be given by

$$\frac{2b}{a} = \frac{K_c\sqrt{\pi}}{1.12\sigma_t\sqrt{c}} \qquad \text{as long as } \frac{2b}{a} \le \pi \qquad (10.11)$$

$$\text{or} \qquad \frac{2b}{a} = \frac{S\sqrt{\pi}}{1.12\sigma_t} = 1.58\frac{S}{\sigma_t} \quad \text{where} \quad S = \frac{K_c}{\sqrt{c}} \text{ as long as } \frac{2b}{a} \leq \pi \qquad (10.12)$$

from (10.1) and (10.10) where 2b is the spacing of the cracks, a is the crack depth and c is the dimension of the starter cracks. S is a parameter, with units of MPa, which describes the resistance to fracture of the rock mass and can be seen as the dimensional equivalent of the tensile strength of the rock mass. Note that the factor of 2 introduced to calculate the spacing cancels out because the stress at the surface is halved (using the principle of superposition of stresses) owing to the interacting stress shadows of the two adjacent cracks (again, we assume only two adjacent fractures affect the initiation between them).

If $2b/a > \pi$ no crack initiation will occur because the stress is insufficient to generate cracking in the material. This leads to the conclusion that an increase in the resistance to fracture of the material will lead to an increase in the spacing of cracks and that increasing magnitudes of remote tensile stress form more closely spaced cracks. The size of the starter crack will also control the spacing, larger starter cracks leading to more closely spaced fractures. In the following calculations, I will investigate the variation of fracture spacing in terms of the fracture resistance parameter S. Finally, the experimental data can be used to constrain the possible values of S that can be used.

In a similar way to the calculations used for table 10.1, we can also find the minimum stress that will open a crack of any kind in a rock mass with fracture resistance parameter S. Treating the cracks as edge cracks and inserting the values for constants in (10.1) we find that

$$\sigma_t \geq 0.5S \text{ for crack initiation} \qquad (10.13)$$

where σ_t is the remote tensile stress and S the rock mass fracture resistance. Also, we can rearrange (10.1) to show that

$$c_{\min} = \left(\frac{K_c}{S}\right)^2 \qquad (10.14)$$

where c_{min} is the minimum starter crack size required for crack initiation and K_c is the fracture toughness of the rock.

10.6. Equilibrium fracture spacing.

The calculations of section 10.4 describe the penetration depth of a set of fractures with a given spacing as a function of remote tensile stress. 10.5 describes the initiation of cracks between adjacent fractures of known depth, and from this a calculation of the ratio of depth to spacing can be made. By combining these results we can find the spacing, depth, size of starter crack and remote tensile stress consistent with any given fracture spacing. Using (10.11), we can plot 2b against a onto fig. 10.8 for various values of remote tensile stress and rock mass damage parameter, S. Then, by finding the point at which the lines for two equivalent remote stresses cross, we can plot fracture spacing against remote tensile stress. The plots for equilibrium spacing for S = 10, 20 and 35MPa are shown in fig. 10.10, in which the straight lines emanating from the origin are lines of consistent stress shadow fracture initiation from (10.12) and the curved lines are reproduced from figure 10.8.

The equilibrium fracture spacing is shown as a function of remote tensile stress and depth figs. 10.11 and 10.12 respectively. Fig. 10.11 shows that the value of S is a key controlling factor in the spacing of CSPF (S is equivalent to the gradient of the stress shadow lines in fig. 10.10). The majority of CSPF measured in this study have spacings between 0.8 and 1.2km which, according to this model, is most consistent with a rock mass fracture resistance of between 10 and 35 MPa. Lower values of S consistent with spacings of 0.8-1.2km require remote tensile stresses too low to initiate fractures and cannot form CSPF. Also apparent is that a stronger rock mass (i.e a larger value of S) leads to wider separation and deeper penetration of fractures. The shape of the curves in fig. 10.11 demonstrates that increasing remote tensile stress decreases the spacing at a decreasing rate, indicating a finite limit to how small the spacing of CSPF can be. With decreasing remote tensile stress, however, the fracture spacing increase is curtailed when the stress is insufficient to initiate fracture. This puts a bound on the maximum spacing that CSPF can achieve for a given remote tensile stress.

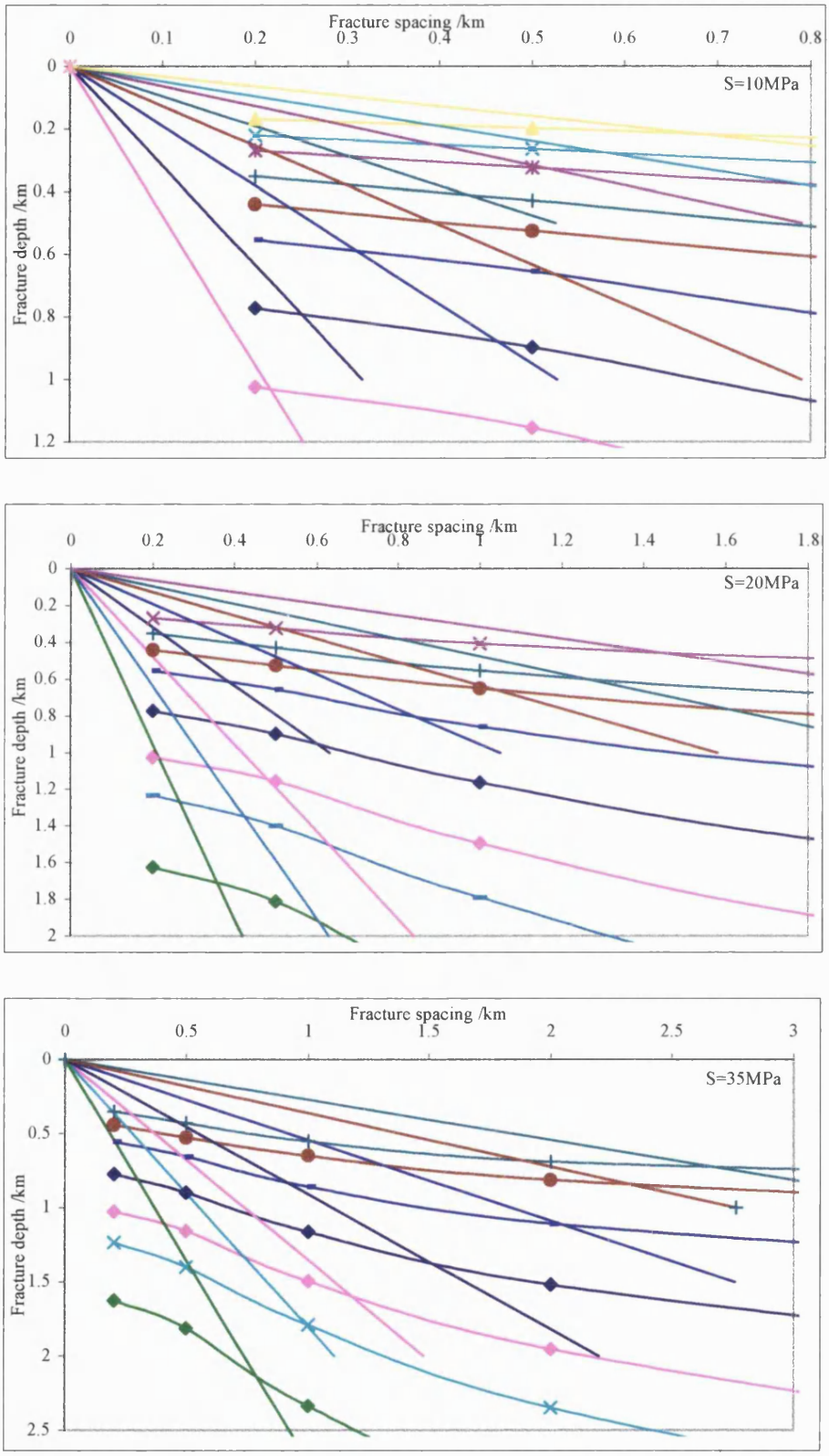

Fig. 10.10. Equilibrium spacing plots for S=10, 20 and 35 MPa. Yellow, σ_t = 5MPa, light-blue (crosses), σ_t = 7.5MPa, purple, σ_t = 10MPa, dark green, σ_t = 15MPa, brown, σ_t = 20MPa, mid-blue, σ_t = 30MPa, dark-blue, σ_t = 50MPa, pink, σ_t = 75MPa, light-blue (lines) , σ_t = 100MPa, bright-green, σ_t = 150MPa. Only results for $T \geq 0.5S$ are shown.

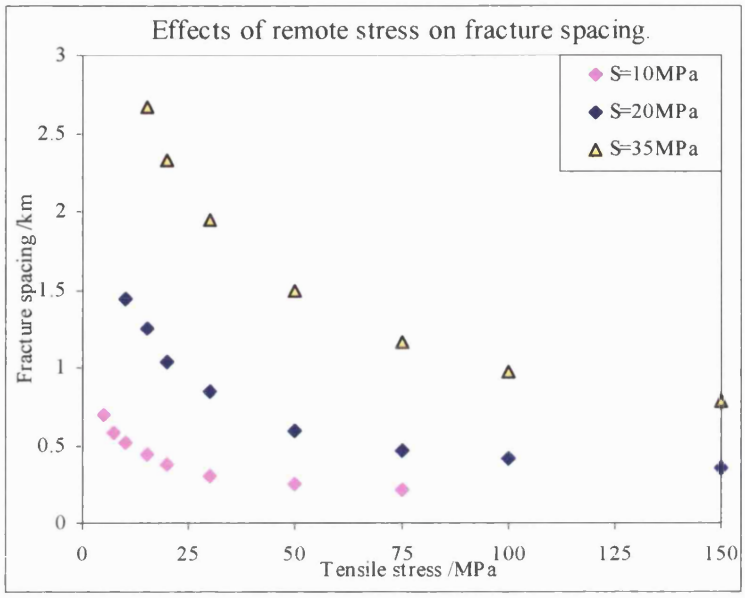

Fig. 10.11. Fracture spacing as a function of remote tensile stress for S=10, 20 and 35 MPa. Lowest values for tensile stress indicate the level below which no cracks can initiate.

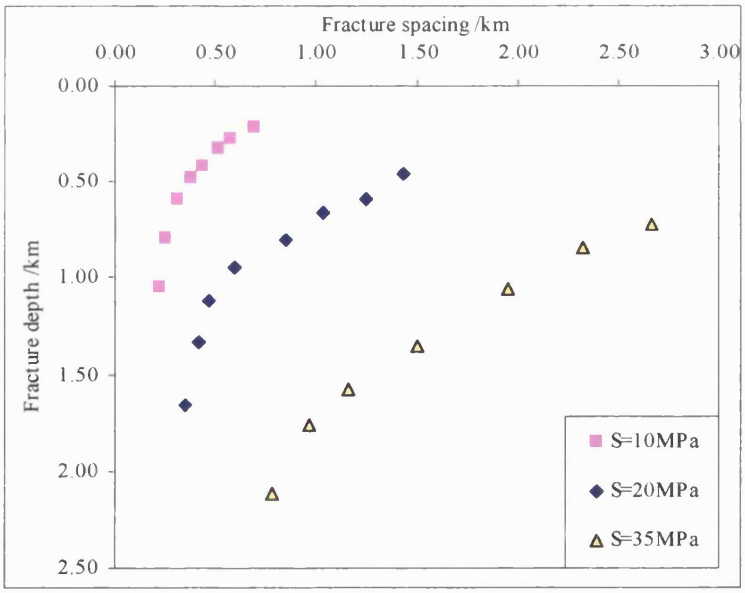

Fig. 10.12. Fracture spacing and associated fracture depth for S = 10, 20 and 35MPa. Furthest extents of data plotted are bounded by smallest stress that can initate fracture (on the right hand side) and by σ_t=150MPa, the highest stress level used in the model.

10.7. Faulting vs. fracturing.

Fig.10.13 shows the depth variation of fractures plotted together with the criterion for normal fault initiation. The criterion for normal faulting only applies, however, where the normal stress is much greater than the cohesion of the rock mass (Ranalli, 1995). Schultz (1993) states that the cohesion of basalt at Venusian conditions is likely to be 0.5-5MPa. This means that for remote stresses below about 10MPa, at

depths of less than about 0.5km (and for lower stresses at greater depths), this criterion is invalid. Fig. 10.13 shows that extensional features formed at the surface are unlikely to remain vertical for their entire depth and will instead form normal faults in almost all cases. Only at shallow depths and low tensile stresses will normal faulting not occur because the magnitudes of the stresses are insufficient to overcome the cohesion of the rock mass.

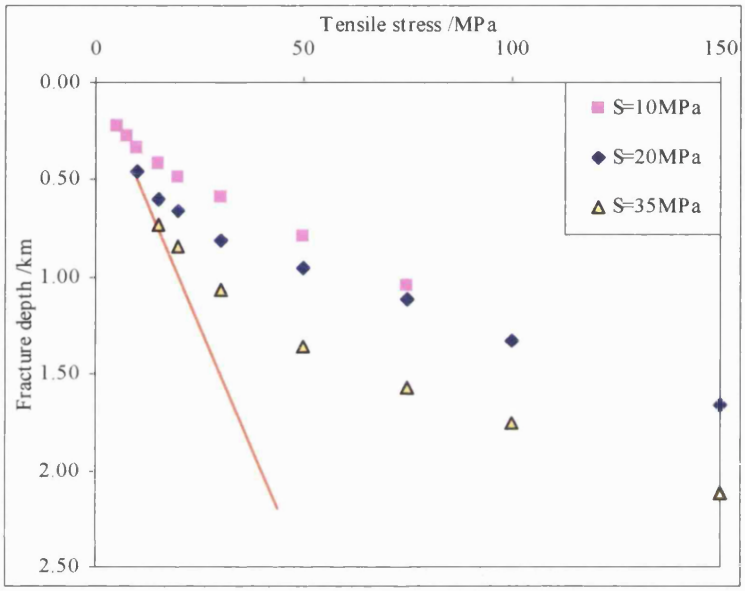

Fig. 10.13. Depth of crack penetration as a function of remote tensile stress for S = 10, 20 and 35 MPa. Also shown is faulting criterion (red line) from (4.33). Normal faulting occurs to the right of the criterion.

The conditions that favour extensional fractures rather than faulting are only met for stresses that are just large enough to initiate fractures at the very edge of the stress shadow, data-points to the extreme left in fig. 10.13. These stresses can be labelled $\sigma_{t(crit)}$ where

$$\sigma_{t(crit)} = 0.5\ S, \text{ based on (10.14)}, \sigma_t \geq 0.5\ S. \qquad (10.15)$$

Fracture spacing must, therefore, be about πa where a is the fracture depth, otherwise the fractures would show graben or tilted-block morphology (Papparlardo and Greeley, 1995). By adding the line $2b=\pi a$ to fig. 10.12 (where 2b is the crack spacing and a is the depth), we can find the spacing consistent with the transition from jointing to faulting and plot S parameter against this spacing. This result is shown in fig. 10.14.

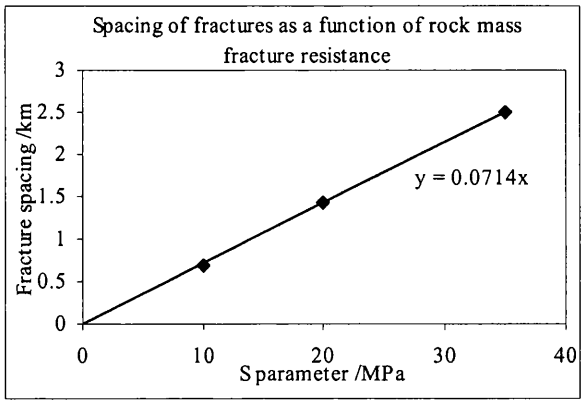

Fig. 10.14. Fracture spacing as a function of rock mass fracture resistance parameter, S, in the case where $2b = \pi a$ to ensure that extension occurs rather than faulting.

The linear best fit line shown in fig. 10.14 can then be used to give an estimate of the size of the S parameter for the observed spacings. From chapter three, the measured spacings in the study area were generally betweeen 0.8 and 1.2km. This equates to an S value of 11-17 MPa, which will be associated with a tensile stress, σ_t, just large enough for fracture initiation of 5.5-8.5MPa.

10.8. Implications of fracture length and fracture width measurements.

An alternative estimate of the tensile stress required to open fractures such as CSPF can be made by simple fracture mechanics analysis. We can use the constraint that the width of the cracks is less than 1 pixel in the imagery (75m) to consider the problem as deformation of a crack in an infinite plane as shown in fig. 10.15.

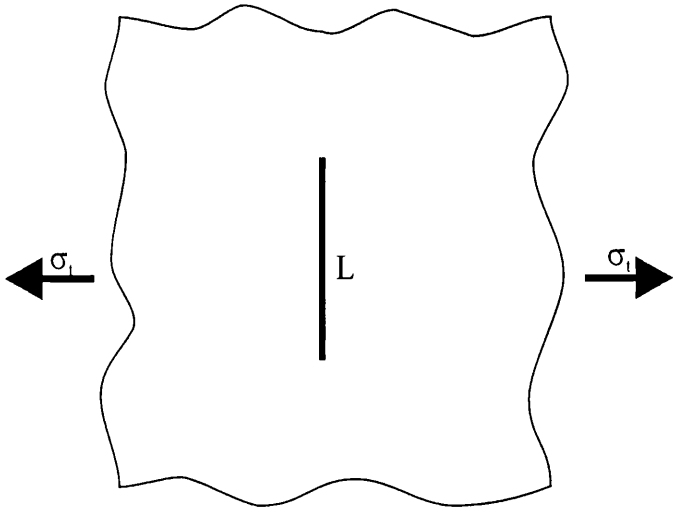

Fig. 10.15. Plan-view of a crack of length L in an infinite plane deformed by a remote tensile stress, σ_t.

In this case, the crack is viewed from above, rather than the side as in sections 10.2-10.5. We can consider an individual crack in this way if:

- The rock mass is approximated by a homogeneous, isotropic, elastic material.
- The tensile stress loading the crack and the material properties of the rock are constant across its length.

For the purposes of this study, we can assume that both these criteria are met for CSPF. Then, following the method of Gudmundsson (1983), we use

$$\sigma_t = \frac{E}{2(1-\nu^2)}\frac{W}{L} \tag{10.16}$$

where σ_t is the tensile stress that produced the fracture, E is the Young's Modulus of the rock mass, estimated to be 50GPa (Jaeger and Cook, 1976; Schultz, 1993), ν is the poisson's ratio of the rock mass, estimated to be 0.25 (Schultz, 1993), W is the maximum width of the fracture at its centre point, and L is the length of the fracture. Typical measurements of length of CSPF are 10-60km as described in chapter three. W is less than 75m and may be much less than this value depending on the SAR energy return from the fracture surface. Also, as described in Nur (1981), the fractures are almost certainly not perfectly sharp and may be surrounded by a disturbed area of material called the shatter zone that also appears radar bright. For these reasons, I estimate that the widths of the fractures range from 10 to 50m. The value of tensile stress that formed these fractures can then be calculated from (10.16) and gives 4.5MPa for a fracture with 10m width and 60km length. For a fracture 50m wide with a length of only 10km, this value would be about 130MPa.

10.9. Experimental measurements applied to modelling results.

The values of S consistent with the spacings measured for CSPF from chapter three are 11-17MPa with an associated remote tensile stress of 5.5-8.5MPa. We can use the experimental measurement of K_c, 3.0MPam$^{1/2}$ to calculate the size of flaws that would be consistent with these results. Using (10.14), we can calculate the size of flaws found in the pre-existing rock mass. For values of S consistent with the measures spacing, 11-17MPa, the initial flaw size is 0.03-0.07m. This result should be used with caution, however, because it represents a 2-dimensional approximation with all cracks aligned in a perpendicular, and hence most damaging, sense to the tensile stress. This result is discussed further in chapter 11.

10.10. Conclusions.

The model used in this chapter is based upon the principles of fracture mechanics and constrained by the experimental data and the transition between extensional fracture and faulting. Variation in the spacing of the fractures is interpreted in terms of rock mass fracture resistance, S, which is dimensionally the same as remote stress required to initate fracture, $\sigma_{t(crit)}$. The scaling factor between S and σ_t depends upon the type and orientation of the initial flaws. In this simple, 2-dimensional model, the factor is 0.5, but, for a two-dimensional model with a population of semi-elliptical cracks, the factor would be nearer 0.9 (Tada *et al.*, 2000). This would also change the gradient of the stress shadow lines calculated from (10.10) and (10.11). Thus the model is useful in assessing the effect of flaw size, but cannot realistically describe the actual size of precursor flaws. Despite this, other results from the model can be applied directly to Venus.

- For CSPF to form, the remote tensile stress must be just high enough to initiate fracture in the unfractured (except by precursor flaws) rock mass. The fracture resistance, S (i.e. fracture toughness of the rock and size of flaws existing in the rock mass) of the rock mass will govern the spacing of the fractures. If the remote tensile stress increases beyond the level required for fracture initiation, then normal faulting is likely to occur. From the Bazant approximation (10.10), this means that the spacing of purely extensional tension fractures is about π times their depth.
- The S parameter used to characterise the rock mass controls the spacing of the CSPF. Higher values of S result in more widely spaced fractures that penetrate deeper and require higher remote tensile stresses before CSPF can form. There is a linear dependence on fracture spacing with S, and therefore σ_t.
- In the region studied, CSPF spacing was about 0.8 to1.2km. This is consistent with a remote tensile stress of about 5.5-8.5MPa, based on the 2-dimensional approximation for initial flaw distribution.

The results generated from this model show that the fracture toughness of the material plays a controlling role in the spacing of CSPF. This is in agreement with the stress shadow result of Banerdt and Sammis (1992) except that their model requires a rock mass with about twice the tensile strength. With knowledge of the spacing of CSPF and experimental measurements of K_c, we can estimate the tensile

stress that formed the fractures, and give a qualitative description of the level of damage in the pre-existing rock mass. Implications of this work for a more generalised discussion on Venusian tectonism can be found in chapter 11.

Chapter 11

Discussion of results and directions for further work.

11.1. Introduction.

In this chapter, I summarise the results from each section of this thesis and discuss the reliability of the data and efficacy of the apparatus and modelling techniques used. Initially, I deal with interpretation of imagery and experiments data separately but I draw the two themes together in discussion of the modelling results. Also presented is a general discussion of the implications of this work and, finally, a brief summary of potential further work in this area of research.

11.2. Imagery.

11.2.1. Summary of results.

A striking result of the work presented in chapter three is the clear trend in azimuthal direction displayed by CSPF. The fractures appear to exist in at least three distinct sets and individual sets tend to follow a well-defined concentric pattern.

The spacings between individual fractures in the study area (324-348°E, 12-35°N, an area just to the East of the large topographic rise of Western Eistla Regio centred at 355°E, 22.5°N) was between 0.8 to 1.0km. Mean fracture spacing is related to the standard deviation by the relationship $\sigma=0.36d$, where σ is the standard deviation and d is the mean spacing for each profile. The spacings of the CSPF are constrained within this narrow band over an area greater than about 1000x1500km.

Seven out of the 13 profiles constructed show at least a slight decreasing trend in fracture spacing across their length with increasing distance from their Eastern end. Additionally, the mean spacing for each profile shows a slight decreasing trend in spacing with distance from the rise when plotted for all profiles.

Stratigraphic studies place the plains with CSPF amongst the oldest units in the study area. This is reinforced by imagery showing that CSPF formation predates other tectonic features, and of particular interest is the fact that CSPF predate wrinkle ridges (WR) which have a concentric pattern around Western Eistla Regio (McGill, 1994).

11.2.2. Discussion arising from imagery results.

The CSPF follow the edge of the large topographic rise of Western Eistla Regio, which has an approximate radius of 2500km. An alternative interpretation for CSPF formation in this area is that they formed as a result of local uplift. The two main sets of CSPF observed in this study can both be associated with local centres with a radius of curvature of between 500 and 1000km. There is some variation in topography over the curve extents of the CSPF and the margin of the southern black set of CSPF is about 1km lower than the centre. There is no clear circular structure that suggests doming. The difference in height between the centre and margin of the red set is about 1.5km and more consistent with a domed topography. The consistent spacing of the fractures over a radius of 500-1000km, however, argues for a larger scale process governing the stress field suggests that stress field that produced CSPF was more likely to be controlled by regional and not local deformation.

The stratigraphic association between CSPF and WR implies that the sense of the regional stress has reversed completely during the geological record visible from the imagery. The relatively low position in the stratigraphic column of CSPF accords with formation as a result of the growth of the topographic rise. WR are also almost certainly associated with the dynamics of Western Eistla Regio because of their concentric distribution around this rise. The most obvious explanation for the stratigraphic relationship between WR and CSPF is that CSPF were formed as part of a large, dynamically compensated, doming event that generated tensile stress in the crust as the rise was formed with volcanic constructs forming as part of this process. Volcanism may have continued throughout the evolution of the rise; when the topography ceased to rise and relaxed, the compressional stress field that may have formed the WR was generated.

11.3. Experimental results.

11.1. Summary of results.

The results from this study show that the fracture toughness of basalt increases from 2.4MPam$^{1/2}$ at ambient pressure to 3.0MPam$^{1/2}$ at CO_2 pressures greater than 5MPa. The fracture toughness values show no clear trend with temperature and, in general, are independent of temperature in the range 0-600°C except for a large increase in fracture toughness at about 150°C.

Level II testing allowed the use of the method described by Matsuki (1991) to assess whether the fracture resistance curve reaches a plateau value where fracture toughness becomes a size-independent material property. At ambient pressures and temperatures, the expected plateau was observed in the data; it gave a size-independent value for K_c of about 2.5 $MPam^{1/2}$ within the experimental error of the mean value obtained from level II tests. At higher temperatures and pressures the results from the Matsuki method do not show a plateau.

Observation of the crack surfaces of the samples after testing shows that the mode of failure is brittle for all experimental conditions.

The fracture toughness tests also allowed measurement of Young's modulus. The Young's modulus calculated from all tests has a mean of around 12GPa for basalt but, using P and S-wave velocity measurements, is around 46GPa, much closer to the accepted values of about 50GPa (Schultz, 1993). This large discrepancy can, in part, be attributed to the fact that dynamic Young's modulus, measured using seismic wave velocities, is higher than static Young's modulus measured using rock mechanics tests (Wright, 1998). However, the ratio of dynamic to static modulus is commonly about 2.0 (Cheng and Johnston, 1981), that is, about half the observed discrepancy.

11.3.2. Discussion of experimental results.

11.3.2a Size of specimens.

The plateaux visible in the K-resistance curves from experiments performed at ambient conditions show that the sample size was sufficient for reliable fracture toughness measurements. Because the size of the non-linear zone in rocks is not due to plasticity and but more to increased microcracking (Atkinson, 1987), standard fracture mechanics estimates (e.g. Gdoutos, 1993) of process zone size cannot be used. ISRM (1988) suggest that the diameter of the rock sample should be greater than 10 times the largest grain size, in which case our tests fulfil the criterion by two orders of magnitude. Schmidt (1980) suggests that fracture toughness is not a valid material property until the approximate inequality

$$a > 2.5\left(\frac{K_c}{T_0}\right) \qquad (11.1)$$

where a is the crack length and σ_T is the tensile strength of the material, has been met. Even for temperatures as high as 800°C, the tensile strength of basalt is greater than a few MPa (Clarke, 1966) so that the crack length requirement for valid fracture toughness tests is only a few millimetres. This criterion has been met for all the tests in this study based as K_c is measured at a ~20mm for level II tests.

11.3.2b. Pressure effects.

An increase in fracture toughness with confining pressure has been observed in this study and others (e.g. Atkinson and Meredith, 1987, table 11.5) although I believe this is the first set of experiments to use gas as confining medium. The results of Winter (1983) and Muller (1984), summarised in Atkinson and Meredith (1987), show that, if the rock is saturated with a pore fluid with equal pressure to the confining medium, the fracture toughness is similar to that of the unconfined, unsaturated rock. The increase in fracture toughness with pressure can be accounted for by one of two mechanisms which occur because rocks are complicated polycrystalline materials rather than perfectly elastic continua:

- The process zone is the region of non-linear behaviour near the crack-tip that contains an increasing density of microcracks as the stress loading the crack increases (Atkinson, 1987). Eventually, crack linkage of the most appropriately aligned microcracks occurs and the macrocrack extends. Increased confining pressure suppresses the formation of microcracks in the process zone and causes crack-closure of pre-existing microscopic flaws. In this way crack linkage is inhibited and the rock is more resistant to fracture.
- Polycrystalline materials such as rocks commonly fracture both by inter and intra-granular failure. The rough crack faces can cause friction behind the crack tip as shown in fig. 11.1 below. At higher confining pressures, this effect is amplified due to the increased compressive force acting parallel to the crack that tends to increase the normal force and therefore the frictional interaction between the crack faces.

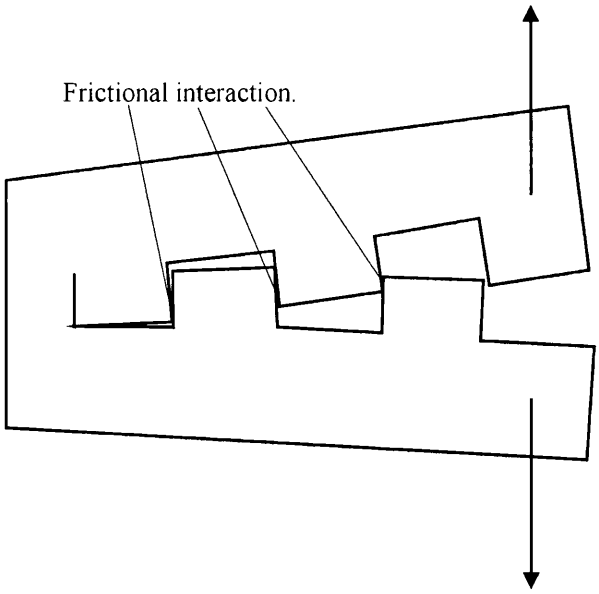

Fig. 11.1. Frictional interaction between crack faces occurs behind the crack tip and resists the tensile opening force shown by the arrows.

The data from experiments show an increase in fracture toughness with pressure followed by a plateau with no further increase. This suggests that the first mechanism is dominant because full crack closure will occur at a certain pressure whereas the frictional effects will scale with the confining pressure. The results from Winter (1983 and Muller (1984) support this because the pore fluid pressure will tend to keep microcracks open, resulting in no increase in fracture toughness with confining pressure. However, the confining pressure at which this plateau occurs in our experiments seems small. The majority of the fracture toughness experiments performed at pressure, the results of which are collated in Atkinson and Meredith (1987), show further increases in fracture toughness with confining pressure up to pressures of several tens of MPa. The very small grain size of the basalt used in this study may tend to reduce the effects of crack face friction and may mean that microcracks will be smaller and more easily closed, but the high Young's modulus of basalt will tend to make crack closure difficult. I therefore conclude that the effects of microcrack closure may have increased the fracture toughness of the samples tested under higher confining pressure. The fracture toughness of rocks on Venus will be similarly high owing to the small grain size, low vesicularity and higher ambient temperatures (which will lead to less thermal microcrack formation upon cooling of the lava flows). Also, the ~10MPa confining pressure will suppress microcrack formation at the crack tip leading to a relatively fracture resistant rock mass.

11.3.2c. Temperature effects.

The increase in fracture toughness at 150°C and the levelling off after this point is also found in samples of gabbro tested at high temperatures (Meredith and Atkinson, 1985). Meredith and Atkinson (1987) attribute this behaviour to initial decreases in microcrack density caused by closure of microcracks within the sample by thermal expansion at temperatures of about 50-150°C. This has the effect of restricting microcrack linkage and of toughening the sample. At higher temperatures, normally about 300-400°C, differential thermal expansion between the minerals that compose the sample causes formation of new microcracks which decreases the toughness of the rock dramatically owing to enhanced microcrack linkage. This effect has been confirmed by permeability measurements in granite which show a decrease in permeability by a factor of two at 100-200°C followed by a fourfold increase in permeability at 500-600°C (Glover *et al.*, 1995).

The experiments designed for the present study were intended to remove this effect by preheating all the samples, thus allowing temperature effects, rather than the influence of thermally-induced microcracks, to be measured. This is appropriate for Venus because the rocks would have cooled to 450°C directly, unlike Earth analogues, which have to be heated from 20-30°C to Venusian surface temperatures.

Although the apparatus had excellent thermal insulation, heating times for the sample still had to be kept as short as possible to reduce any heating effects in the actuator piston, which could not easily be insulated, which might degrade the seals. The samples therefore had to be heated much more quickly (by about an order of magnitude) during this process than when they were thermally cracked in the heat treatment process. Meredith and Atkinson (1985) note that rapid temperature changes produce correspondingly large increases in microcrack density, and the re-heating almost certainly caused further microcracking. This is borne out by the experimental results, which show an increase in fracture toughness at 150°C followed by a decrease in fracture toughness at higher temperatures (fig. 9.6). These results therefore confirm the work of Meredith and Atkinson (1985) and Glover *et al.* (1995) and must be accepted as a flaw in the experimental method given that the intention was to remove these cracking effects. Further work should use a heating time similar to that of the heat treatment procedure when raising the samples to the testing temperature and may require substantial modification of the heating system. Alternatively, monitoring crack damage

during the heating process by measuring acoustic emissions may be effective in separating thermal microcracking and temperature effects on fracture toughness.

11.3.2d. Young's modulus measurements.

The value of Young's modulus for basalt measured using the fracture toughness data is surprisingly low. However, the thermal cracking introduced into the sample would tend to reduce the Young's modulus significantly compared with untreated samples. The low measured values may be caused by compliance of the apparatus, thus underestimating the initial stiffness of the samples and therefore the Young's modulus. The slope of the compliance curve in fig. 6.16, thought to represent the stiffness of the apparatus, can be used to calculate the maximum Young's modulus of SR samples that can be measured by the apparatus using (9.14). According to fig. 6.16, the compliance of the load line of the apparatus is 2.63×10^{-8}m/KN. Therefore samples with a Young's modulus of 54GPa or below should not have their deformation behaviour completely masked by that of the apparatus, although the measured Young's modulus for samples with similar stiffness would be half their true value because the displacement in the apparatus matches that of the sample. It is thought that the level II fracture toughness data are reliable because they use differential measurements of CMOD and the compliance of the apparatus is not so low as to obscure the shape of the graph at the measurement points.

The results from our Young's modulus tests suggest that the compliance of the apparatus was higher than shown in fig. 6.16. On the other hand, the observation that confining pressure slightly increased the measured Young's modulus (as commonly observed by Clarke, 1966, among others), argues for the apparatus being sufficiently stiff to be able to detect these variations. Typical values for Young's modulus of basalt are around 50GPa (Schultz, 1993), similar to that of the apparatus, and therefore we might expect Young's modulus to be underestimated by a factor of about two using data from the fracture toughness measurements. Alternatively, the increase in Young's modulus measured at pressure could be due to an increase in the stiffness of the apparatus. The only possible scenario where this might occur is where the actuator medium contained small gas bubbles, making it slightly compressible and the apparatus compliant. If a confining pressure was applied, the actuator medium would have to be held at higher pressure and any gas bubbles would be at higher pressure, thus reducing their compressibility of the medium and stiffening the apparatus. However, the air was

always bled from the actuator medium specifically to remove bubbles whenever the medium was replaced so this effect should be small, although, as noted in chapter six, some problems with actuator seals still remain unresolved.

Incorrect calibration of the displacement transducer or actuator pressure transducer would also have the effect of changing the value of Young's modulus measured but would not affect the level II tests, which use differential measurements of displacement. Displacement is far more likely than actuator pressure to be the factor that is incorrectly calibrated because level I fracture toughness tests, which scale only with the force required to cause failure, agree with previous measurements (e.g. Atkinson and Meredith, 1984, table 11.3). Introducing a scaling factor of 0.3-0.5 into the displacement calibration output would make the results from the Young's modulus measurements agree with those measured using seismic velocities, but a further, highly detailed programme of calibration would be necessary to verify whether this is the cause of the discrepancy. The difficulties with calibrating the displacement absolutely are described in chapter six and further calibration methods are discussed in section 11.5.

In summary, the low measured values of Young's modulus are probably due to either the stiffness of the apparatus being similar to that of the rock sample or to a systematic error in calibration of the displacement transducer.

11.3.2e. Apparatus compliance.

Apparatus compliance may explain poor turnover associated with many level II tests, although it does not explain why poorer turnover occurred in tests which used extremes of temperature and pressure. Also, if the apparatus was overly compliant the force-displacement plot used to make level II tests would be too shallow at the start of the test, and failure would not occur at half the initial sample stiffness. This was observed in some tests.

Associated with the poor turnover and low values of Young's modulus data are the shapes of the Matsuki method curves produced from the level II plots. If the change in slope of the load/CMOD plot with crack propagation were too small (as would be the case if the apparatus were compliant) the application of the Matsuki method would be inappropriate and would lead to the observed results. This discussion is further complicated by the fact that, although reasonable Matsuki method results were generated from the tests made at ambient temperatures and pressures the Young's modulus was still found to be low. An explanation for this effect has still to be found.

As the actuator housing was changed to a one-piece design during the project, it is thought that this part of the apparatus is sufficiently stiff not to deform during loading. Because there are few other obvious sources of compliance, the actuator piston is its most likely source. Compressibility of the medium and deformation of the piston body and seals are therefore the most likely candidates for sources of compliance. Steps that can be taken to reduce these effects in further modifications to the apparatus are described in section 11.5.

11.4. Results of modelling.

The observations that the fractures show no fault-like morphology is crucial to our understanding of how they formed. Also crucial are the regular spacing of the fractures and the fracture toughness of the rocks themselves, measured by experiments on analogue terrestrial rocks.

11.4.1. Precursor flaw size and the shortcomings of a two-dimensional model.

The model for CSPF used in this project shows that the fracture properties of the rocks that form the Venusian plains are critical to the spacing of extensional fractures. Beyond depths of penetration of more than about 100m, the fracture toughness of the rock plays almost no part in controlling the depth to which fractures propagate. The fracture toughness does, however, control the point at which new fractures initiate and penetrate to a depth controlled by the overburden pressure. In particular, the spacing of fractures is controlled by the rock-mass fracture resistance parameter, S (a combination of flaw size and fracture toughness), which can be considered to scale directly with the tensile strength of the rock mass.

The scaling factor used here is based upon a 2-dimensional model and has a value of 0.5 but this will change for the type of model used. Fig. 11.2 shows the problems with using a 2-dimensional model to simulate a three dimensional problem. Although the depth of penetration of flaws is accurately described in 2-dimensions, the initiation of new cracks may not be.

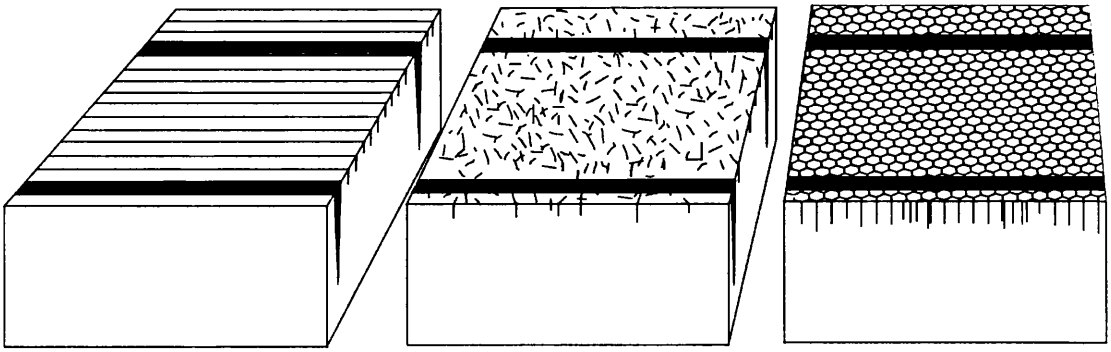

Fig. 11.2. Sketch of a section of Venusian plains material with some fracturing caused by a remote tensile stress acting perpendicular to the large fractures. Heavy lines represent deep, penetrating fractures such as CSPF, thin lines represent the starter flaw population a) 3-dimensional extension of 2-dimensional approximation used in this study. The parallel starter flaws are inferred from the 2-dimensional model. This model clearly under-estimates the strength of the rock mass for a given flaw dimension. b) A more realistic crack population suitable for a 3-dimensional extension of the 2-dimensional model. c) An approximation of the likely real configuration of a freshly emplaced volcanic plain on Venus.

Fig. 11.2 demonstrates how the model used here underestimates the strength of the rock mass because all starter flaws are perfectly aligned with the tensile stress field. A 3-dimensional extension to this model might consider the flaw population as semi-circular cracks in the surface with random orientation. In reality, the surface flaws are likely to be polygonal or sub-polygonal joints, which may penetrate to depth of several metres or more. The effect of using a 2-dimensional model is to generate unrealistically small precursor crack sizes for a given tensile stress. For example, the flaw size most consistent with the experimental measurements of fracture toughness ($3.0 MPam^{1/2}$) and measured spacings of CSPF (0.8-1.2km) is 0.03-0.07 metres. This is unrealistically small for a real planetary surface and would be expected to be two orders of magnitude greater.

11.4.2. Properties of rock mass required for CSPF formation.

The small flaw size predicted is an important result, however. It means that CSPF with the observed spacing, form only in relatively undeformed material with high tensile strength. The observations of the surface made by the Venera landers showed some jointing, but none of those missions landed in terrain deformed by CSPF. If CSPF only form in relatively unjointed material, this may imply that low eruption temperature lava may have formed the surface. The closer the solidification temperature and elastic-

plastic transition temperature of lava is to Venusian ambient temperature, the lower the stresses generated by cooling and the less pronounced the jointing. This is clearly shown using the method of Johnson and Sandwell (1992)

$$\sigma_{Th} = \frac{\alpha E \Delta T}{1 - \nu} \tag{11.2}$$

where σ_{Th} is the thermal stress caused by cooling, α is the coefficient of linear thermal expansion, E is Young's modulus, ν is Poisson's ratio and ΔT is the temperature drop from initial elastic-plastic transition temperature (or "blocking" temperature in Johnson and Sandwell, 1992) to the ambient temperature.

Chapter four describes how carbonatite has a solidification temperature close to that of the current Venusian atmosphere and could therefore be expected to form largely undeformed igneous provinces. If, in (11.2), we use the values $\alpha=10^{-5}$ (Johnson and Sandwell, 1992), E=50GPa and ν=0.25 (Schultz, 1993) and $\Delta T \lesssim 50^{\circ}C$ for carbonatite and $\Delta T \approx 450\text{-}500^{\circ}C$ for basalt (Johnson and Sandwell), we find that σ_{Th} would be of the order of 30MPa for carbonatite or 300MPa for basalt. If the tensile strength of undeformed carbonatite is of the same order as basalt, jointing will be heavily suppressed. The fracture toughness testing of carbonatite proposed in this project would therefore have given information on whether its fracture properties were consistent with a highly fracture-resistant rock mass such as that required for CSPF formation. Whether carbonatite or, more likely, basalt form the surface of Venus, the initial rock mass must have possessed relatively few fractures and have had a high fracture toughness similar to that measured in experiments.

Despite the caveat that the precursor flaw size predicted seems too small, the use of the scaling factor, S, in the model allows the appropriate tensile stress and depth of penetration consistent with the spacing of CSPF to be calculated. For a given value of S, closer fractures require larger remote tensile stresses and penetrate more deeply into the crust. However, referring to the criterion for normal faulting, these conditions are those most likely to be associated with normal faulting than CSPF formation. In fact, the normal faulting criterion constrains CSPF formation to occur at shallow depths of penetration and high spacing, consistent with lower tensile stresses (fig. 10.13). The ideal conditions therefore occur where the stress is just high enough to initiate fracture in a rock mass, leading to the fracture resistance parameter S being the controlling factor in CSPF spacing. Note that if a fluid were generating a pore fluid pressure in the

crust then the normal faulting criterion would change (4.34) and CSPF formation would be inhibited. We can therefore conclude that the presence of CSPF rule out any significant pore fluid (such as carbonate melt) in the Venusian crust at the time CSPF formed.

11.4.3. Remote tensile stresses and penetration depths consistent with observed spacing of CSPF.

The depth to which CSPF penetrate, based upon the observed spacings, is about 250-400m. The tensile stresses consistent with these measurements are 5.5-8.5 MPa and are considered to be similar to the tensile strength of the rock mass in these areas. A peculiar result of the application of the faulting criterion is that wider spacing in CSPF is associated with greater fracture resistance and therefore can only be produced by larger tensile stresses. This result conflicts with data on CSPF spacing based on fracture mechanics alone and ignoring the normal faulting criterion. In effect, the spacing of CSPF is controlled only by S, the rock mass fracture resistance parameter. This also sets a minimum level of stress required for initiation of CSPF formation. The tensile stress associated with CSPF implies that the width of individual fractures in sets of CSPF will be less than a few tens of metres, which is not unreasonable to judge from the imagery (see section 10.7).

11.4.4. Spatial variation of CSPF spacing.

The spatial variation of spacing in the study area was found to be very small. Slight decreasing trends were found along individual profiles and across the wider area. The variation of spacing with S, and therefore tensile stress, is linear as shown in fig. 10.14. The variation of spacing in the study area may therefore represent a slight change in rock mass fracture resistance, the initiation of wider fractures being caused by a rise in tensile stress. Note that small rises in remote tensile stress may lead some of the more closely spaced fractures to become normal faults at depth. For slight increases, it is unlikely that any surface manifestation of this change would be visible in Magellan imagery.

It should also be noted that the linear variation of spacing with S can only be postulated because of the faulting criterion. If the magnitude of the criterion were slightly smaller, for example owing to enhanced internal friction in the rock mass, then the slope of the faulting line of fig. 10.13 would be lower. The friction for Venus rocks

may be greater than for those on Earth as shown by the fact that tensile fault intersection angles on Venus are slightly larger (McGuire, 1996), implying that new failure, rather than sliding on old fractures, is favoured on Venus. If the faulting criterion on Venus is weaker, then a variety of depths and spacings of CSPF could exist for a given rock mass with fixed fracture resistance. In this way, slight variations in spacing could be due to changes in remote tensile stress, closer spacings being associated with higher stresses. Large differences in spacing, however, are likely to be due to differences in rock mass fracture resistance.

11.4.5. Sources of tensile stress in the upper crust.

Granted that the spacings of CSPF are consistent with a remote tensile stress of 5.5 to 8.5MPa, the question arises as to what this reveals about stresses in the upper crust. Chapter three showed that the CSPF are distributed in approximately concentric patterns and are most likely to be associated with local uplift. We can approximate the largest tensile forces at the surface of the lithosphere by considering the bending of a beam. Fig. 11.3 shows a beam with thickness $2z_o$ deformed so as to give an uplift of h, over a width 2λ. In this case, the stress in the x direction in the beam (actually, the stress perpendicular to the beam but in this case the two are virtually identical) would be given by

$$\sigma_x = \frac{E}{1-\nu^2}(z_o - z)\frac{2h}{\lambda^2} \qquad (11.3)$$

as used by Nur (1981) and assuming that $\lambda >> h$ and $r >> (z-z_o)$. σ_x is the force in the x direction, E is the Young's Modulus, v is the Poisson ratio, h is the height of uplift and λ the half-width of the area of uplift. $2z_o$ is the thickness of the elastic lithosphere and z is the depth into the lithosphere.

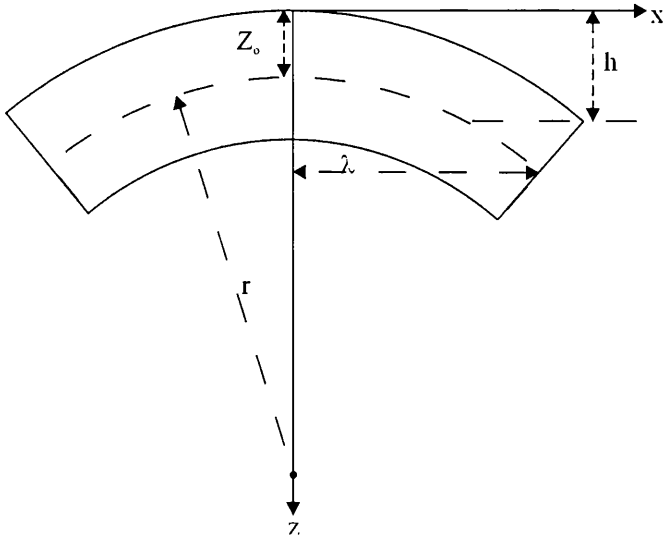

Fig. 11.3. Deformed beam representing uplift of a segment of the lithosphere. After Nur (1981).

In the case of uplift associated with the topographic rise of Western Eistla Regio, we take z to be 0 for the surface of the lithosphere, E to be 50GPa (Schultz, 1993), ν to be 0.25 (Schultz, 1993) and $2z_o$ to be 30-50km (Smrekar, 1994). Western Eistla Regio measures 2000 by 2400km and has a swell height of about 1.8km (Smrekar, 1997). This gives a tensile stress of between 2.8 and 4.7MPa which is close to the levels of stress required for CSPF with spacings of 0.8-1.2km. Smaller radius deformation generates significantly greater forces than increased uplift so that to generate the same force a longer wavelength feature requires a much larger vertical uplift.

Gudmundsson (1983, 1987) suggests that the stresses that caused the Vogar fissure swarm in Iceland (a set of irregular extensional fractures with typical spacings of 300-1000m) are of the order of a few MPa. These features are smaller than CSPF but probably form in a similar way. Typical values for stress drop during large continental earthquakes on Earth are 1-10MPa (Foster and Nimmo, 1996), which may be close to the total stress acting on the faults. Thus there are examples from the Earth of stress fields associated with faulting and fracturing of a comparable magnitude to those generated by uplift in Western Eistla Regio and consistent with the spacing of CSPF. The maximum tensile stress will obviously occur at the point of greatest curvature. The stress will diminish away from the topographic rise, and may also diminish towards the centre if the uplifting force is spread over a large area to generate a flat-topped dome. In short, the formation of CSPF, as opposed to normal faulting, requires a narrow band of material properties and applied stress. This explains the scarcity, but ubiquitous global distribution, of CSPF as they will tend to occur wherever a high strength rock mass

exists contemporaneous with the relatively low stresses required. Such features are rare on Earth because the presence of pore fluid pressure make the transition to faulting much shallower so that only smaller scale jointing at shallower depths is likely to be observed.

11.5. Further work.

11.5.1. Imagery.

The analysis of the results from this study have highlighted some simple observations that could be made in the study area to improve understanding of the process of CSPF formation. Firstly, there are large areas in the study area that have more than one set of CSPF and the angle of intersection for these sets over a wide area could easily be measured in a similar way to Bowman *et al.*, 1995. Though time-consuming, this would give information whether new sets of CSPF are preferentially formed rather than old ones re-opened when the stress field changes orientation or gradient.

The approximation used to estimate the tensile stress that formed a fracture with a given width (Gudmundsson,1983) could be investigated further by measuring the brightness of CSPF and plotting it against length. Wider fractures should have wider shatter zones and rubble filled areas and should therefore generate a stronger radar return in the imagery.

11.5.2. Experiments and apparatus.

An obvious theme for further work associated with this study is the continuation of the experimental program. If more carbonatite can be sourced and usable cores extracted fracture toughness and tensile strength testing can be used to assess whether large carbonatite flows are likely to form cooling joints or not and whether their fracture toughness is sufficient to generate the large fracture resistance required for formation of CSPF.

The apparatus has been shown to be successful in measuring level II fracture toughness using a variety of extreme conditions but some results indicate that more development is needed to resolve outstanding issues. Further calibration using deformation of a sample which has a Young's modulus that has been accurately measured at a variety of temperatures and pressures is necessary to resolve whether

calibration error or apparatus compliance is the source of discrepancies in the data. If calibration is the culprit then this procedure should improve the results obtained significantly and enable the data presented here to be reanalysed. If compliance in the apparatus is found to be the source of error, further modifications will be necessary.

The use of an internal actuator facilitated testing of the samples under pressure and temperature and is a novel solution to a most challenging engineering problem. However, the piston is probably the source of any excessive compliance that exists in the apparatus. Thus removing the need for an actuator medium and an internal piston would be advantageous to future designs. An alternative experimental configuration would be to place the apparatus on its side and use a servohydraulic universal load frame to provide the sample deformation force (a similar method has been used for ice and is described in Sammonds *et al.*, 1998). A new endplate for the aparatus would have to be constructed so that the loading arm of the load frame could be admitted through a low-friction, single acting seal.

The advantage of this system is that the loading system would be much stiffer and that larger diameter seals could be used. As described in chapter six, seals in the piston had to be double acting and the sealing area was large with respect to the diameter of the piston, leading to instability and compressibility in the sealand to bleed-through possibly causing apparatus compliance. A further advantage would be that simple LVDTs could be used to measure the displacement of the load arm *outside* the demanding environment found within the pressure vessel. Thus displaceent calibration would be facilitated because LVDT calibration is very simple and reliable.

A disadvantage of the load frame method would be that the confining pressure in the vessel would react against the loading arm with a force proportional to the cross sectional area. This could lead to poor control in the load frame and would call for matching the load with the confining pressure as it was increased. Nevertheless, these modifications would reduce both identified sources of error in the measurements.

Other modifications to the apparatus would include using a larger vessel that could contain more insulating material and giving priority to reducing the volume of gas to a minimum. Placing the vessel on its side would reduce the height over which convection could occur and minimise thermal gradients. Improved insulation would mean that the sample could be heated for longer periods so as to eliminate thermal cracking effects and then allowed to equilibrate for a several hours in order to reduce thermal gradients. Active cooling of some parts of the apparatus would possibly be

necessary. Experiments using both high pressure and high temperature could then be performed and a direct measurement of fracture toughness at Venus surface conditions obtained.

In summary, the apparatus presented in this thesis is novel and capable of simulating a range of challenging planetary environments. Some improvements can undoubtedly be made but they are likely to be expensive and time consuming and will require as much development as the work presented in chapter six.

11.5.3. Modelling.

As described in section 11.4.1, the model used here has certain intrinsic flaws because it uses a two dimensional approximation. A more advanced model should consider a three dimensional crack population, and would be able to determine where the initiation occurred given knowledge of the stress shadow and stress intensity of an arbitrary field of cracks. Such a model would require the use of analytical solutions to equations highlighted in chapter 10 at all points in a plane and hence the use of extensive computer time. The work presented here provides all the underlying relationships necessary for its construction.

11.6. Final conclusions.

It has been demonstrated that the fracture toughness of basalt increases with confining pressure but quickly reaches a constant plateau. Temperature effects from this study show no clear trend and may have been affected by thermal cracking effects. The fracture properties of rock have been shown to be critical to the understanding of spacing of extensional fractures on Venus and a simple 2-dimensional fracture mechanics model has been used to adequately describe the observed spacing of the features. The stresses calculated from this model are consistent with those generated by uplift of a large topographic rise.

Detailed analysis of CSPF in the study area showed that the azimuthal directions of the fractures follow a concentric trend to the edge of the topographic rise of Western Eistla Regio and that the features are very low in the stratigraphic column and form within a single geological unit. This is consistent with their being formed in association with early uplift of the rise.

The use of a new, holistic methodology for investigating tectonic features has been vindicated and it is hoped that the techniques developed here can be adapted for the investigation of brittle deformation on other planetary surfaces. Improvements in the specific techniques used as a part of this methodology will surely lead to its more widespread use.

Appendix I

Safety of pressure vessel.

I.1 Safe working pressure of vessel.

Using the guidelines given in the HPTA handbook (1975) for construction of high-pressure vessels, working limits for the fracture mechanics pressure vessel used in this study can be derived. It is most rigorous to fully test the materials from which the vessel is constructed in the orientation in which they are used. However, no such tests were performed prior to the construction of the vessel and it was impossible to apply testing without destroying the vessel. As such, a suitable theoretical method had to be applied to give a suitable estimate of the maximum working pressure using the dimensions of the vessel and properties of the material from which it is constructed.

The K value of a pressure vessel is simply the ratio of the external diameter to the internal diameter. If K is greater than 1.20 the vessel is classed as 'thick-walled' and if K is less than 1.20 as 'thin-walled'. The fracture mechanics apparatus pressure vessel has an i.d. of 95.5mm and an o.d. of 162.4 mm. giving a K value of 1.70. This sets the vessel well into the 'thick-walled' regime. Important physical quantities are the ultimate tensile strength (UTS or σ_u) and yield strength (σ_y) of the material the vessel is constructed from. These govern the mode of deformation of the vessel.

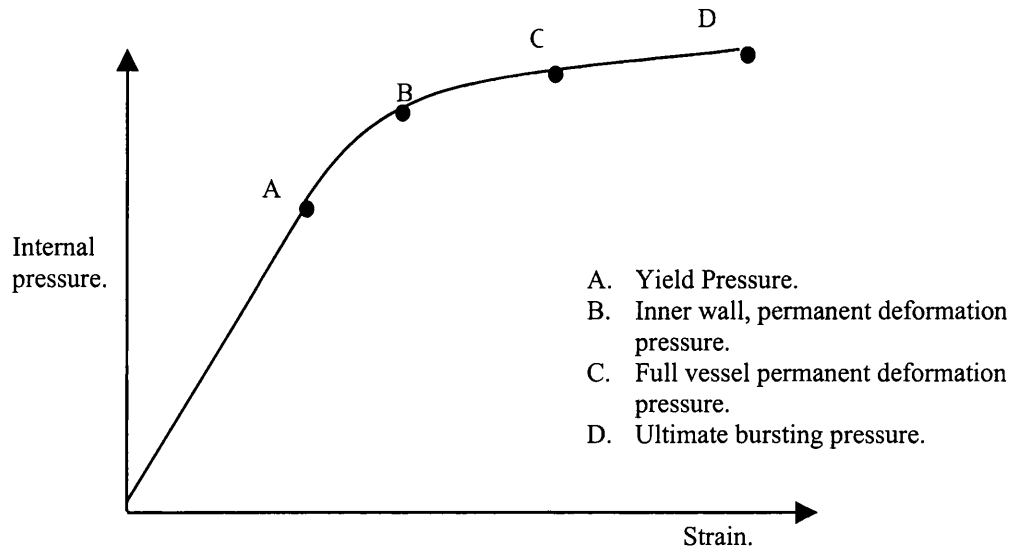

Fig. I.1. Strain in thick-walled vessel. After HPTA (1975).

Referring to fig. I.1, the vessel behaves elastically under pressure until A, the yield pressure, corresponding to the yield strength, σ_y, of which the material the vessel is constructed from. Point B indicates where this yield produces a permanent deformation so that the inner wall of the vessel will not return to its original shape even if the pressure is removed. C indicates the pressure at which the entire vessel will be permanently deformed. Further increases in pressure lead to 'ballooning' of the vessel until its ultimate rupture at D. This pressure is known as the 'ultimate bursting pressure' and corresponds to the UTS of the material the vessel is constructed from.

σ_y and σ_u must be assessed in the orientation of which the vessel is constructed. For example, tensile data for Hastelloy C22 can readily be found for longitudinal bars but, in a pressure vessel, the tensile stress is mainly concentric. As the billets used to make vessels are usually rolled from bars, there is some small amount of grain alignment in the material. This can lead to varying strengths in the different orientations which must betaken into account. This can be achieved by multiplying the σ_u and σ_y given for longitudinal bars by a factor less than one. Experience in constructing pressure vessels in the UCL Rock and Ice Physics Laboratory has shown that this factor is rarely less than 0.75 and generally greater than 0.95. To leave a margin of safety the factor 0.75 was assumed.

The HPTA guidelines (1975) use the following formulae for unknown (i.e. untested) thick-walled pressure vessels with outer diameter less than 150mm. (Although the vessel is slightly larger than this, the equations can still be used owing to the large safety factor as described above)

$$P_y, \text{ Yield pressure} = 0.5[\sigma_y (K^2 - 1)/K^2] \quad \text{(I.1)}$$

$$P_b, \text{ Burst Pressure} = 2\sigma_u[(K-1)/(K+1)] \quad \text{(I.2)}$$

where σ_y and σ_u are 0.75 times the values quoted in the Hastelloy C-22 data sheet (Haynes International 1997) produced by the suppliers of the alloy from which the vessel is constructed. These results are shown in fig. I.2.

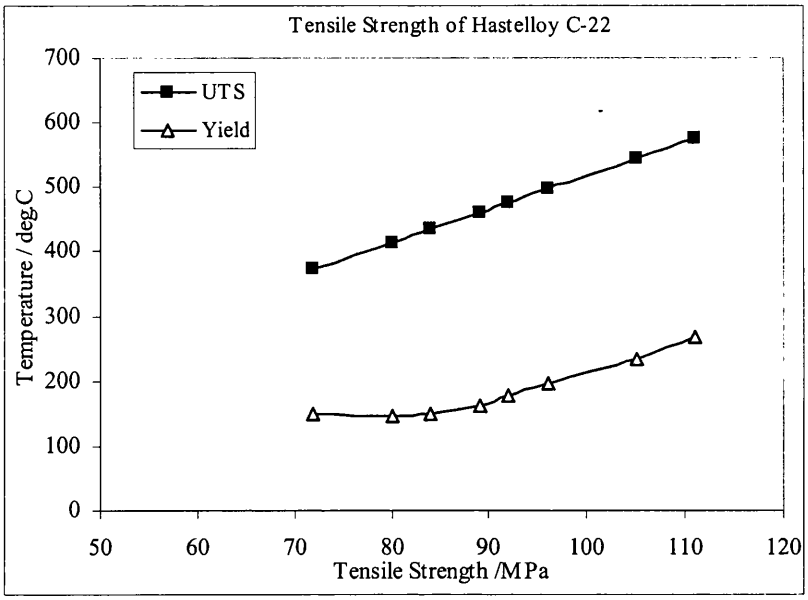

Fig. I.2. Tensile strength of Hastelloy C-22 alloy corrected for 0.75 factor. Data averaged from 8-16 tests (Haynes International, 1997).

The maximum working pressure is given by HPTA (1975) guidelines to be the lesser of $0.67\sigma_y$ or $0.25\sigma_u$. This enables a graph of maximum working pressure against temperature to be plotted to evaluate the working pressure.

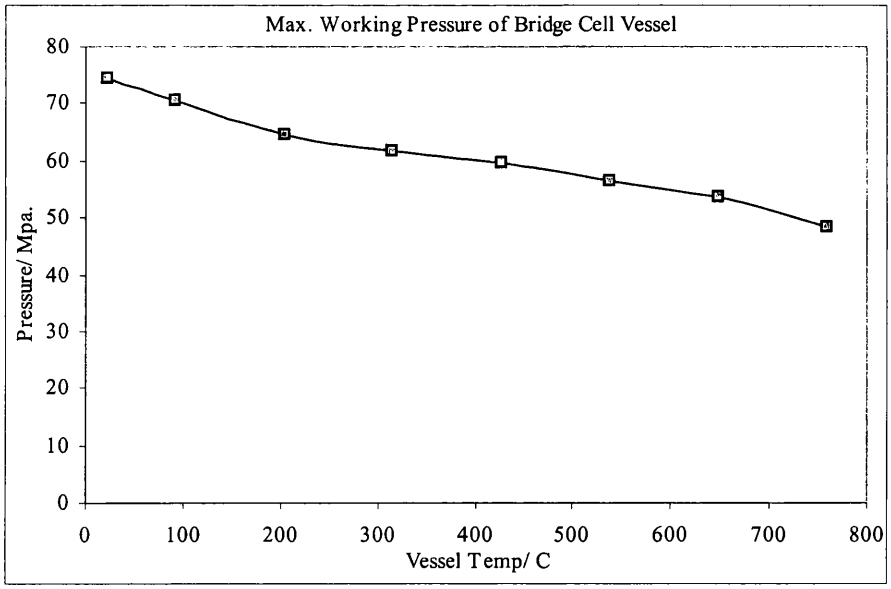

Fig. I.3 The maximum working pressure of the Hastelloy C-22 pressure vessel. Note that this takes no account of the thermal stresses induced by differential heating of the bore compared with the outer wall.

Figure I.3 shows that the vessel is well within the safety limits even for the extreme conditions used in this study (20MPa and ~600°C). Catastrophic failure of the

vessel is very unlikely and the most important type of failure to assess for safety is small component ejection.

I.2. Assessment of internal energy of pressurised vessel.

In order to assess the internal energy of the compressed gas in the vessel, we partition the internal energy of the system E_s into three components

$$E_s = E_1 + E_2 + E_3 \quad (I.4)$$

where E_1 = fluid expansion energy, E_2 = chemically released energy and E_3 = elastic strain energy of vessel. The elastic strain energy is typically small compared with the expansion energy, especially with gas as confining medium (HPTA, 1975). As CO_2 expands adiabatically there will be no chemical reaction and so the calculation can be simplified by considering only the change in fluid expansion energy. This can be calculated using thermodynamic data for CO_2 at high temperature and pressure and applying equation (I.5)

$$\Delta E_1 = \Delta H - \Delta(PV) \quad (I.5)$$

where H is the enthalpy, P is the pressure and V the volume. For the purposes of calculations, the volume of the vessel is $0.001 m^3$ (1 litre).

	T = 300K		T = 700K,	
Pressure /MPa	H / $kJKg^{-1}$	ρ / kgm^{-3}	H / $kJKg^{-1}$	ρ / kgm^{-3}*
0.1	213.6	1.97†	-	-
10	-	-	602.4	75
20	-	-	589.8	150
50	-	-	564.7	374

Table I.1.Thermophysical Properties of carbon dioxide. Enthalpy data, Vargaftik (1975). †, Din (1956). *, calculated from PV = nRT (estimated to be approximately 20% low at temperatures >400°C in the absence of thermophysical data). No data were available for temperatures greater than 700K.

In all cases, the internal energy is calculated from Eqn. I.5 giving the values in table I.2, below.

Pressure / MPa	E_s kJ (T = 700K)
10	26.8
20	51.33
50	116.6

Table I.2. Internal Energies for 1 litre of compressed CO_2.

The HPTA recommend the following partitioning of energy for different failure modes:

Mode 1). Catastrophic brittle failure of vessel.

Kinetic energy of fragments $= 0.2\ E_s$

Shock wave energy $= 0.8\ E_s$

Mode 2). Ejection of major vessel assembly (e.g. end closure).

Kinetic energy of ejected element $= 0.6\ E_s$

Shock wave energy $= 0.4\ E_s$

Mode 3). Ejection of small fragments through ductile failure or ejection of fittings through local failure.

Kinetic energy as calculated in section I.3, below.

Shock wave energy: low.

I.3. Fracture mechanics vessel failure criterion.

Failure mode 1 and 2 are deemed to be unlikely at the relatively low pressures at which the apparatus was used. In particular, brittle catastrophic failure (mode 1) can be eliminated by consideration of the fracture toughness of the vessel material. Sammonds (1988) describes the modes of failure of pressure vessels in detail and highlights the case of contrast between ductile and brittle failure. For different crack orientations within solid bodies, the stress intensity factor, K, has the general form

$$K = \sigma\sqrt{Q\pi a} \tag{I.6}$$

where σ is the tensile stress, Q is a factor dependant on the geometry and a is a parameter associated with the size of the crack. (Lawn, 1993). Brittle failure will only occur if K exceeds the fracture toughness K_c. This premise leads to a critical fracture size and associated tensile stress necessary before brittle failure can occur. Thus, by estimating the hoop stress in the vessel and the largest flaw the vessel can contain we can determine whether K in the vessel exceeds K_c for Hastelloy C22. This will provide a failure criterion we can apply to determine the likely mode of failure.

For a thick walled vessel the maximum hoop stress is at the inner bore. This is a tensional force, the magnitude of which can be found using standard tables (Young, 1989).

$$\sigma_2 = P\frac{\left(a^2 + b^2\right)}{\left(a^2 - b^2\right)} \tag{I.7}$$

where σ_2 is the hoop stress, P the internal pressure and a and b the outer and inner diameter of the vessel. For the fracture mechanics cell pressure vessel, this means σ_2 = 2.06 P, where P is the confining pressure. The largest perpendicular circular crack that could be contained within the wall of the vessel will have a radius equal to half the wall thickness. The best approximation to a circular crack in a thick walled vessel is the case of an elliptical surface crack in a semi-infinite body for which the Q factor (I.6) is $1.2/\Phi^2$ where Φ depends upon the geometry of the crack but is $\pi/2$ for a semicircular crack. The vessel wall thickness = 33.5mm (which must be the limiting crack radius) and therefore K, the stress intensity factor, is equal to

$$2.06\times P\times\frac{1.2}{(\pi/2)^2}\sqrt{\pi\times 0.0335}\approx 0.325P \tag{I.8}$$

where P is the vessel confining pressure in the vessel.

Vessel confining pressure /MPa	Maximum Stress intensity factor, K MPa.m$^{1/2}$
10	3.25
20	6.5
30	16.25

Table I.3. Maximum vessel stress intensity factors.

In order to assess the failure mode, the fracture toughness of Hastelloy C22 must be known. There is currently little experimental data on this subject but comparisons with other metals can be used to approximate a value. A survey of available literature (Stephens *et al.*, 1978; Groves and Wallace 1977; Venne, 1975; Floreen, 1976) yielded 30 values of K_c for a variety of steels and alloys and for aluminium bar (Calister, 1994). K_c of aluminium was found to be 36MPa.m$^{1/2}$ whilst the fracture toughness of steels and alloys, which span the UTS and yield strengths of Hastelloy C22, ranged from 50 to 170MPa.m$^{1/2}$ at room temperature. It is therefore almost certain that the fracture toughness of Hastelloy C22 is much greater than the critical stress intensity factor required for brittle failure in the fracture mechanics cell pressure vessel so that this mode of failure can be discounted.

I.4. Penetration of safety barricade by ejected fragments.

The vessel and associated fittings are encased in a dural housing 10mm thick with top and bottom plates made from 22mm mild steel. This study attempts to deal with the possible modes of failure as fully as possible and attaches safety margins on top of those suggested by the HPTA guidelines where necessary.

Failure of the vessel by mode 1 is thought to be extremely unlikely and it is thus most important to classify the mode 2 or 3 effects of fitting/end-closure failure. This treatment is also relevant of to the case of ductile failure with the ejection of a projectile 'sliver' (Sammonds, 1988). To assess the risk of penetration of the barrier in the event of a failure, the geometry of the apparatus must first be considered. Most of the fittings and bolts are at the top of the vessel and so it is very unlikely that an end closure would be ejected anywhere other than upwards. The dural barricade is intended to protect against small projectiles such as slivers ejected from ductile failure (Sammonds, 1988) or ricocheting small fittings caused by local failures. HPTA (1975) provides a penetration equation for dural barricades by small fragments (I.9). In order to apply this equation, real situations must be simplified whilst keeping a satisfactory margin for safety. It is therefore assumed that ejected masses are cylindrical and that the pressure within the vessel acts upon the ejected mass for a distance of 50mm. This is greater than the thickness of the vessel wall and so is applicable to fragment ejection due to ductile failure of the vessel. In addition, 50mm is greater than the length of the thread of the taper-seal fittings such as T-pieces, valves and elbow-joints and so would apply equally to failure of the joints.

Simple mechanics can be used to assess the kinetic energy of fragments with varying masses. Obviously, as the force scales with the square of radius, the geometry of the fragment is important. To simplify matters, it has been assumed that the fragments are cylinders with diameter equivalent to their length. This leads to an expression for kinetic energy (and therefore velocity) as a function of mass, which has been plotted in fig. I.4 for objects less than 10 grams (10mm diameter cylinder) to greater than 1.0kg (30mm diameter cylinder). This graph can then be used in conjunction with the HPTA (1975) equations for penetration of dural by blunt objects to calculate the effectiveness of the barrier.

$$\text{Penetration} = 8 \times 10^{-5} m^{1/3} V \qquad \text{(I.9)}$$

where V is the fragment velocity, m is fragment mass.

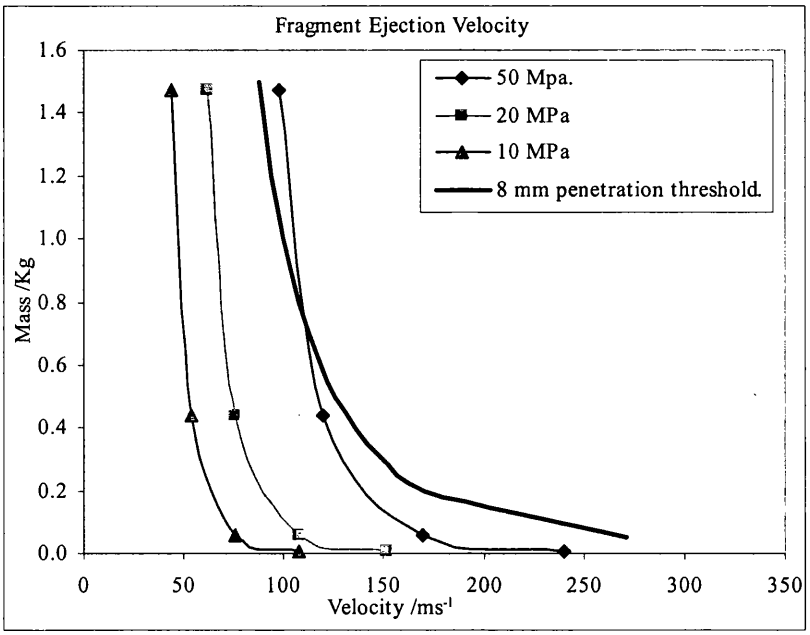

Fig. I.4. Ejection of fittings. Ejected fragments to the right of the dark line may penetrate 8mm or more. 8mm was used as opposed to 10mm to provide a measure of safety. The diagram shows that only the ejection of large fittings (more massive than a valve) at pressures of 50 MPa or more would penetrate the barrier.

Mode 2 failure of the vessel was felt to be unlikely at the low pressures used in this project, but end closures will generally have large kinetic energy and an assessment of their penetrating power is required for the sake of completeness. The only way a closure failure could occur is if the top retaining nuts failed and the entire top closure was ejected. This would have a mass of approximately 15kgs and a circular cross section of $0.05m^2$. The ejection velocities for the top closure are shown in table I.4, below. It should be noted, however, that even at 50MPa, the force on each of the twelve large retaining nuts is only 32 kN. The 75% yield strength for M16 steel bolts is approximately 70 kN. This means there is a large safety margin before failure of the bolts and hence ejection of the top closure is very unlikely.

Confining pressure /MPa	Ejection velocity $/ms^{-1}$	Penetration depth /mm
10	60	1
20	83	2
50	125	4

Table I.4. Top closure ejection velocities. Penetration depth estimated using HPTA (1975) equation for penetration by large projectiles (I.10).

$$\text{Penetration depth, } t = \frac{Cm}{A}\log\left(1 + 5\times10^{-5}V^2\right) \qquad (I.10)$$

where m is the fragment mass (5kg), A is the fragment face area ($0.03m^2$), C is the estimated penetration coefficient ($0.5x10^{-4}$) and V is the velocity.

The penetration thickness for all pressures is less than 4mm. The conclusion is that the top barricade is sufficient to protect against fragment penetration for all failure modes at 50MPa or less.

I.5. Penetration of barricade by shock wave.

Consideration of a mode two 2 failure is incomplete without including analysis of shock wave energies. One method of assessing this to use explosive energy TNT equivalents where 1 kg of TNT ≡ 4,500 kJ, (HPTA, 1975).

Pressure /MPa.	Mode 2 shock wave energy /kJ.	Mode 2 shock wave energy /g TNT equivalent.
10	10.7	2.5
20	20.5	4.0
50	46.7	10.5

Table I.5. Shock wave TNT equivalents.

The dural barricade surrounding the vessel can be treated as a sealed cubicle. Thus, the equivalent static pressure on the cubicle for a shock wave can be calculated using the HPTA (1975) standard equation

$$P = 7.6\left[\left(E/10^6\right)/V\right]^{0.72} \quad bar. \tag{I.11}$$

where P is the equivalent static overpressure, E is the shock wave energy and V the volume of the cubicle, here 0.24 m^3 (See HPTA, 1975, for qualifications).

Confining Pressure /MPa	Shock wave equivalent static over pressure /MPa	Force per side /kN
10	0.08	47
20	0.13	76
50	0.23	135

Table I.6. Equivalent shock wave static overpressure.

Each side of the vessel is fixed by 10 M6 steel bolts. These have a 75% yield strength of 8kN. Therefore, the design of the cubicle is sufficient to prevent damage to the cubicle at the pressures used in this study (<20MPa) but reinforcement of the barricades is necessary if higher pressures are to be used. To assess whether the shock

wave will be transmitted through the shielding, the impulse on the wall of the cubicle must be calculated (HPTA, 1975).

$$I = 0.024E^{1/3}\left(R/E^{1/3}\right)^{-1.2} \qquad (I.11)$$

Where I is the impulse, E is the shock wave energy and R is the distance to the wall from the vessel (0.15m). The initial, velocity of the wall due to this impulse can then be calculated using

$$V = I/M \qquad (1.12)$$

where V is the initial velocity of the wall and M the mass of the cubicle wall per m^2 ($35kgm^{-2}$) and M is the mass per unit area of the barricade ($35kgm^{-2}$.

Confining Pressure /MPa	Wall Velocity /ms^{-1}
10	2.0
20	3.2
50	5.9

Table I.7. Initial wall velocities for shock wave transmission.

HPTA (1975) guidelines suggest that there is only risk of eardrum damage if V is greater than $10ms^{-1}$ and so I conclude that the cubicle is sufficient to prevent transmission of the shock wave.

I.6. Conclusions.

Fracture mechanics considerations of the behavior of the vessel show that catastrophic brittle failure is extremely unlikely. The only possible modes of failure are the expulsion of the end closure, ductile failure or local fitting failure. At the pressures and temperatures used in this study (<20MPa and <900K) the barricades are sufficient to prevent penetration of fragments or fittings for any of these modes of failure. In addition, the shock wave generated in the unlikely event of a mode 2 failure is insufficient to be of any danger to operators owing to the shielding effects of the cubicle.

Appendix II

Fieldwork logs.

II.1. Tanzania natrocarbonatite sample collection, 29/3/99-10/4/99

29/3/99. Overnight flight to Nairobi airport.

30/3/99. Arrived at Nairobi early morning. Met driver and drove into Nairobi to find the shipping company to pick up the rock saw. The Rock saw was held by customs until the following day. Purchased supplies and food for the next two weeks and met with Tony Church, owner of Safaris Unlimited, the company responsible for loan of 4WD and tents.
Stayed in a Hotel in Nairobi.

31/3/99. Collected rock saw from shipping company and drove to Tanzania to meet representatives of Ministry of Energy and Minerals in Arusha. Arranged to return the next day to meet Zonal Mines Officer and to collect maps.
Camped overnight near Arusha.

1/4/99. Heavy rain overnight. Drove to Arusha and made arrangements for export of rock samples.
Drove to Engare Sero, the village near the base of Oldoinyo Lengai. The journey was very hard along hazardous tracks.
Set up camp and contacted local guide and porters.

2/4/99. Heavy rain overnight. A group of tourists were unable to climb Lengai the previous night owing to flooding of lower approaches.
Reconnoitred lower slopes and discovered a passable route to the setting off point.
Toured local area of rift valley, investigated some small cones.

3/4/99. Little rain overnight. Drove approx. 10 km to set off point and began climb at 4.00 am
By dawn, the summit was visible and was cloaked with 'mist'.
Reached summit at 10.30 am and rested for an hour.
Mist appeared to be produced by evaporation of water owing to a recent eruption. Some flows were still hot to touch but no fluid lava was visible. There was extensive fumaroles activity in the crater.
Mist cleared by the afternoon and allowed extraction of two large blocks of dense lava using the rock saw and a sturdy rock hammer.
Porters carried rock-saw and one block of lava down volcano. The weather was fine until the rocks were packaged in plastic with silica gel, then rained heavily.
Prepared camp on crater rim well away from fumeroles.

4/4/99. Camped overnight on crater rim. Very heavy rain overnight. Mist so thick in crater that walking around became dangerous.
Began descent at 12.00. The first part of the descent was highly dangerous owing to heavy packs, steep slopes and difficult footing. Heavy rain added to these problems.
Met up with 4WD at 5.00 and drove back to camp

5/4/99. Confined to camp due to illness/exhaustion. Packed rocks in new airtight/waterproof bags and added more silica gel.

6/4/99. Broke camp at Engare Sero and drove to campsite near Arusha to make camp.

7/4/99. Drove to Arusha and met Zonal Mines Officer. The rocks were packed and sealed with an official stamp.
Returned to camp near Arusha. Very heavy rain.

8/4/99. Drove to Nairobi and checked into Hotel.

9/4/99. Arranged return shipping for rock-saw and samples.
Flew overnight back to London.

10/4/99. Arrived London early morning.

II.2. Iceland basalt sample collection, 28/8/99-1/9/99.

28/8/99. Arrived Reykjavik late afternoon. Booked into Youth Hostel. Arranged to meet Kirsty Langley (MSci student working in Reykjavik) next day.

29/8/99. Met Kirsty, Dr Cathy Stafford and Nick Ross (geophysicists undertaking fieldwork in Iceland) and Haldor Torfason (geologist working for HOFDI Asphalt plant) at 9.30am.
Drove to 'Seljadalur' quarry, 20-30 km East of Reykjavik.
Haldor left once he had shown us the way. Examined broken basaltic joint-columns for best samples. Loaded 10 blocks into 4WD and took them back to Youth Hostel Campsite. Returned in the afternoon and collected 11 more blocks.

30/8/99. 9.00am Went to Icelandic Institute of Natural History (on same block as Natural History museum) to collect export licence.
10.00am took all 21 blocks of basalt to Eimskip shipping company (close to Youth Hostel) and had them wrapped and palletted.
1.00pm drove up to Glacier with Cathy and Nick to visit their field area.

31/8/99. a.m. Spent morning on glacier. Visited coring sites and inspected apparatus.
p.m. Went to Gulfoss (spectacular waterfall into canyon) and Geyser (where there is a large geyser).

1/9/99 a.m. Flight back to England.

References

Abbot, M. M and Ness, H. C., Theory and problems of thermodynamics, 2nd edition, McGraw-Hill, New York, 1989.

Anderson, E. M., The dynamics of faulting and dyke formation with applications to Britain, 2nd edition, Oliver and Boyd, Edinburgh, United Kingdom, 1951.

Anderson, F. S. and Smrekar, S. E., Tectonic effects of climate change on Venus, J. Geophys. Res., 104, 30,743-30,756, 1999.

Ashby, M. F. and Hallam, S. D., The failure of brittle solids containing small cracks under compressive stress states, Acta. Metall., 34, 497-510, 1986.

Atkinson, B. K., Subcritical crack propagation in rocks: theory, experimental results and applications, J. Struct. Geol., 4, 41-56, 1982.

Atkinson, B. K. (Editor), Fracture mechanics of rocks, Academic Press, London, England, 1987.

Atkinson, B. K. and Meredith, P. G., Stress corrosion cracking of quartz: a note on the influence of the chemical environment, Tectonophysics, 77, T1-T11, 1981.

Atkinson, B. K. and Meredith, P. G., The theory of subcritical crack growth with applications to minerals and rocks, in Atkinson, 1987.

Ayling, M. R., Meredith, P. G., Murrell, S. A. F., Microcracking during triaxial deformation of porous rocks monitored by changes in rock physical properties, I. Elastic-wave propagation measurements on dry rocks, Tectonophysics, 245, 205-221, 1993.

Bailey, N. T. J., Statistical methods in Biology, English University Press, London, England, (corrected version) 1964.

Baker, V. R., Komatsu, G., Parker, T. J., Gullick, V. C., kargel, J. S., Lewis, J. S., Channels and valleys on Venus: Preliminary analysis of Magellan data, J. Geophys. Res., 97, 13,421-13,444, 1992.

Banerdt, W. B. and Golombek, M. P., Deformational models of rifting and folding on Venus. J. Geophys. Res., 93, pp 4,759-4,772, 1988.

Banerdt, W. B. and C. G. Sammis, Small-scale fracture patterns on the volcanic plains of Venus, J. Geophys. Res., 97, 16,149-16,166, 1992.

Barenblatt, G. I., The mathematical theory of equilibrium cracks in brittle fracture. Adv. Appl. Mech., 7, 1962.

Barriot, J. P., Vales, N., Balmino, G., Rosenblatt, P. A., 180th degree and order model of the Venus gravity field from Magellan line of sight residual Doppler data, Geophys. Res. Let., 25, 3743-3746, 1998.

Barsukov, V. L., Venusian Igneous Rocks, in Barsukov, V. L., Basilevsky, A. T., Volkov V. P., Zharkov V. N., (Editors), Venus, Geology, Geochemistry and Geophysics, University of Arizona press, Tucson, 1992.

Baslilevsky, A. T., Concentric wrinkle ridge pattern around Sif and Gula (Abstr.), LPSC XXV, 63, 1994.

Basilevsky, A. T., Head, J. W., Schaber, G. C., Strom, R. G., The resurfacing history of Venus, in Bougher *et al.*, 1997.

Basilevsky, A. T. and Head, J. W., The geologic history of Venus: A stratigraphic view, J. Geophys. Res., 103, 8,531-8544, 1998.

Bazant, Z. P. and Cedolion, L., Stability of structures: elastic, inelastic, fracture and damage theories, Oxford University Press, Oxford, 1991.

Bentham, J. P. and Koiter, W. T., Asymptotic approximations to crack problems, in Sih, 1973.

Bilotti, F. and Suppe, J., The global distribution of wrinkle ridges on Venus, Icarus, 139, 137-157, 1999.

Bougher, S. W., Hunten, D. M., Phillips, R. J. Venus II: Geology, Geophysics, Atmosphere, and Solar Wind Environment, University of Arizona Press, Tucson, 1997.

Bowman, D. D., C. G. Sammis, W. B. Banerdt. Spacing distributions and intersection angles for kilometre scale lineations on the plains of Venus (Abstr). LPSC XXVI, 155, 1994.

Bowman, D. D. and C. G. Sammis, Implications of small-scale fracturing on Guinevere Planitia (Abstr.), LPSC, XXV, 155, 1995.

Brown, E. T. and Hoek, E., Determination of shear failure envelope in rock masses, J. Geotech Eng. Div. Am. Soc. Civ. Eng., 114, 371-376, 1988.

Brown, G. J. and Reddish, D. J., Experimental relations between rock fracture toughness and density, Int. J. Rock Mech. Min. Sci., 34, 153-155, 1997.

Bubshey, R. T., Munz, D., Pierce, W. S., Shannon, J. L., Compliance calibration of the short rod chevron notch specimen for fracture toughness testing of brittle materials, Int. Journal of Fracture, 18, 2, 125-133, 1982.

Bullock, M. A. and D. H. Grinspoon, Geological forcing of surface temperature on Venus (Abstr.), Lunar Planet. Sci.(CD-ROM) XXIX, abstract no. 1542, 1998.

Calister, W., Material Science and Engineering: An Introduction, 3rd Edition, John Wiley & Sons, London, 1994.

Chen, Y. and Johnston, D. H., Dynamic and static moduli, Geophys. Res. Lett., 8, 39-42, 1981.

Church, A. A., The petrology of the Kerimasi carbonatite volcano and the carbonatites of Oldoinyo Lengai with a review of other occurrences of extrusive carbonatites, PhD thesis, Univ. of London, London, 1995.

Clarke, J. R. (Editor), Handbook of physical constants, Geological Society of America, Memoir 97, 1966.

Copp, D. L., Observations of stratigraphy and volcanism from Guinevere and Sedna Planitae: Venus, PhD Thesis, Univ. of London, London, 1997.

Copp. D. L. and Guest, J. E., Sedna Planitia Quadrangle, V19; Venus, unpublished.

Copp. D. L. and Guest, J. E., Sif Mons Quadrangle, V31; Venus, U.S. Geological Atlas of Venus, U.S. Geol Surv., in review, 2000.

Dawson, D., Sodium carbonatite extrusions from Oldoinyo Lengai, Tanzania: Implications from carbonatite complex genesis, in Bell, K. (Editor), Carbonatites, genesis and evolution, Unwin-Hyman, London, 1989.

Din, F., Thermodynamic functions of gases, Butterworths Scientific Publications, London, 1956.

Dobson, D. P., Jones, A. P., Rabe, R., Sekine, T., Kurita, K., Taniguchi, T., Kondo, T., Kato, T., Shimomura, O., Urakawa, S., In-situ measurement of viscosity and density of carbonate melts at high pressure, Earth and Plan. Sci. Letters, 143, 207-215, 1996.

Evans, B., Fredrich, J. T. and Wong, T-F., The brittle ductile transition in rocks. Recent experimental and theoretical progress, in Duba, A.G., Durham, W. B., Handin, J. W. and Wang, H. F. (Editors), The Heard Volume- The brittle ductile transition in rocks, American Geophysical Union, Geophysical Monograph 56, 1-21, 1990.

Evans, J.P., Textures, deformation mechanisms and the role of fluids in the cataclastic deformation of granitic rocks, In Snipe, R. J. and Rutter, E. H. (Editors), Deformation

mechanisms, rheology and tectonics, Geological Society special edition, No. 54, 29-39, 1990.

Fagents, S.A. and Wilson, L., Explosive volcanism on Venus: transient volcanic explosions as a mechanism for localized pyroclast dispersal. J. Geophys. Res. 100, 26,327-26,338, 1995.

Fegley, B., Klingelhofer, G., Lodders, K., Wideman, T., Geochemistry of surface-atmosphere interactions on Venus, In Bougher *et al.*, 1997.

Ford, J. P. and Pettengill, G. H., Venus topography and kilometre scale slopes, J Geophys. Res., 97, 13,103-13,114, 1992.

Ford, J. P., Plaut, J. J., Weitz, C. M., Farr, T. G., Senske, D. A., Stofan, E. R. Michaels, G., Parker, T. J., Guide to Magellan image interpretation, JPL publication 93-24, 1993.

Foster, A. and Nimo, F., Comparison between the ridt systems of East Africa, Earth and Beta Region, Venus, Earth Plan. Sci. Let., 143, 189-195, 1996.

Floreen, S., The Fracture Toughness of Cast High Strength Steels, Journal of Engineering, 1976.

Fowler, C. M. R., An introduction to global geophysics, Cambridge University Press, United kingdom, 472pp, 1990.

French, R.H., Open channel hydraulics, McGraw Hill, New York, 1994.

Frost, H. J. and Ashby, M. F., Deformation-mechanism maps, Pergammon Press, Oxford, 1982.

Garvin, J. B., Head, J. W., Zuber, M. T., Helfenstein, P., Venus: The nature of the surface from Venera panoramas, J. Geophy. Res., 89, 3381-3399, 1984.

Gdoutos, E. E., Fracture mechanics. An introduction, Kluwer Academic Publishers, Dordrecht, 1993.

Geyer, J. F. and Nemat-Nasser, S., Experimental investigation of thermally induced interacting cracks in brittle solids, J. Solids Structures, 18, 349-356, 1982.

Glover, P. W. J., Baud, P., Darot, M., Meredith, P. G., Boon, S. A., LeRevalec, M., Zoussi, S., Reuschle, T., α/β phase transition in quartz monitored using acoustic emissions, Geophys. J. Int., 120, 775-782, 1995.

Gregg, T. K. P., and Greeley, R., Formation of Venusian canali: Considerations of lava types and their thermal behaviours, J. Geophys. Res., 98, 10,873-10,882, 1993.

Griffith, A. A., The phenomenon of rupture and flow in solids. Phil. Trans. Roy. Soc. London. 221 A587, 163-198, 1920.

Griffith, A. A., the theory of rupture, In Biezeno, C. B. and Burgers, J. M. (Editors), Proc. 1st Int. Congr. Appl. Mech., J. Waltman Jr, Delft, 54-63, 1924

Griggs, D. T and Handin, J (Editors), Rock deformation, Geol. Soc. Am. Memoir 79, pp193-226, 1960.

Grimm, R. E. and Hess, P. C. The crust of Venus, in Bougher, *et al.*, 1997.

Groves, M. T. and Wallace, J.F, Plane strain fracture toughness of cast and wrought steels, Journal of Steel Castings Research, No. 80, 1977.

Gudmundsson, A., Stress estimates from the length/width ratios of fractures, J. Struct. Geol., 5, 623-626, 1983.

Gudmundsson, A., Geometry, formation and development of tectonic fractures on the Reykjanes peninsula, southwest Iceland, Tectonophysics, 95, 295-307, 1987.

Guéguen, Y. and Palciauskas, V., Introduction to the physics of rocks, Princeton University Press, Princeton, New Jersey, 1994.

Guest, J. E and Stofan, E. R., A new view of the stratigraphic history of Venus, Icarus, 139, 55-66, 1999.

Guest, J. E., Bulmer, M., H. Aubele, J., Beratan, K., Greeley, R., Head, J. W., Michaels, G., Weitz, C., Wiles, C., Small volcanic edifices and volcanism in the plains of Venus, J. Geophys. Res, 97, 15,949-15,966, 1992.

Hall. A., Igneous Petrology, Longman Scientific and Technical Press, Harlow, England, 1987.

Hartranft, R. J. and G. C., Alternating method applied edge and surface crack problems in Sih, 1973.

Harvey, J. F., Pressure component construction, design and materials application, Van-Nostrand Reinhold, New York, 1980.

Hashimoto, G. L., Abe, Y., Sasaki, S., Maximum CO_2 amount on Venus: Present and past (Abstr.), LPSC XXVII, 1996.

Haynes International, Hastelloy C-22 data sheets, Haynes International publication, Manchester, 1998.

Head, J. W. and Wilson, L. Magma Reservoirs and neutral buoyancy zones on Venus: Implications for the formation and evolution of volcanic landforms, J. Geophys. Res., 97, 3877-3903, 1992.

Heard, H. C., Transition from brittle fracture to ductile flow in Solohofen Limestone as a function of temperature, confining pressure and interstitial fluid pressure, In Griggs and Handin, 1960.

Herrick, R. R. Resurfacing history of Venus, Geology, 22, 703-706, 1994.

High Pressure Technology Association, High pressure Safety Code, High Pressure technology Association publication, 1975.

Hu, M. S. and Evans, A. G., The cracking and decohesion of thin films on ductile substrates, Acta Metall., 37, 917-925, 1989.

Huack, S. A., Phillips, R. J., Price, M. H., Venus: crater distribution and plains resurfacing models, J. Geophy. Res., 103, 13,625- 13,642, 1998.

Hulme, G., Turbulent lava flow and the formation of Lunar Sinuous Rilles, Modern Geology, 4, 107-117, 1973.

Incropera, F. P. and DeWitt, D. P., Fundamentals of heat and mass transfer (fourth ed.), John Wiley and sons, New York, 1996.

Inglis, C. E., Stresses in a plate due to the presence of cracks and sharp corners, Trans. Inst. Nav. Archit., 55, 219, 1913.

Irwin, G. R., Fracture, In Flugge, S. (Editor), Handbuch der physik, Springer-Verlag, Berlin, 245-251, 1958.

ISRM Commission on testing methods, Suggested methods for determining the fracture toughness of rock. Int. J. Rock mech. Min. Sci. & Geomech. Abstr., 25, 71-97, 1988.

Jaeger, J. C. and Cook, N. G., Fundamentals of rock mechanics, 2nd ed., Chapman and Hall, London, England, 1976.

Johnson, C. L. and D. T. Sandwell, Joints in Venusian lava flow, Journal of Geophys. Res., 97, 13,601- 13,610, 1992.

Jones, C., Sammonds, P., R., Murrel, S.A.F., Meredith, P. G., Laboratory experiments on extensional fracture and its coupling with fluid permeability in MOR rocks (Abstract), EOS, T32A-20, 1996.

Journal of Geophysical Research, Magellan at Venus special edition, 97, 1992.

Kargel J. S., Kirk, R. L. Fegley jr., B., Treiman, A. H., Carbonate-sulphate volcanism on Venus?, Icarus, 112, 219-252, 1994.

Keszyelthi, L. and Self, S., Some physical requirements for the emplacement of long basaltic lava flows J. Geophys. Res., 103, 27,447-27,464, 1998.

Khan, I A., Fluid mechanics, Holt, Rhinehart and Windsor, New York, 1987.

Kilburn, C. R. J., Guest J. E., Aa lavas of Mount Etna, Sicily, In Kilburn, C. R. J., Luongo, G. (Editors), Active Lavas, UCL press, London, 1993.

Komatsu G., Baker, V. R.,. Gullick, V. C., Parker, T. J., Venusian channel and valleys; distribution and volcanological implications, Icarus, 102, 1-25, 1993.

Komatsu G., and Baker, V. R., Meander properties of Venusian Channel, Geology, 22, 67-70, 1994.

Kreslavsky, M. A. and Head, J. W., Morphometry of small shield volcanoes on Venus: Implications for the thickness of regional plains, J. Geophys. Res., 18,925-18,932, 1999.

Lancaster, M. G., J. E. Guest, K. M. Roberts, Great lava fields on Venus, Icarus, 118, 69-86, 1995.

Lancaster, M.G., Guest, J. E., Magee, K. P., Great lava flow fields on Venus, Icarus, 118, 69-86, 1995.

Lawn, B. Fracture of brittle solids, Cambridge University Press, England, 1993.

Masurky, H., E. Eliason, P. G. Ford, G. E. McGill, G. H. Pettengill. C. G. Schaber, G. Schubert, Pioneer Venus radar results: Geology from images and altimetry, J. Geophys. Res., 85, 8, 232-8,260, 1980.

Matsuki, K., Hasibuan, S., Takahashi, H., Specimen size requirements for determining the inherent fracture toughness of rocks according to ISRM suggested methods, Int. Journal of Rock. Mech. Min. Sci. and Geomech. Abstr., 28, 5, 365-374, 1991a.

Matsuki, K, Matsune, S, Takahashi, H., Boundary element analysis for standard specimen configurations in the ISRM suggested methods for determining the fracture toughness of rocks, Int. J. Rock. Mech. Min. Sci. and Geomech. Abstr., 28, 5, 355-363, 1991b.

McGill, G. E., Wrinkle ridges, stress domains and kinematics of Venusian plains, Geophys. Res. Lett., 20, 2407-2410, 1993.

McGill, G. E., Hotspot evolution and Venusian tectonic style, J. Geophys. Res., 99, 23,149-23,161, 1994.

McGuire, J. C., Davis,D. M., Consolmagno, S. J., Crossing fractures and the strength of Venus crustal rocks (Abstract), Lunar and Planetary Science Conference XXVII, 1996.

Meredith, P. G., A fracture mechanics study of experimentally deformed crustal rocks, PhD Thesis, University of London, London, 1983.

Meredith, P. G., Atkinson, B. K., Fracture toughness and subcritical crack growth during high-temperature tensile deformation of Westerly granite and Black gabbro, Phys. Earth Planet. Inter., 39, 33-51, 1985.

Meredith, P. G., Murrell, S.A.F., Sammonds, P.R., Jones, C., Final technical Report for NERC Research Grant GST/02/0995 (bridge 38), Submarine Rifting: Laboratory studies of tensile and extensional fracture and fluid permeability in mid-ocean-ridge rocks, Submitted January 1998.

Müller, W., Bruchzahigkeitsmessungen an geisteinin, Diplomarbeit, Institut für Geophysik, Bochum, W. Germany, 1984.

Murrell, S. A. F., the effect of high pressure on brittle fracture, Physics and chemistry of high pressures, 150-152, 1958.

Murrell, S. A. F. and Digby, P. J., The theory of brittle fracture initiation under triaxial stress conditions II, Geophys. J. R. Astron., 19, 499-512, 1970.

Murrell, S. A. F., Brittle to ductile transitions in polycrystalline, non-metallic materials, in Barber, D. J. and Meredith, P. G. (Editors), Deformation processes in minerals ceramics and rocks, Unwin Hyman, London, 1989.

Murrell, S. A. F., General report: The measurement of the properties at great depths of rocks and rock masses. In Maury, V. and Fourmaintraux, D. (Editors), Rock at great depths, Balkema, Rotterdam, 1219-1228, 1990.

Nied, H. F., Periodic array of cracks in a half plane subjected to arbitrary loading, ASME Journal Applied Mechanics, 54, 642-648, 1987.

Nimmo, F. and McKenzie, D., Volcanism and tectonism on Venus, Annu. Rev. Earth. Planet. Sci., 26, 23-51, 1998.

Nur, A., The origin of tensile fracture lineaments, Journal of Struct. Geol., 4, 31-40, 1982.

Ouchterlony, F., Review of fracture toughness testing of rock, Swed. Detonic. Res. Found., Report DS 1980, 15, Stockholm, Sweden, 1980.

Ozisic, M. N., Heat transfer, a basic approach, McGraw Hill, New York, 1985.

Pappalardo, R. T. and Greeley, R., A review of the origins of subparallel ridges and troughs: Generalised morphological predictions from terrestrial models, J. Geophys. Res., 100, 18,985-19,007, 1995.

Paterson, M. S., Experimental rock deformation: The brittle field, Springer-Verlag, Berlin, 1978.

Phillips, R. J., Raubertas, R. F., Arvidson, R. E., Sarkar, I. C., Herrick, R. R., Izenberg, N., Grimm, R. E., Impact craters and Venus resurfacing history, J. Geophys. Res., 97, 15,923-15,948, 1992.

Ranalli, G, Rheology of the Earth, Chapman and Hall, London, England, 1995.

Reidel, S.P, Emplacement of Columbia River flood basalt, J. Geophys. Res., 103 27,393-27,410, 1998.

Rist, M. A., Sammonds, P. R., Murrell, S. A. F., Meredith, P. G., Oeter, H., Doake, C. S. M., Experimental fracture and mechanical properties of Antarctic ice: preliminary results. Annals of Glaciology, 23, 284-292, 1996.

Rist, M. A., Sammonds, P. R., Murrell, S. A. F., Meredith, P. G., Doake, C. S. M., Oeter, H., Matsuki, K., Experimental and theoretical fracture mechanics applied to Antarctic ice fracture and surface crevassing, J. Geophys. Res., 104, 2973-2987, 1999.

Roberts, K.M., Guest, J. E., Head, J. W., Lancaster, G., Mylitta fluctus, Venus: Rift-related, centralised volcanism and the emplacement of large volume flow units J. Geophys. Res., 97, 15991-16015, 1992.

Rosatelli, G., Stoppa, F., Jones, A. P., Intrusive calcite caarbonatite occurrence from Mt. Vulture volcano, southern Italy, Min. Mag., 64, 615-624, 2000.

Saemundsson, K., Einarsson, S., Geological map of Iceland, sheet 3, SW-Iceland, second edition, Museum of Natural History and the Iceland Geodetic Survey, Iceland, 1980.

Sammonds, P. R., Triaxial deformation experiments on natural sea-ice as a function of temperature and strain rate, Ph.D. Thesis, Univ. of London, London, 1988.

Sammonds, P. R. Murrell, S. A. F, Rist, M. A., Fracture of multiyear sea ice, J. Geophys. Res., 103, 21,795-21,815, 1998.

Sammonds, P. R., Understanding the fundamental physics governing the evolution and dynamics of the Earth's crust and ice sheets, Phil. Trans. R. Soc. Lond., A 357, 3377-3401, 1999.

Sassolas, C., Pfeffer, T., Amadei, B, Stress interactions between multiple crevasses in glacier ice, Cold Regions Science and technology, 24, 107-116, 1996.

Schaber, G. G., Strom, R. G., Moore, H. J., Soderblom, L. A., Kirk, R.L., Chadwick, D. J., Dawson, D. D., Gaddis, L. R., Boyce, J. M., Russell, J., Geology and distribution of impact craters on Venus: what are they telling us? J. Geophys. Res., 97, 13,257-13,301, 1992.

Schmidt, R. A., in Proc. 18th U.S. Symp. Rock Mech., Keystone Colorado, 2A2/1-2A2/6, 1980.

Schubert, G., Solomatov, V. S., Tackley, P. J., Turcotte, D. L., Mantle convection and the thermal evolution of Venus, In Bougher *et al.*, 1997.

Schultz, R. A. Brittle strength of basaltic rock masses with application to Venus, J. Geophys. Res, 98, 10,883-10,895, 1993.

Schultz, R.A., Limits on strength and deformation properties of jointed basaltic rock masses, Rock Mechanics Rock Eng., 28, 1-15, 1995.

Shannon, J. L., Bubshey, R. T., Pierce, W. S. Munz, D, Extended range stress intensity factors for chevron notched short bar and short rod fracture toughness specimens, Int J. Fracture, 19, 52-58, 1982.

Sibson, R. H., Frictional constraints on thrust, wrench and normal faults, Nature, 249, pp161-163, 1974.

Sih, (Editor) Mechanics of fracture, Vol. 1, Methods of analysis and solution of crack problems, Noordhoff, Leiden (Holland), 1973.

Sjogren, W. J., Banerst, W. J., Chodas, P. W., Konopliv, A. S., Balmino, G., Barriot, J. P., Arkani-Hamed, J., Colvin, T. R., Davies, M. E., The Venus gravity field and other geodetic parameters, in Bougher *et al.*, 1997.

Smrekar, S. E., Evidence for active hotspots on Venus from analysis of Magellan gravity data, Icarus, 12, 2-26, 1994.

Smrekar, S. E., Kiefer, W. S., Stofan, E. R., Large volcanic rises on Venus, in Bougher *et al.*, 1997.

Solomon, S. C., Head, J. W., Kaula, W. M., McKensie, D., Parsons, B., Phillips, R. J., Schubert, G., Talwani, M, Venus Tectonics: Initial analysis from Magellan, Science, 252, 181-344, 1991.

Stofan, E. R., Hamilton, V. E., Janes, D. M., Smrekar, S. E., Coronae on Venus: morphology and origins, in Bougher *et al.*, 1997.

Strom, R. G., Schaber, G. G., Dawson, D. D., Kirk, R. L., The global resurfacing of Venus, J. Geophys. Res., 99, 10,899-10,926, 1994.

Tada, H., Paris, P. C., Irwin, G. C., The stress analysis of cracks handbook (3rd Ed.), ASME Press, New York, 2000.

Turcotte, D.L. and Schubert, G.,. Application of continuum physics to geological problems, John Wiley and Sons, New York, 1982.

Turcotte, D. L., An episodic hypothesis for Venusian tectonics, J. Geophys. Res., 98, 17,061-17,068, 1993.

Vargaftik, N. B., Tables on the thermophysical properties of liquids and gases, 2nd edition, Hemisphere, New York, 1975.

Venne, L. J., The application of fracture toughness criteria to steel castings, Steel Foundry Facts, No. 313, 1975.

Wall, S. D., S. L. McConnell, C. E. Leff, R. S. Austin, K. K. Beratan, M. J. Rokey, User guide to the Magellan synthetic aperture radar images, NASA reference publication 1356, Jet Propulsion Laboratory, California, 1995.

Weitz, C. M. and Basilevsky, A. T., Magellan observations of the Venera and Vega landing site segions, J. Geophys. Res., 98, 17,069-17,097, 1993.

Williams, H., and. Macbirney, A., Volcanology, Freeman Cooper and Co., San Francisco, 1976.

Williams-Jones, G., Williams-Jones, A.E., Stix, J., The nature and origin of Venusian canali, J. Geophys.Res., 103, 8,545-8,555, 1998.

Winter, R. B., Bruchmechanische gesteinsuntersuchungen mit dem bezug zu hydraulischen frac-veruchen in tiefbohrungen, Bochum, W. Germany, 1983.

Wright, D., Formation and development of fissures at the East Pacific rise: Implications for faulting and magatism at mid-ocean ridges, American Geophysical Union Geophysical Monograph 106, 137-151, 1998.

Young, W. C., Rourk's Formulas for stress and strain, McGraw Hill, New York, 1989.